

2013-01-01

# Development Of A Thermal Imaging Feedback Control System In Electron Beam Melting

Emmanuel Rodriguez

University of Texas at El Paso, [emmanuel.rodriguez129@gmail.com](mailto:emmanuel.rodriguez129@gmail.com)

Follow this and additional works at: [https://digitalcommons.utep.edu/open\\_etd](https://digitalcommons.utep.edu/open_etd)



Part of the [Mechanical Engineering Commons](#)

---

## Recommended Citation

Rodriguez, Emmanuel, "Development Of A Thermal Imaging Feedback Control System In Electron Beam Melting" (2013). *Open Access Theses & Dissertations*. 1919.

[https://digitalcommons.utep.edu/open\\_etd/1919](https://digitalcommons.utep.edu/open_etd/1919)

This is brought to you for free and open access by DigitalCommons@UTEP. It has been accepted for inclusion in Open Access Theses & Dissertations by an authorized administrator of DigitalCommons@UTEP. For more information, please contact [lweber@utep.edu](mailto:lweber@utep.edu).

DEVELOPMENT OF A THERMAL IMAGING FEEDBACK CONTROL  
SYSTEM IN ELECTRON BEAM MELTING

Emmanuel Rodriguez, B.S.M.E.  
Department of Mechanical Engineering

APPROVED:

---

Ryan B. Wicker, Ph.D., Chair

---

Eric MacDonald, Ph.D.

---

Norman Love, Ph.D.

---

Benjamin C. Flores, Ph.D.  
Dean of the Graduate School

Copyright ©

by

Emmanuel Rodriguez

2013

This Thesis is Dedicated to my Daughter and my Mom.

DEVELOPMENT OF A THERMAL IMAGING FEEDBACK CONTROL  
SYSTEM IN ELECTRON BEAM MELTING

by

EMMANUEL RODRIGUEZ, B.S.M.E.

THESIS

Presented to the Faculty of the Graduate School of

The University of Texas at El Paso

in Partial Fulfillment

of the Requirements

for the Degree of

MASTER OF SCIENCE

Department of Mechanical Engineering

THE UNIVERSITY OF TEXAS AT EL PASO

May 2013

## **ACKNOWLEDGEMENTS**

I would like to thank Dr. Ryan Wicker, director of the W.M. Keck Center for 3D Innovation (Keck Center), for presenting me with this opportunity to perform this research and for providing me with added motivation throughout this project. I would also like to thank Frank Medina, manager of the Keck Center, for giving me guidance and helping with the day to day operations of this research work. David Espalin , a research associate at the Keck Center, deserves a great deal of credit for giving me the initial motivation and guidance needed to be a researcher.

Several other student researchers in the laboratory deserve recognition for their various efforts. I would like to thank Jesus Dominguez, Jesus Castro, and David Rodriguez for their assistance in experimental setups, machining, and construction of several components. My co-workers at the Keck Center: Cesar Terrazas, Sara Gaytan, and Jorge Mireles have assisted greatly in the completion of this work. I would also like to thank Glen Liddell and Jenny Olsson with Arcam AB for providing various levels of support throughout the initial phase of the project.

Finally, I would like to express my deepest gratitude to my mom for her support and always being there when I needed her most and the rest of my family for helping me get through this great venture of higher education. My daughter, although she doesn't know it, has given me the motivation and willpower to strive for more and to never give up on anything I truly aspire to achieve.

## ABSTRACT

The scope of the project is to incorporate infrared (IR) thermal imaging in the fabrication process of Electron Beam Melting (EBM) to provide layer-by-layer feedback and ensure quality products are produced in the Arcam A2 (Arcam, Sweden) metal additive manufacturing (AM) system. Layer-by-layer build surface temperature profiles were imaged and analyzed, providing information that was used to modify build parameters (i.e. beam current, beam speed, focus offset, heating times, etc.) for proceeding build layers.

The first task completed was to make the necessary machine modifications for a successful transformation into a fully automated feedback system. In collaboration with Arcam, a pneumatic system was installed for the purpose of opening and closing a shutter mechanism to protect the infrared camera's viewing window from metallization during a build. Proceeding successful hardware installation was the development of a custom *EBM Control* (Arcam, Sweden) software version that provides "triggers" when called to allow image capture, yielding an automated image acquisition process.

With an appropriate calibration procedure developed, temperature data within an appropriate level of certainty was desired. The operator must provide the camera with several input parameters necessary to support the camera's internal measurement functions, such as, the target's emissivity and the reflected temperature. A step-by-step procedure was developed to obtain a solid metal's emissivity. Also, a mathematical model was established to determine the view factors associated with Arcam A2's heat shield. The view factors were found to be critical when seeking a true temperature value from IR measurements. Along with shield wall measurements and the view factor, it then becomes possible to determine the mean radiant temperature. The mean radiant temperature is representative of an isothermal enclosure in which radiation heat exchange with the sample equals the radiation heat exchange with the actual enclosure [Cengel, 2007].

An automated solution was achieved by using LabVIEW measurement and programming software. The duration of EBM builds varies significantly; the range may lie anywhere between 4 hours to 80 hours. It is for this reason that a major focus of this work was to produce an automated solution to acquire images throughout the entirety of a build. The images were captured at the designated process step during the build (layer) cycle and then archived making it possible to correlate the image number in the sequence to the layer number. By knowing this correlation, it is then possible to pinpoint any discrepancy or defect observed in a particular image to the location (Z-height) of the part. The IR images captured were analyzed and processed to search for “cold” spots or abnormal regions on the parts surface. Parameters were modified as necessary; parameters included the beam power (current), focusing current, scan speed, preheating time, and post-heating time. The automated image capture solution will be the gateway to achieving a fully-automated feedback control system that will make real-time parameter modification.

A core objective of this project was to obtain true temperature measurements of the surface bed, and in particular, the solid part (the melted material). To accomplish this, a blackbody radiator was fabricated, which becomes an essential tool in determining the solid material’s emissivity. This cavity-type blackbody will have radiation coming in through the opening and undergoes multiple reflections once inside allowing for the radiation to be reflected by the interior surfaces of the cavity before the radiation can escape [Cengel, 2007]. Once fabricated, the part was taken out of the machine for thorough cleaning of the internal cavity. Fabricating the radiator via EBM allows for the emissivity of interest to be in the material’s ‘EBM’ form; that is, emissivity is a function of surface morphology, and therefore the uniqueness of this surface will be the same as future builds in EBM. Experiments were then carried out to find the material’s unique property, emissivity. Emissivity of Ti-6Al-4V was found to be 0.25, and literature would prove that the value remains nearly constant up to about 760 °C before the material begins to oxidize and the emissivity increases rapidly.



Having the ability to measure surface temperatures during a build enabled this project to modify individual part-parameters for a more consistent build. An experimental setup was designed to analyze how neighboring parts would affect heat transfer to each other in comparison to the heat transfer of a single part (no neighboring parts). An IR image of the build's surface was captured after every melt cycle for the entire course of the build. The results obtained from the images demonstrate that non-uniform temperatures do exist on the build's surface area. After analyzing an IR image of a standard build at a build height equal to 36.24 mm, a temperature difference of up to 88 °C was noticed among part surfaces. The build parameters of individual parts were modified in an attempt to achieve more uniform surface temperatures. The temperature difference among the same cylinders was successfully reduced to 5 °C. The two parameters modified during the build were the speed function, which controls the scanning speed of the beam during melting, and the beam's current.

Surface temperature measurement data can be used as a tool that may assist with fabrication of unique materials, that is, materials that are not necessarily tailored for the EBM process. These data may be used to quantify the impact that various parameters have on the material being melted. Process development has been done in the past by visual inspection of the part's surface during the melting process through the observer window located in front of system's build chamber. But this requires an operator with a certain level of experience and requires lots of empirical work. By knowing the correlation between parameters and surface temperatures, the amount of experimental work can be reduced significantly.

Infrared imaging was used as a process development tool in the EBM fabrication of copper. A major obstacle when fabricating copper components via EBM was the localized swelling on parts' surfaces due to excessive heat, that is, temperature beyond the material's melting point. IR thermography allowed for the quantification of this phenomenon by measuring the parts' surface. A heat sink was implemented into copper builds that helped maintain a constant temperature across the

duration of the build. With the modified heat sink, copper parts with internal features were successfully fabricated.

# TABLE OF CONTENTS

ACKNOWLEDGEMENTS.....	v
ABSTRACT .....	vi
TABLE OF CONTENTS .....	x
LIST OF TABLES.....	xii
LIST OF FIGURES .....	xiii
CHAPTER 1 INTRODUCTION .....	1
1.1 PROJECT OVERVIEW .....	1
1.2 LABORATORY INVOLVED .....	2
1.3 ADDITIVE MANUFACTURING .....	3
1.4 ELECTRON BEAM MELTING: STATE OF THE ART .....	4
1.5 RESEARCH MOTIVATION .....	7
1.6 SUMMARY OF RESULTS .....	8
1.7 THESIS OUTLINE .....	9
CHAPTER 2 LITERATURE SURVEY .....	10
2.1 ADDITIVE MANUFACTURING .....	10
2.2 THERMOGRAPHY FOR NON-DESTRUCTIVE TESTING .....	11
2.3 HEAT TRANSFER .....	15
2.4 RADIATION PROPERTIES OF SURFACES .....	17
2.5 THERMAL EMISSION .....	21
2.5 BLACKBODY RADIATION .....	22
2.6 RADIATION HEAT TRANSFER .....	24
2.7 INFRARED TECHNOLOGY .....	27
2.8 SPECTROPYROMETER – A MULTI-WAVELENGTH PYROMETER .....	29
CHAPTER 3 EXPERIMENTAL SETUP AND PROCEDURES .....	33
3.1 ARCAM A2 SYSTEM MODIFICATIONS FOR IR CAMERA INSTALLATION .....	33
3.2 METHODOLOGY FOR IR FEEDBACK CONTROL IN ARCAM A2 SYSTEM .....	37
3.3 IR CAMERA CALIBRATION .....	39
CHAPTER 4 SOFTWARE DEVELOPMENT .....	61
4.1 AUTOMATED IR IMAGE AQUISITION .....	61

4.2 IMAGE ANALYSIS .....	79
CHAPTER 5 TECHNIQUE DEMONSTRATION AND VALIDATION .....	84
5.1 MEAN RADIANT TEMPERATURE .....	84
5.2 VALIDATION .....	87
5.3 EMISSIVITY STUDIES .....	92
5.4 FEEDBACK CONTROL DEMONSTRATION .....	96
5.5 MEASUREMENT UNCERTAINTY ANALYSIS.....	102
CHAPTER 6 INFRARED IMAGING AS A PROCESS DEVELOPMENT TOOL.....	105
6.1 ELECTRON BEAM MELTING OF COPPER.....	105
6.2 EBM FABRICATION METHOD FOR COPPER.....	110
6.2 MECHANICAL PROPERTIES OF EBM FABRICATED COPPER .....	117
CHAPTER 7 CONCLUSIONS AND RECOMMENDATIONS.....	123
7.1 CONCLUSIONS .....	123
7.2 RECOMMENDATIONS.....	126
REFERENCES .....	128
APPENDIX A IR IMAGES OF CYLINDRICAL BUILDS WITH SURFACE TEMPERATURE PLOTS .....	131
APPENDIX B VIEW FACTOR DIAGRAMS .....	163
VITA.....	166

## LIST OF TABLES

Table 3-1 External optics testing of ZnSe window- IR image parameters assigned .....	43
Table 3-2 Arcam A2 View Factors.....	60
Table 5-1 A2 Shield Temperature Measurements .....	86
Table 5-2 Mean Radiant Temperature Calculations .....	87
Table 5-3 Temperature Measurements for Validation.....	89
Table 5-4 Mean Radiant Temperature Calculations for Validation Experiment.....	90
Table 5-5 Emissivity data of Ti-6Al-4V (solid) .....	95
Table 5-7 Summary of assigned parameters for four builds.....	101
Table 5-9 Uncertainty Calculation.....	103
Table 6-1 Cu parameters.....	115
Table 6-2 Mechanical Properties of Cu .....	119
Table 6-3 Ultimate Tensile Strength of EBM fabricated Cu versus Annealed ..... <b>Error! Bookmark not defined.</b>	120
Table 6-4 Yield Strength of EBM fabricated Cu versus Annealed ..... <b>Error! Bookmark not defined.</b>	120
Table 6-5 Density of EBM fabricated Cu versus Annealed .....	122
Table A-1 Standard Build- Assigned Parameters for Build and IR Camera .....	131
Table A-2 “Cold” Build- Assigned Parameters for Build and IR Camera .....	137
Table A-3 Elevated Build- Assigned Parameters for Build and IR Camera .....	145
Table A-4 “Hot” Build- Assigned Parameters for Build and IR Camera.....	154

## LIST OF FIGURES

Figure 1-1 Schematic sequence of AM process [Brandl, E., <i>et. al.</i> , 2011] .....	4
Figure 1-2 Schematic of the electron beam column and vacuum chamber [Arcam AB, 2011].....	6
Figure 2-1 Electromagnetic spectrum [My NASA data, 2012].....	14
Figure 2-2 The absorption and reflection of incident radiation by an opaque (e.g. metal) surface.....	18
Figure 2-3 Comparison of the emissivity (a) and emissive power, (b) of a real surface with those of a gray surface and a blackbody at the same temperature [Cengel, 2007]. .....	21
Figure 2-4 Blackbody cavity with radiation interchange characteristics.....	24
Figure 2-5 Geometry for the determination of the view factor between two surfaces [Cengel, 2007]. ....	26
Figure 2-6 Schematic of the various sources of radiation that an IR camera measures. ....	28
Figure 2-7 Schematic of spectropyrrometer; from US Patents 5772323 and 6379038B [Felice, 2012]. ....	32
Figure 3-1 Removal of column assembly and camera with film drive. The O-ring surface of the lower column is covered and protected. ....	34
Figure 3-2 Top of chamber with steel “template” indicating the size and placement of holes to be drilled. ....	35
Figure 3-3 Top of Arcam A2’s build chamber with new component location and IR camera .....	36
Figure 3-4 A2 System with IR camera upgrade .....	37
Figure 3-5 Architecture for IR feedback control in Arcam A2 system .....	39
Figure 3-6 A schematic representation of the general thermographic measurement situation. 1: Surroundings, 2: Object, 3: Atmosphere, 4: Camera. [FLIR Systems AB].....	40
Figure 3-7 Common IR window transmittance at different wavelengths [IRISS, 2009] .....	42
Figure 3-8 IR image of Omega hot plate without the use of the ZnSe window .....	43
Figure 3-9 IR image of Omega hot plate with the ZnSe window installed .....	44

Figure 3-10 IR image of Omega hot plate with the ZnSe window installed and adjusted transmission parameter .....	44
Figure 3-11 Blackbody cavity .....	46
Figure 3-12 Wire frame view (with hidden lines) of blackbody cavity model specimen-cylinder (left) and rectangular prism (right) .....	47
Figure 3-13 CAD rendering of the Arcam A2 vacuum chamber with IR Camera.....	48
Figure 3-14 CAD rendering of heat shield and build platform; making a 6-surface enclosure. ....	50
Figure 3-15 CAD rendering of the bottom view of the Arcam A2 heat shield (wide).....	51
Figure 3-16 Schematic representation of surface to top shield geometric relation. ....	52
Figure 3-17 View factor between two aligned parallel rectangles of equal size [Cengel, 2007] .....	53
Figure 3-18 Schematic representation of surface to side (left) shield geometric relation. ....	55
Figure 3-19 View factor configuration: Two rectangles <b>A1</b> and <b>A2</b> , with one common edge and included angle $\phi$ between the two planes [Hamilton, 1952]. ....	56
Figure 3-20 Schematic representation of surface to rear shield geometric relation. ....	57
Figure 3-21 Schematic representation of surface to front shield.....	58
Figure 3-22 View factor between two perpendicular rectangles with a common edge [Cengel, 2007]....	59
Figure 4-1 Camera theme with assigned signal process steps .....	62
Figure 4-2 Process steps with ‘Delay’ themes for image capture .....	63
Figure 4-3 Example of Net theme parameters for ‘dummy’ build .....	64
Figure 4-4 NI cRIO 9074 modular controller.....	65
Figure 4-5 Circuit diagram of digital output A3. Courtesy of Arcam AB. ....	66
Figure 4-6 Circuit diagram of digital output A3 (cont.). Courtesy of Arcam AB.....	67
Figure 4-7 Front panel (user interface) of IR image acquisition <i>vi</i> .....	69

Figure 4-8 Block diagram – Image acquisition.vi (Module ‘A3’ Digital output/Voltage Signal - “True” state) [1/4] .....	72
Figure 4-9 Block diagram – Image acquisition.vi (“Single Snapshot Recording” - “True” state) [2/4] ...	73
Figure 4-10 Block diagram – Image acquisition.vi (Module ‘A3’ Digital output/Voltage Signal - “False” state/No signal output) [3/4] .....	74
Figure 4-11 Block diagram – Image acquisition.vi (“Single Snapshot Recording” - “False” state) [4/4]	75
Figure 4-12 Front panel – A2 Chamber – addtl TC’s.vi.....	76
Figure 4-13 Block diagram - A2 Additional TC’s.vi.....	78
Figure 4-14 IR image capture of copper cylinders after the melt cycle with the center cylinder’s temperature profile.....	81
Figure 4-15 IR image capture of Ti-6Al-4V cylinders after the melt cycle with the center cylinder’s temperature profile.....	82
Figure 5-1 Vacuum chamber with additional thermocouples put in place for heat shield temperature measurement. ....	85
Figure 5-2 Arcam A2 heat shield (wide) with cemented thermocouples .....	86
Figure 5-3 IR image of blackbody radiator with cemented on thermocouple .....	90
Figure 5-4 Temperature plot for validation experiment .....	91
Figure 5-5 Emissivity of Ti-6Al-4V (solid) with a thin layer oxide.....	93
Figure 5-6 Emissivity plot of Ti-6Al-4V .....	94
Figure 5-7 Arcam A2 build chamber CAD rendering with installed spectropyrometer .....	96
Figure 5-8 CAD model for tensile bar build.....	97
Figure 5-9 IR image of build surface at z=36.24 mm – no parameter modification .....	98
Figure 5-10 IR image of build surface at z=86.40 mm – with parameter modification. ....	99
Figure 5-11 IR image of five cylinders during EBM fabrication (standard build).....	100



Figure 6-1 Effects of copper swelling of cylinders during EBM fabrication .....	106
Figure 6-2 CAD rendering of Cu cylinders on Cu start plate.....	107
Figure 6-3 IR image of Cu cylinders .....	108
Figure 6-4 Surface temperature plot of Cu cylinders via IR (top) compared with temperature recorded via thermocouple under start plate (bottom).....	109
Figure 6-5 Surface temperature of Cu parts with incorporated time delay .....	110
Figure 6-6 CAD rendering of Cu part with incorporated heat sink.....	112
Figure 6-7 Surface temperature plot of Cu part with incorporated heat.....	113
Figure 6-8 CAD rendering of Cu part with modified heat sink.....	113
Figure 6-9 Surface temperature plot of Cu part with modified heat sink.....	114
Figure 6-10 IR image of Cu part with internal channels .....	115
Figure 6-11 Cross section of Cu part showing internal channels .....	<b>Error! Bookmark not defined.</b> 116
Figure 6-12 IR image of Cu part with observed porosity or un-melted particles.....	117
Figure 6-13 Engineering stress-strain diagram of Cu fabricated via EBM .....	118
Figure 6-14 Cu EBM fracture sample .....	118
Figure 6-15 Cu particle accelerator, or electron “gun”, prototype fabricated via EBM.....	122
Figure A-7-1 IR image of standard build cylinders at Z= 0.14 mm .....	132
Figure A-2 IR image of standard build cylinders at Z= 3.5 mm .....	133
Figure A-3 IR image of standard build cylinders at Z= 17.5 mm .....	134
Figure A-4 IR image of standard build cylinders at Z= 35.00 mm .....	135
Figure A-5 Average surface temperature measurements of all five cylinders in the standard build throughout the course of the build. ....	136
Figure A-6 IR image of cold build cylinders at Z= 0.84 mm.....	138
Figure A-7 IR image of cold build cylinders at Z= 3.5 mm.....	139

Figure A-8 IR image of cold build cylinders at Z= 17.5 mm.....	140
Figure A-9 IR image of cold build cylinders at Z= 35.00 mm.....	141
Figure A-10 IR image of cold build cylinders at Z= 52.50 mm.....	142
Figure A-11 IR image of cold build cylinders at Z= 70.00 mm.....	143
Figure A-12 Average surface temperature measurements of all five cylinders in the “cold” build throughout the course of the build. The drop in temperature at about 2000 sec was due to a system halt, due to opening the external system’s helium valve that led to a build abort, the system was then restarted.....	144
Figure A-13 IR image of elevated build cylinders at Z= 0.77 mm.....	146
Figure A-14 IR image of elevated build cylinders at Z= 3.50 mm.....	147
Figure A-15 IR image of elevated build cylinders at Z= 17.50 mm.....	148
Figure A-16 IR image of elevated build cylinders at Z= 35.00 mm.....	149
Figure A-17 IR image of elevated build cylinders at Z= 52.50 mm.....	150
Figure A-18 IR image of elevated build cylinders at Z= 70.00 mm.....	151
Figure A-19 IR image of elevated build cylinders at Z= 87.22 mm.....	152
Figure A-20 Average surface temperature measurements of all five cylinders in the elevated build throughout the course of the build. ....	153
Figure A-20 IR image of hot build cylinders at Z= 1.12 mm.....	155
Figure A-21 IR image of hot build cylinders at Z= 3.50 mm.....	156
Figure A-22 IR image of hot build cylinders at Z= 17.50 mm.....	157
Figure A-23 IR image of hot build cylinders at Z= 35.00 mm.....	158
Figure A-24 IR image of hot build cylinders at Z= 52.50 mm.....	159
Figure A-25 IR image of hot build cylinders at Z= 70.00 mm.....	160
Figure A-26 IR image of hot build cylinders at Z= 76.16 mm.....	161

Figure A-27 Average surface temperature measurements of all five cylinders in the “hot” build throughout the course of the build. ....	162
Figure B-7-2 a.) Top surface, b.) Bottom surface. The distance between both surfaces is 305 mm.....	163
Figure B-7-3 a.) Left/Right surface, b.) Bottom surface. The angle between both surfaces is 71.5° ....	164
Figure B-4 a.) Front surface, b.) Bottom surface. The angle between both surfaces is 90° . ....	164
Figure B-5 a.) Rear surface, b.) Bottom surface. The angle between both surfaces is 70.5° . ....	165

# CHAPTER 1 INTRODUCTION

## 1.1 PROJECT OVERVIEW

The scope of the project is to incorporate infrared (IR) thermal imaging in the fabrication process of Electron Beam Melting (EBM) to provide layer-by-layer feedback and ensure quality products are produced in the Arcam A2 (Arcam, Sweden) metal additive manufacturing (AM) system. Layer-by-layer build surface temperature profiles were imaged and analyzed, providing information that was used to modify build parameters (i.e. beam current, beam speed, focus offset, heating times, etc.) for proceeding build layers.

The first task in the integration of an IR imaging system in the A2 system was to make the necessary machine modifications for a successful transformation into a fully automated feedback system. In collaboration with Arcam, a pneumatic system was installed for the purpose of opening and closing a shutter mechanism to protect the infrared camera's viewing window from metallization during a build. Metallization can reduce the transmission of infrared rays and consequently reduce the acquisition of accurate temperature measurements. Proceeding successful hardware installation was the development of a custom *EBM Control* (Arcam, Sweden) software version that provides "triggers" when called to allow image capture, yielding an automated image acquisition process.

To acquire temperature data within an appropriate level of certainty, a calibration procedure was established. The operator must provide the camera with several input parameters necessary for the camera's internal measurement functions; most noteworthy is the target's emissivity. A step-by-step procedure was developed to obtain a solid metal's emissivity, the mean radiant temperature (reflected temperature), and external optics transmission. Other contributing parameters are discussed.

With the assistance of the custom EBM Control software, it was possible to successfully intercept voltage signals from the A2's output module to act as a trigger source to open and close the shutter mechanism that gives the IR camera the visual of the build surface inside the chamber. Using

the programming software LabVIEW (National Instruments, Austin, Texas), a code was developed to capture single-snapshot images during designated process steps in the layer build cycle.

The thermographs obtained from the images were analyzed to identify defects or cool temperature zones on the build's surface. An experimental setup was designed to analyze the effects of part placement on the start plate, and, in essence, providing insight to the heat transfer taking place inside the build chamber. Using the acquired surface temperature data, parameter build modifications were implemented manually to assess the impact of temperature feedback on product quality control.

Additionally, the thermal imaging system was also used as a tool to develop processing parameters for the fabrication of copper via EBM. Copper is a non-standard material in EBM technology, and due to its high thermal conductive nature, it was quite a challenge to maintain a constant temperature throughout the fabrication process for appropriate melting with the electron beam. Surface temperatures versus layer plots were attainable due to the infrared images acquired during the parameter exploration phase; the plots were found to be a big advantage in the time to successfully develop optimal processing conditions. Finally, the feasibility of full and automated implementation of the IR imaging system in a closed-loop control algorithm for part fabrication within the existing Arcam A2 EBM machine is discussed.

## **1.2 LABORATORY INVOLVED**

The work accomplished for this thesis was completed at the W.M. Keck Center for 3D Innovation (Keck Center) within the University of Texas at El Paso (UTEP) Mechanical Engineering Department. In 2000, the state-of-the-art additive manufacturing laboratory was established through a grant from the W.M. Keck Foundation and has been growing in research and innovation since. The Keck Center was recently awarded funding from the Texas Emerging Technology Fund (ETF), the University of Texas System and industry partners that resulted in an expansion to over 13,000 square feet [Office of research and sponsored projects, 2012].

The center now houses more than 40 AM machines, both commercial and experimental, consisting of at least 10 distinct layer processing methods, with several custom AM-based patented and patent-pending systems [Wicker, 2012]. The laboratory has over 50 actively involved faculty, staff, and students in various multi-disciplinary projects. The wide scope of these research projects may include manufacturing functional devices that include 3D structural electronics, metallic structures of numerous alloys for the aerospace and medical industry, cardiovascular flow research, and tissue engineering [Wicker, 2012]. The lab's researchers have access to combined facilities for advanced manufacturing and machining, reverse engineering, metrology and inspection, materials characterization and testing, and experimental fluid mechanics [Office of research and sponsored projects, 2012]. The facility hosts more than 1,000 visitors each year to people ranging from artists, K-12 students, educators, to various high-level government and industrial scientists and engineers.

### **1.3 ADDITIVE MANUFACTURING**

Many see additive manufacturing as the “renaissance in manufacturing”, especially to those economies associated with high-technology industries [Murr *et. al*, 2009]. The technology did not always have this optimistic outlook, during its early development the process was known to many as rapid prototyping (RP). The emphasis was on creating something quickly with the output being a prototype or basis model for manufacturing further design models and eventually the final product [Gibson, *et. al.*, 2010]. Users of RP technology have come to realize that this term is insufficient and does not fully describe the more recent applications of AM. Improvements in the fabrication process and raw material have closed the gap between “prototypes” to the final product in various AM technologies.

The basic principle of AM technology is that a model, initially a three-dimensional model generated using computer aided design (CAD) software, can be fabricated without any specialized tooling for the uniqueness of the model. AM technology certainly simplifies the process of producing complex 3D parts, as opposed to other manufacturing process that require detailed analysis of the part

geometry to consider things such as the order in which different features will be fabricated, what tools and processes need to be used, and any additional fixtures that may be required to successfully fabricate the final part [Gibson, *et. al.*, 2010].

AM parts are created by taking its respective 3D CAD model “slicing” it into successive layers of a specified thickness, this slicing is done by special software that will output digital data that can be read by the AM machine. The AM parts are made by adding material in layers, each of these layers is a thin cross-section of the slices already created and being interpreted by the machine (Figure 1-1). Obviously, each layer must have a finite thickness to it and so the resulting part will be an approximation of the original 3D CAD model [Gibson, *et. al.*, 2010], and hence the goal of most AM research is to replicate this CAD model to precision. The major differences between the various AM technologies are the materials that can be used, how the layers are created, and how the layers are bonded, other than that all AM machines use a layer based approach [Gibson, *et. al.*, 2010]. These differences become significant when they become the factors that will determine accuracy of the final part, material properties, mechanical properties, fabrication time, post-processing time, the size of the AM machine, and the overall cost of the machine and process [Gibson, *et. al.*, 2010].

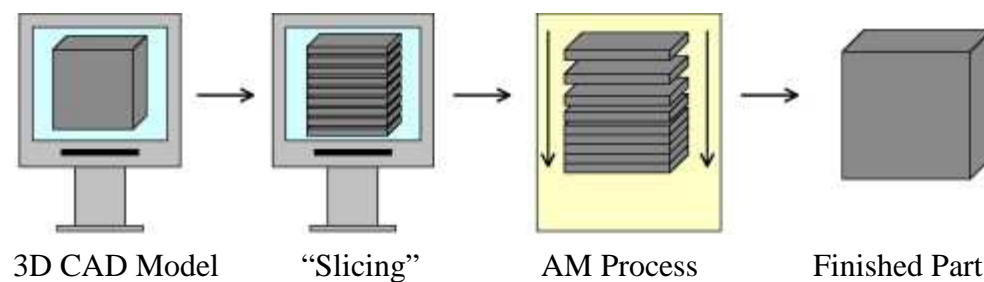


**FIGURE 1-1 SCHEMATIC SEQUENCE OF AM PROCESS [BRANDL, E., *ET. AL.*, 2011]**

#### **1.4 ELECTRON BEAM MELTING: STATE OF THE ART**

The EBM technology is a relatively new direct-metal freeform fabrication process that has been commercialized by *Arcam* [Cormier, *et. al.*, 2004]. The machine uses a metal powder (10  $\mu\text{m}$ - 160  $\mu\text{m}$  diameter) to build solid parts in layer-wise fashion inside a vacuum chamber maintained at  $10^{-4}\text{mbar}$

(Figure 1-2 Schematic of the electron beam column and vacuum chamber [Arcam AB, 2011]) by following 4 steps: 1) spreading a layer of metal powder (typically in the range 0.05 – 0.20 mm thick) across the build platform by using the machine's raking mechanism, 2) preheating the layer to approximately 50% of the metal's melting temperature (760°C for Ti6Al4V) using the electron beam gun at relatively low beam current and high scan speed (the preheating step lightly sinters the metal powder to hold it in place for subsequent melting and also transmits heat to the part that helps maintain a low thermal gradient between the melted layer and the rest of the part –greatly reducing residual stresses), 3) selectively melting the preheated powder by increasing the beam power and reducing the scan speed to effectively reach the material's melting point, and 4) lowering the build platform an amount equal to one layer thickness [Cormier, *et. al.*, 2004]. The process is repeated until the part is complete.

#### **1.4.1 THE PRINCIPLE OF THE ELECTRON BEAM**

The electron beam is generated inside the electron beam column by heating a tungsten filament to above 2000 °C by the filament current. At these high temperatures the electrons are “released” from the filament [Arcam AB, 2011]. The electron, itself, is a negatively charged elementary particle of very small matter ( $\sim 9.1 \times 10^{-31} kg$ ) [Arcam AB, 2011]. The released electrons are then accelerated within an electrical field, obtained by applying a high voltage ( $\sim 60 kV$ ) between the filament and the anode (Figure 1-2). The beam current, the number of electrons within the beam, is controlled by the control electrode, or grid cup. The beam is focused by the focusing coil, an electromagnetic coil [Arcam AB]. Figure 1-2 is a schematic of the beam column with its major parts and the vacuum chamber where the fabrication takes place.



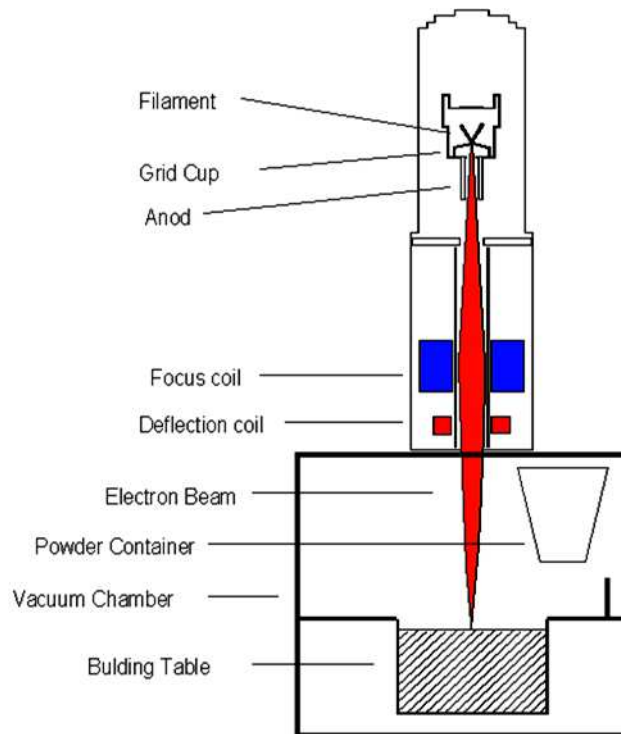


**FIGURE 1-2 SCHEMATIC OF THE ELECTRON BEAM COLUMN AND VACUUM CHAMBER**  
[ARCAM AB, 2011]

The electrons are accelerated at about 0.1 to 0.4 times the speed of light, with the energy density of the electron beam reaching  $10^6 \text{ kW/cm}^2$  [Arcam AB, 2011]. To avoid any collision of the electron beam with gas atoms, both the electron beam column and powder surface are maintained at low pressure levels of  $10^{-4} \text{ mbar}$  (vacuum environment). Once the electrons reach the powder surface, and further into the powder grains, their velocities slow to turn their kinetic energy into thermal energy [Arcam AB, 2011], effectively reaching the metal's melting point, as long as the powder is already being maintained at about half its melting point from the preheating process step. Failing to maintain the powder at this elevated temperature can cause poor melting, resulting in un-melted particles. To maneuver the electron beam, the electron beam column uses electromagnetic lenses, or deflection coils, facilitating the electron beam to scan the powder surface from one side to the other melting the metal powder at the positions corresponding to the digital data from the “sliced” CAD model.

## 1.5 RESEARCH MOTIVATION

The Electron Beam Melting process is a promising technology in the rapid manufacturing of metal components. EBM has the potential to reduce the cost of metal parts by minimizing the use of raw materials and machining time. The EBM technology has several advantages over other additive manufacturing (AM) technologies of metal, such as manufacturing speed and mechanical properties of the finished parts. For the process to be accepted in the aerospace industry as a flight-ready manufacturing technology, however, improved control and feedback must be implemented in the building process for better part quality and uniform production in manufacturing. As part of this research, an IR imaging system was implemented in an Arcam A2 EBM (Arcam AB, Sweden) system providing another level of control for the EBM process that could lead to rapid certification of flight-ready parts.

The integrated thermal-imaging system will permit defect detection on the part surface. These defects can be classified as “cold” spots on the part surface that may indicate a localized region with unmelted particles that may result in porous product. Detecting defects to a certain level of accuracy and size becomes critical when developing a closed loop feedback control system. Additionally, infrared thermography is an excellent non-contact temperature measurement tool. Measuring absolute temperature values aids in the development of process parameters for various metals that may be compatible with EBM. Maintaining a constant target temperature throughout the entirety of the build cycle becomes critical to a successful build. If the powder surface temperature is too hot, the electron beam may cause swelling or distortion of the part; if the temperature is too low, this may cause poor melting and porosity. Although, a uniform temperature is usually desired for a given build, future research activities may call upon for a part with a gradient temperature, this system yields the capacity to do both. The only feedback from the commercial Arcam A2 system (Arcam, AB) is a single temperature measurement from a thermocouple placed under the start plate, and this causes many

limitations to capabilities of the EBM technology. By having a temperature measurement of the part's surface, process parameters may be modified as necessary to reach the target temperature that will yield quality parts.

## **1.6 SUMMARY OF RESULTS**

Emissivity is a critical parameter in making IR measurements. A procedure was implemented to determine the emissivity of the unique surface of Ti-6Al-4V built components. Emissivity of Ti-6Al-4V was found to be 0.25, and literature would prove that the value remains nearly constant up to about 760 °C before the material begins to oxidize and the emissivity increases rapidly. A vital calibration procedure was established to make true surface temperature measurements of the Arcam A2's build surface.

This calibration procedure made it possible to determine several input parameters that must be assigned to the IR camera to make accurate measurements with a certain level of accuracy. Atmospheric and external optics transmission was found to be 94%. Reflective sources also need to be accounted for since an IR camera will measure not only thermal radiation being emitted by the target object but also any radiation being reflected off the sample. It is for this reason that a mean radiant temperature, or reflected temperature, needed to be calculated. This was done by determining the necessary view factors associated with the geometry of the Arcam A2's heat shield. After calculating the view factors it was then possible to use them in published formulae to determine the mean radiant temperature associated with Ti-6Al4V builds, and was found to 341 °C.

The development of process parameters for unique materials not tailored for the EBM process has shown to be lengthy and requires a lot of empirical work. Surface temperature measurements can be correlated to the various parameters being modified throughout the course of the build. In this study, IR surface measurements became a tool in developing processing parameters for non-standard materials such as copper to be used in the EBM system. Surface measurements helped quantify integrated thermal

management solutions into copper builds. The most promising solution in fabricating copper parts with internal features was to incorporate a heat sink into the build that helped in maintaining a more uniform temperature throughout the course of the build.

## **1.7 THESIS OUTLINE**

The subsequent chapters cover the literature review, experimentation, calibration, findings, and results. They are organized as follows. Chapter 2 covers a literature review of thermography for non-destructive testing, theory of infrared thermography, blackbody radiation, emissivity, heat transfer analysis, and infrared technology. Chapter 3 describes the experimental setup and procedures, the machine modifications necessary to install the IR camera, architecture for IR feedback control, and the IR camera calibration procedure. Chapter 4 covers the software development phase of the project, the initial manual IR image acquisition, automated image acquisition, and image processing. Chapter 5 provides technique demonstration and validation by presenting the necessary blackbody calibrations, emissivity studies, infrared temperature measurements, and qualification of these results. Chapter 6 introduces infrared feedback as a process development tool by discussing the process parameter development of copper in EBM, the fabrication method implemented, and mechanical properties of EBM fabricated copper samples. Finally, Chapter 7 concludes this thesis by giving final conclusions of the project and recommendations.

## **CHAPTER 2 LITERATURE SURVEY**

A background in additive manufacturing, electron beam melting technology, infrared thermography, and radiation heat transfer is essential to understand the context of this work. The following sections include a literature review that will support the data, findings, and conclusions presented in this work. There is enormous research and literature related to infrared thermography and even more on radiation heat transfer. The literature survey presented in this chapter is relevant to the present study and key contributions to the subject are cited.

Topics include the modern use of thermography for non-destructive testing and theory of infrared thermography. Important concepts pertaining to this theory include blackbody radiation, emissivity, and radiation heat transfer with an emphasis on evacuated enclosures all of which will be discussed in detail in their corresponding section. An introduction to modern infrared technology is also presented.

### **2.1 ADDITIVE MANUFACTURING**

As described in Chapter 1, every part fabricated with AM technology begins as a three-dimensional CAD model; the model is then “sliced” into successive layers of a specified thickness. This sliced model is now ready to be read by the AM machine. The AM system will fabricate the 3D model to as close precision to that of the model by successively adding material in layers. AM materials are divided into two main categories: polymers and metals. Polymer AM technologies include stereolithography (SLA), fused deposition modeling (FDM), and selective laser sintering (SLS). SLA uses laser technology to cure layer upon layer of photopolymer resin, that is, polymer that changes properties when exposed to a light source of a specific wavelength. The laser is directed into a pool of resin where it traces the cross-section of the sliced model for that particular layer and cures (solidifies) the resin. A platform that holds the part being built, is then lowered to the specified layer thickness, and begins the new layer.

The FDM process uses a polymer that changes to liquid when heat is applied, and solidifies when cooled, called thermoplastic [AM, 2013]. The material is injected, or extruded, through a nozzle onto a platform while tracing the cross-section of the particular layer; the material solidifies before the application of the next layer. SLS, or SLM for metals, technology uses a high power laser to fuse small particles of material (polymer, metal, ceramic, or glass) being dispensed into the lasers path. Like SLA, the platform is then lowered by the specified layer thickness to begin the next layer.

EBM is different from SLM in that it operates in a vacuum environment without the need for an inert gas, such as nitrogen or argon. Also, the EBM build platform is maintained at a high temperature during the fabrication process which reduces the thermal gradient between the part and platform, effectively reducing the thermal gradients. As discussed in Chapter 1, EBM makes use of a powerful electron beam to melt the metal powder; the beam is controlled by magnetic coils to correspond to the digital data from the CAD model. After the melt cycle has completed for a given layer, the platform is then lowered to the desired layer thickness, typically in the range 0.05 – 0.20 mm, the system's rake mechanism then fetches powder from the gravity-fed hoppers to re-coat the platform with a new layer of material.

## **2.2 THERMOGRAPHY FOR NON-DESTRUCTIVE TESTING**

Thermography is one of many techniques used to “see the unseen.” Generally speaking, thermography is a contactless technique that records a distribution of surface temperature. The procedures that are currently used in thermography fall under two main categories: *passive* and *active* thermography [Maldague, 2001]. In thermodynamics, temperature is an important state variable that can be used to help determine energy states as well as assist in determination of heat transfer. Heat transfer, or temperature, is an important state variable that should be measured and monitored.

In *passive thermography*, abnormal temperature profiles denote a potential problem – the temperature difference ( $\Delta T$ ) with respect to some reference that is of concern. Passive thermography is

usually a qualitative process since the goal is simply to identify irregularities. In the case of thermal modeling, the investigations provide quantitative measurements, such as relating measured surface temperatures to surface flaws [Maldague, 2001]. As an example of passive thermography, an infrared camera can be used to gather thermal data during high-speed needle sewing in the automobile industry. Understanding needle heating during high-speed operations makes it possible to optimize sewing operations through needle redesign. Due to the millions of products sewed daily (seat cushions, airbags, etc.), the implemented IR data acquisition will bring substantial economic and product quality benefits [Maldague, 2001]. The proposed thermal imaging system falls under this category.

*Active thermography* makes it necessary to bring some energy to the specimen inspected in order to obtain the required temperature differences to observe the presence of any surface anomalies and defects. Depending on the particular application, there are various methods that can be adopted. *Pulsed thermography* (PT) consists of heating the specimen from a few milliseconds for high-conductivity materials to a few seconds for low-conductivity materials and then recording the temperature decay curve. In *step heating* (SH) the increase in surface temperature is monitored during application. *Lock-in thermography* (LT) is executed by periodic deposition of heat on a specimen's surface while the resulting oscillating temperature field in the stationary regime is recorded remotely through thermal infrared emission [Maldague, 2001]. *Vibrothermography* (VT) is another common technique wherein mechanical vibrations are induced externally to a structure and heat is released by friction at locations where defects such as cracks are located [Maldague, 2001].

### **2.2.1 HISTORICAL NOTES**

Before further discussion of this state-of-the-art measurement technique, it is beneficial to turn back for some historical context on infrared technology. Heat transfer has been a concern throughout the existence of mankind. Early mankind struggled with a reliable method of creating fire by means of friction so that the fire could provide light and heat and to keep away dangerous animals. Later, good

quality metal and glass work depended on the ability of skilled artists to relate the “glowing” (brightness and color) of a gob of glass to the moment it is ready to be shaped, that is, the relationship between target temperature and emitted radiation to accomplish their work [Maldague, 2001]. Today, the concerns are possibly more sophisticated dealing with such things as weather forecasts and environmental temperature extremes.

Galileo took the first step toward accurate measurement of temperature when he designed the first glass thermometer. A few centuries later William Herschel accidentally discovered the planet Uranus on March 13, 1793 [FLIR, 2010]. It was this event that would lead him to the discovery of infrared rays. In the year 1800, the existence of the infrared portion of the electromagnetic spectrum was not known (Figure 2-1 Electromagnetic spectrum [My NASA data, 2012]). Herschel was searching for an optical filter material to reduce the brightness of the sun’s image in telescopes [FLIR, 2010]. During his tests of several samples of colored glass which gave similar reductions in brightness, he was attentive to find that some of the samples passed very little of the sun’s energy while others passed so much heat energy that he ran the risk of eye damage after only a few seconds.

This led Herschel to set up a formal and systematic experiment with the objective of finding a single material that would have the desired reduction in brightness and a maximum reduction in heat transfer. He decided to conduct an experiment that had similarly been performed by Sir Isaac Newton where a prism was used to separate the various colors of light from blue to red [Maldague, 2001]. Using a mercury thermometer, he noticed that temperature was still elevated beyond the red band where radiation was no longer visible. Unlike Newton, Herschel was the first to notice that the distance where the heating was greatest had a specific location, directing him toward the notion of the existence of different wavelengths [Maldague, 2001]. He called his discovery “invisible rays” or “rays that occasion heat.” It is now known that visible light and infrared energy are both forms of electromagnetic radiation of different wavelength and frequency. The first infrared image was produced by Herschel’s son, John



Herschel, in 1840 with the use of an evaporograph- the image was formed by differential evaporation of a thin film of oil [Maldague, 2001]. This series of events has brought infrared technology to where it is today.

## 2.2.2 THE ELECTROMAGNETIC SPECTRUM

Figure 2-1 Electromagnetic spectrum [My NASA data, 2012] shows the electromagnetic spectrum. An object's "electromagnetic spectrum" is the characteristic distribution of electromagnetic waves that the particular object will absorb or emit. The spectrum is divided subjectively into wavelength regions called "bands." Thermography uses the infrared band that is arbitrarily subdivided into four smaller bands. They are:  $0.75 \mu\text{m} \leq \text{near infrared} \leq 3 \mu\text{m}$ ;  $3 \mu\text{m} \leq \text{middle infrared} \leq 6 \mu\text{m}$ ;  $6 \mu\text{m} \leq \text{far infrared} \leq 15 \mu\text{m}$ ;  $15 \mu\text{m} \leq \text{extreme infrared} \leq 100 \mu\text{m}$ . Infrared cameras make best use of the *mid-infrared* region since hot objects such as metals radiate strongly in this range.

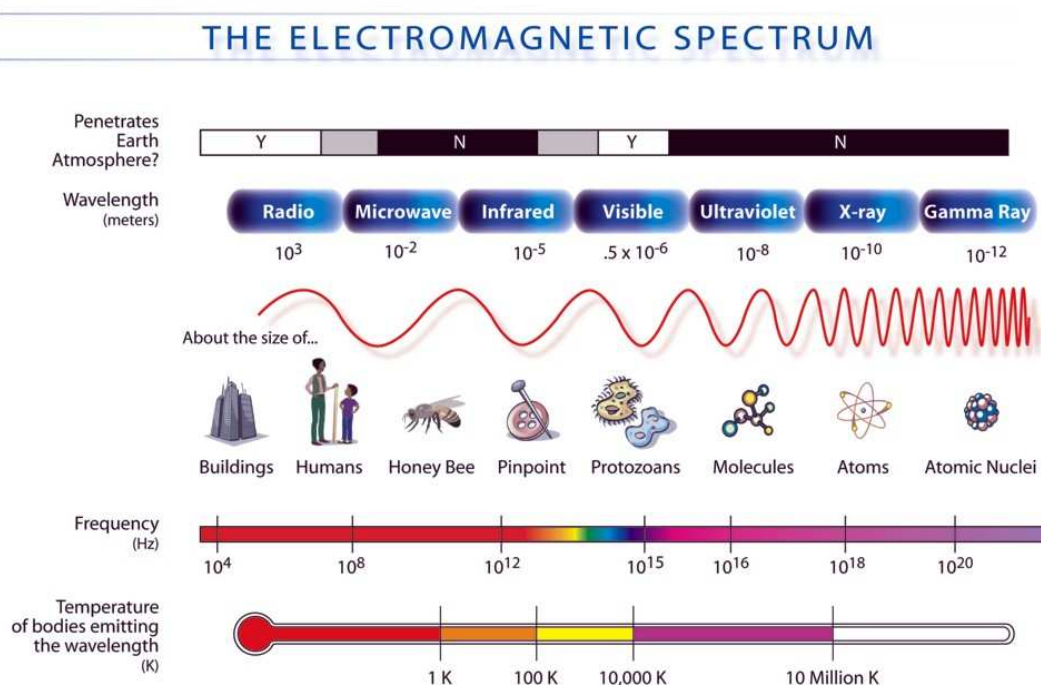


**FIGURE 2-1 ELECTROMAGNETIC SPECTRUM [MY NASA DATA, 2012]**

## 2.3 HEAT TRANSFER

A frequently asked question is the difference between thermodynamics and heat transfer. Thermodynamics deals with the study of systems in thermal equilibrium and the amount of heat transfer as a system undergoes a process from one equilibrium state to another, while heat transfer deals with the rate at which this takes place [Cengel, 2007; Maldague, 2001]. Heat transfer adds the time variable, is concerned with calculations of temperature distribution, and heat transfer exchange in a system [Maldague, 2001]. Heat may be defined as the form of energy that can be transferred from one system to another as a result of temperature difference; the science that deals with the rates of such energy transfers is heat transfer [Cengel, 2007]. Heat transfer science gives the ability to predict the energy transfer taking place between two bodies solely on a temperature difference. Such a prediction is extremely valuable in helping observe phenomena such as abnormal temperature patterns, in studying building envelopes, to compute heat losses, insulation factors, the size and position of heat sinks used repeatedly in engineering systems.

There are three basic mechanisms of heat transfer: convection, conduction, and radiation. Convective heat transfer is the mode in which heat is transferred from a surface by moving fluid (liquid or gas). It involves the combined effect of conduction and fluid motion. Heat transfer by conduction is the transfer of energy from the more energetic particles of a substance to the adjacent, less energetic ones. The rate at which heat transfer by conduction will occur has to deal with the material's thermal conductivity, denoted  $k$ , and will be introduced in the following sections as well. The final mechanism is radiation, which is the energy emitted by matter in the form of electromagnetic waves (or photons) as a result of the changes in the electronic configurations of the atoms or molecules [Cengel, 2007]. The latter two are of interest for this thesis work, since convection effects are minimal, if any, due to the system's vacuum environment. That is, there is no fluid motion taking place inside the vacuum chamber during the fabrication process since it is held at extremely low pressures ( $10^{-4}mbar$ ). For this reason, only conduction and radiation effects will be considered and discussed in following sections and for the remainder of this thesis.

### 2.3.1 CONDUCTION

Heat transfer by conduction is the transfer of energy from the substance's more energetic particles to the adjacent, less energetic ones. This can take place in solids, liquids, or gases. Conduction in liquids and gases is due to the collisions and diffusion of the molecules during their random motion. In solids, conduction occurs by the combination of vibrations of the molecules and the energy transport by free electrons. Conduction through solids is of interest for this work. The rate of heat conduction through a medium depends on the geometry, its thickness, material's thermal conductivity, and the temperature difference across the medium. It has been concluded that the rate of heat conduction through a plane layer is proportional to the temperature difference across the layer and the heat transfer area, but inversely proportional to the thickness of the layer (Equation 2-1)

$$\text{Rate of heat conduction} \propto \frac{(\text{Area})(\text{Temperature difference})}{\text{Thickness}} \quad 2-1$$

$$\dot{Q}_{cond} = -kA \frac{dT}{dx} \quad 2-2$$

Equation 2-2  $\dot{Q}_{cond} = -kA \frac{dT}{dx}$  2-2 is called Fourier's law of heat conduction where  $k$  is the thermal conductivity,  $A$  is the area normal to the direction of heat transfer, and  $dT/dx$  is the temperature gradient. The temperature gradient (the rate of change of  $T$  with  $x$ ) is the slope of the temperature curve on a  $T$ - $x$  diagram at location  $x$  [Cengel, 2007]. Since heat is conducted in the direction of decreasing temperature, then the temperature gradient becomes negative as  $T$  decreases with increasing  $x$ , the negative sign in Equation 2-2 ensures a positive quantity.

#### 2.3.1.1 THERMAL CONDUCTIVITY

Thermal conductivity of a material is defined as the rate of heat transfer through a unit thickness of the material per unit area per unit temperature difference [Cengel, 2007]. In other words, the material property thermal conductivity is a measure of the material's ability to conduct heat. A high thermal

conductivity value means that the material is a good conductor, and a low thermal conductivity value means the material is a poor conductor, usually classified as an insulator. Metals tend to be good thermal conductors, such as copper and silver that have a thermal conductivity of 401 W/m °C and 429 W/m °C, respectively [Cengel, 2007]. Insulators will have much lower thermal conductivity values such as brick ( $k = 0.72$  W/m °C) and air ( $k = 0.026$  W/m °C) [Cengel, 2007].

### **2.3.2 THERMAL RADIATION**

Radiation is the energy emitted by matter in the form of electromagnetic waves (or photons) due to the rotational movements of the atoms or molecules. Since particles at a temperature higher than 0 K are always moving, radiation (thermal) is always emitted, only increasing with temperature. Heat transfer by radiation differs from convection and conduction in that it does not require an intervening medium. This is the fastest form of heat transfer (at the speed of light) and suffers no decrease in speed in a vacuum. In solids, radiation is usually considered to be a surface phenomenon for opaque (non-translucent) surfaces such as metals, since emitted radiation by interior regions of the metallic body will never reach the surface, and the incident radiation on such a surface is absorbed within a few microns [Cengel, 2007].

Heat transfer by radiation is a complex phenomenon that needs to be analyzed thoroughly when conducting temperature measurements by radiation exchange. The theory on this is covered in detail in section 2.6. First, it is important to identify the different properties of surfaces, and address their impact on radiation analysis.

## **2.4 RADIATION PROPERTIES OF SURFACES**

### **2.4.1 ABSORPTIVITY, REFLECTIVITY, AND TRANSMISSIVITY**

When measuring temperature of surfaces, one must be able to identify certain characteristics to accurately analyze the interchange of radiant energy. Since most engineering materials do not behave like blackbodies, it is then necessary to know the absorption, reflection, and transmission characteristics of the given material to make accurate surface temperature measurements. When radiation strikes a

surface, a part of it will be absorbed, a part is reflected, and the remaining is transmitted. These material properties or variables are then defined as dimensionless quantities, known as the absorptivity  $\alpha$ , reflectivity  $\rho$ , and transmittance  $\tau$ , all with a value between zero and one [Sparrow, *et.al.*, 1978; Maldague, 2001; Cengel, 2007]. For opaque surfaces, such as metals, the transmittance is zero ( $\tau = 0$ ) – these are the surfaces of interest for this thesis, therefore these surfaces will be analyzed in further detail. Figure 2-2 shows the radiation flux incident, called “irradiation,” denoted by  $G$ , on an opaque surface such as a metal sample.

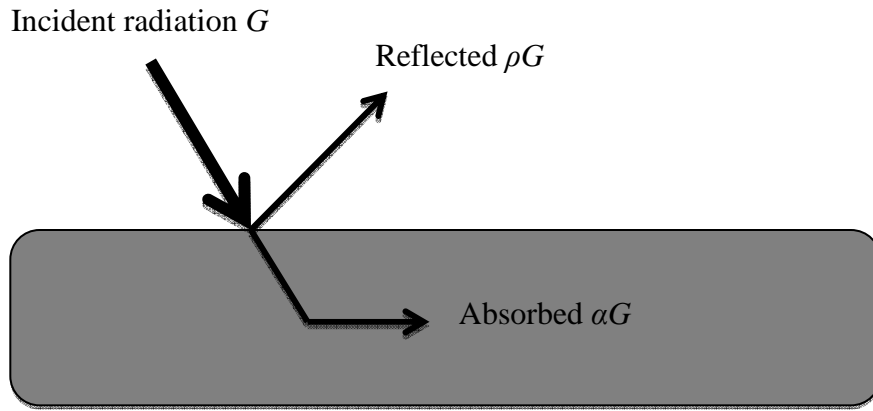


**FIGURE 2-2 THE ABSORPTION AND REFLECTION OF INCIDENT RADIATION BY AN OPAQUE (E.G. METAL) SURFACE.**

That is,

$$\alpha = \frac{\text{Absorbed radiation}}{\text{Irradiation}} = \frac{G_{abs}}{G} \quad 2-3$$

$$\rho = \frac{\text{Reflected radiation}}{\text{Irradiation}} = \frac{G_{ref}}{G} \quad 2-4$$

where  $G$  is the radiation flux incident on the surface, and  $G_{abs}$ , and  $G_{ref}$  are the absorbed and reflected portions of it, respectively. According to the first law of thermodynamics, the summation of the absorbed, reflected, and transmitted radiation will be equal to that of the incident radiation. Dividing

each term in this summation by the incident radiation  $G$  and noting that  $\tau=0$  for opaque surfaces, yields the relation

$$\alpha + \rho = 1 \quad 2-5$$

The above definitions pertain to total hemispherical properties, since the incident radiation flux on the surface from all directions over the hemispherical space and over all wavelengths. Meaning that,  $\alpha$  and  $\rho$  are the average properties of a medium for all directions and all wavelengths [Cengel, 2007]. To define these properties for a specific wavelength and/or direction, the spectral directional absorptivity and spectral directional reflectivity of a surface are defined as,

$$\alpha_{\lambda,\theta}(\lambda, \theta, \phi) = \frac{I_{\lambda,abs}(\lambda, \theta, \phi)}{I_{\lambda,i}(\lambda, \theta, \phi)} \quad \text{and} \quad \rho_{\lambda,\theta}(\lambda, \theta, \phi) = \frac{I_{\lambda,ref}(\lambda, \theta, \phi)}{I_{\lambda,i}(\lambda, \theta, \phi)} \quad 2-6$$

In the same fashion, the spectral hemispherical absorptivity and spectral hemispherical reflectivity of a surface are defined as,

$$\alpha_{\lambda}(\lambda) = \frac{G_{\lambda,abs}(\lambda)}{G_{\lambda}(\lambda)} \quad \text{and} \quad \rho_{\lambda}(\lambda) = \frac{G_{\lambda,ref}(\lambda)}{G_{\lambda}(\lambda)} \quad 2-7$$

where  $G_{\lambda}$  is the spectral irradiation incident on the surface, and  $G_{\lambda,abs}$  and  $G_{\lambda,ref}$  are the absorbed and reflected portions of it, respectively [Cengel, 2007]. The average absorptivity and reflectivity of a surface can also be defined as follows in spectral terms as,

$$\alpha = \frac{\int_0^{\infty} \alpha_{\lambda} G_{\lambda} d\lambda}{\int_0^{\infty} G_{\lambda} d\lambda} \quad \text{and} \quad \rho = \frac{\int_0^{\infty} \rho_{\lambda} G_{\lambda} d\lambda}{\int_0^{\infty} G_{\lambda} d\lambda} \quad 2-8$$

## 2.4.2 EMISSIVITY

Any real surface has a distinct surface property that states its ability to emit energy, this correction factor is called emissivity, denoted  $\varepsilon$  and varies between zero and one [Cengel, 2007; Maldague, 2001]. The emissivity of a surface is defined as the ratio of the radiation emitted by the surface at a given temperature to the radiation emitted by a blackbody at the same temperature [Cengel, 2007]. In other words, emissivity is a measure of how closely a surface approximates a blackbody, for

which  $\varepsilon=1$ . The fundamentals behind the blackbody tool will be discussed in detail in section 2.5

### Blackbody Radiation.

The emissivity of a surface is not constant; it varies with the surface temperature, the wavelength, and the direction of the emitted radiation [Cengel, 2007]. It is then appropriate to introduce the spectral directional emissivity, defined as the ratio of the intensity of radiation emitted by the surface at a specified wavelength and direction to the intensity of radiation emitted by a blackbody at the same temperature and wavelength, defined by Equation 2-9.

$$\varepsilon_{\lambda,\theta}(\lambda, \theta, \phi, T) = \frac{I_{\lambda,e}(\lambda, \theta, \phi, T)}{I_{b\lambda}(\lambda, T)} \quad 2-9$$

The total hemispherical emissivity, or simply the average emissivity, of a surface at a given temperature represents the ratio of the total radiation energy emitted by the surface to the radiation emitted by a blackbody of the same surface area at the same temperature.

$$\varepsilon(T) = \frac{E(T)}{E_b(T)} = \frac{\int_0^\infty \varepsilon_\lambda(\lambda, T) E_{b\lambda}(\lambda, T) d\lambda}{\sigma T^4} \quad 2-10$$

Radiation is a complex phenomenon, and by considering the wavelength and direction dependence of emissivity makes the analysis that much more complicated, assuming the acquisition or data on these properties even exist. In radiation analysis, bodies are usually assumed to be gray and diffuse surfaces. A diffuse surface has properties independent of direction, and a gray surface has properties independent of wavelength. When a surface is assumed to be gray and diffuse, the emissivity of this surface is the total hemispherical emissivity, or average emissivity, because it is independent of direction and wavelength [Cengel, 2007].

Although these approximations are usually made in radiation analysis, the validity of these assumptions is really close to its real value. According to Cengel, emissivity with respect to direction  $\varepsilon_\theta$ , where  $\theta$  is the angle measured from the normal to the surface, for conductors such as metals  $\varepsilon_\theta$

remains nearly constant for about  $\theta < 40^\circ$ . This becomes important when considering the angle at which the instrument (IR camera) is acquiring emissivity and temperature measurements, discussed in more detail in Chapter 3. Figure 2-3 shows the minimal effect of the gray approximation on emissivity and emissive power of a real surface. Many of the calculations done in this thesis use the grey approximation assumption and such assumptions are always stated.

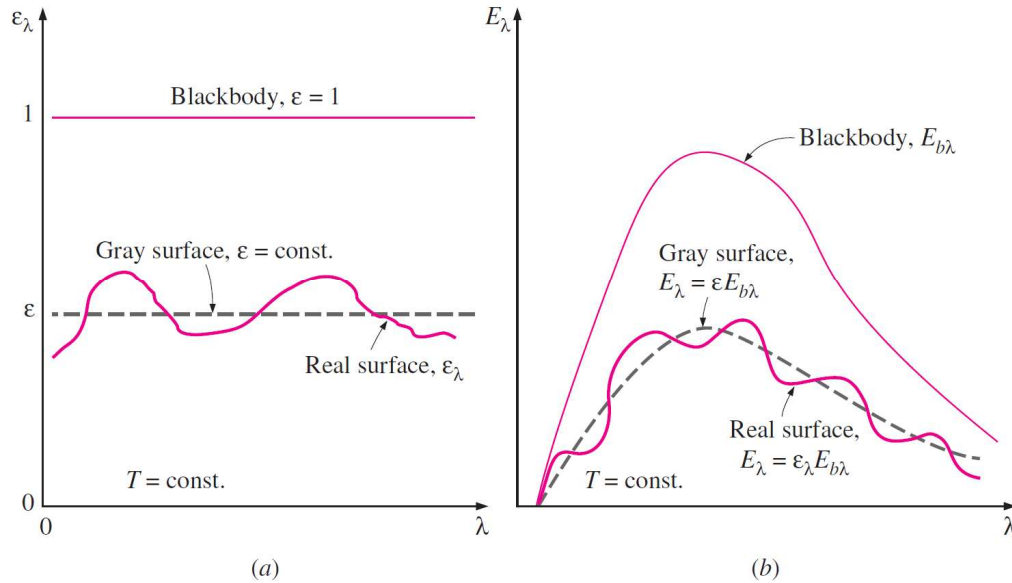


**FIGURE 2-3 COMPARISON OF THE EMISSIVITY (A) AND EMISSIVE POWER, (B) OF A REAL SURFACE WITH THOSE OF A GRAY SURFACE AND A BLACKBODY AT THE SAME TEMPERATURE [CENGEL, 2007].**

## 2.5 THERMAL EMISSION

All matter produces thermal emission. A distinction does exist between gases, liquids and solids. In the case of gases, thermal emission is volumetric; particles within the gas contribute to the emission. As for liquids and solids, the emission is a surface phenomenon, which will be the focus of the following discussion. Energy is released by particles in oscillation in the form of thermal emission [Maldague, 2001]. Particle (electrons, ions, atoms, or molecules) oscillations themselves are caused by the temperature of the matter. Energy transfer by radiation travels at the speed of light and does not



decrease in a vacuum environment [Cengel, 2007]. In fact, heat transfer in an evacuated space can occur only by radiation, in the same manner that the sun's radiation reaches the earth through space.

Thermal emission transportation is better understood by considering two concepts: electromagnetic waves and photon emission. Electromagnetic waves transport energy just like other waves, at the speed of light  $c_0 = 2.9979 \times 10^8 \text{ m/s}$ , and are characterized by their frequency  $f$  or wavelength  $\lambda$  [Cengel, 2007]. The two properties are related by

$$\lambda = \frac{c}{f} \quad 2-11$$

Where  $c$  is the speed of transmission of a wave in that medium. The speed of transmission in a medium is related by  $c = c_0/n$ , where  $n$  is the index of refraction of that medium. For air and most gases the refractive index is essentially one, for glass and water it is about 1.5 and 1.33, respectively [Cengel, 2007]. The unit of wavelength is generally expressed in micrometer ( $\mu\text{m}$ ). The frequency of an electromagnetic wave depends only on the source, unlike the wavelength, it is independent of the medium through which the wave travels, and is expressed in hertz (Hz) (the number of oscillations per second).

The second concept, photon emission, where, according to Max Planck in 1900, photons are energy particles with zero mass at rest and with a collection of discrete quantity of energy called quantum [Cengel, 2007 and Maldague, 2001]. Planck states that each photon of frequency  $f$  has a liberated photonic energy  $W$  given by

$$W = hf = \frac{hc}{\lambda} \quad 2-12$$

Where  $h = 6.626069 \times 10^{-34} \text{ J} \cdot \text{s}$  is Planck's constant. It is important to understand that the energy emitted from a surface has various anomalies; the emitted wavelengths have an unequal distribution of energy, furthermore, emission is not uniform in all directions [Maldague, 2001]. This phenomenon of radiation brings us to the next concept of blackbody radiation or a perfect radiator.

## 2.5 BLACKBODY RADIATION

The amount of radiation energy emitted from a surface at a given wavelength depends on the material, condition of the surface, and its surface temperature. Therefore, two distinct bodies at the same temperature will emit different amounts of radiation per unit surface area. To know the maximum amount of radiation that can be emitted by a unique surface or material at a given temperature requires defining an idealized body, called a “blackbody.”

At a specific temperature and wavelength no surface can emit more energy than a blackbody, and so it is defined as a perfect emitter and absorber of radiation [Cengel, 2007]. A blackbody essentially becomes an instrument that absorbs all irradiated energy from any direction and wavelength. The instrument also has the property of reemitting this energy until thermodynamic equilibrium is reached with its surrounding environment, thus earning the name of a perfect radiator [Maldague, 2001]. The amount of radiation energy emitted by a blackbody per unit time and per unit surface area is defined as

$$E_b(T) = \sigma T^4 \quad 2-13$$

where  $\sigma = 5.670 \times 10^{-8} \text{ W/m}^2 \cdot \text{K}^4$  is known as the Stefan-Boltzmann constant and  $T$  is the absolute temperature of the surface in Kelvin [Cengel, 2007]. Equation 2-13 is known as the Stefan-Boltzmann law where  $E_b$  is the blackbody emissive power with unit  $\text{W/m}^2$ .

Although blackbodies are mostly theoretical and a mathematical concept, they do, in fact, exist. They can be made from a large cavity with a small opening. The idea is that radiation coming in through the opening undergoes multiple reflections inside cavity, and thus it has several chances to be absorbed by the cavity walls before any radiation can escape, see Figure 2-4. Once the surface of the cavity has reached an isothermal state, the radiation reflected out of the cavity, after undergoing multiple reflections, has a diffuse nature. This is what makes the cavity act as a perfect absorber and emitter, and producing a blackbody at the small opening on the surface [Cengel, 2007].

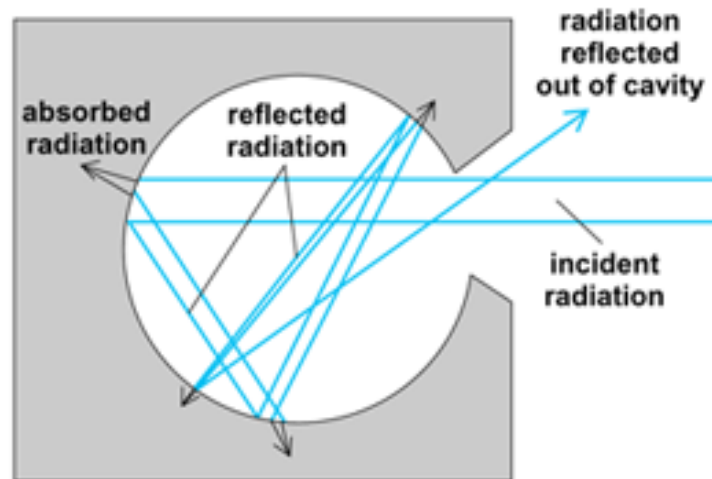


**FIGURE 2-4 BLACKBODY CAVITY WITH RADIATION INTERCHANGE CHARACTERISTICS.**

## **2.6 RADIATION HEAT TRANSFER**

The true nature of radiation and its transport mechanism have not been fully understood to date [Arpaci, 1991]; fortunately there are tools that make the complexity of the analysis much easier by making assumptions and using certain factors that makes radiation heat transfer analysis achievable. Radiative heat transfer does not require a medium to transfer its energy, thus radiation exchange is based solely on surfaces relative to each other, or “reflections”, due to the enclosure walls. Thus, the primary interest in radiation problems is the quantity of radiation exchange between two or more surfaces. Radiation heat transfer between surfaces depends on the orientation of surfaces relative to each other and their radiation properties and temperatures. A parameter referred to as a view factor defines the fractions of incident radiation is absorbed, reflected, or transmitted to another surface. The theory of view factors and their dependence on the surface enclosure is discussed in detail the following sections. The determination of view factors for this work is presented in Chapter 3.

### **2.6.1 THE ENCLOSURE**

When calculating the radiant interchange at any surface, it is required to include radiation arriving at that surface from all directions in space [Sparrow and Cess, 1978]. To make certain that all radiation is accounted for, it is essential to construct an enclosure and specify the thermal state and the

radiation properties of each wall of the enclosure. An important assumption to consider when developing surface enclosures is that not all surfaces need to be material surfaces, such as an open window. This “open window” may be assigned radiation properties and blackbody temperatures that correspond to the rate at which radiant energy passes through the fictitious surface into the enclosure [Sparrow and Cess, 1978].

When conducting radiation transfer calculations, an assumption that is usually made is assume black surfaces, and this assumption makes the radiation problem relatively easy to solve, but in practice most enclosures involve non-black surfaces. These non-black surfaces allow multiple reflections to occur, and, in turn, makes the radiation problem very complex unless some commonly-accepted assumptions are made [Cengel, 2007]. To make these radiation problems possible, surfaces are usually assumed to be opaque, diffuse, and gray. These terms make surfaces out to be nontransparent, they are diffuse emitters and diffuse reflectors, and their radiation properties are independent of wavelength. Additionally, each surface of the enclosure is isothermal, and both the incoming and outgoing radiation is uniform over each surface [Cengel, 2007].

## **2.6.2 VIEW FACTORS**

The view factor, denoted  $F_{ij}$ , is not only a parameter but a necessary tool to have in the analysis of radiation heat transfer. This factor is dependent only on the geometry of the enclosure, and may be defined as representing the fraction of radiation leaving a uniform surface  $i$  that directly strikes surface  $j$  [Love, 1968]. In general, this determination is the most tedious part of diffuse radiant-exchange problems. The view factor is based on the assumption that the surfaces are diffuse emitters and diffuse reflectors, that is the reflectance is not a function of the incident nor direction in which it leaves [Cengel, 2007; Love, 1968]. For diffuse surfaces, the radiation leaving the surface (via emission and reflection) will be the intensity times  $\pi$ , called radiosity  $J$ . Radiosity is also defined as the total radiation energy leaving a surface per unit time and per unit area [Cengel, 2007].

$$J_1 = I_1 \pi \quad 2-14$$

In order to develop a general expression of the view factor, two differential surfaces  $dA_1$  and  $dA_2$  on two arbitrarily oriented surfaces  $A_1$  and  $A_2$  are considered, as seen in Figure 2-5.

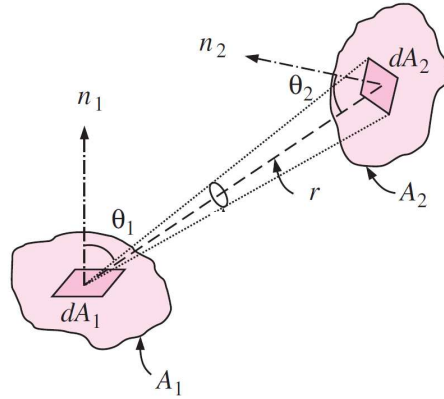


**FIGURE 2-5 GEOMETRY FOR THE DETERMINATION OF THE VIEW FACTOR BETWEEN TWO SURFACES [CENGEL, 2007].**

The distance between the two differential areas is  $r$ , the angle between the surface normal of  $dA_1$  to the line  $r$  is  $\theta_1$  and  $\theta_2$  for surface normal  $dA_2$  to the same line  $r$ . The total rate at which radiation leaves  $dA_1$  via emission and reflection in all directions is the radiosity times the surface area.

$$\dot{Q}_{dA_1} = J_1 dA_1 = \pi I_1 dA_1 \quad 2-15$$

It is important to note that the radiation leaving a surface consists of emitted and reflected parts, and the calculation of radiation heat transfer between surfaces involves the total radiation energy streaming away from a surface, with no regard to its origin. As discussed in the previous section, for the assumption that surface  $1$  is gray and opaque ( $\varepsilon_1 = \alpha_1$  and  $\alpha_1 + \rho_1 = 1$ ), the radiosity may be expressed as

$$J_1 = (\text{Radiation emitted by surface 1}) + (\text{Radiation reflected by surface 1})$$

$$= \varepsilon_1 E_{b1} + \rho_1 G_1$$

$$= \varepsilon_1 E_{b1} + (1 - \varepsilon_1) G_1 \quad 2-16$$

Where  $E_{b1} = \sigma T_1^4$  is the blackbody emissive power of surface  $1$  and  $G_1$  is the radiation incident on surface  $1$  per unit time per unit area, or irradiation.

The fraction of radiation leaving  $dA_1$  that strikes  $dA_2$  directly, is the differential view factor, denoted  $dF_{dA_1 dA_2}$ .

$$dF_{dA_1 dA_2} = \frac{\dot{Q}_{dA_1 dA_2}}{\dot{Q}_{dA_1}} = \frac{\cos \theta_1 \cos \theta_2}{\pi r^2} dA_2 \quad 2-17$$

Finally, to determine the fraction of radiation leaving finite area  $A_1$  and striking finite area  $A_2$ , which is the view factor  $F_{12}$ , is given by [Cengel, 2007]

$$F_{12} = F_{A_1 A_2} = \frac{\dot{Q}_{A_1 A_2}}{\dot{Q}_{A_1}} = \frac{1}{A_1} \int_{A_2} \int_{A_1} \frac{\cos \theta_1 \cos \theta_2}{\pi r^2} dA_1 dA_2 \quad 2-18$$

The view factor  $F_{21}$  is determined from Equation 2-18 by interchanging the subscripts  $1$  and  $2$ . This integration may become rather complicated and often must be accomplished by numerical methods. For many problems and common geometries, however, the engineer may resort to published formulas, tables, or graphical schemes for the determination of the needed view factors [Love, 1968]. This is what was done for the present work. The formulas used are presented and implemented in Chapter 3 where the determination of reflective sources is carried out.

## 2.7 INFRARED TECHNOLOGY

### 2.7.1 THEORY OF OPERATION

Today's infrared (IR) thermal imagers are capable of providing excellent qualitative thermal images, but their accuracy is only as good as the accountability of environmental conditions. Measuring the environmental conditions is critical to the calibration procedure of IR cameras. As emphasized in the previous sections, the radiant energy received from an object will be a function of its temperature, spectral emissivity, reflections from its surroundings, and atmospheric transmission. Figure 2-6 is a schematic representation of the sources that are being measured by the IR camera in conjunction with

the target object. As radiation passes through the atmosphere, the strength may be attenuated due to scattering and absorbed in the atmosphere. Fortunately, scattering is negligible for wavelengths longer than  $2\text{ }\mu\text{m}$ ; IR cameras are designed to operate above this range. In the regions of minimal disturbance from the atmosphere, the spectral range for the FLIR SC645 IR camera (FLIR Systems, Wilsonville, OR) is  $7.5\text{-}13\text{ }\mu\text{m}$ . The main sources of “disturbance” are reduced to ambient sources, or reflecting sources, and the target’s emissivity itself. A thorough calibration procedure to account for this is detailed, and executed in Chapter 3.

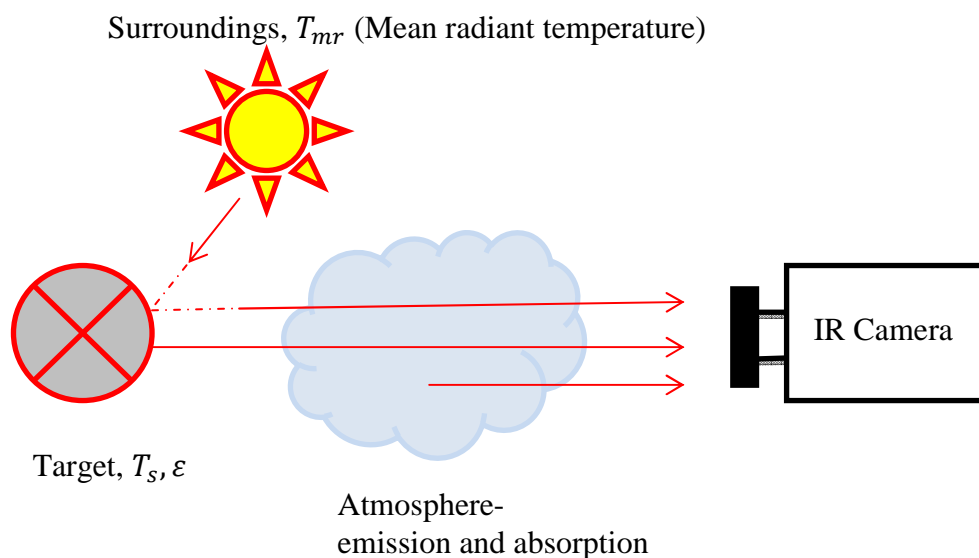


**FIGURE 2-6 SCHEMATIC OF THE VARIOUS SOURCES OF RADIATION THAT AN IR CAMERA MEASURES.**

## **2.7.2 THERMAL DETECTORS**

IR cameras use thermal detectors as their source for converting thermal radiation to a measured signal that can then be converted temperature value. The incident radiation on the thermal detector heats the surface and the heating affects a property of the heated material such as the electrical conductivity, This translates into variation of the signal output [Maldague, 2001]. Thermal detectors respond to absorbed radiant power, regardless of its spectral distribution [De Lara, 2001]. The various types of thermal detectors available are many, such as, bolometers, microbolometer, ferroelectric, thermopiles,

pyroelectric, photonic, quantum, etc; each with its own response time and thermal sensitivity characteristics. The IR camera used in this work uses large-dimensional infrared array, also known as a “focal plane array,” with an uncooled microbolometer detector. It is appropriate to give a brief description on the mechanisms behind this technology.

#### **2.7.2.1 FOCAL PLANE ARRAYS**

Infrared images can be obtained by the use of an infrared imager, one type is the focal plane array (FPA). This chip does not require any electromechanical scanning mechanism (no moving parts) for image forming [Maldague, 2007]. FPA imagers are based on the charged-coupled-device principle; they are made of an appropriate objective, a detector array (e.g. microbolometer), and associated electronics. Advantages of FPAs are their relatively simple construction, quick reading time, and simultaneous acquisition by all detectors in the array [De Lara, 2001]. Modern FPA imagers have a nonuniformity correction built into its architecture due to the relative nonuniformity from detector to detector in response to temperature. This is normal due to variations in the manufacturing process and the detector’s material [De Lara, 2001].

#### **2.7.2.2 UNCOOLED MICROBOLOMETER**

A microbolometer is a specific type of resistor. It is a vanadium-oxide (VOx) resistor with a large temperature coefficient on a silicon element with large surface area, a low heat capacity, and good thermal isolation [FLIR, 2008]. When infrared radiation from a specific range of wavelengths strikes the vanadium oxide, upon doing so, the radiation changes its electrical resistance. These changes in scene temperature cause changes in the bolometer temperature which are converted to electrical signals and finally processed into an image.

### **2.8 SPECTROPYROMETER – A MULTI-WAVELENGTH PYROMETER**

A multi-wavelength pyrometer, or spectropyrometer [Felice, 2012], which uses a spectrophotometer as its detector has been commercially available since 1997. The data output of the instrument includes: temperature of the object, the tolerance (the accuracy of the measurement), and signal strength (an emissivity value at given wavelength) [Felice, 2012]. This instrument’s data was



used compared with that of the IR camera's data for analysis of the spectropyrometer's functionality and capability. These data is presented in Section 5.3 Emissivity Studies.

The spectropyrometer works by adding wavelength intensities given off by a material at an elevated temperature, this instrument works in the range of 300 °C to 2000 °C [Felice, 2002]. Electromagnetic radiation is given off by materials upon being heated, the spectropyrometer detects this radiation and relates it back to a look-up table which uses the concept of Planck's law, or as mentioned earlier the law that defines an ideal blackbody radiator. The law describes the amount of electromagnetic energy with a certain wavelength radiated by a blackbody in thermal equilibrium defined by,

$$L_{\lambda} = \frac{2hc^2}{\lambda^5} \left[ e^{\frac{hc}{\lambda k_B T}} - 1 \right]^{-1} \quad 2-19$$

Where  $L_{\lambda}$  is the radiance in energy per unit area per unit time per steradian per unit wavelength interval,  $h$  is Planck's constant,  $c$  is the speed of light,  $\lambda$  is the wavelength of the radiation,  $k_B$  is Boltzmann's constant, and  $T$  is the absolute temperature of the material. Solving Planck's law for temperature by dividing the intensities at two different wavelengths and making the usual short-wavelength-temperature assumption yields [Felice, 2012],

$$T_{12} = \frac{c_2(1/\lambda_1 - 1/\lambda_2)}{\ln R - 5 \ln (\lambda_2/\lambda_1)} \quad 2-20$$

Where  $c_2$  is the second radiation constant, and  $R$  is the ratio intensities at the two wavelengths. The method employed by the spectropyrometer multi-wavelength pyrometer, is to calculate all possible  $T_{ij}$  for an collective of discrete wavelength/intensity pairs and average them [Felice, 2012]. This method is well suited for noise-free data collected on greybody or blackbody sources, and for non-ideal targets an alternate approach has been implemented.

Making use of the standard deviation, or the instrument's tolerance output, if the result is a single-value, it indicates that the sample is a greybody and any absorptions that may be present are not significant [Felice, 2002]. If the calculated standard deviation is large (greater than a single-value result), it indicates one of the following: emissivity is a function of wavelength, atmospheric absorptions are present, the temperature is not single-valued, or the optical elements have changed characteristics

[Felice, 2002]. The first two items can be detected and corrections can be made. Since it is known that un-oxidized metals typically exhibit an emissivity that decreases with wavelength, previous work has shown that a three-wavelength pyrometer can solve for temperature if the dependence of emissivity is linear [Felice, 2002]. The capacity of multiple wavelengths of the spectropyrometer, a correction that assumes emissivity can be represented by a linear relationship. The assumption is deemed to be successful if the result of the standard deviation is single-valued [Felice, 2002].

### **2.8.1 DESIGN AND APPARATUS**

The multi-wavelength pyrometer, or spectropyrometer, uses a fiber optic cable to direct laser light to the target object and simultaneously detecting wavelengths emitted by the target by making use of a spectrophotometer which is device that separates the wavelengths. An electrical transmission line then sends the information to the analog-to-digital conversion system within the device where computations are executed and results (temperature, signal strength, and tolerance) are displayed to the operator. These computations use an algorithm comprising an expert system to make the calculations and determinations discussed earlier and are incorporated into software suitable for a desktop computer [Felice, 2002]. Figure 27 shows the schematic of the spectropyrometer system patented by FAR Associates (Macedonia, OH). The detector operates in the spectral range of 1000 – 1700 nm with a spectral resolution of 3 nm, as mentioned earlier, provides the system with a temperature range of 300 to 2000 °C [Felice, 2002]. The experimental setup and results of the spectropyrometer are discussed in Chapter 3.

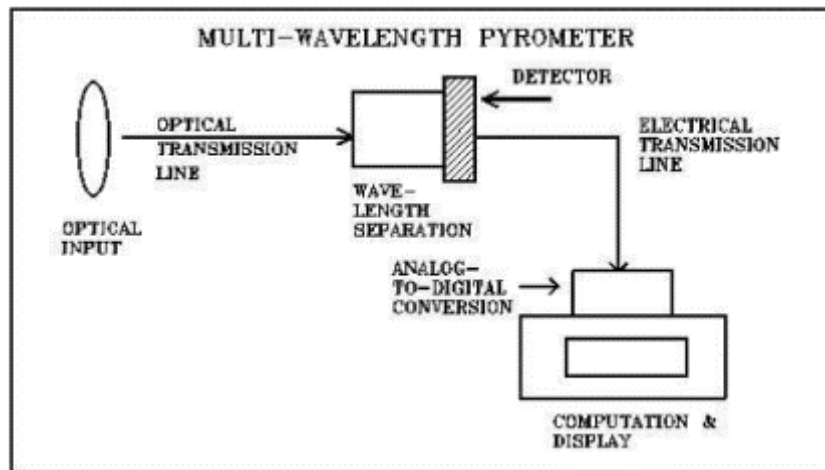


**FIGURE 2-7 SCHEMATIC OF SPECTROPYROMETER; FROM US PATENTS 5772323 AND 6379038B [FELICE, 2012].**

## CHAPTER 3 EXPERIMENTAL SETUP AND PROCEDURES

This chapter describes the experimental logistics and setup used to acquire IR images. The Arcam A2 (Arcam AB, Sweden) system is not commercially designed for the purposes of infrared thermography; therefore a majority of the energy on this project was focused on transforming the A2 machine into a fully automated thermal imaging feedback-control system. As mentioned earlier, the commercially available A2 system's feedback is in the form a single temperature measurement from a thermocouple placed under the start plate. The front window allows for the operator to observe the build surface as the machine works, but this is quite a weakness since this requires a certain level of experience and provides little to no quantitative data. Infrared imagery allows for a full-field temperature mapping of the surface, and additionally, provides a non-intrusive (non-destructive) technique to verify quality of the products being fabricated.

### 3.1 ARCAM A2 SYSTEM MODIFICATIONS FOR IR CAMERA INSTALLATION

Several modifications were made to the *Arcam A2* system to integrate the FLIR SC645 IR camera. First, there were a number of items removed to make way for the drilling of new holes for the flap mechanism and actuator. The upper and lower chamber door cowling, column turbo pump, and column assembly with film drive were all removed (Figure 3-1). Five holes were drilled atop the build chamber using a steel template provided by Arcam AB indicating the size and placement of the holes (Figure 3-2). It is important to note that these holes were drilled with precaution to preserve the high vacuum requirements within the electron beam melting build chamber. The components were then reinstalled, and an additional chamber frame that is used to hold the FLIR camera mount was also put in place. The mount was then installed and the following components were put in place (see Figure 3-3):

- Zinc-selenide (ZnSe) glass with O-rings above and below the glass. The retaining ring is held in place with two clamps.
- Flap feed-thru mechanism with O-ring seal. The feed-thru collar holds this in place.
- Air-supply is then connected to the input regulator on the pneumatic panel.

- The pneumatic panel is powered by tapping into the chamber vacuum gauge in the wire breakout panel on the wall of the chamber cabinet. A parallel cable is run from the new D-sub connector in the electronics rack to the connection box on the pneumatic panel.
- The pneumatic piston is now connected to the pneumatic panel.
- The push button switch that attaches to the connection box is then installed outside the system (Figure 3-4 A2 System with IR camera upgrade).
- Once powered, the flap is in the closed position and the micro-switch is in the ‘normally closed’ state allowing the beam to come on.
- The IR camera is now put into position for image capture.
- A stainless steel covering is placed around the new camera upgrade to protect against the leakage of X-rays. Due to the zinc-selenide’s excellent transmittance in the infrared spectrum, this also holds true in the transmittance of X-rays, therefore this protective shield was designed to protect against any harmful radiation (Figure 3-4 A2 System with IR camera upgrade).

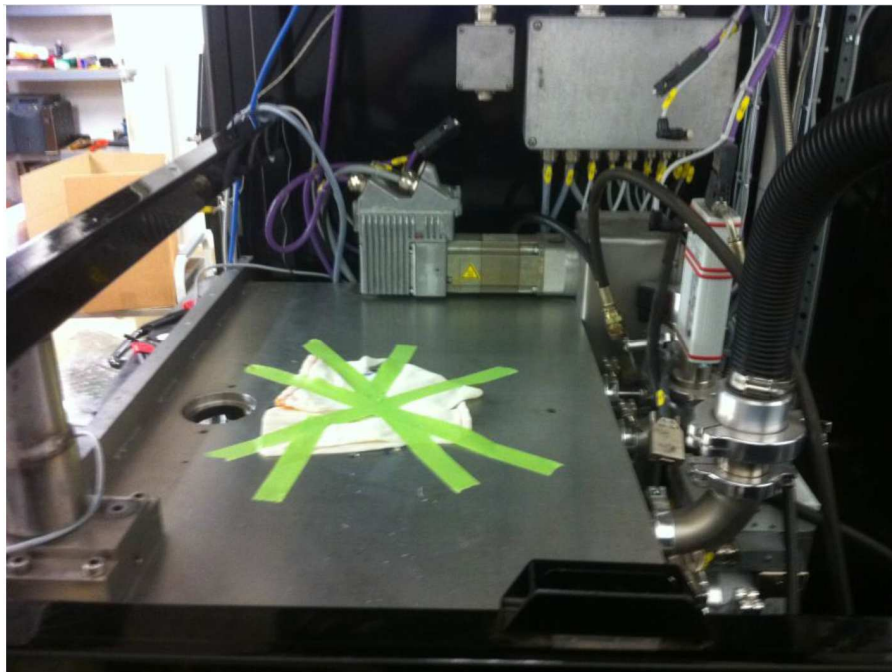


**FIGURE 3-1 REMOVAL OF COLUMN ASSEMBLY AND CAMERA WITH FILM DRIVE. THE O-RING SURFACE OF THE LOWER COLUMN IS COVERED AND PROTECTED.**

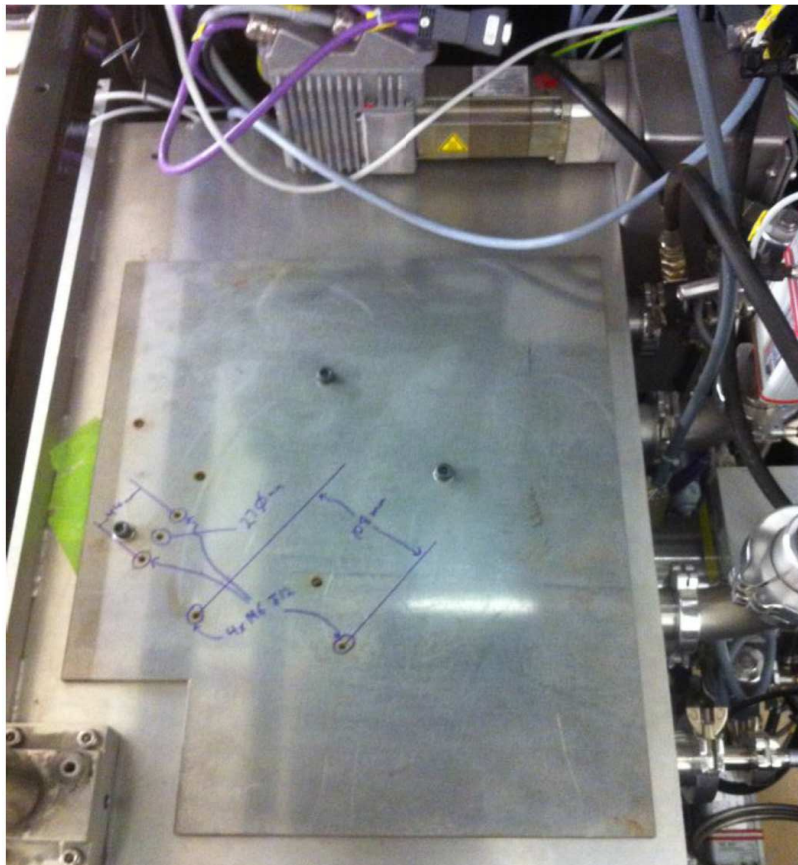


**FIGURE 3-2 TOP OF CHAMBER WITH STEEL “TEMPLATE” INDICATING THE SIZE AND PLACEMENT OF HOLES TO BE DRILLED.**

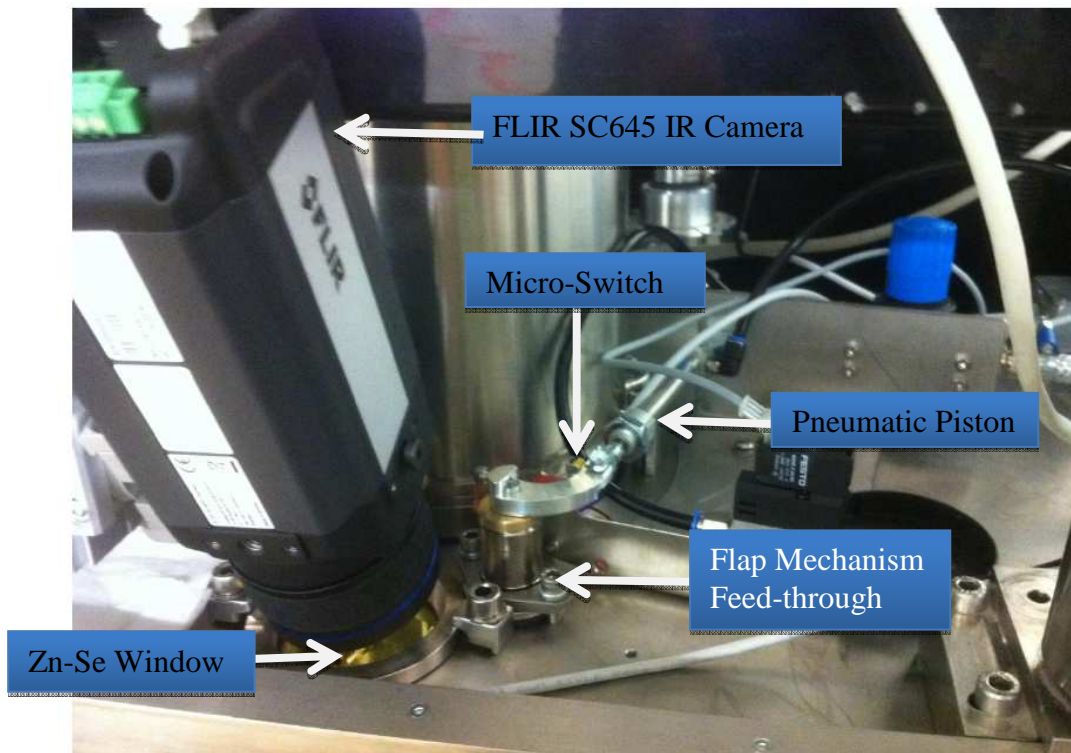


**FIGURE 3-3 TOP OF ARCAM A2'S BUILD CHAMBER WITH NEW COMPONENT LOCATION AND IR CAMERA**



**FIGURE 3-4 A2 SYSTEM WITH IR CAMERA UPGRADE**

### **3.2 METHODOLOGY FOR IR FEEDBACK CONTROL IN ARCAM A2 SYSTEM**

The methodology for IR image capture is presented here in the form of a flow diagram (Figure 3-5). To automate the opening of the flap mechanism (or shutter), capturing a voltage signal, to act as a trigger, from the Arcam system was required. This signal was received and interpreted by a modular controller from National Instruments (NI cRIO-9074, Austin, TX). These signals were then



incorporated into the standard process steps (first is a preheat step, followed by the melt step) for a given layer. There are three different process signals that can be used during the build process for a layer. For example, signal one can be assigned to assert before the preheat step, signal two before the melt, and signal three after the melt. A collaborative effort with Arcam AB resulted in a new version of the *EBM Control* software that allows the selection of these process steps to be incorporated into the standard process step cycle. A detailed description on how to implement these new process steps into the standard process steps of a build is discussed in Chapter 4.

To complete the implementation of a feedback control system, the next step was to intercept the output signals from the A2's output module. The intercepted signal is fed to an electromechanical relay (opens/closes the flap mechanism) that connects to the modular controller. The NI cRIO-9074 controller is the central unit for feedback from the A2 system. This unit allowed the attachment of various modules to realize tasks such as measuring signals and issuing commands. Once the controller received the signal to open the shutter, *LabVIEW* was used to program the IR camera to render a snapshot of the surface bed. Thermal images are recorded, archived, processed and analyzed. Chapter 4 discusses this software development phase of the project in detail.

Once images are captured, the operator then analyzes the IR images to justify (e.g. "cold spots", or defects detected) if there is a need to modify parameters. The two main parameters modified during the experimentation of Ti-6Al-4V builds, were the speed function (scan rate) and the beam current. These parameters were chosen because they have the biggest influence on surface temperature manipulation of the part once the part has already started the build cycle. Otherwise, the initial starting temperature would be the more obvious parameter to choose. This would easily cause the temperature change required.

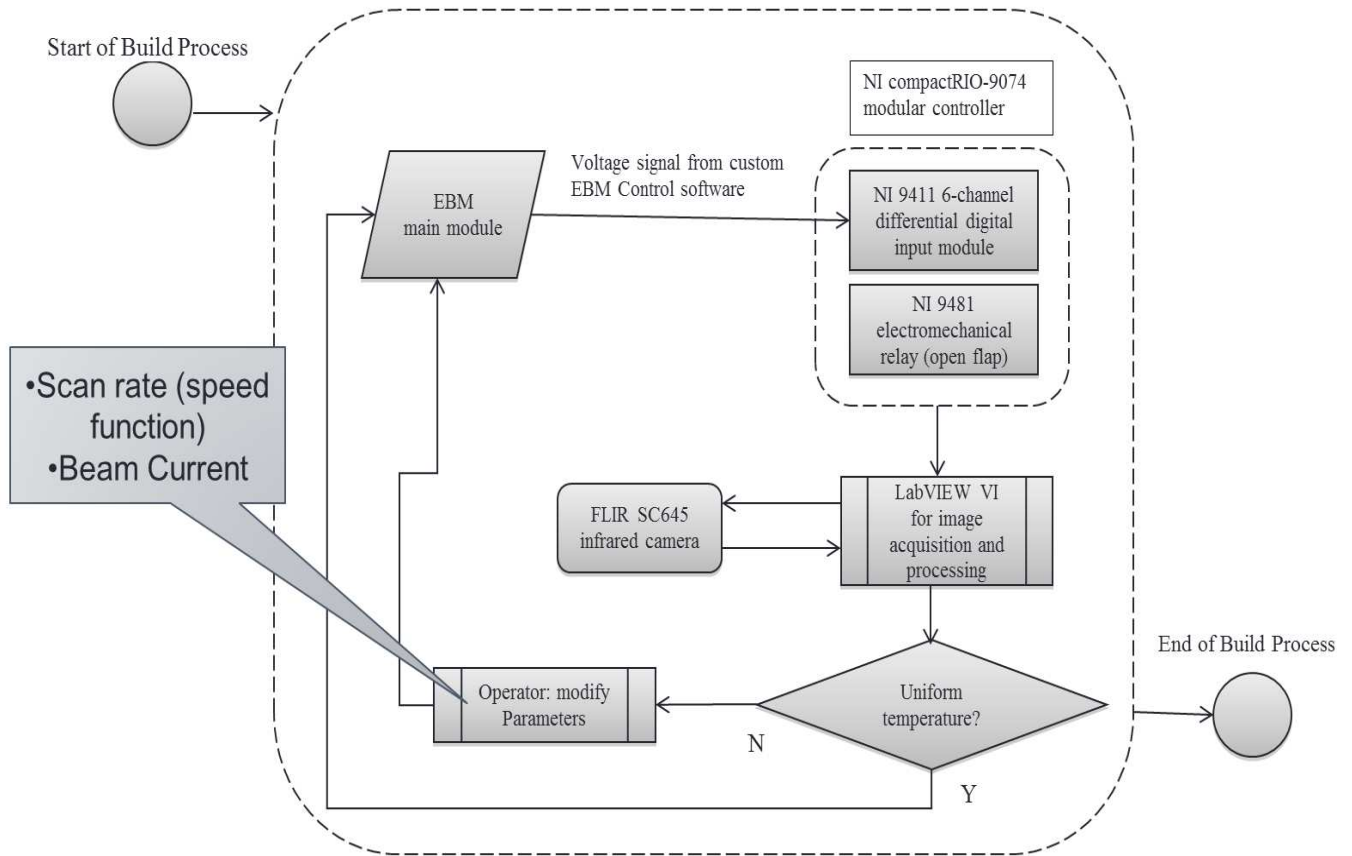


**FIGURE 3-5 ARCHITECTURE FOR IR FEEDBACK CONTROL IN ARCAM A2 SYSTEM**

### 3.3 IR CAMERA CALIBRATION

The FLIR SC645 used here images and measures the emitted IR radiation from an object. As shown in Figure 3-6 Figure 3-6 A schematic representation of the general thermographic measurement situation. 1: Surroundings, 2: Object, 3: Atmosphere, 4: Camera. [FLIR Systems AB, the radiation measured by the camera is made up of emission from the object,  $\varepsilon\tau W_{obj}$ , reflected emission from ambient sources,  $(1 - \varepsilon)\tau W_{refl}$ , and emission from the atmosphere,  $(1 - \tau)W_{atm}$ . For the camera to measure temperature accurately, the following parameters are required to be known and supplied to the camera: emissivity of the object, reflected apparent temperature, and temperature and emission of the atmosphere.

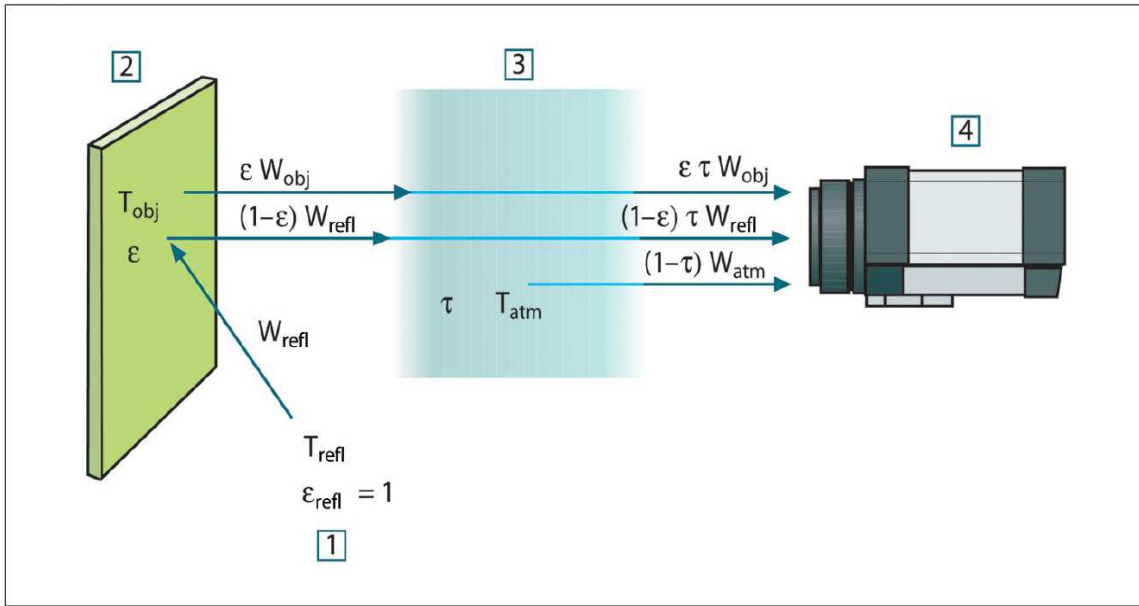


**FIGURE 3-6 A SCHEMATIC REPRESENTATION OF THE GENERAL THERMOGRAPHIC MEASUREMENT SITUATION. 1: SURROUNDINGS, 2: OBJECT, 3: ATMOSPHERE, 4: CAMERA. [FLIR SYSTEMS AB]**

Figure 3-6 shows three different sources of power,  $W$ , that the IR camera receives and translates to a camera signal  $U$  that is proportional to the power input (power linear camera) [FLIR, 2010]. The signal  $U$  is obtained by multiplying a constant  $C$  (FLIR Systems AB) by the radiation power  $W$  [Maldague, 2001]. The total received radiation power can now be written in terms of the total measured camera output voltage  $U_{tot}$ .

$$U_{tot} = \epsilon \tau U_{obj} + (1 - \epsilon) \tau U_{refl} + (1 - \tau) U_{atm} \quad 3-1$$

Here,  $\epsilon$  is the emissivity of the object and  $\tau$  is the transmittance of the atmosphere and the zinc-selenide window. By supplying the IR camera with the required parameters, the FLIR Systems thermographic equipment will use the above general formula to solve for  $U_{obj}$ .  $U_{obj}$  is the calculated camera output voltage for a blackbody of temperature  $T_{obj}$ - a voltage that can be directly converted into true requested object temperature [FLIR, 2010].

### **3.3.1 CAMERA ANGLE**

An important factor to consider throughout this thesis work is the fact that the IR images captured appear cooler atop the image. This appearance is caused by the camera angle to the surface normal, which is at 25 ° and the relatively small size of the window that the camera must look through (see Figure 3-3) – the camera must be positioned to the correct angle for maximum visual. Any slight deviation from this will significantly cause a reduction in visual area. Assuring maximum visual can be accomplished by adjusting the tilt angle (with the build's start plate already put in place on the powder bed) and watching the camera display to ensure that the maximum area of the start plate is in view. Once the camera has been tilted to the appropriate angle, the hex-screws on the adjustment mechanism are tightened while simultaneously holding the camera to avoid angle deviation. It should also be noted that FLIR SC645 camera comes with a default 25 degree lens and by using a higher degree lens, such as a 45 degree lens available from FLIR (FLIR Systems, Inc., Wilsonville, OR)- the maximum surface area in visual may be significantly increased.

### **3.3.2 ATMOSPHERE AND EXTERNAL OPTICS**

When using external optics as a viewing window for the camera, the transmittance and temperature of the optics need to be assigned to the camera. The external optics used in the Arcam A2 system is a zinc-selenide glass, an ideal choice for the FLIR SC 645 IR camera's spectral range, 7.5-13 um, because it has the highest transmittance when compared to other common IR window materials. Figure 3-7 shows ZnSe as the only material to stay above 90 % for the operating spectral range of the uncooled microbolometer FLIR SC 645 model.

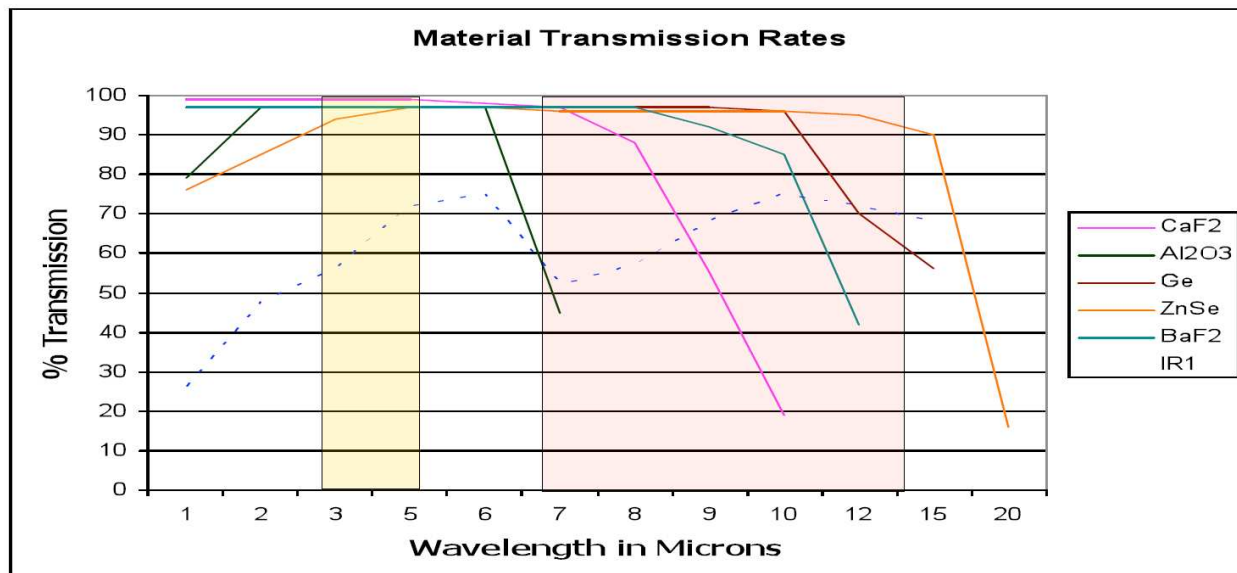


**FIGURE 3-7 COMMON IR WINDOW TRANSMITTANCE AT DIFFERENT WAVELENGTHS [IRISS, 2009]**

Determining the correct transmittance coefficient becomes critical when aiming to acquire true temperature readings. To do this, two images are needed, one without the use of the window and the other with the window installed. An Omega blackbody hot plate calibration source (Omega model: BB-2A, Stamford, Connecticut) was heated to 300°C. The following steps were then carried out:

1. In *ThermaCAM Researcher* set the emissivity to 1.00 in the object parameters settings tab.
2. Place the hot plate in the chamber, get it up to target temperature and allow at least 10 minutes to elapse for temperature stabilization (this is the approximate amount of time for the hot-plate to reach steady-state as determined through experimentation).
3. Via *ThermaCAM Researcher*, measure a large area average temperature on the surface of the blackbody without the ZnSe window present.
4. Install the ZnSe window.
5. Change the “External Optics” setting until it reads the temperature from step 3.

The transmission of the ZnSe window was found to be 94%. In the calculation, anything that is not transmission is considered emission. Therefore, 6% of the radiation reaching the detector is from the window and the software needs to account for this. This procedure should be repeated frequently (at minimum every 10 builds) as the window is exposed more often, and the metallization of the window is more likely to occur. To lessen the likelihood of transmittance reduction, the ZnSe glass was cleaned every three builds using Kimwipes (Kimberly-Clark Global Sales, Inc., Roswell, GA) and isopropyl-alcohol.

**TABLE 3-1 EXTERNAL OPTICS TESTING OF ZNSE WINDOW- IR IMAGE PARAMETERS ASSIGNED**

Object Parameters and Analysis						
Figure	Label	Emissivity	Ext. Optics Temp.	Ext. Optics Transmission	Avg. Temp.	Std. Dev.
3.5	Without ZnSe	1.00	20 °C	1.00	309 °C	5 °C
3.6	With ZnSe	1.00	20 °C	1.00	298 °C	2 °C
3.7	With ZnSe	1.00	20 °C	0.94	309 °C	2 °C

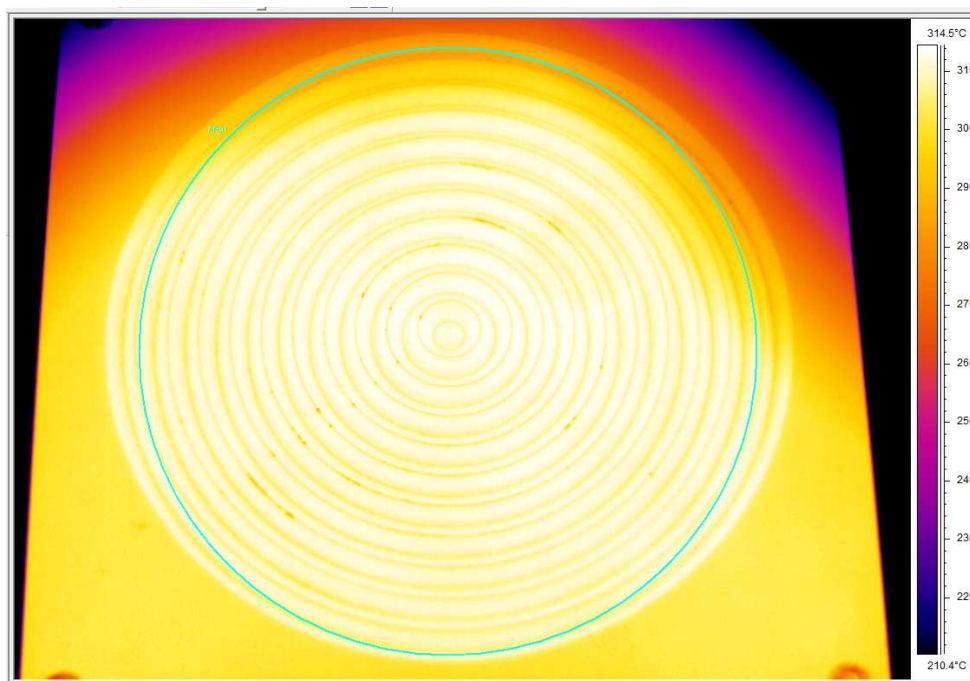


**FIGURE 3-8 IR IMAGE OF OMEGA HOT PLATE WITHOUT THE USE OF THE ZNSE WINDOW**

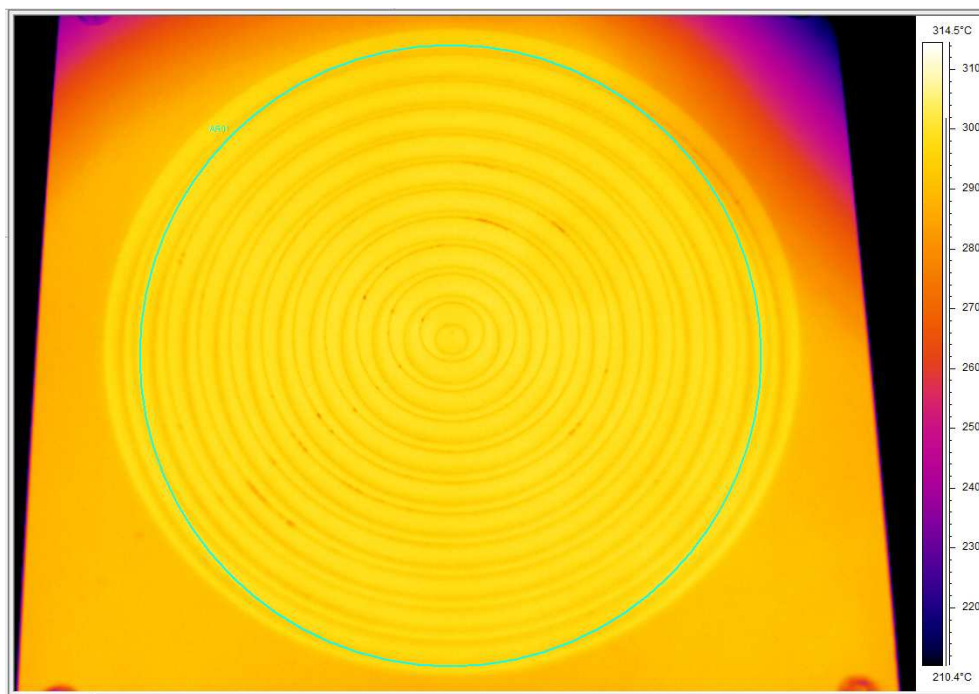


**FIGURE 3-9 IR IMAGE OF OMEGA HOT PLATE WITH THE ZNSE WINDOW INSTALLED**

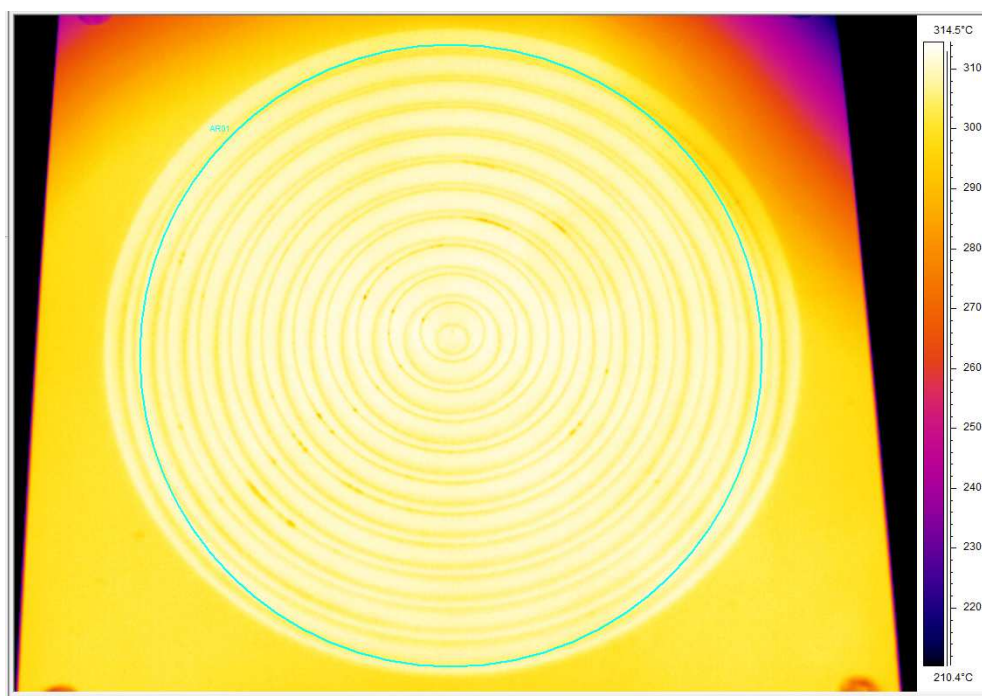


**FIGURE 3-10 IR IMAGE OF OMEGA HOT PLATE WITH THE ZNSE WINDOW INSTALLED AND ADJUSTED TRANSMISSION PARAMETER**

Figure 3-8 shows an IR image capture of the blackbody calibration source without the ZnSe window put in place. In this case, only the atmosphere was acting as a medium between the camera and

surface, hence the external optics transmission parameter was set to 1.00. The blackbody was set to a target temperature of 300 °C, and the average temperature was then measured by using a circular area tool placed on the blackbody “zone” of the hot plate, using *ThermaCAM Researcher* software. The recorded temperature was measured and recorded to be 309 °C. Figure 3-9 is an image capture of the blackbody at the same temperature setting as Figure 3-8, but now with the ZnSe window installed. The window now acts as a medium between surface and the camera, with the external optics transmission still set at 1.00, the recorded temperature was 298 °C. The external optics transmission coefficient was then reiterated until the average temperature matched the temperature of the image taken without the window. Following this procedure, the external optics transmission coefficient (0.94) was then assigned to the camera to produce a corrected image (Figure 3-10) to match the original image (Figure 3-8).

### **3.3.2 CREATING A BLACKBODY SPECIMEN**

An isothermal cavity heated to a uniform temperature generates blackbody radiation, called a cavity radiator, the characteristics of which are determined solely by the temperature of the cavity. This cavity radiator becomes a necessary tool when determining material radiation characteristics and for calibrating thermographic instruments such as an IR camera.

The construction of a blackbody source is simple. A common blackbody used in IR measurements is a cavity with a small opening (Figure 3-11 Blackbody cavity). This cavity-type blackbody will have radiation coming in through the opening and undergoes multiple reflections once inside allowing for the radiation to be reflected by the interior surfaces of the cavity before the radiation can escape [Cengel, 2007]. The level of blackness, or emissivity, obtained at the aperture is  $99.4 \pm 0.2$  [Castrejon-Garca *et.al.*, 2010] using the given dimensions (shown in Figure 3-12) and is capable of handling almost all wavelengths.



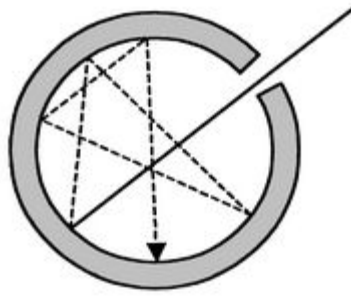


**FIGURE 3-11 BLACKBODY CAVITY**

To determine the emissivity of a Ti-6Al-4V specimen, a rectangular prism with outside dimensions of 37 mm x 37 mm x 40 mm was built via EBM. For the cavity, an orifice diameter of 2.5 mm with a depth of 5 mm was fabricated with an internal spherical cavity of diameter 30 mm (Figure 3-12). A second sample was also built, a cylinder: 37 mm (diameter) x 40 mm (height), with same dimensions for the internal cavity (Figure 3-12). It is important to note that the construction of these samples in EBM also helps support the true emissivity value since emissivity is a function of surface morphology, and therefore the uniqueness of this surface will be the same as future builds in EBM. Once fabricated, the parts were then cleaned to remove un-melted powder from inside the cavity. One specimen was then placed back in the A2 system, the vacuum chamber was activated, and the block was heated to 760°C with the electron beam. The beam is stopped and sequences of images were captured. Using *ThermaCAM Researcher Professional* software, the emissivity of the aperture, which closely resembles a blackbody, was set to 0.99 [Castrejon-Garcia *et.al.*, 2010]. Using a spot measurement tool, the temperature of the aperture is recorded. Now the measurement function is moved to the specimen surface. Using the software to determine the emissivity of the sample's surface, or simply equating Stefan-Boltzmann for both surfaces (the aperture and the Ti-6Al-4V surface) and solving for the unknown emissivity, yields the new emissivity value. The emissivity data gathered is presented in section 5.3 Emissivity Studies.

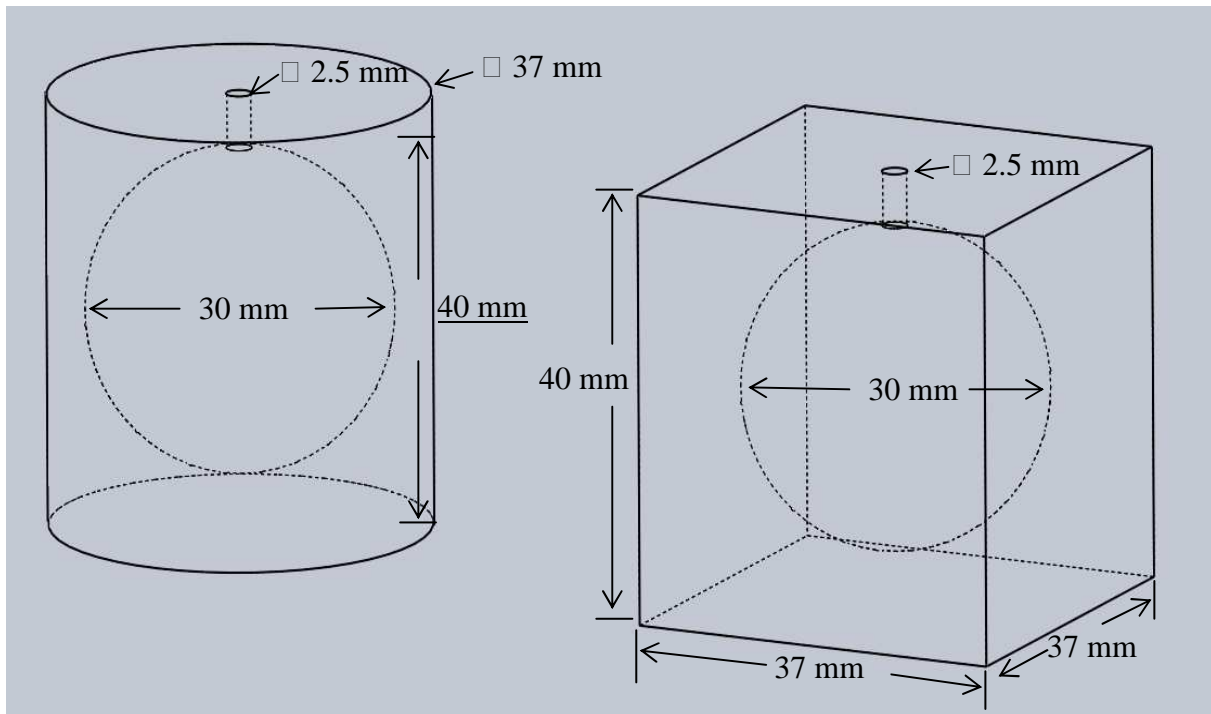


**FIGURE 3-12 WIRE FRAME VIEW (WITH HIDDEN LINES) OF BLACKBODY CAVITY MODEL SPECIMEN-CYLINDER (LEFT) AND RECTANGULAR PRISM (RIGHT)**

### 3.3.2 REFLECTIVE SOURCES

The influence that surrounding surfaces have on a sample is critical to account for when conducting infrared measurements. As discussed in the literature review in Chapter 2 section 2.4, radiation of an object being measured and “seen” by the IR camera consists of radiation being emitted by the target object and reflections striking the target from the surrounding environment. The goal here is to obtain the view factors associated with the wide heat shield used in the Arcam A2. Recall, that the view factor is used to account for the geometric relations involved in how surfaces view each other [Narayana, 1998]. Once the view factors have been calculated, temperature data of the enclosure (heat shield) walls is used to determine the mean radiant temperature  $T_{mr}$  that can then be accounted for in infrared measurement calculations to acquire a true temperature value of the surface. Mean radiant temperature data and surface temperature measurements are presented in Chapter 5.

The following procedure will help reduce the error in temperature measurements significantly. Although the analysis may be cumbersome and tedious, it becomes necessary to conduct accurate surface temperature measurements. Fortunately, the view factors is the most tedious variable to determine, and the same view factors calculated here may be used for future measurements in the Arcam A2 system, regardless of the material being used; as long as surface wall temperature measurements are gathered for said materials.

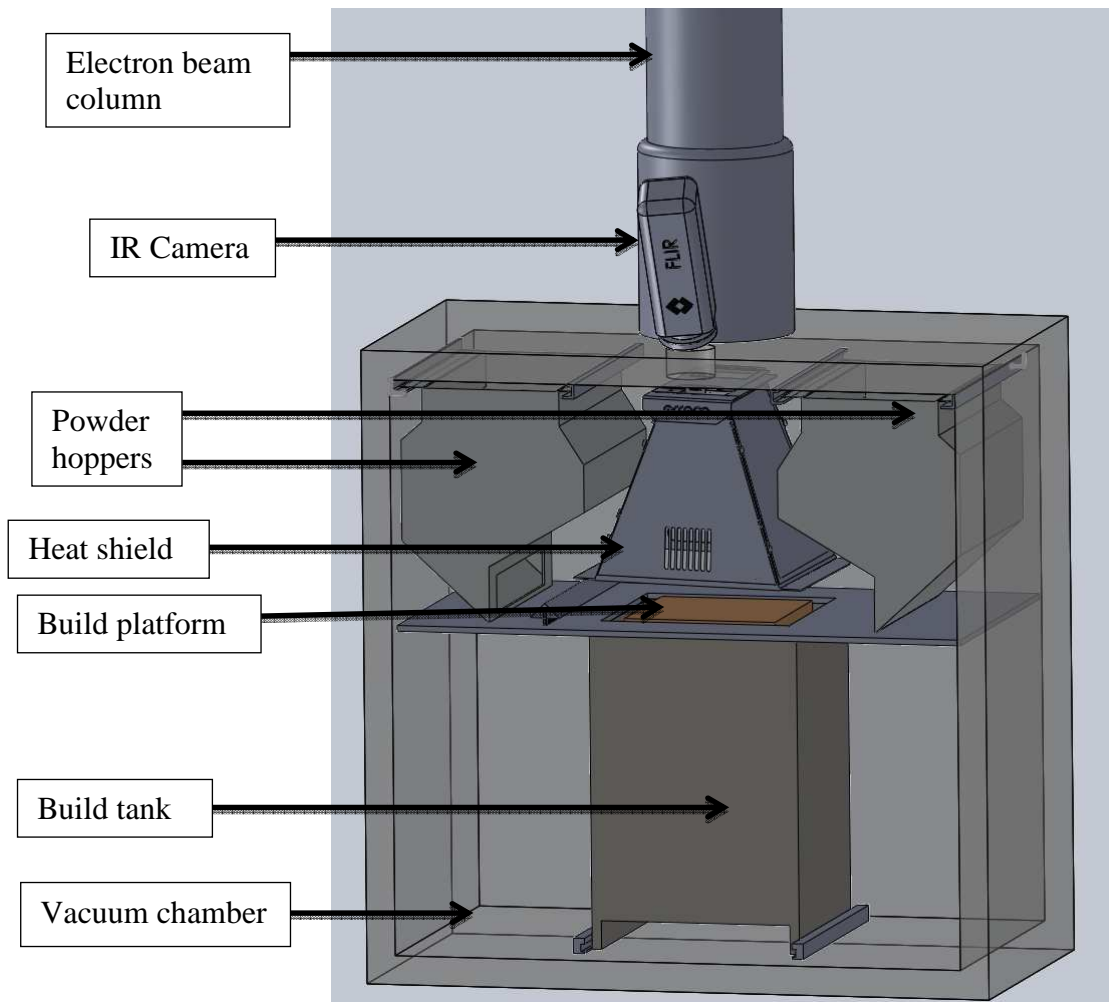


**FIGURE 3-13 CAD RENDERING OF THE ARCAM A2 VACUUM CHAMBER WITH IR CAMERA**

### 3.3.2.1 SIX-SURFACE ENCLOSURE

The first step in determining the mean radiant temperature  $T_{mr}$  is to identify the reflections striking a surface. The Arcam A2 system uses a heat shield that is placed atop of the build surface that serves as an insulator of the build platform- to help constrain the heat being generated by the electron beam to within the powder bed. The heat shield is placed directly over the build platform, as seen in Figure 3-13. The heat shield is the primary source of reflection onto the build surface- the target of interest and what is seen by the IR camera. The heat shield (front, left, rear, right, and top shield) and the build surface make a six-surface enclosure.

Figure 3-14 shows a CAD rendering of the Arcam A2's heat shield, and the build platform. Note, the size of the build platform used in the following calculations is equal to 160 mm X 120 mm which is representative of the field of view that the IR camera can see at its stationary position 0.3 m above the build surface. When calculating radiant interchange at any surface, it is necessary to include radiation arriving at that surface from all surfaces that make up the enclosure. This is to make certain all radiation is fully accounted. Once the enclosure is identified, the thermal state and radiation properties on each surface of the enclosure are specified [Sparrow and Cess, 1978]. In the current analysis, the surfaces are assumed to be opaque, diffuse, and gray, meaning that the surfaces are nontransparent, they are diffuse emitters and diffuse reflectors, and are independent of wavelength. This is a common assumption made in radiation problems to make a simple analysis possible [Cengel, 2007]. Also, since the heat shield rests 50 mm above the build platform, leaving an open space between the build surface and the shield walls, equivalent radiation properties are assigned to the side and top openings found in the enclosure. These assumptions are most often required in radiation analysis. This fictitious enclosure is represented by the dashed lines seen in Figure 3-14. This assumption may be seen as analogous to a control volume assumption made in thermodynamics and fluid mechanics problems. Also, each surface

of the enclosure is isothermal and both the incoming and outgoing radiation is uniform over each surface [Cengel, 2007].

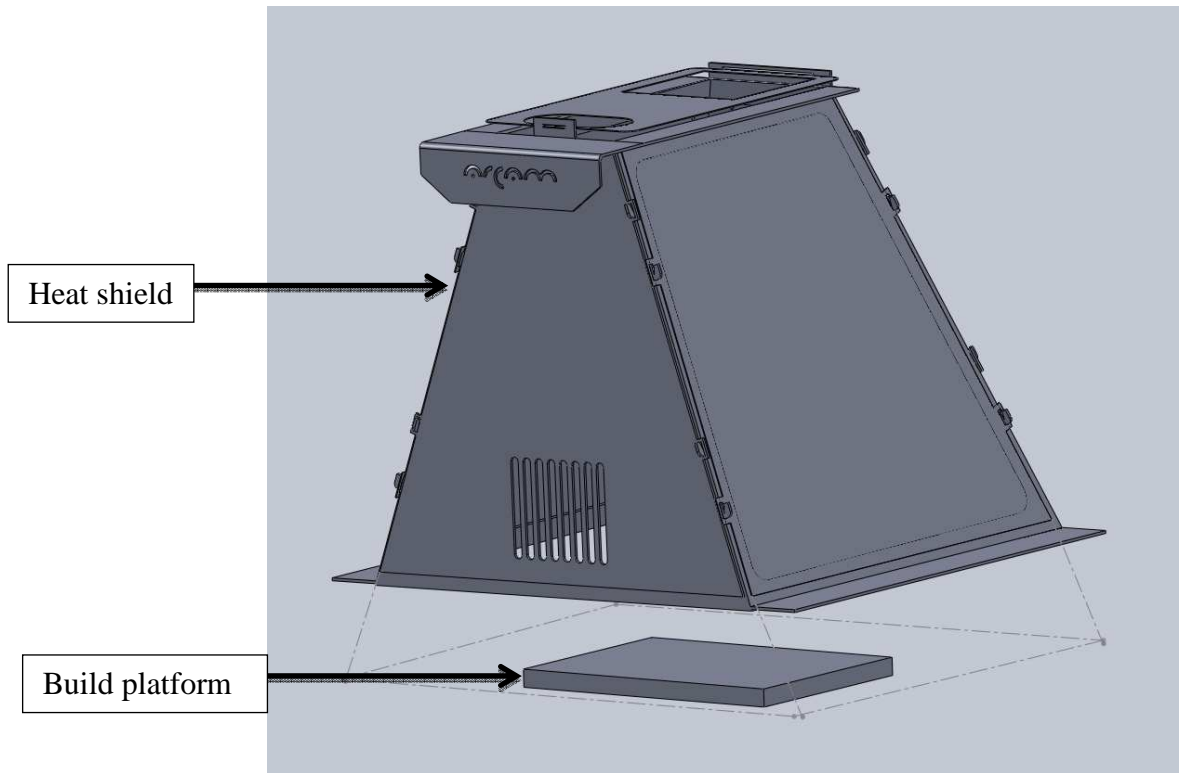


**FIGURE 3-14 CAD RENDERING OF HEAT SHIELD AND BUILD PLATFORM; MAKING A 6-SURFACE ENCLOSURE.**

### 3.3.2.2 CALCULATING THE VIEW FACTORS

In radiation analysis, an enclosure consisting of  $N$  surfaces requires the evaluation of  $N^2$  view factors [Cengel, 2007]. The evaluation of 36 view factors is neither practical nor necessary, since the mean radiant temperature may be calculated experimentally by only evaluating the view factors associated with the target surface to the surrounding walls, that is, only five view factors for a six-surface enclosure. The mean radiant temperature may be defined as the temperature of an isothermal cavity whose radiation heat transfer to the sample is the same as the real cavity [Coppa and Consorti, 2005].  $T_{mr}$  is determined from the following equation

$$T_{mr} = \sqrt[4]{\sum_j T_j^4 F_{s-j}} \quad 3-2$$

Where,  $F_{s-j}$  is the view factor between the sample and the  $j$ -th wall which represents the fraction of the radiation leaving the surface  $s$  that strikes the  $j$ -th wall, and  $T_j$  is the temperature of the  $j$ -th wall [Coppa and Consorti, 2005]. Temperatures of the shield walls were gathered using thermocouples; the procedure is discussed in the following section.

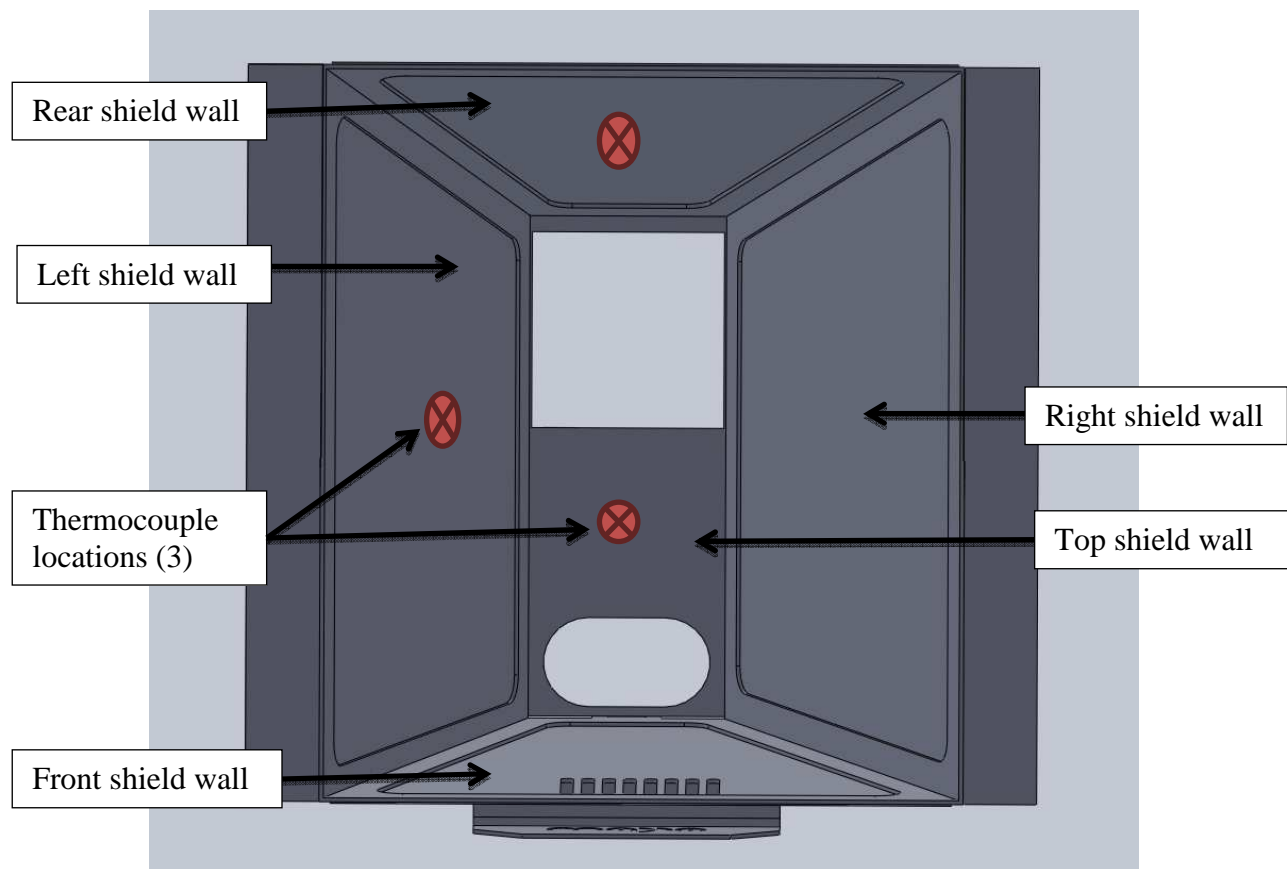


**FIGURE 3-15 CAD RENDERING OF THE BOTTOM VIEW OF THE ARCAM A2 HEAT SHIELD (WIDE)**

Figure 3-15 shows the bottom view the heat shield, or how the build surface “sees” its enclosure. The view factor for each wall of the enclosure was calculated independently by using published formulae and plots, and were then verified using Matlab software (MathWorks, Natick, MA). A summary of all view factors calculated is given at the end of this section. The following sub-sections present the procedure in which each was calculated.

### 3.3.2.2.1 SURFACE TO TOP SHIELD

First, the view factor from the surface to the top shield is analytically calculated by using published graphs with view factors that are necessary to conduct the evaluation. The first step in the procedure is to represent both surfaces by a schematic (Figure 3-16) with the same dimensions as the two real surfaces. This drawing will aid in quickly determining surface areas, any symmetry that may become useful and any distances required. The configuration seen in Figure 3-16 is two rectangles of unequal size in parallel planes. Published graphs and tables only exist for two parallel rectangles of equal size, therefore, the two unequal rectangles are sectioned into equal rectangles to where flux algebra may be applied to determine the sought after view factor.

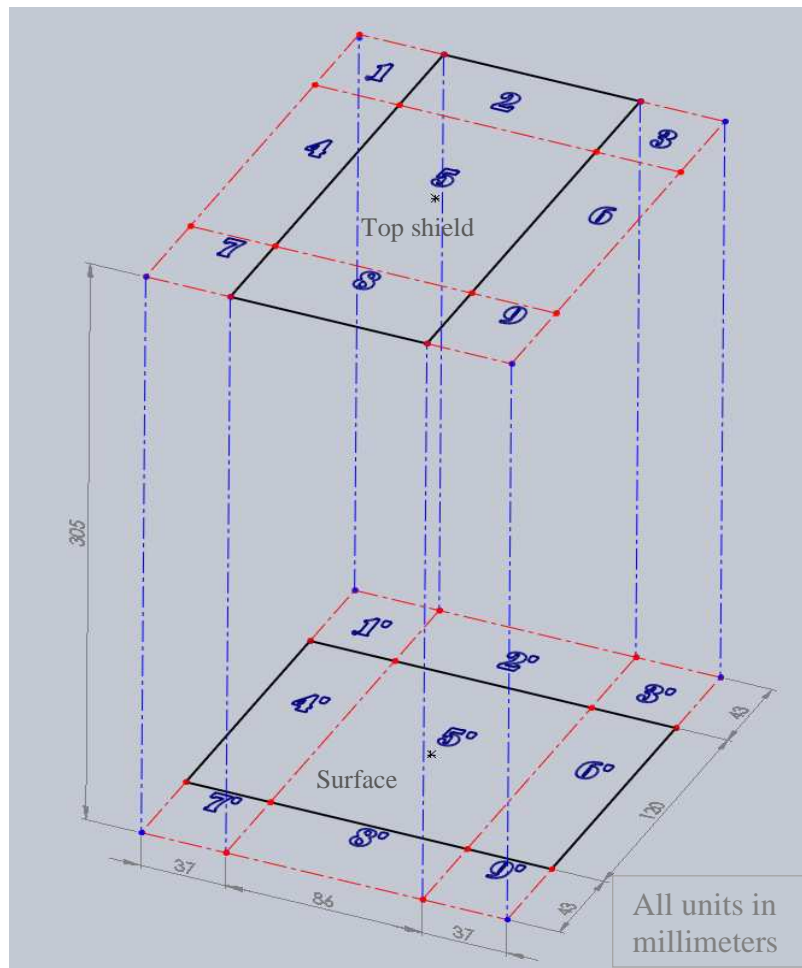


**FIGURE 3-16 SCHEMATIC REPRESENTATION OF SURFACE TO TOP SHIELD GEOMETRIC RELATION.**

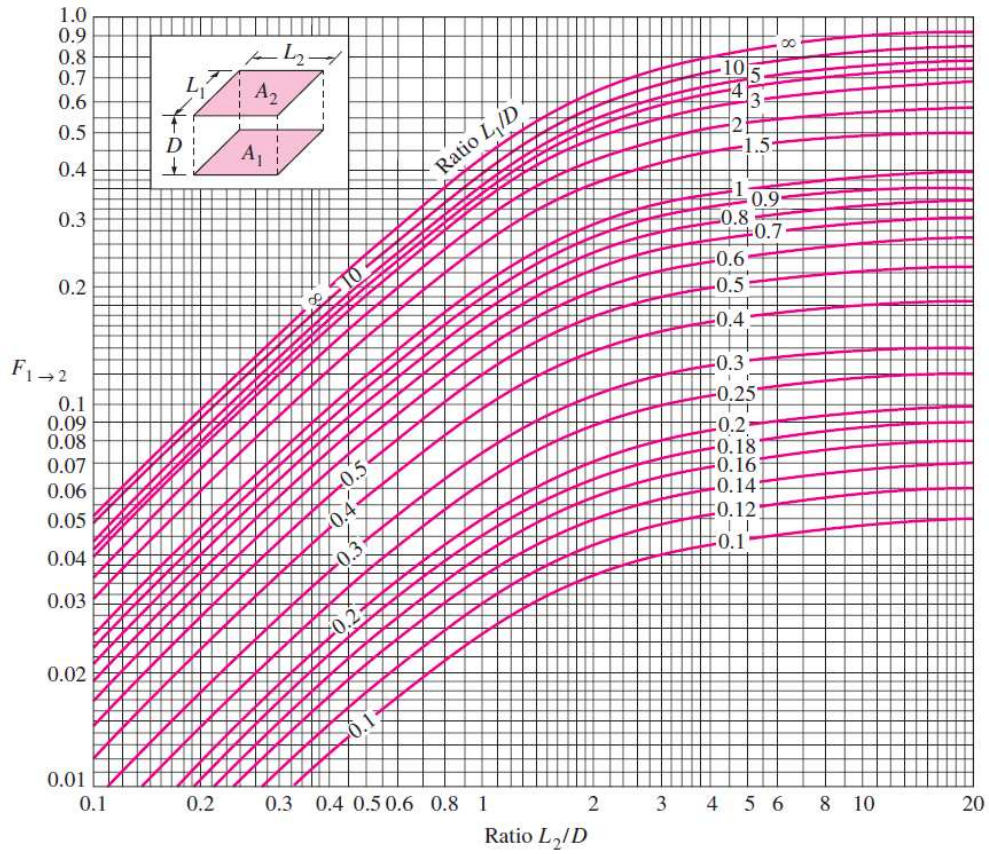


**FIGURE 3-17 VIEW FACTOR BETWEEN TWO ALIGNED PARALLEL RECTANGLES OF EQUAL SIZE [CENGEL, 2007]**

The view factor to be determined is denoted  $F_{s-top}$  (surface- top shield) or from the diagram,  $F_{4',5',6'-2,5,8}$ . To determine this view factor, it must first be divided into smaller sections of the known view factors From Figure 3-17. For instance, from Figure 3-17 the following view factors are known:  $F_{5',2'-5,2} = 0.0430$ ,  $F_{5'-5} = 0.0328$ , and  $F_{2'-2} = 0.0123$ . From reciprocity, it is known that

$$A_{2'}F_{2'-5} = A_{5'}F_{5'-2} \rightarrow F_{2'-5} = \frac{A_{5'}}{A_{2'}}F_{5'-2} \quad 3-3$$

From flux algebra,

$$F_{5',2'-5,2} = F_{5'-5} + F_{2'-5} + F_{5'-2} + F_{2'-2} \quad 3-4$$

Then applying reciprocity to each term,

$$A_{5',2'}F_{5',2'-5,2} = A_{5'}F_{5'-5} + A_{2'}F_{2'-5} + A_{5'}F_{5'-2} + A_{2'}F_{2'-2} \quad 3-5$$

Then solving for  $F_{5'-2}$  by using 3-3, gives,



$$F_{5'-2} = \frac{A_{5',2'}F_{5',2'-5,2} - A_{5'}F_{5'-5} - A_{2'}F_{2'-2}}{2A_{5'}} \quad 3-6$$

Equation 3-6 yields numerical value,  $F_{5'-2} = 0.0106$ . Calculations for the remaining view factors that make-up the view factor of interest,  $F_{4',5',6'-2,5,8}$ , are carried out in a similar fashion, with the exception of making use of the special reciprocity relation in some cases. Special reciprocity occurs because of the symmetry with which the various areas are located [Wiebelt, 1966]. That is, whenever sets of areas located on planes are arranged such that the limits of integration on the four dimensions are interchangeably equal, reciprocity will be valid [Wiebelt, 1966]. A special reciprocity relation used in the calculation of the this view factor was,

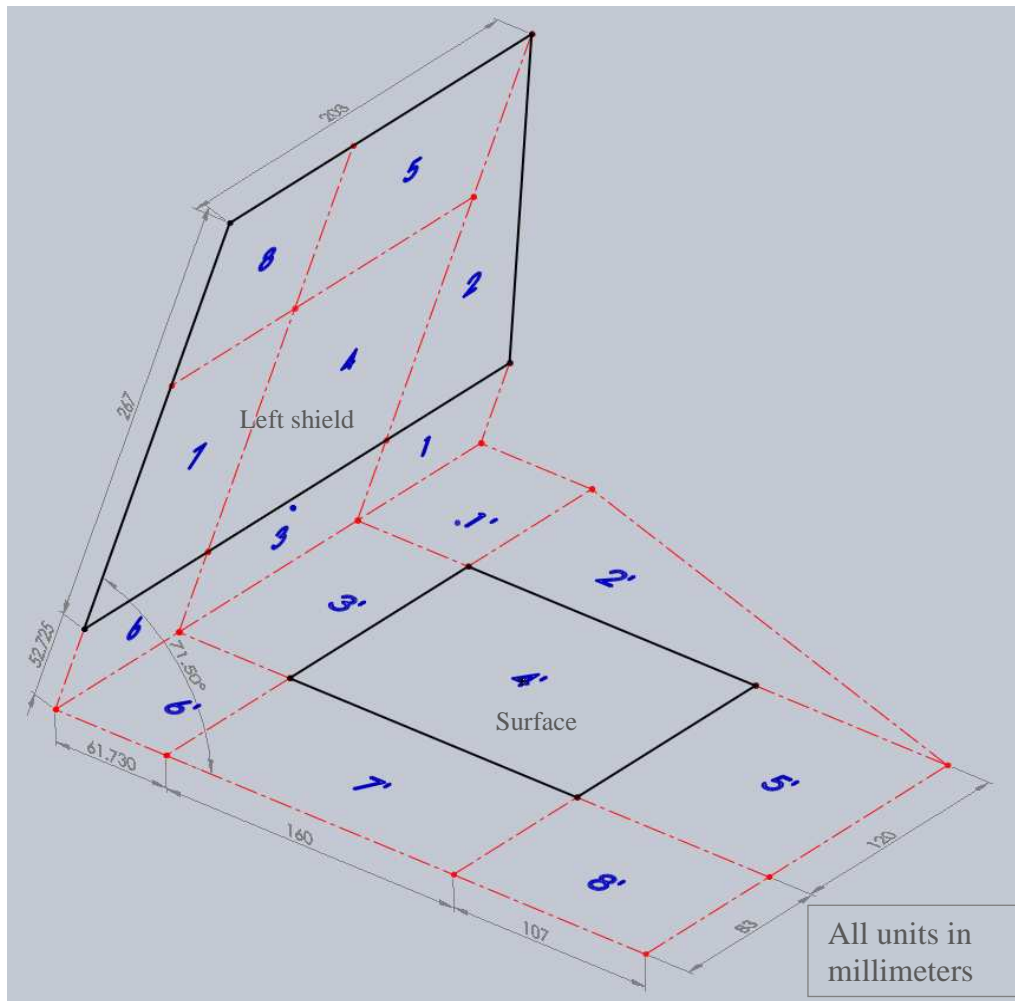
$$A_{4'}F_{4'-2} = A_{5'}F_{5'-1} \quad 3-7$$

View factor  $F_{4',5',6'-2,5,8}$  will expand by the principle of flux algebra and applying reciprocity to each term results in,

$$A_{4',5',6'}F_{4',5',6'-2,5,8} = A_{4'}F_{4'-2} + A_{4'}F_{4'-5} + A_{4'}F_{4'-8} + A_{5'}F_{5'-2} + A_{5'}F_{5'-5} + A_{5'}F_{5'-8} + A_{6'}F_{6'-2} + A_{6'}F_{6'-5} + A_{6'}F_{6'-8} \quad 3-8$$

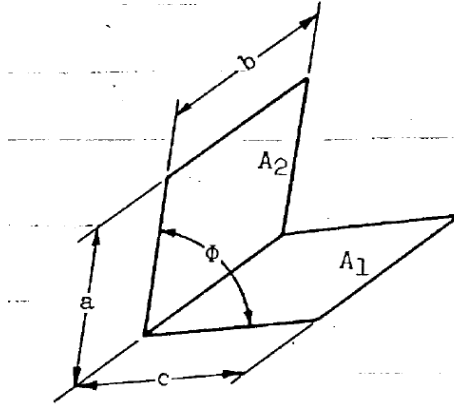
### 3.3.2.2.2 SURFACE TO LEFT, RIGHT, AND REAR SHIELDS

Figure 3-18 represents the geometry for the surface to the left shield wall,  $F_{4'-2,4,5,7,8}$ .



**FIGURE 3-18 SCHEMATIC REPRESENTATION OF SURFACE TO SIDE (LEFT) SHIELD GEOMETRIC RELATION.**

The surfaces here are more distinctive than the previous case, mostly due to the irregular angle between the two surfaces (71.5°) and the addition of a right triangular extension on one side of the rectangle, therefore no published tables or graphs exist for this particular setup. Instead, a published formula for the configuration of two rectangles with one common edge and an included angle between the two planes was used, see Figure 3-19 and Equation 3-9.



**FIGURE 3-19 VIEW FACTOR CONFIGURATION: TWO RECTANGLES  $A_1$  AND  $A_2$ , WITH ONE COMMON EDGE AND INCLUDED ANGLE  $\Phi$  BETWEEN THE TWO PLANES [HAMILTON, 1952].**

The governing equation to the configuration above is,

$$F_{12} = \frac{1}{\pi L} \left( L \tan^{-1} \left( \frac{1}{L} \right) + N \tan^{-1} \left( \frac{1}{N} \right) - \sqrt{N^2 + L^2} \tan^{-1} \left( \frac{1}{\sqrt{N^2 + L^2}} \right) + \frac{1}{4} \ln \left\{ \left[ \frac{(1+L^2)(1+N^2)}{(1+N^2+L^2)} \right] \left[ \frac{L^2(1+L^2+N^2)}{(1+L^2)(1+N^2)} \right]^{L^2} \left[ \frac{N^2(1+L^2+N^2)}{(1+N^2)(L^2+N^2)} \right]^{N^2} \right\} \right)$$

**3-9**

Where,  $N=a/b$  and  $L=c/b$ . Equation 3-9 was evaluated using the Mathematica software (Wolfram, Champaign, IL) for the various sub-rectangles in Figure 3-18 and solved in the same fashion as the previous view factor (surface to top shield), by using flux algebra and reciprocity relations. Although there was an assumption made in the calculation, note that in Figure 3-18 surface 2 is the only triangle, it was assumed that half the radiation striking surface 8 and 7 is striking surface 2. The logic is that a triangle is half the area of a rectangle. That is,  $F_{4'-2} = \frac{1}{2} F_{4'-7,8}$ . Note that due to symmetry, the view factor for the surface to the left shield wall is equal to the view factor striking the right shield wall.

View factor surface to rear shield is calculated with Equation 3-9 as well, also by making the same assumptions. Here, the rear shield has a triangle on either side, each was assumed to be rectangle to determine the view factor in the same manner as the previous, then when acquired reduced by half (a triangle has half the area of a rectangle).

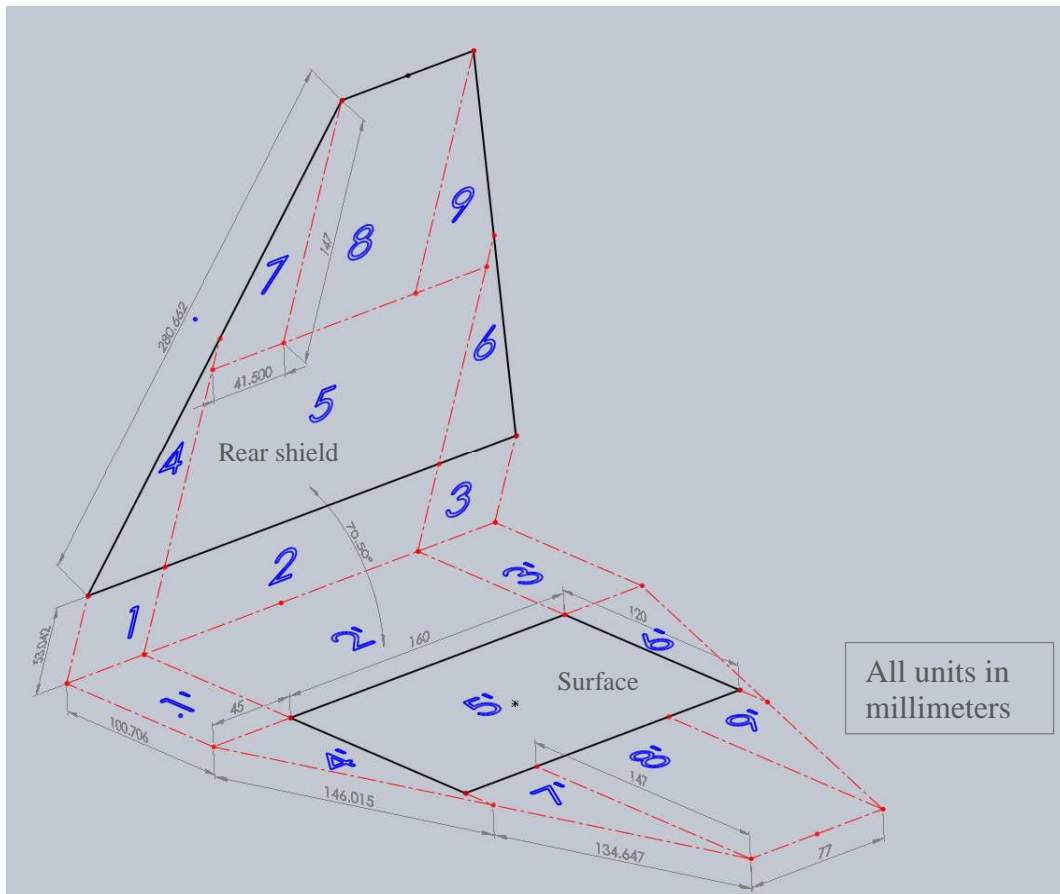


**FIGURE 3-20 SCHEMATIC REPRESENTATION OF SURFACE TO REAR SHIELD GEOMETRIC RELATION.**

### 3.3.2.2.3 SURFACE TO FRONT SHIELD

To determine the view factor of the surface to the front shield, the configuration is first identified as perpendicular rectangles with a common edge. The real edges of the surface do not actually meet, but the fictitious edges of both surfaces ( $1', 2', 3' - 1, 2, 3$ ) do. Therefore, the method in determining the view factor will be the same as in calculating the surface to top shield view factor, only now making use of view factor graphs for perpendicular rectangles with a common edge (Figure 3-22). The front shield also has triangular sides, and therefore the same assumption was made here as before. The triangles are first assumed to be rectangles. Once the view factor is calculated for this “rectangle” it is then divided in half based on the awareness that a triangles area is half of a rectangle under the assumption that these

surfaces are isothermal and both the incoming and outgoing radiation is uniform over each surface [Cengel, 2007].

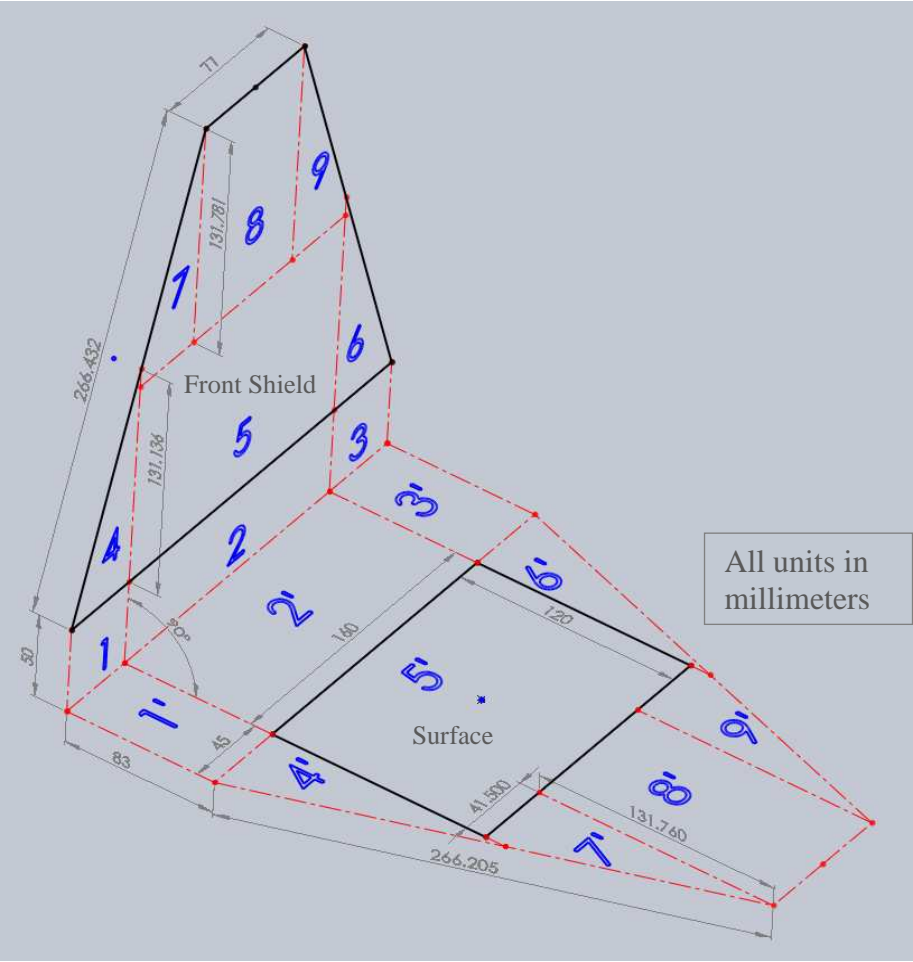
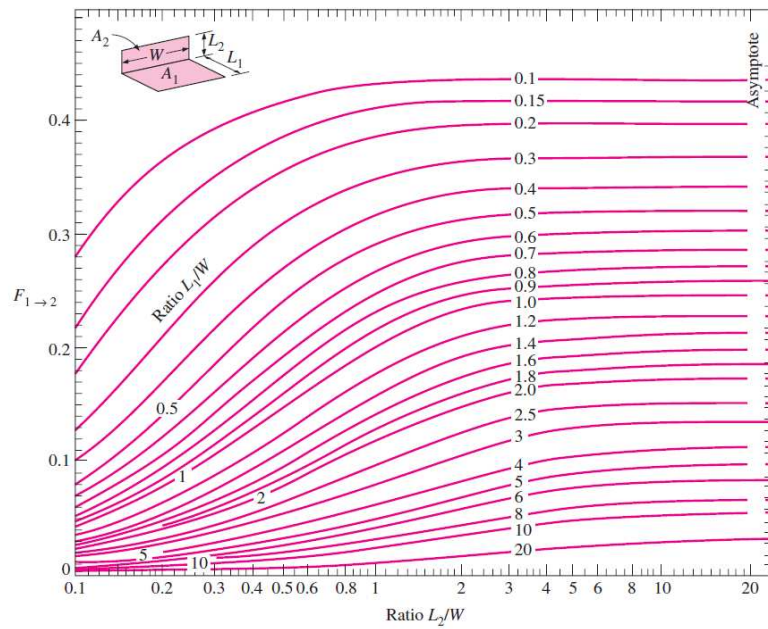


FIGURE 3-21 SCHEMATIC REPRESENTATION OF SURFACE TO FRONT SHIELD



**FIGURE 3-22 VIEW FACTOR BETWEEN TWO PERPENDICULAR RECTANGLES WITH A COMMON EDGE [CENGEL, 2007].**

### 3.3.2.3 VIEW FACTORS RESULTS

The view factor result from the analysis of each wall independently is summarized here. These factors will be used to determine the mean radiant temperature  $T_{mr}$  presented in Chapter 5 where  $T_{mr}$  plays a critical role in measuring true temperature values of the surface bed.

**TABLE 3-2 ARCAM A2 VIEW FACTORS**

View Factors for the Arcam A2's Heat Shield- A Six Surface Enclosure					
				Analytical	MatLAB
					% Diff.
Surface to Top Shield:	F(S-TS)=	F(4'5'6'-258)=	0.052323	<b>0.0524622</b>	0.27
Top Shield to Surface:	F(TS-S)=	F(258-4'5'6')=	0.056779	<b>0.0568567</b>	0.14
Surface to Left/Right Shield:	F(S-LS)=F(S-RS)=	F(4'-24578)=	0.25324	<b>0.256632</b>	1.32
Left/Right Shield to Surface:	F(S-LS)=F(S-RS)=	F(24578-4')=	0.072741	<b>0.0756361</b>	3.83
Surface to Rear Shield:	F(S-RrS)=	F(5'-456789)=	0.16953	<b>0.183491</b>	7.61
Rear Shield to Surface	F(RrS-S)=	F(456789-5')=	0.072184	<b>0.0807008</b>	10.55
Surface to Front Shield:	F(S-FrS)=	F(5'-456789)=	0.11393	<b>0.118385</b>	3.76
Front Shield to Surface:	F(FrS-S)=	F(456789-5')=	0.052726	<b>0.0551668</b>	4.42

Note that both the analytical value and those calculated by MatLAB (MathWorks, Natick, MA) are tabulated, as mentioned in the beginning of the section, the MatLAB software was used as a verification tool of the analytical and graphical calculations. In Chapter 5 the MatLAB values will be used in the analysis, since it has a higher order of precision, the results will be more accurate. This is because MatLAB uses a 64 bit double precision for its calculations (about 16 digits), and a Ti-89 calculator (used in the calculation) uses a 32 bit precision (about 12 digits) [Mathworks, 2013; Ti, 2013]. Additionally the assumptions made during the analytical analysis may have caused some deviation from the real value, such as the triangle assumption being half of the rectangular view factor.

## **CHAPTER 4 SOFTWARE DEVELOPMENT**

The duration of EBM builds varies greatly with respect to size and geometry of the part being fabricated. This range may lie anywhere between 4 hours to 80 hours. It is for this reason that a major focus of this work was to produce an automated solution to acquire images throughout the entirety of any build. The images were to be captured at the designated process step during the build (layer) cycle and then archived making it possible to correlate the image number in the sequence to the layer number. By knowing this correlation, it is then possible to pinpoint any discrepancy or defect observed in a particular image to the location (Z-height) of the part.

Additionally, the automatic image capture will be the gateway to achieving a fully-automated feedback control system that will make real-time parameter modification. The IR images captured will be analyzed and processed to search for “cold” spots or abnormal regions on the parts surface. Parameters will be modified as necessary; these parameters may include the beam power (current), focusing current, scan speed, preheating time, and post-heating time. Similarly, Olszewska and Friedel [2004] proposed a system based on neural networks for controlling the acquisition and processing of information of an electron welding machine which allowed the real-time correction of parameters. Recently, IR monitoring has been successfully employed in the monitoring of other additive manufacturing (AM) processes (e.g. selective laser melting) with valuable results [Griffith, *et.al.* 1999; Hu and Kobacevic, 2003; Xiong, *et.al.*, 2009].

### **4.1 AUTOMATED IR IMAGE AQUISITION**

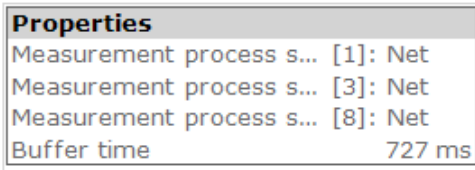
#### **4.1.1 CAMERA SIGNAL SETUP**

In order to automate the opening of the flap mechanism (or shutter) that is used to protect the zinc-selenide window from metallization during a build, a voltage signal output from the Arcam system was required. This signal was received and interpreted by the modular controller NI compactRIO-9074 (National Instruments, Austin, TX). There are three different process signals that can be implemented to



a layer during the course of an entire build. For example, signal one can be assigned to come on before the preheat step, signal two before the melt, and signal three after the melt. A collaborative effort with Arcam software engineers resulted in a new version of the EBM Control (Arcam AB, Sweden) software that allows the selection of these process steps. The following shows how to set-up the signal-process steps in EBM Control:

- In EBM Control, set Menu\Machine Setup\Film Feeder\ Camera = true and a camera theme will appear on the process setup page.
- Use the camera theme on the process setup page to decide in which process steps to take camera images (seen in Figure 4-2 Process steps with ‘Delay’ themes for image capture).



Properties	
Measurement process s...	[1]: Net
Measurement process s...	[3]: Net
Measurement process s...	[8]: Net
Buffer time	727 ms

**FIGURE 4-1 CAMERA THEME WITH ASSIGNED SIGNAL PROCESS STEPS**

- Figure 4-1 shows an example of implemented process signal steps in camera theme (step numbers 1,3, and 8). On the process setup page set a Net theme as the step for capturing an image (see Figure 4-2 Process steps with ‘Delay’ themes for image capture). The process step number is when the EBM ‘A3’ output module will supply the 24 V signal.

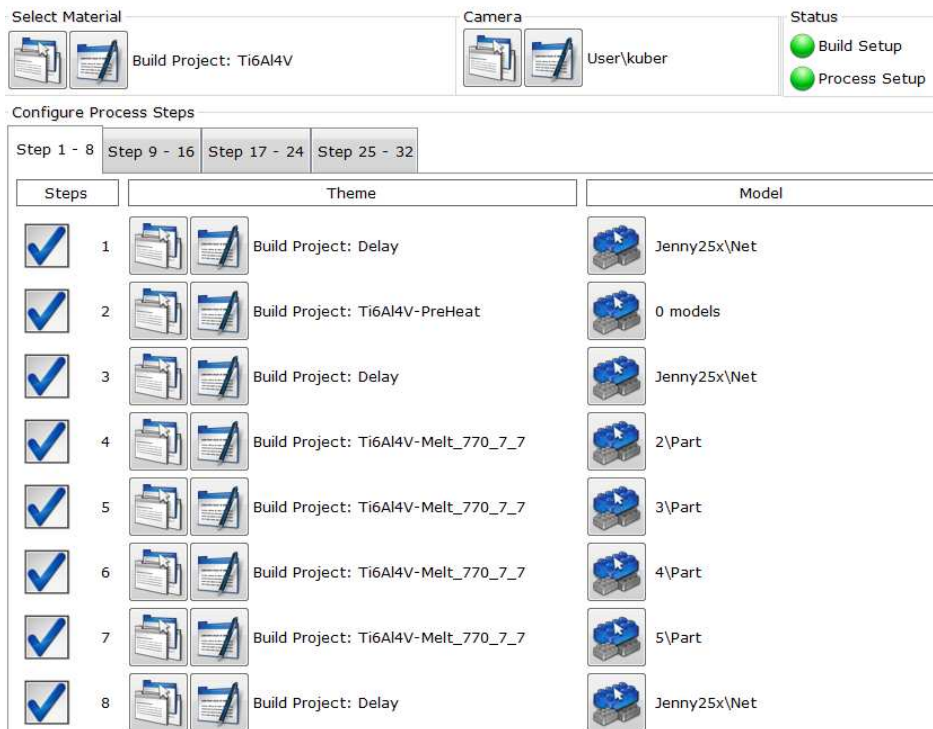


**FIGURE 4-2 PROCESS STEPS WITH ‘DELAY’ THEMES FOR IMAGE CAPTURE**

- To control the time of the delay there are two options (as recommended by Arcam) :
  1. Create a model with a number (e.g. 25) of small cylinders of the same height as the real build. In a Net theme, set
    - Current = 0 mA
    - Spot time = delay time / number of cylinders. Delay time should be at least 2000 ms to ensure compensation of the input delay time of the NI 9411 digital input module.
    - Offset > the radius of the cylinders (will leave just a spot to melt)
    - Block offset = true
  2. Create a model with rectangular prisms of the same height as the real build. In a Net theme, set
    - PointDist = contour length of the rectangle/number of points with zero current.

- Current = 0 mA
- Spot time = delay time number of points with zero current. Delay time should be at least 2000 ms.

Properties	
Enabled	True
Current	0 mA
Spot time	100 ms
Focus offset	0 mA
Multispot Deflection slew rate	
Min length	8 mm
Max length	30 mm
Length proportionality	0,42
Jump distance to ena...	60 mm
Speed	155000 mm/s
Enabled	False
Properties	
Offset	0 mm
Block offset	True
PointDist	0,1 mm
Heating	
Enabled	False
Maximum heat time	20 s
Heating factor	0,7
Heating between models	True

**FIGURE 4-3 EXAMPLE OF NET THEME PARAMETERS FOR ‘DUMMY’ BUILD**

Note, that the delay time is equal to the spot time multiplied by the number of cylinders in the dummy build (e.g. 25). From the example in Figure 4-3 Example of Net theme parameters for ‘dummy’ build the delay time is calculated as follows,

$$\text{delay} = \text{Spot time} \times \# \text{ of parts} = 100 \text{ ms} \times 25 = 2500 \text{ ms} \quad 4-1$$

#### 4.1.2 VOLTAGE SIGNAL INTERCEPT

Now that the EBM software has been customized to output digital signals, the next step in the implementation of a feedback control system is to intercept the output signals from the A2’s output module. In the electrical cabinet of the A2, digital output module ‘A3’ was powered from the 24 V power unit ‘T4,’ - 18L+ to socket 11 and 9M to socket 20. Sockets 12, 13, and 14 (from module ‘A3’) output a 24 V signal for process steps 1, 2, and 3, respectively (see Figures 14 and 15). These sockets

were wired using a solid single-conductor wire, 20 AWG, rated at maximum of 30 V, directly to the NI 9411 6-channel differential digital input module. The NI 9411 digital input and the NI 9481 electromechanical relay (opens/closes the flap mechanism) are mounted on to the modular controller NI compactRIO-9074 (Figure 4-4).

The NI compactRIO-9074 controller was the central unit for feedback from the A2 system. This unit allowed the attachment of various modules to realize tasks such as measuring of signals and issuing of commands. As has been mentioned before, this controller received the initial voltage signals from the Arcam machine and sent the open command to the flap mechanism, allowing the IR camera to view the surface bed. The controller then received the thermal image and processed the data to issue commands, as needed, to the Arcam control unit. This automated solution, in the future, will allow the remote control of build parameters. Figure 3-5 is the architecture for IR feedback control in the Arcam A2 system.

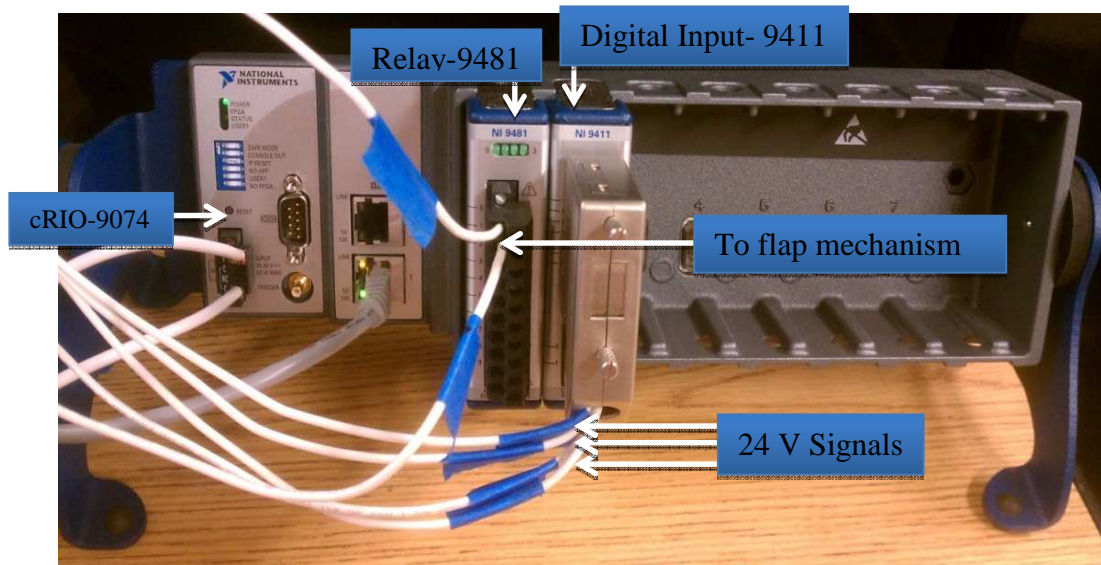


**FIGURE 4-4 NI CRIO 9074 MODULAR CONTROLLER**

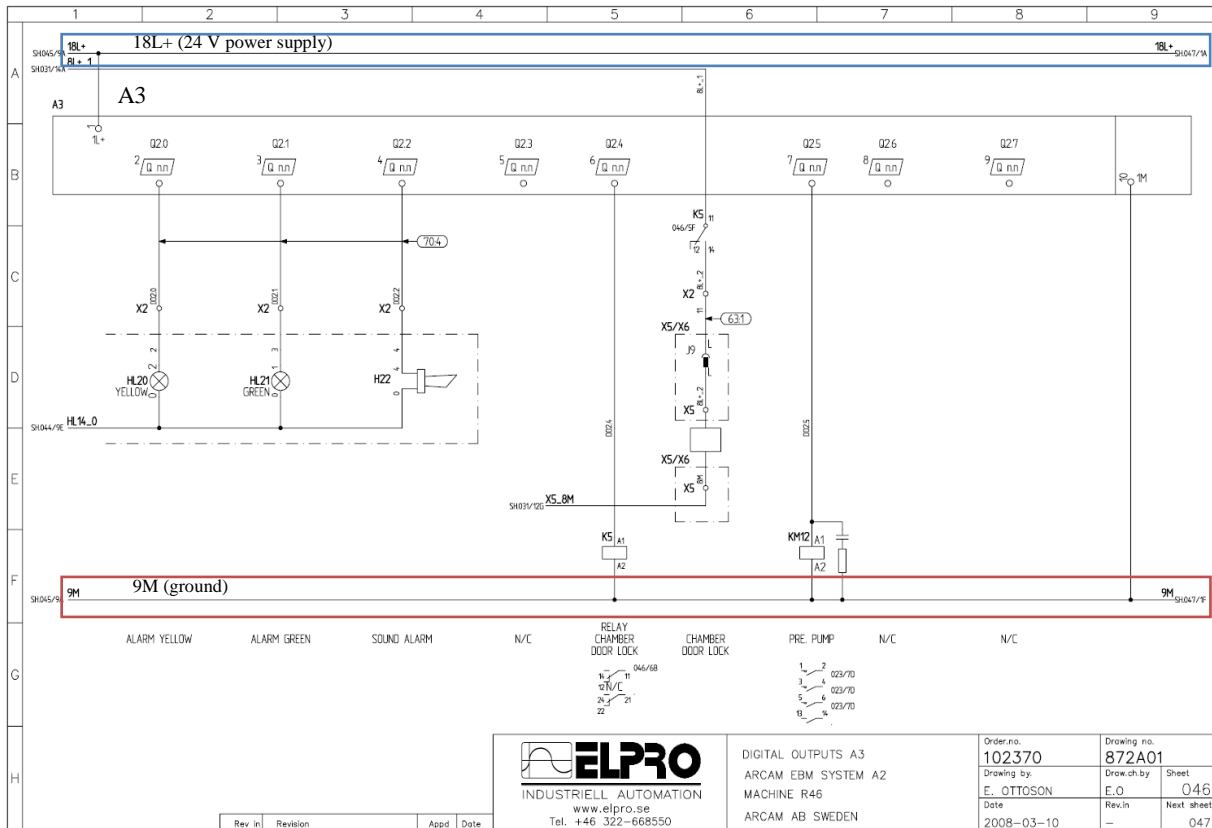


**FIGURE 4-5 CIRCUIT DIAGRAM OF DIGITAL OUTPUT A3. COURTESY OF ARCAM AB.**



**FIGURE 4-6 CIRCUIT DIAGRAM OF DIGITAL OUTPUT A3 (CONT.). COURTESY OF ARCAM AB**

#### 4.1.3 SOFTWARE USER INTERFACE – FRONT PANEL

The user interface or ‘front panel’ - *Image acquisition.vi* seen in, is the primary software used to acquire images automatically. The operator must first supply the ‘Pre-Run Settings’ (camera type, device, interface) followed by the object and camera parameters. The object parameters that are assigned here are critical when attempting to acquire true temperature values. The ambient temperature (Kelvin), or reflected temperature, is used to compensate for the radiation being reflected from the object being measured. The object distance (the distance between the surface of the object and the lens of the camera), relative humidity, and atmospheric temperature may be left at their default values since the camera is at a short distance (0.3 m) from its target object, and therefore have negligible effects on the amount of radiation lost to the atmosphere. The external optics temperature and transmission (0.94

and 315 K, respectively) are set according the measured values discussed in section 3.3.1. The reference temperature is simply a reference value to make relative measurements to this user-specified value; the result is simply the difference between these two values. Finally, the emissivity for the material is assigned.

The user may now execute the program by pressing the play button on the front panel window toolbar. The 'IR Image Display' section provides the user with temperature data corresponding to a specified pixel, and the real-time camera display. In the 'System Monitoring' section the user has the flexibility to manually open the flap mechanism (shutter), without the input of a voltage signal from the 'A3' module, by toggling the 'Open/Close Shutter' switch. This section also includes three 'LED' displays with their corresponding signal number that comes on once a voltage signal is received. The 'Stop' button ends the entire image acquisition process. It can easily be restarted by clicking the play button, and the image sequence will begin from its last image capture.

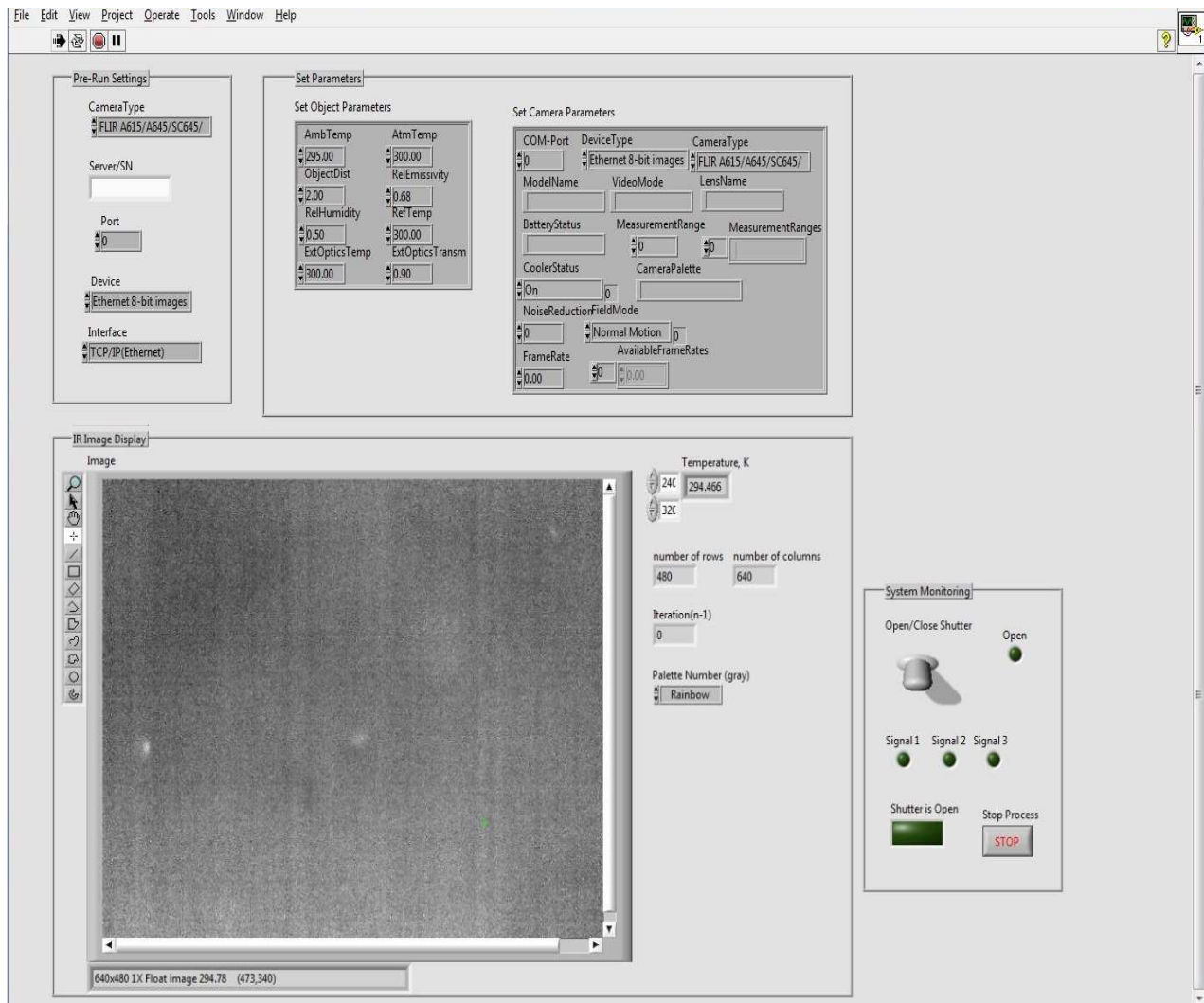


**FIGURE 4-7 FRONT PANEL (USER INTERFACE) OF IR IMAGE ACQUISITION VI**

#### **4.1.4 PROGRAM CODE – BLOCK DIAGRAM**

The program code (*virtual instrument* or simply *vi*, introduced in Figure 3-5 Architecture for IR feedback control in Arcam A2 system) developed via LabVIEW is described here. To successfully employ an image acquisition program using a FLIR product (SC 645 IR camera) through the National Instruments' (NI) data acquisition and programming software LabVIEW, the suitable solution was to use the ThermoVision LabVIEW Digital Toolkit software developed by FLIR (FLIR Systems, Wilsonville, OR) for quick integration with the inputs (shared variables) being grabbed from the NI modular controller (cRIO 9074). By using the toolkit developed by FLIR, the time devoted to



programming was reduced considerably by avoiding creating ‘sub-vi’s’ needed for controlling camera requirements, such as the assignment of input parameters for accurate measurements. Figure 4-8 through Figure 4-11 below show the block diagram (code) that makes the IR automation solution possible.

Step one in the diagram uses the *open.vi* as a ‘driver’ to establish the camera connection. This digital *vi* is then wired to two parameter configuration *vi*’s: *set camera parameters.vi* and *set object parameters.vi*. As mentioned earlier, assigning the correct object parameters (external optics transmission and temperature, emissivity, ambient temperature, etc.) becomes critical to obtaining true temperature values. The *IMAQ create.vi* (or simply *IMAQ*), also seen in step one, creates a temporary memory location for an image, this *vi* will yield the real-time display of the camera image by wiring the sub-*vi*’s- *IMAQ array to image.vi* and *IMAQ window draw.vi* (seen above the case structure in Figure 4-8).

Within the while loop (the grey boundary line) step 2 takes place wherein the signal is intercepted from the EBM main module to act as a trigger for image capture. The purpose of the while loop is so that everything inside of it continuously executes during the course of a build, only stopping after the operator pushes the ‘Stop Process’ button on the front panel (discussed later). The three signals generated from the digital output ‘A3’ are seen in LabVIEW as shared variables *DI0*, *DI1*, and *DI2* (digital inputs) for process signals 1, 2, and 3, respectively. The logic carried out in block diagram 1 is to generate a Boolean true value when any one of the three signals from module ‘A3’ is activated or the manual open button is pressed. The Boolean true value is then passed over to *DO0* (digital output 0) - the electromechanical relay. Once activated, the electromechanical relay then closes the circuit and opens the shutter (flap mechanism). If the Boolean value is false, then no command will be sent to capture images - step 6 in Figure 4-10.

Now that the signal has been intercepted, it acts as a trigger to send a Boolean true value (step 3 in block diagram 1) to the image acquisition case structure. The case structure in its ‘true’ state is seen

in step 4 from block diagram 2 (Figure 4-9). To capture images, four *thermovision digital vi*'s are used. Together, *get recording parameters.vi* and *set recording parameters.vi* create a file path to save multiple images in a designated folder. These *vi*'s are then wired to the *recording action.vi* that directs an action to take place once called – in this case the constant 'single snapshot recording' is used to acquire only one image at a time. This *vi* is called every time the 'A3' output module supplies a 24 V signal. That is, the case structure will capture and save an image during the execution of the allocated 'delay' theme step number (see Figure 4-2 for an example of the 'delay' theme in the process steps). If the Boolean value is "False" then no image is captured – step 7 in Figure 4-11.

The fourth and final *vi* in the image acquisition process (step 4) is the *recording action.vi*, which was configured with a 'stop recording' action constant to end the camera's internal recording function. A time delay is also placed inside the 'true' case structure equal to 1500 ms (1.5 s) to account for the time delay between the electromechanical relay (NI 9481) and the opening of the flap mechanism – this avoided capturing an image of the protective flap instead of the EBM work piece. The image acquisition cycle ends outside of the case structure and out of the while loop. Here, the image display window is closed with *IMAQ wind close.vi* and the temporary memory space created with *IMAQ.vi* is destroyed and cleared with *IMAQ dispose.vi*. Finally, the connection to the camera is closed with the *digital close.vi*.

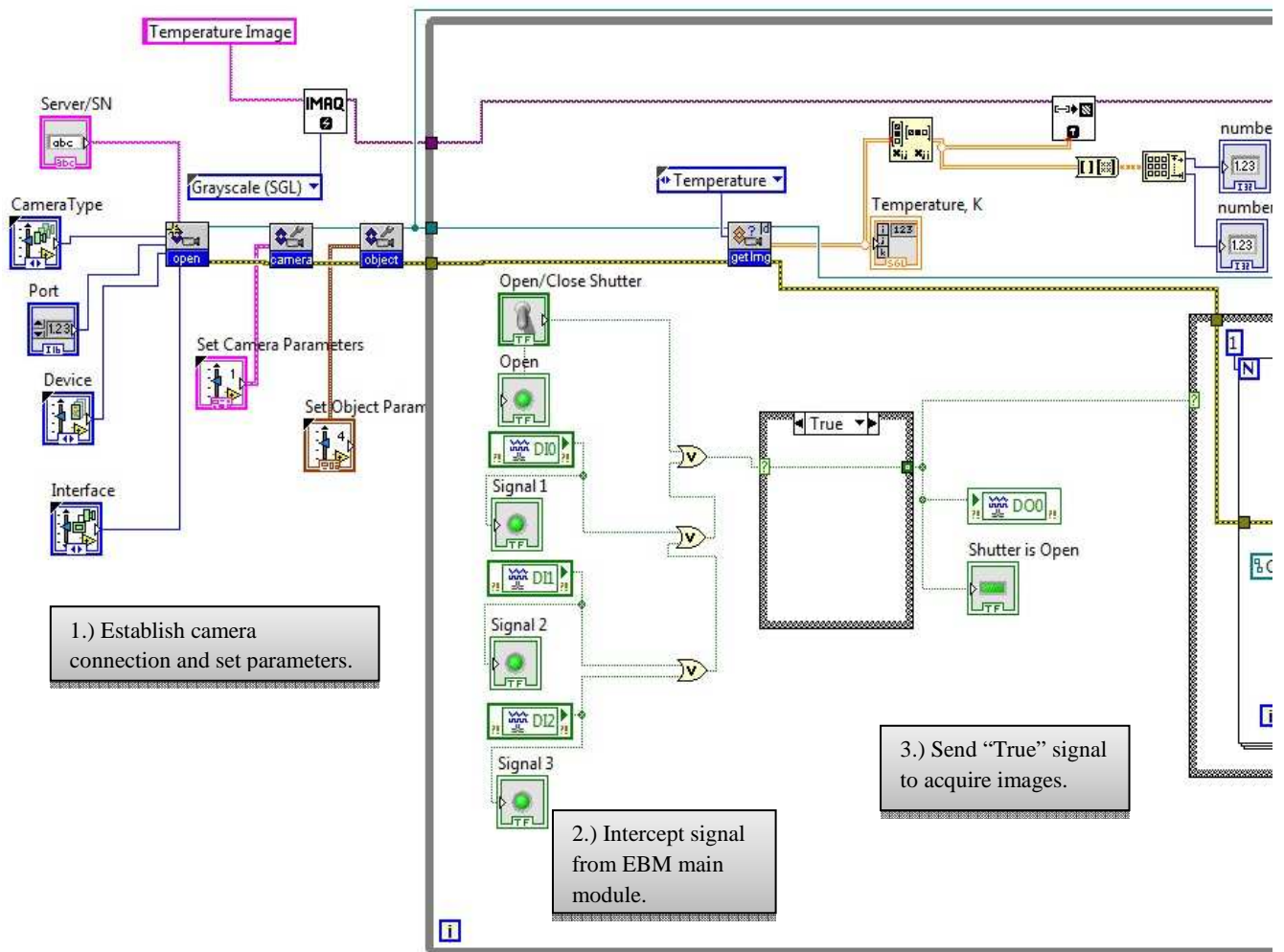


**FIGURE 4-8 BLOCK DIAGRAM – IMAGE ACQUISITION.VI (MODULE ‘A3’ DIGITAL OUTPUT/VOLTAGE SIGNAL - “TRUE” STATE) [1/4]**



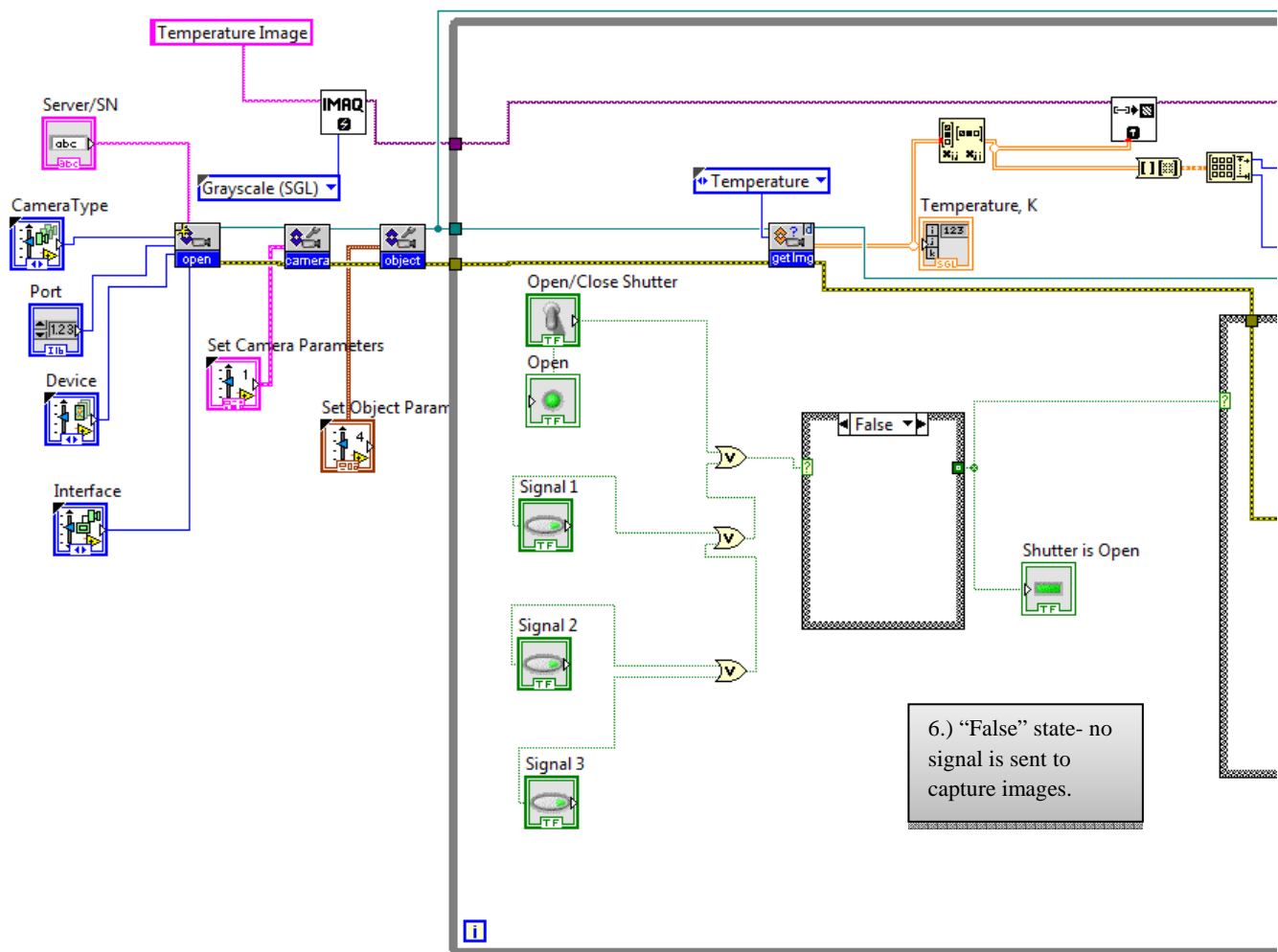


**FIGURE 4-10 BLOCK DIAGRAM – IMAGE ACQUISITION.VI (MODULE ‘A3’ DIGITAL OUTPUT/VOLTAGE SIGNAL - “FALSE” STATE/NO SIGNAL OUTPUT) [3/4]**

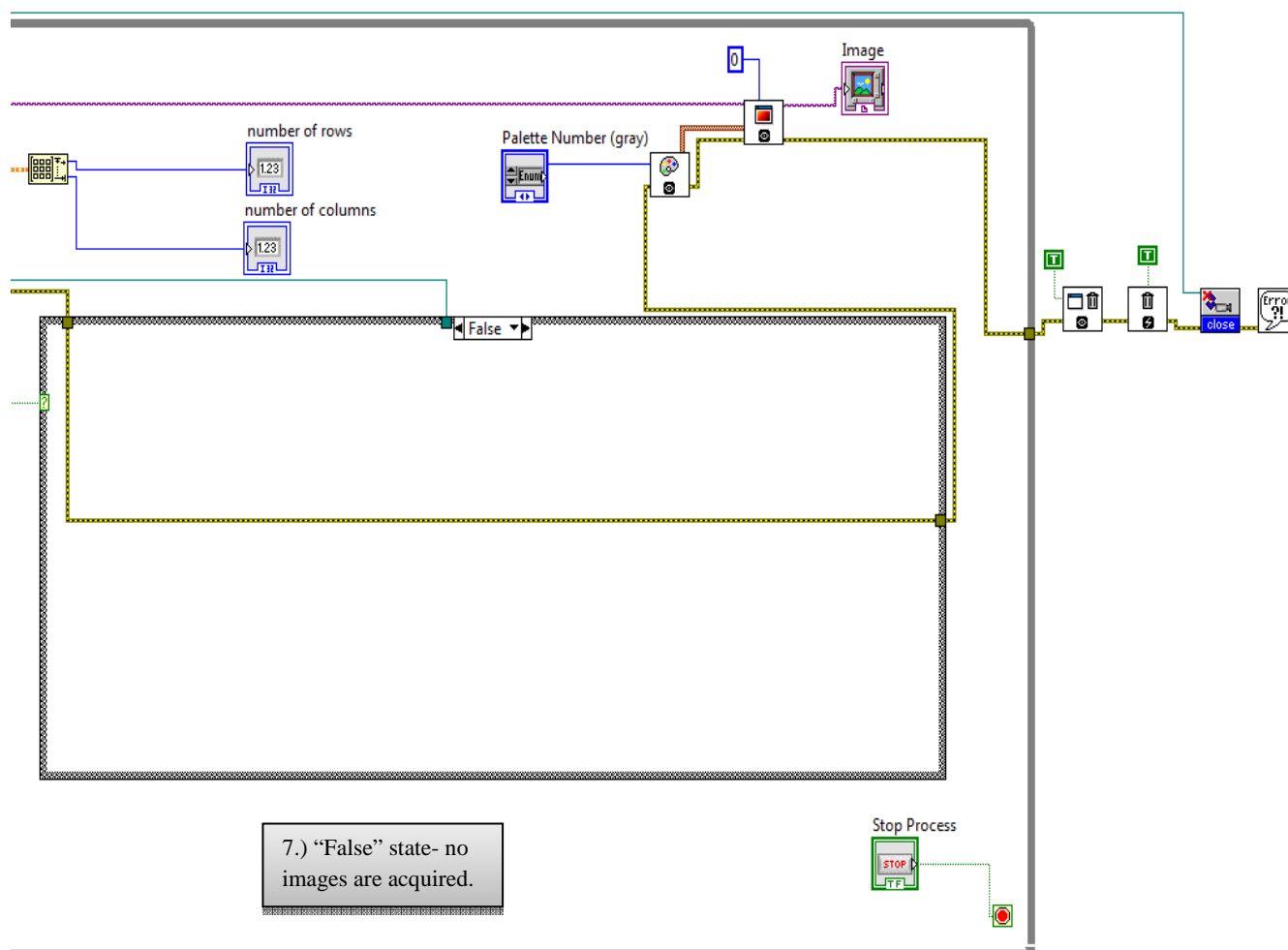


**FIGURE 4-11 BLOCK DIAGRAM – IMAGE ACQUISITION.VI (“SINGLE SNAPSHOT RECORDING”  
- “FALSE” STATE) [4/4]**

The scope of this project required simultaneous multiple surface temperature measurements to be made. The system works in a vacuum environment and requires that a high standard of vacuum pressure ( $10^{-4} \text{ torr}$ ) be maintained if any external equipment is to be installed inside the vacuum chamber. A special thermocouple feed-through (Model: 120XTK016-5-S, Feedthrough, Thermocouple, Type K, ISO-KF NW 16, Pfeiffer Vacuum Inc., Boston, MA) was used to add three additional thermocouples to the inside of the chamber (this feed-through may handle up to five thermocouples). To acquire and save

data, the thermocouples were connected to a National Instruments thermocouple input module (NI 9213, Austin, TX). This module then connects to the same chassis (cRIO-9072, National Instruments, Austin, TX) that the electromechanical relay and digital input module use, seen in Figure 4-4. Figure 4-12 is the front panel that shows the temperature ( $^{\circ}\text{C}$ ) readings to the additional thermocouples inside the chamber.

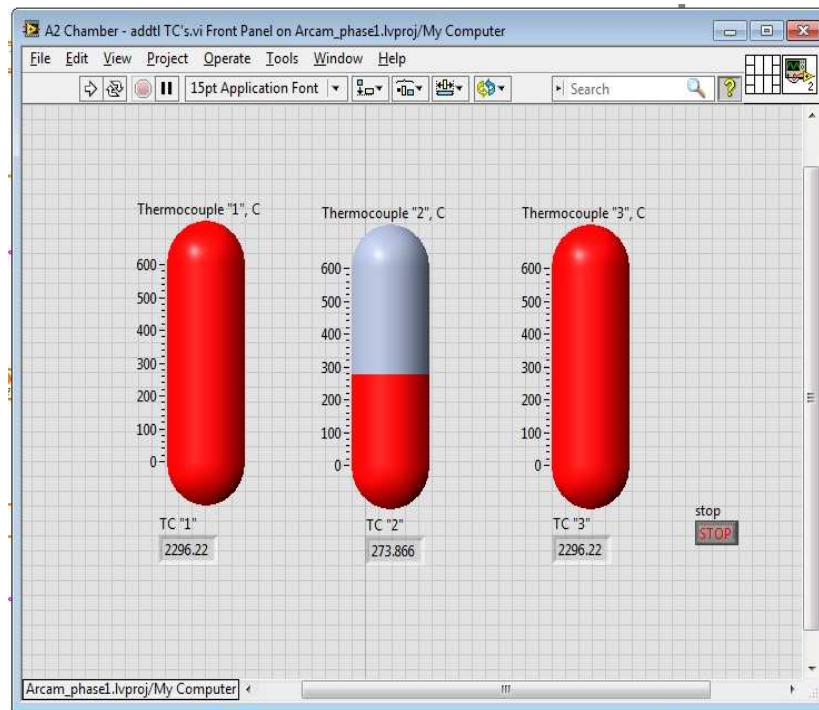


**FIGURE 4-12 FRONT PANEL – A2 CHAMBER – ADDTL TC’S.VI**

A thermocouple that is connected to slot 1 in the module is seen as a shared variable “1” in the project. The shared variable (TC1) is placed inside a while loop so that a temperature display is constantly displayed while the program is running. TC1 is connected to a thermometer and a digital display as seen above in the front panel. The TC1 wire is connected to Insert-Into-Array.vi that will act as a temporary holder of all data measured during the execution of the while loop. From there, the data are taken outside the while loop via a shift register into Number-To-Fractional-String.vi then to Build-Array.vi where the final data measurements are gathered and finally sent to Write-To-Spreadsheet.vi – once the program is stopped, this vi will prompt where to save the data and name it. Get-Date/Time-In-

Seconds.vi and Get-Date/Time-String.vi both make-up the second set of data acquired- the time stamp, and are fed to Write-To-Spreadsheet.vi in the same fashion.



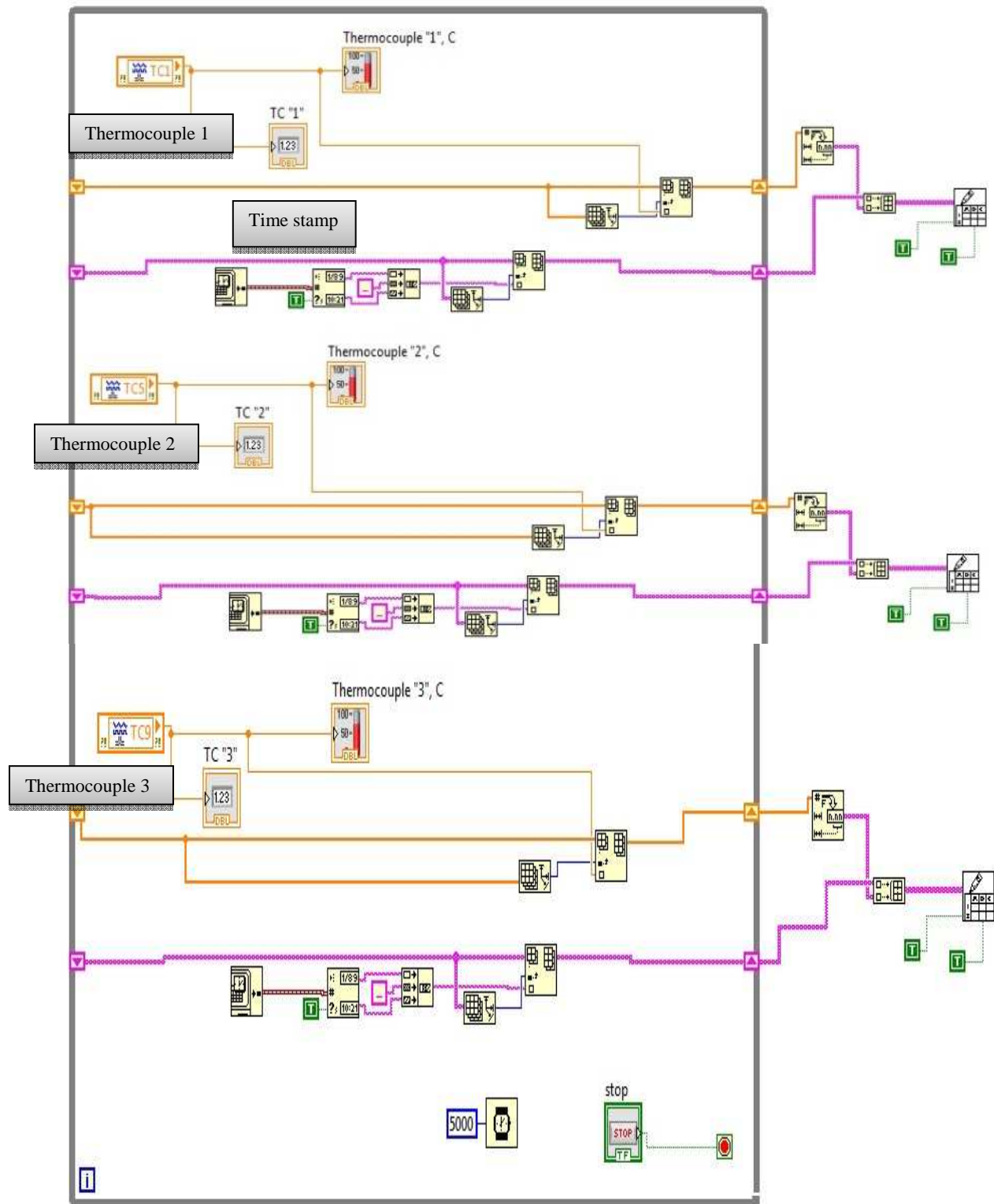


**FIGURE 4-13 BLOCK DIAGRAM - A2 ADDITIONAL TC'S.VI**

## 4.2 IMAGE ANALYSIS

The scope of this project dealt more with the analysis of images rather than image processing. The two should not be confused. Image processing deals with the manipulation of images by using look-up tables, filtering, morphology, and segmentation that helps to clean up and alter images to aid in the examination of an IR image [Klinger, 2003; Relf, 2004]. Image analysis uses image pixel intensities to compute measurements and statistics, most noteworthy temperature values. Analyzing images becomes a form of nondestructive testing to validate and quantify part quality. The images were analyzed using the software *ThermaCAM Researcher Professional* [FLIR Systems, Wilsonville, OR]. This software has the capability of assigning an emissivity value to a region of interest (ROI) that may differ from that of the rest of the image. This becomes critical when investigating accurate absolute temperature values of an AM part during fabrication, that is, the solidified (melted) geometrical area seen in the image. Due to the fact that emissivity is extremely variable; it varies with material composition, crystalline structure, phase, surface morphology, temperature and wavelength [Felice, 2012], it is therefore critical to assign the correct emissivity to its pertaining area in the image. The emissivity of a metal powder, sintered powder, and of a solid metal will be significantly different; the analysis of pixel intensities will be focused on the solid metal region, emissivity data acquisition for a solid metal will be discussed in Chapter 5.

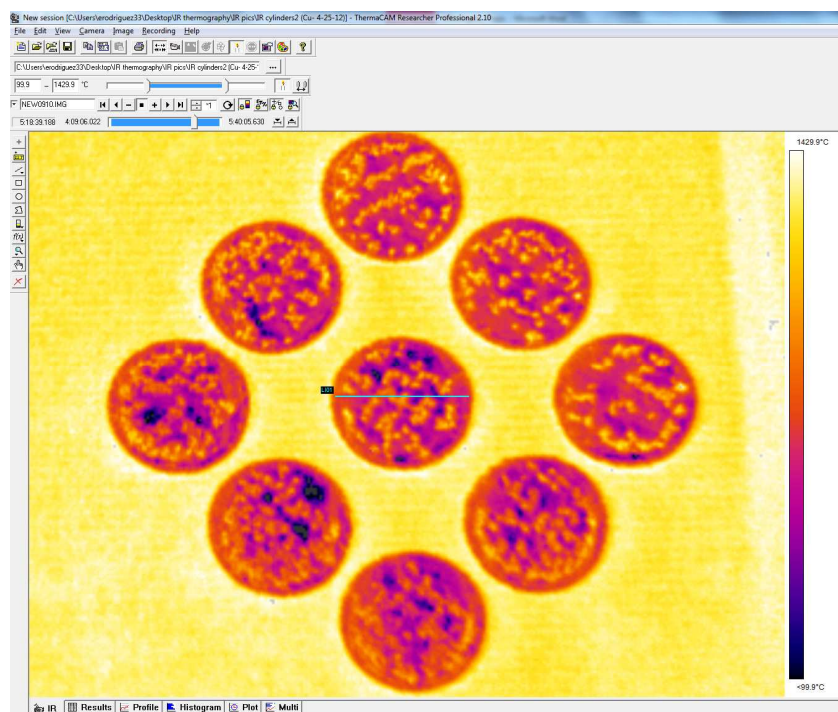
### 4.2.1 TEMPERATURE PROFILES

Temperature profiles become useful when evaluating the temperature variation along or across the surface of an object. The line profile function simply visualizes the pixel values along a line [Klinger, 2003] – the line may be manually drawn over the area of interest (most convenient). Several of these lines may be drawn on different regions of the image. The direction of the line may also be reversed depending on how the data are to be presented.

Figure 4-14 IR image capture of copper cylinders after the melt cycle with the center cylinder's temperature profile shows an IR image of a group of copper cylinders after the melt cycle of a particular layer. A line was drawn on the center cylinder, with its respective profile displayed below the image.

From the profile, the wide distribution (non-uniform) in temperature across the surface can be easily observed, having a minimum of  $<100\text{ }^{\circ}\text{C}$  and maximum of  $933\text{ }^{\circ}\text{C}$  with a standard deviation of  $202\text{ }^{\circ}\text{C}$  (Figure 4-14). This scattering in temperature measurement across the circle's surface is attributed to surface morphology and not necessarily the temperature intensity of the pixels. That is, the geometry has a rough surface and extreme curvature that causes fluctuations in emissivity across part's surface. These images were taken during the parameter development phase of copper in EBM (discussed in more detail in Chapter 6) and therefore the optimal focusing current was not established yet, causing this "bubble" like surface. These discrepancies on the surface can be easily seen for this particular image and the line tool may not necessarily be required here, but the need does arise for materials in which surface inconsistencies may not be so apparent, especially when modifying parameters to obtain a smooth surface.

Figure 4-15 is an IR image of a group of cylinder organized in the same fashion as Figure 4-14, in this image the cylinders are of the titanium alloy (Ti-6Al-4V). The image was also captured after the melt cycle had finished. A line was once again drawn on the center cylinder. The line profile now shows a more uniform temperature, yet there is still some deviation of about  $26\text{ }^{\circ}\text{C}$  from the average that is not easily detected by simply looking at the IR color scale. The line profile plays an important role for cases like these. The values provided by the line profile are the maximum and minimum values of intensity, maximum minus minimum value, average value, and standard deviation.



Label	Value [°C]	Min	Max	Max - Min	Avg	Stdev
Image		<100	1462	*1362		
LI01		<100	933	833	*583	202

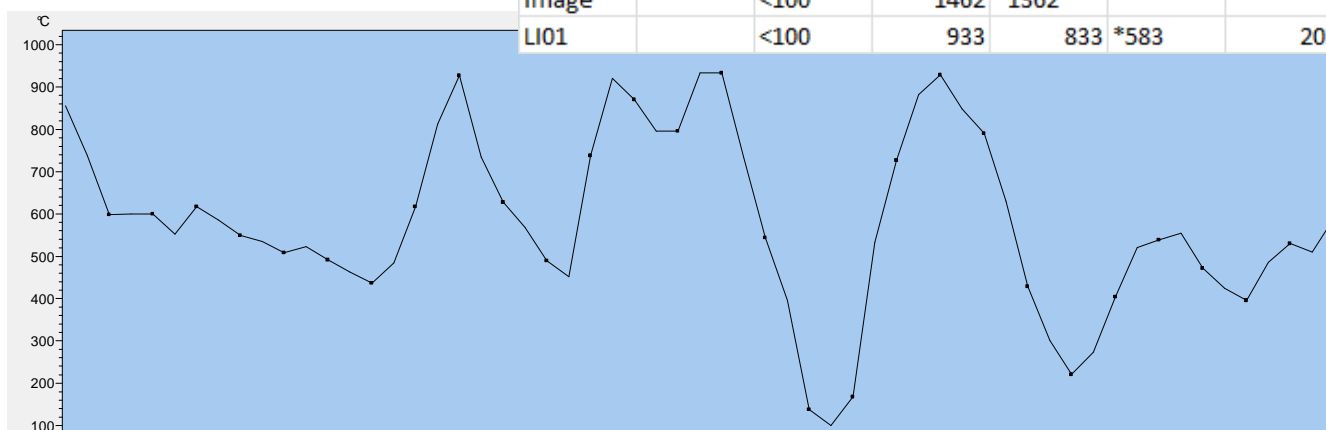


**FIGURE 4-14 IR IMAGE CAPTURE OF COPPER CYLINDERS AFTER THE MELT CYCLE WITH THE CENTER CYLINDER'S TEMPERATURE PROFILE**

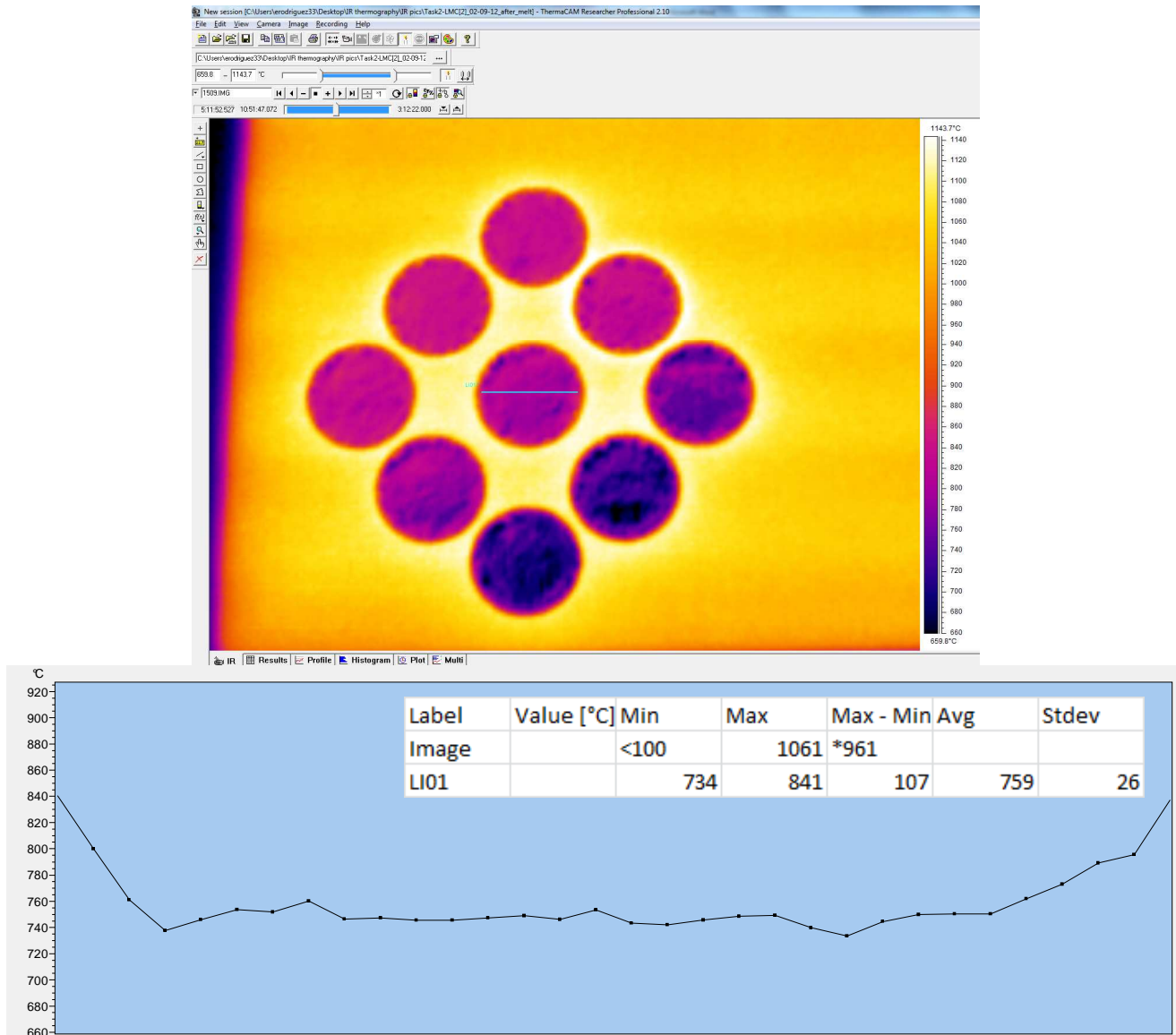


**FIGURE 4-15 IR IMAGE CAPTURE OF TI-6AL-4V CYLINDERS AFTER THE MELT CYCLE WITH THE CENTER CYLINDER'S TEMPERATURE PROFILE**

#### 4.2.2 QUANTIFY AREAS

To quantify areas or regions of interest (ROI) in the IR image, analysis tools are used which provide valuable measurements and statistical data. The analysis tools come in basic shapes such as circles, squares, spots, and rectangles to more complex shapes such as polygons to allow the measurement of a wide variety of geometries. A spot tool measures the temperature of a single spot on the image. The polygon tool is actually a requirement when measuring surfaces of parts with internal features, since these features will have deposited powder, the intensity of those areas will be

significantly different and must therefore be excluded from the measurement. The polygon tool allows to 'sketch' around those areas that will cause deviation from the desired measurement. An example of one of these images may be seen in Figure 6-10. Using these measurement tools will permit a different emissivity value than that already assigned to the rest of the image to the particular ROI. Since the interest here is to measure temperatures of the solid material, this tool is required to obtain that data. The data output will be the average temperature value, standard deviation, and the minimum and maximum. This tool has been utilized in the determination of parameter modification (discussed in Chapter 5), as it aids in the analysis of per part temperature gathering.

## CHAPTER 5 TECHNIQUE DEMONSTRATION AND VALIDATION

When referring to a ‘true temperature’, it is the absolute temperature of the material. A core objective of this project was to obtain true temperature measurements of the surface bed, in particular, the solid part (the melted material). This chapter presents the acquisition of true temperature measurements of Ti-6Al-4V (solid) during the EBM fabrication process. The procedure discussed in Section 3.3 may be applied to any material to determine its unique surface property, emissivity. To accomplish this, the blackbody radiator fabricated (discussed in Section 3.3.2 Creating a Blackbody Specimen) is an essential tool in determining the solid material’s emissivity. After fabrication, the blackbody radiator was taken out of the machine’s vacuum chamber for removal of the sintered powder inside the cavity. The procedure to clean the internal cavity will be described in detail in Section 5.3

Emissivity Studies. First, the experimental procedure implemented to determine the mean radiant temperature is introduced.

### 5.1 MEAN RADIANT TEMPERATURE

Recall that a sample surrounded by surfaces at different temperatures, can be represented by a mean radiant temperature. This is the temperature of a fictitious isothermal enclosure, in which radiation heat exchange with the sample equals the radiation heat exchange with the actual enclosure [Cengel, 2007]. Coppa and Consorti found that by experimentally measuring the temperatures of the enclosure walls, the mean radiant temperature can be found from [2005],

$$T_{mr} = \sqrt[4]{\sum_j T_j^4 F_{s-j}} \quad 5-1$$

Where,  $F_{s-j}$  is the view factor between the sample and the  $j$ -th wall calculated in section 3.3.2.2

Calculating the view factors and the results summarized in section 3.3.2.3 View factors results, and  $T_j$  is the temperature of the  $j$ -th wall. The temperatures of the enclosure (shield) walls were measured using a type K thermocouple (Model: HKQIN-116U-26, Omega, Stamford, CT) and cemented

onto the shield wall using high-temperature air set cement (Omegabond 400, Omega, Stamford, CT). The open chamber with the heat shield installed and thermocouples put in place is seen in Figure 5-1.

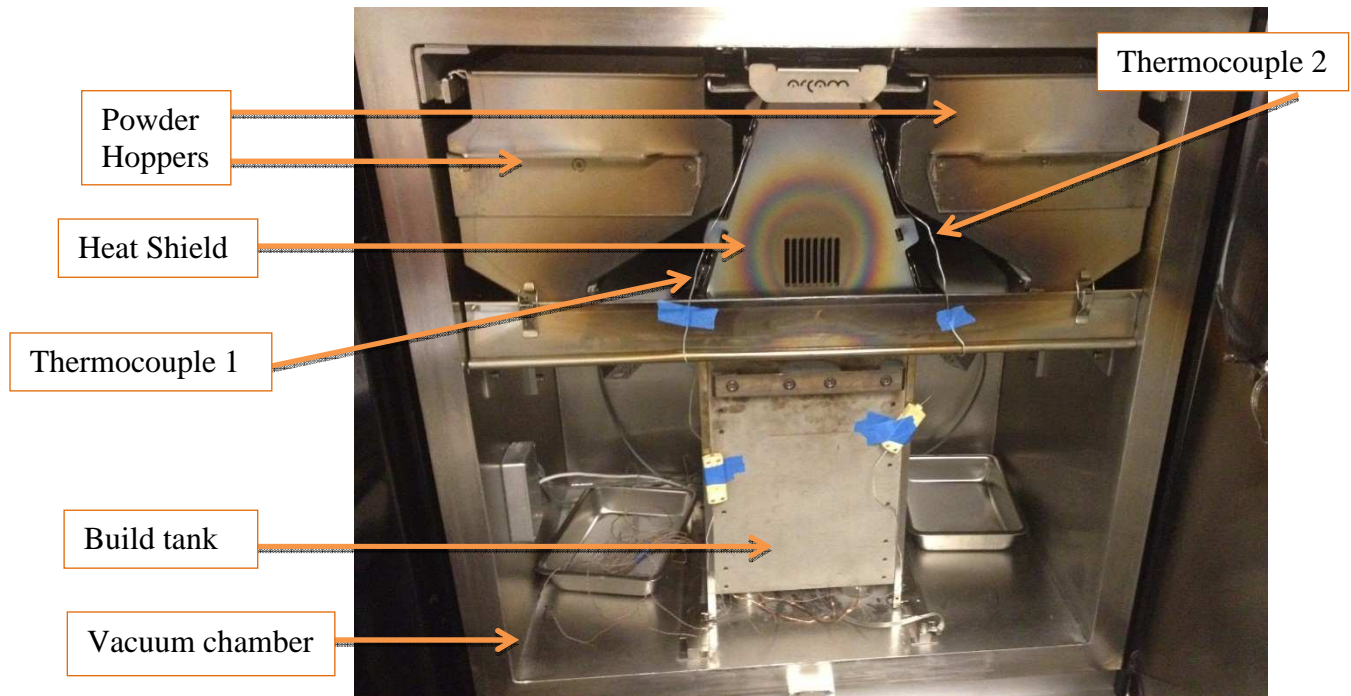


**FIGURE 5-1 VACUUM CHAMBER WITH ADDITIONAL THERMOCOUPLES PUT IN PLACE FOR HEAT SHIELD TEMPERATURE MEASUREMENT.**

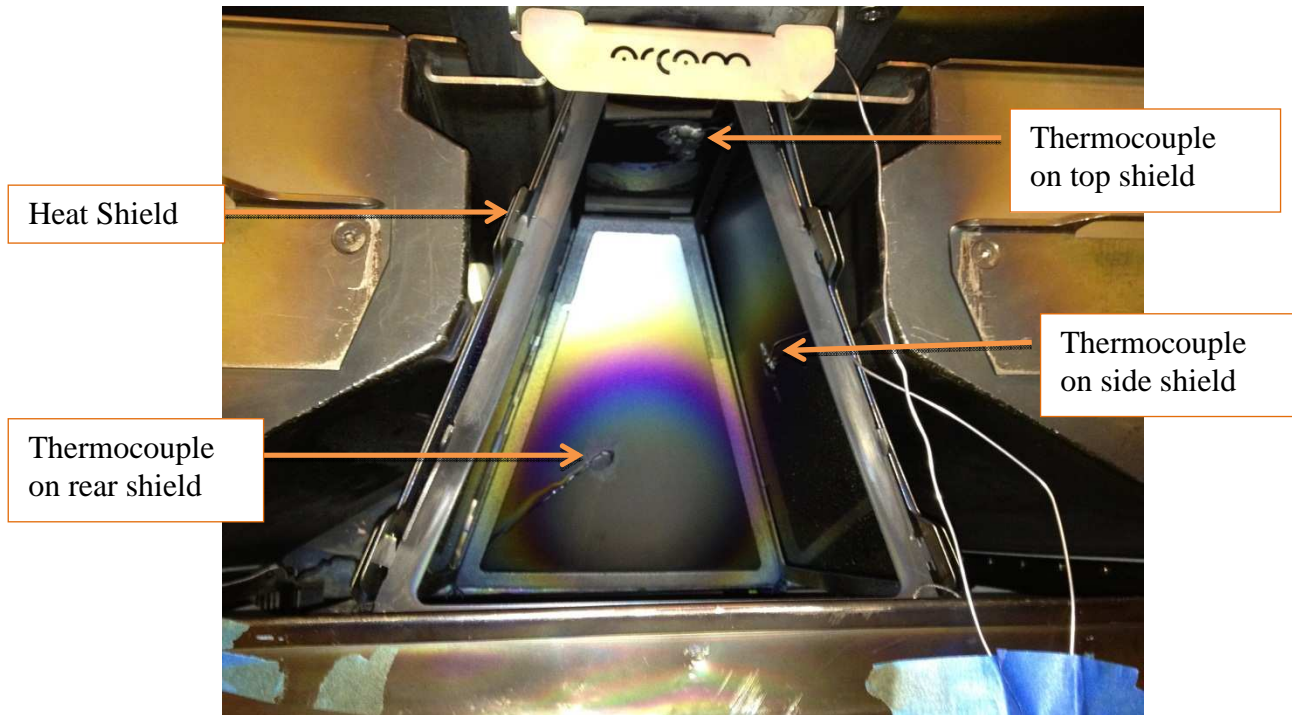
A total of three thermocouples were placed inside the shield on three different walls, left shield wall, rear shield, and top shield. This set-up is shown in Figure 3-15 in Section 3.3.2. The actual heat shield with cemented thermocouples is shown in Figure 5-2, note that the front shield has been removed for visual access. Temperature measurements were recorded during three different builds of Ti-6Al-4V, and the statistical data are presented in

Table 5-1. The thermocouples were also rotated throughout the three different builds to verify consistency in measurement. That is, ‘thermocouple 1’ was placed on the top shield for build 1, then placed on the side shield for build 2, and on the rear shield for build 3; the same was done for the other two thermocouples.



**TABLE 5-1 A2 SHIELD TEMPERATURE MEASUREMENTS**

Shield Surface Wall Temperature Measurements				
	Build 1	Build 2	Build 3	Average
Duration of build	0:41	5:15	13:45	
No. of measurements	83	631	1648	
Top Shield Avg. Temp., °C	301.4510	315.3976	315.5685	<b>310.8057</b>
Top Shield Std. Dev., °C	27.6038	13.3877	8.5798	<b>16.5238</b>
Side Shield Avg. Temp., °C	364.7776	369.3416	369.4226	<b>367.8473</b>
Side Shield Std. Dev., °C	31.0847	14.5647	9.3637	<b>18.3377</b>
Rear Shield Avg. Temp., °C	353.1651	370.9358	371.1597	<b>365.0869</b>
Rear Shield Std. Dev., °C	31.1143	14.5504	9.2179	<b>18.2942</b>
*All builds of Ti-6Al-4V				



**FIGURE 5-2 ARCAM A2 HEAT SHIELD (WIDE) WITH CEMENTED THERMOCOUPLES**

Note that only 3 of the 5 walls were measured due to limited amount of additional thermocouples inside the chamber, and therefore it is assumed the left shield and right shield have the same

temperature, as well as the rear and the front. It is important to note that since the front shield is located adjacent to the machine's observer window, the amount of heat transfer radiated may be significant, and therefore this assumption should be corrected for in future work. Also, recall the assumptions for the surface walls mentioned in Section 3.3.2.1 Six-Surface Enclosure, each surface of the enclosure is isothermal, and both the incoming and outgoing radiation is uniform over each surface. For convenience, the view factors (Table 3-2) used in the following calculations are relisted here, along with the shield wall averages from Table 5-2 **Error! Reference source not found.**

**TABLE 5-2 MEAN RADIANT TEMPERATURE CALCULATIONS**

<b>View Factors and Average Shield Wall Temperatures</b>				
				$T^4 F_{s-j}$
$F_{surface-top shield} =$	0.052462	Top Shield Avg. Temp.(K)=	583.9557	6100509483
$F_{surface-left shield} =$	0.256632	Left Shield Avg. Temp.(K)=	640.9973	43324704506
$F_{surface-rear shield} =$	0.183491	Rear Shield Avg. Temp.(K)=	638.2369	30446852669
$F_{surface-right shield} =$	0.256632	Right Shield Avg. Temp.(K)=	640.9973	43324704506
$F_{surface-front shield} =$	0.118385	Front Shield Avg. Temp.(K)=	638.2369	19643746305
			$\sum_j T^4 F_{s-j} =$	<b>1.42841E+11</b>
			$T_{mr} (K) = \sqrt[4]{\sum_j T^4 F_{s-j}}$	<b>614.7702653</b>
			$T_{mr} (^{\circ}C) =$	<b>341.6202653</b>

The mean radiant temperature  $T_{mr} = 342^{\circ}C$  can be seen as a standard for IR measurements for standard Ti-6Al-4V builds. This value is necessary in order to acquire true temperature measurements, as it is one of the most important input parameters (in line with emissivity) assigned to the IR camera. This parameter is used to compensate for the radiation reflected in the object, if the enclosure walls have a lower temperature than the object, then the emissivity can be strongly influenced by reflection [Coppa and Consorti, 2005].

## 5.2 VALIDATION

To validate that a fundamental procedure has been applied to acquire absolute surface temperature values, an experiment to prove this is necessary. A hot plate (Corning Model PC-420, Corning, Tewksbury, MA) was put inside the vacuum chamber and placed on top of the build platform. The blackbody was placed on the hot plate and a type K thermocouple was cemented (High-temperature cement, Omegabond 400, Omega, Stamford, CT) on the top surface, a second thermocouple was also cemented on one of the side walls of the heat shield enclosure, and the third type K thermocouple was cemented to the top shield of the enclosure. All thermocouples used in this experiment were type K with a range of -270 °C to 1372 °C, Model: HKQIN-116U-26 by Omega (Stamford, CT). Heat shield wall temperatures needed to be acquired again, since this experiment will be operating at a much lower temperature than a standard Ti-6Al-4V EBM build. Therefore, a mean radiant temperature for this particular setup needs to be calculated. The hot plate was set to temperature setting “7”, but in order to gather various temperature data across a larger scale, the setting was changed to setting “5” then to “8” throughout the course of the experiment, IR images of the blackbody specimen were captured and thermocouple temperature measurements were recorded. Some of the data collected is presented in

In Table 5-3,  $T_r$  is the radiant temperature recorded with the IR images by using spot meter tool (discussed in Section 4.2.2 Quantify Areas) placed directly on the blackbody radiator aperture, as seen in Figure 5-3.  $T_s$  is the surface temperature, data recorded using a type K thermocouple and LabVIEW program A2- addtl TC's.vi – see Section 4.1.5.  $T_{left/right\ wall}$  is the temperature recorded from the thermocouple on the left wall – the temperature on the right wall was assumed to be the same.  $T_{left/right\ wall}$  is an estimated temperature since only 3 additional thermocouples are inside the chamber, estimated at  $\sim +2$  °C from the left/right wall temperatures as seen from the wall measurements in the previous section.  $T_{top}$  is the temperature recorded from the thermocouple on the top wall. Emissivity was then computed by the following equation [Coppa and Consorti, 2005],

$$\varepsilon = \frac{T_r^4 - T_{mr}^4}{T_s^4 - T_{mr}^4} \quad 5-2$$

Where  $T_r$  is the radiant temperature of the target's surface,  $T_s$  is the absolute surface temperature, and  $T_{mr}$  is the mean radiant temperature (all temperature values are in Kelvin). Using Thermacam Researcher Professional (FLIR Systems, Inc., Wilsonville, OR) software, the radiant temperature was measured by placing a rectangular region of interest on the blackbody specimen's surface and assigning an emissivity of 0.99 to acquire blackbody radiation. The absolute surface temperature was measured by placing a spot meter tool directly on the blackbody radiator aperture (Figure 5-3). With the given dimensions used in the design of the blackbody cavity, the level of blackness or emissivity obtained at the aperture is  $0.994 \pm 0.2$  [Castrejon, *et. al.*, 2010], therefore, this emissivity value was also assigned to the small opening of the cavity which in turn yields the absolute surface temperature.

**TABLE 5-3 TEMPERATURE MEASUREMENTS FOR VALIDATION**

Validation Experiment: Data Recorded					
Time	$T_r, ^\circ C$	$T_s, ^\circ C$	$T_{left/right wall}, ^\circ C$	$\sim T_{rear/front wall}, ^\circ C$	$T_{top}, ^\circ C$
16:33	228	197.4578	114.9815	117.0000	92.8529
16:35	231	200.1502	114.8377	117.0000	93.4330
16:41	234	204.4601	110.2633	112.0000	91.7885
16:45	216	191.0674	91.9178	94.0000	80.3366
16:47	210	183.6419	86.9649	89.0000	77.4975
16:55	194	165.2760	88.0074	90.0000	76.0777
16:57	201	169.4263	97.0222	99.0000	81.4954
17:00	209	177.2851	102.7834	105.0000	85.2033
17:02	212	181.0878	104.1518	106.0000	86.9202
17:06	217	187.0408	106.4664	108.0000	87.7855
<b>Average:</b>	<b>215.20</b>	<b>185.69</b>	<b>101.74</b>	<b>103.70</b>	<b>85.34</b>

**TABLE 5-4 MEAN RADIANT TEMPERATURE CALCULATIONS FOR VALIDATION EXPERIMENT**

				$T^4 F_{s-j}$
$F_{surface-top\ shield}=$	0.052462	Top Shield Avg. Temp.(K)=	358.49	866472295.6
$F_{surface-left\ shield}=$	0.256632	Left Shield Avg. Temp.(K)=	374.89	5069046002
$F_{surface-rear\ shield}=$	0.183491	Rear Shield Avg. Temp.(K)	376.85	3700742315
$F_{surface-right\ shield}=$	0.256632	Right Shield Avg. Temp.(K)	374.89	5069046002
$F_{surface-front\ shield}=$	0.118385	Front Shield Avg. Temp.(K)	376.85	2387650506
		$\sum_j T^4 F_{s-j}=$		17092957120
		$T_{mr} (K) = \sqrt[4]{\sum_j T^4 F_{s-j}}=$		361.579917
		$T_{mr} (^{\circ}C) =$		<b>88.42991704</b>

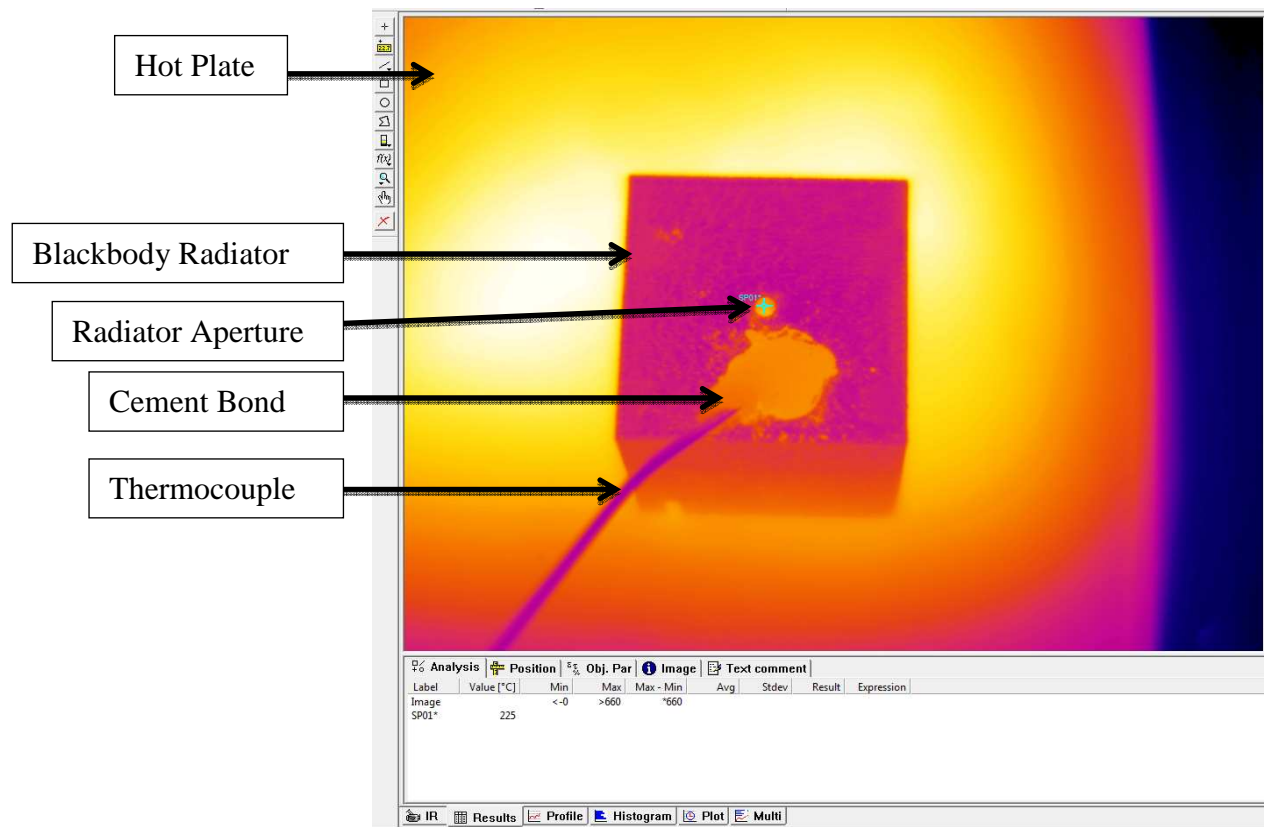


**FIGURE 5-3 IR IMAGE OF BLACKBODY RADIATOR WITH CEMENTED ON THERMOCOUPLE**

Now that all the necessary IR camera input parameters (external optics transmission, mean radiant temperature, emissivity) are in place to theoretically make true surface temperatures

measurements via infrared thermography, their validity (input parameters) can be verified by comparing the IR camera's output temperature measurement to that of the thermocouple cemented on the specimens surface. Emissivity that will be assigned to the IR camera is 0.25, obtained from literature for titanium alloy Ti-6Al-4V [Yang, *et.al.*, 2010], and verified in the next section by using the blackbody radiator. Figure 5-4 shows the temperature recorded for the thermocouple and the IR camera. IR temperature data were acquired via the Thermacam Researcher software by using a box area tool placed on a section of the blackbody specimen's surface, to where it did not enclose the aperture, as this would give faulty data, since the emissivity of the aperture (0.99) is different than that of the metal's surface (0.25). For each set (thermocouple and IR temperatures) of samples recorded, a percent difference was calculated, and then they were averaged together to find average percent difference of 3.14% between thermocouple data and IR data.

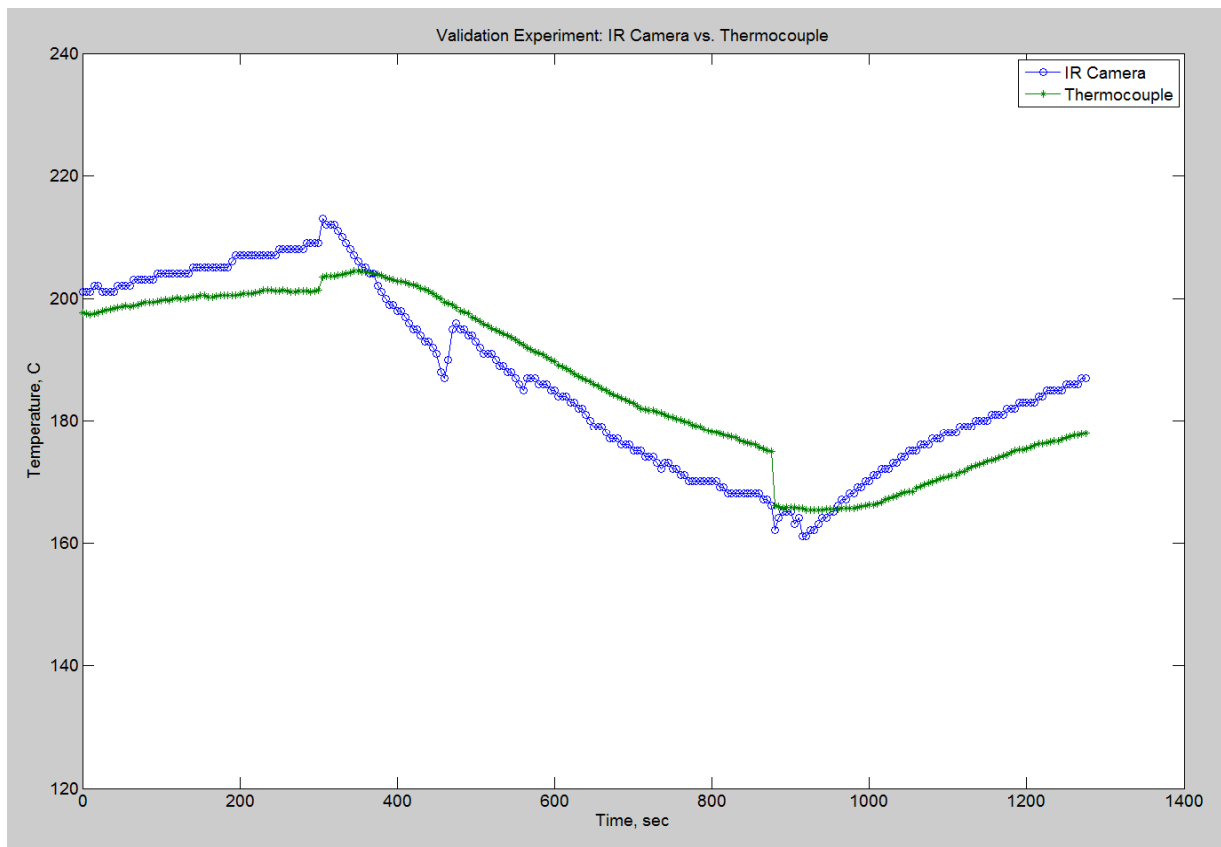


**FIGURE 5-4 TEMPERATURE PLOT FOR VALIDATION EXPERIMENT**

### 5.3 EMISSIVITY STUDIES

As discussed in the introductory paragraph to this chapter, the blackbody radiator was fabricated via EBM in the Arcam A2. Once fabricated, the part was taken out of the machine for thorough cleaning of the internal cavity. A portion of the powder was removed by using Arcam's powder recovery system (PRS) which uses high-pressure air and metal powder to remove sintered powder from the part, this process was executed by directing the hose to the aperture for about fifteen minutes [Arcam AB]. The remaining sintered powder inside the cavity was removed by using an ultrasonic processor (Model CPX500, Cole Parmer Instruments, Vernon Hills, IL) with a power of 500 W, frequency equal to 20 kHz, and an amplitude setting of 77 %. The ultrasonic process was applied to the surface of each side of the rectangular part for about ten minutes per side, with the exception of the top surface as this would change the 'as built' morphology and possibly lead to an emissivity deviation from the one of interest. Once the cavity is thoroughly cleaned of all sintered powder, it is then ready to act as blackbody radiator. Initial trials in calculating emissivity of an EBM sample were carried out in the following way. The blackbody radiator was placed back inside the chamber, the vacuum chamber was activated, and the block was heated to 760°C with the electron beam. It was later realized that the blackbody specimen was undergoing thermal oxidation, after being taken out of the clean vacuum environment into the atmosphere, where a thin layer oxide forms [Dong and Bell, 2000]. After heating again, the oxide layer reacts with the heat turning the surface into a blue-like color. This becomes a problem when analyzing emissivity of a metal; oxidized metals can have an emissivity greater than that of its polished counterpart by at least three orders of magnitude.

Figure 5-5 shows the emissivity versus temperature in its oxidized state. The emissivity differences between samples may be attributed to the optical thickness of the oxide layer [Teodorescu, 2007]. Oxidation causes significant increases in the emissivity of metals, and heavily oxidized metals can have an emissivity comparable to those of non-metals [Cengel, 2007]. Emissivity data on oxidized metals is scarcer

than pure metals, making it challenging when searching for data in literature for comparison purposes. According to work done by Teodorescu [2007], emissivity of metals will differ depending on the thickness of the oxide. During the experimental procedure when obtaining the data recorded in the plot below (Figure 5-5), these variations in oxide layer are evident. As seen with the two rectangular specimen data, the deviation in emissivity is as much as 0.05, or approximately 10 %. The rectangular specimen used for the experiment was the same specimen used for both sets of data; after one experiment was conducted the newly formed oxide layer was removed by using the PRS (powder recover system) to blast away the oxide layer. The amount of exposure (time) to the atmosphere was not measured and this may have been a contributing factor the change in oxide layer thickness from one experiment to the other.

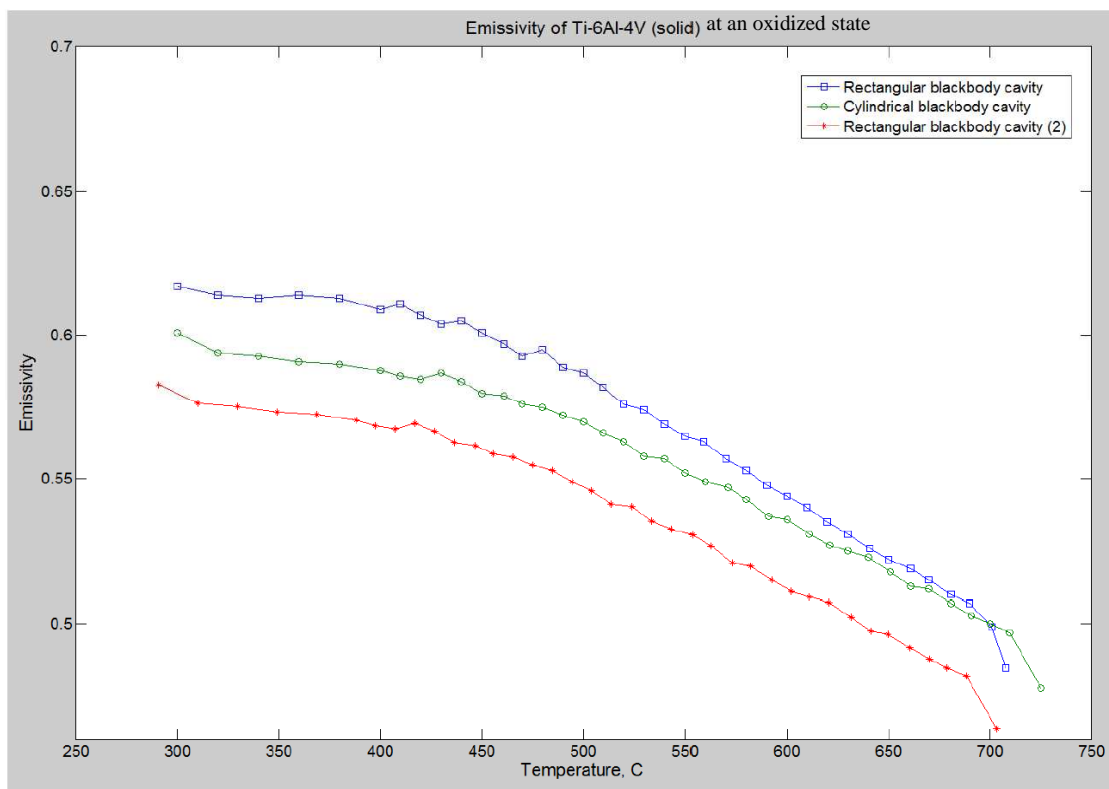


**FIGURE 5-5 EMISSIVITY OF TI-6AL-4V (SOLID) WITH A THIN LAYER OXIDE.**

When interpreting radiation property data from literature, care should be exercised, since the properties strongly depend on surface conditions such as oxidation, roughness, type of finish, and



cleanliness [Cengel, 2007]. The emissivity of interest is in the material's 'EBM' form, that is, since emissivity is a function of surface morphology. The uniqueness of this surface will be the same as future builds in EBM. With the measured surface temperature using the thermocouple cemented on the specimen and with the known radiant temperature from the aperture of the blackbody, absolute emissivity values may now be obtained, for the operating spectral range of IR camera. Figure 5-6 shows the temperature results obtained from the EBM sample (blackbody), also data from literature [Yang, *et.al.*, 2010], which has been verified by the experiment mentioned above. According to Yang, *et.al.*, emissivity of Ti-6Al-4V remains nearly constant up to about 760 °C before the material begins to oxidize and the emissivity increases rapidly. This plot (Figure 5-6) provides emissivity values for the temperature range in which Ti-6Al-4V builds are processed, which makes it a necessary source of data when measuring true surface temperatures. The data is also presented in

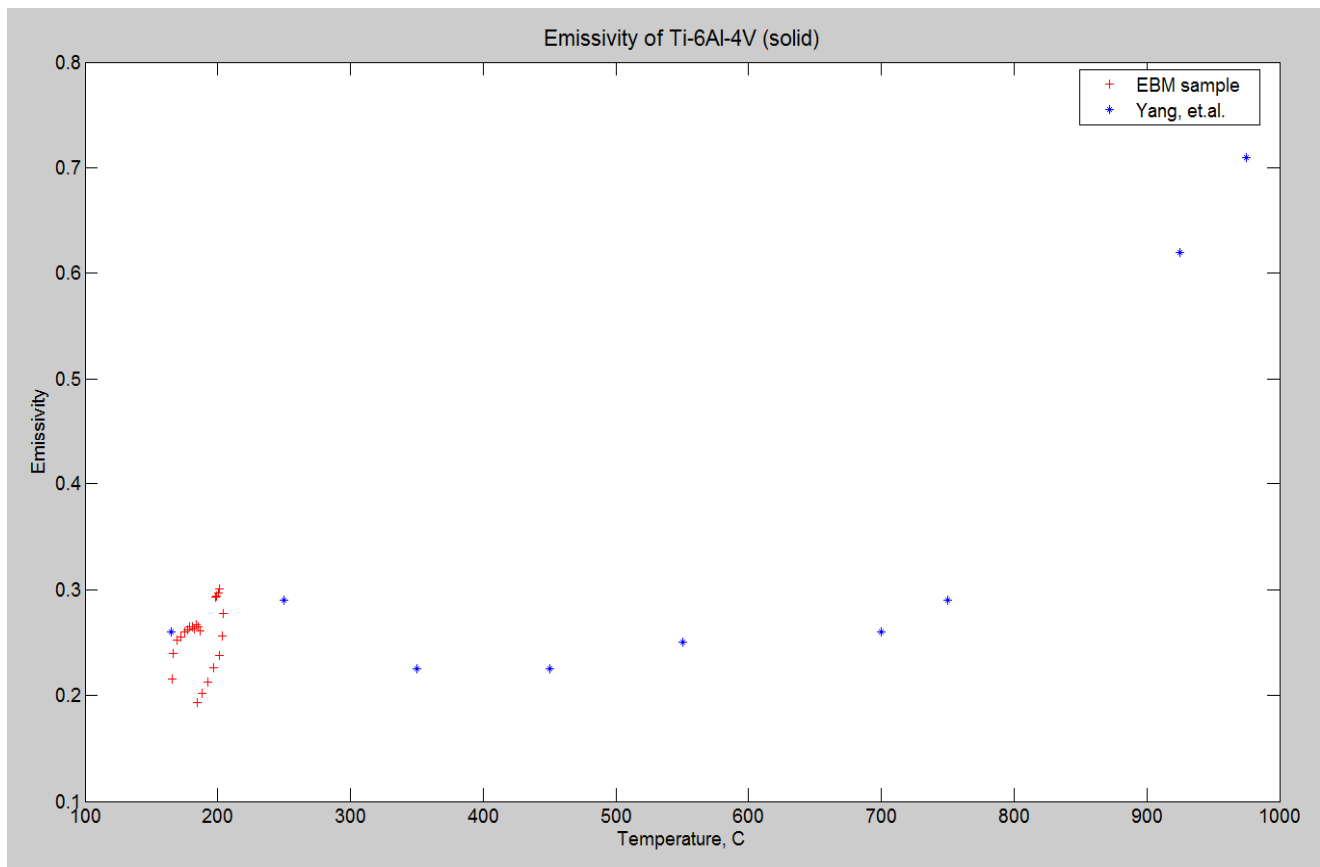


**FIGURE 5-6 EMISSIVITY PLOT OF TI-6AL-4V**

**TABLE 5-5 EMISSIVITY DATA OF TI-6AL-4V (SOLID)**

Sample	Temperature, °C	Emissivity, $\epsilon$	Std. Dev.
EBM 1	177	0.26	0.015
EBM 2	198	0.26	0.041
Yang et.al.	165	0.25	
Yang et.al.	250	0.27	
Yang et.al.	350	0.23	
Yang et.al.	450	0.23	
Yang et.al.	550	0.24	
Yang et.al.	700	0.25	
Yang et.al.	750	0.27	

Measuring a metal's emissivity has proven to be a challenge and a reduction in deviation may be improbable; previous work by different authors performed on the same metal lead to large scatter data, producing differences as high as 50 % with a standard deviation of 20 % or higher [Teodorescu, 2007]. This is typically due to challenges associated with the experimental set-up, measurement conditions, and most notably due to the high reactivity of metals at high temperatures [Teodorescu, 2007]. In order to accurately capture emissivity behavior, specific experimental procedures have been developed, yet this has proven to give deviation in measurement due to the nature of high sensitivity of emissivity.

### 5.3.1 SPECTROPYROMETER EMISSIVITY DATA

The spectropyrometer was installed in place of the IR camera, and the ZnSe window was replaced with a lead coated window. From previous work, the lead coated window proved to be a high-translucent medium for the multi-wavelength pyrometer system [Mireles, 2013]. To measure the emissivity of an EBM fabricated surface, a cylindrical part (50 mm diameter x 3.5 mm height) was designed and placed in the center of the start plate with the pyrometer pointing directly at the center of the part. During the fabrication of the part, the same methodology of the IR image capture was employed, that is, the shutter flap mechanism was opened after the melt cycle of every layer and measurements were recorded. Three different trials were performed and emissivity measurements were

recorded, these data is presented in Figure 5-5. The results show that due to the spectropyrometer's emissivity data deviation, this instrument is not a consistent tool to be used in the EBM process.

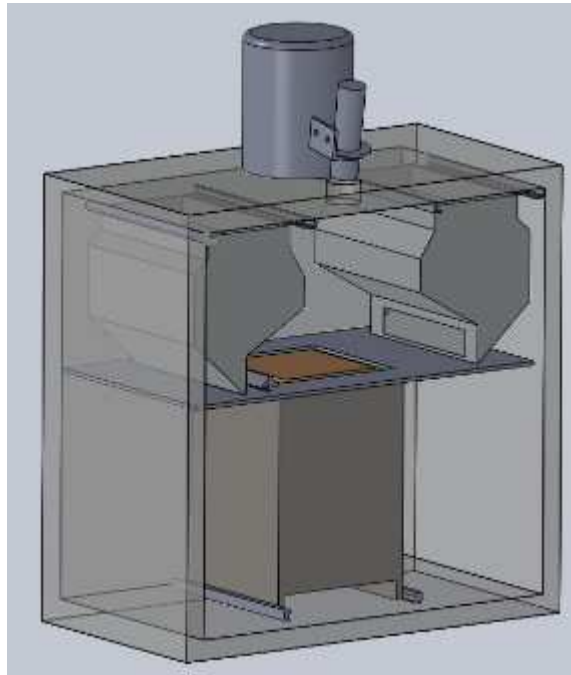


**FIGURE 5-7 ARCAM A2 BUILD CHAMBER CAD RENDERING WITH INSTALLED SPECTROPYROMETER**

**TABLE 5-6 SPECTROPYROMETER EXPERIMENT RESULTS FROM THREE TRIALS**

Build	Temperature, °C	Tolerance, °C	Emissivity (avg)
Trial 1	712.5	0.76	0.62
Trial 2	719.5	0.68	0.32
Trial 3	713.9	0.82	0.17

## **5.4 FEEDBACK CONTROL DEMONSTRATION**

### **5.4.1 PARAMETER MODIFICATION- PER PART**

Having the ability to measure surface temperatures during a build enabled this project to modify individual part-parameters for a more consistent build. A consistent build, may be to maintain a more uniform temperature among part's surfaces that can lead to equal part properties. Or, the intention may be to achieve a specific temperature gradient – this system enables the user to achieve both. The experimental setup was designed to analyze how neighboring parts would affect heat transfer to each

other in comparison to the heat transfer of a single part (no neighboring parts). The model constructed consisted of a group of nine tensile bars (cylinders) located in one corner, and a single bar in the opposite corner all with equal dimensions, 89 mm tall x 16.50 mm diameter (Figure 5-8). The parts were manufactured in the build chamber using the same layout seen in the model. That is, the grouped cylinders are towards the front of the chamber and the single cylinder towards the rear.

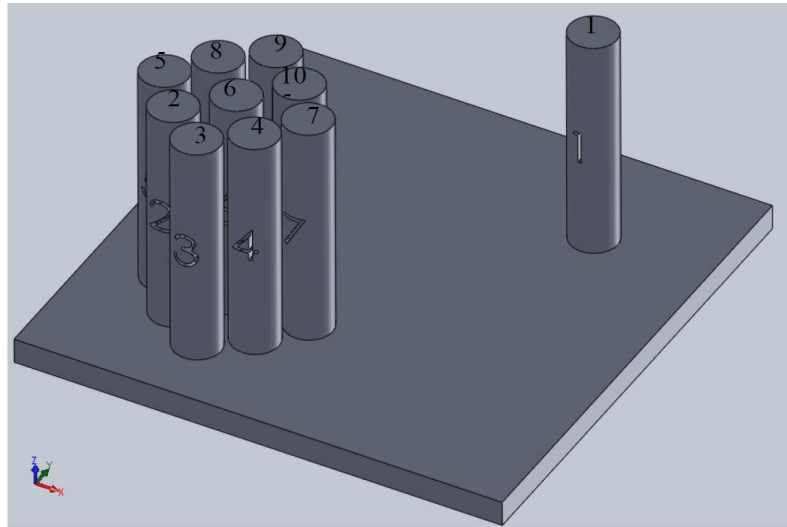


**FIGURE 5-8 CAD MODEL FOR TENSILE BAR BUILD**

An IR image of the build's surface was captured after every melt cycle for the entire course of the build. The results obtained from the images demonstrate that non-uniform temperatures do exist on the build's surface area. By analyzing an IR image of a standard build (i.e., no build parameter modification) at a build height equal to 36.24 mm, one can see a temperature difference of up to 88 °C between cylinders number '3' and number '7' (see the average temperature results column in Figure 5-9).

The build parameters of individual parts were modified in an attempt to achieve more uniform surface temperatures. The temperature difference among the same cylinders was successfully reduced to 5 °C (Figure 5-10). The two parameters modified during the build were the speed function, which controls the scanning speed of the beam during melting, and the beam's current. The speed function's

initial value was set at 36 and was gradually reduced to 5 in decrements of 4 and 5. The beam current was incrementa

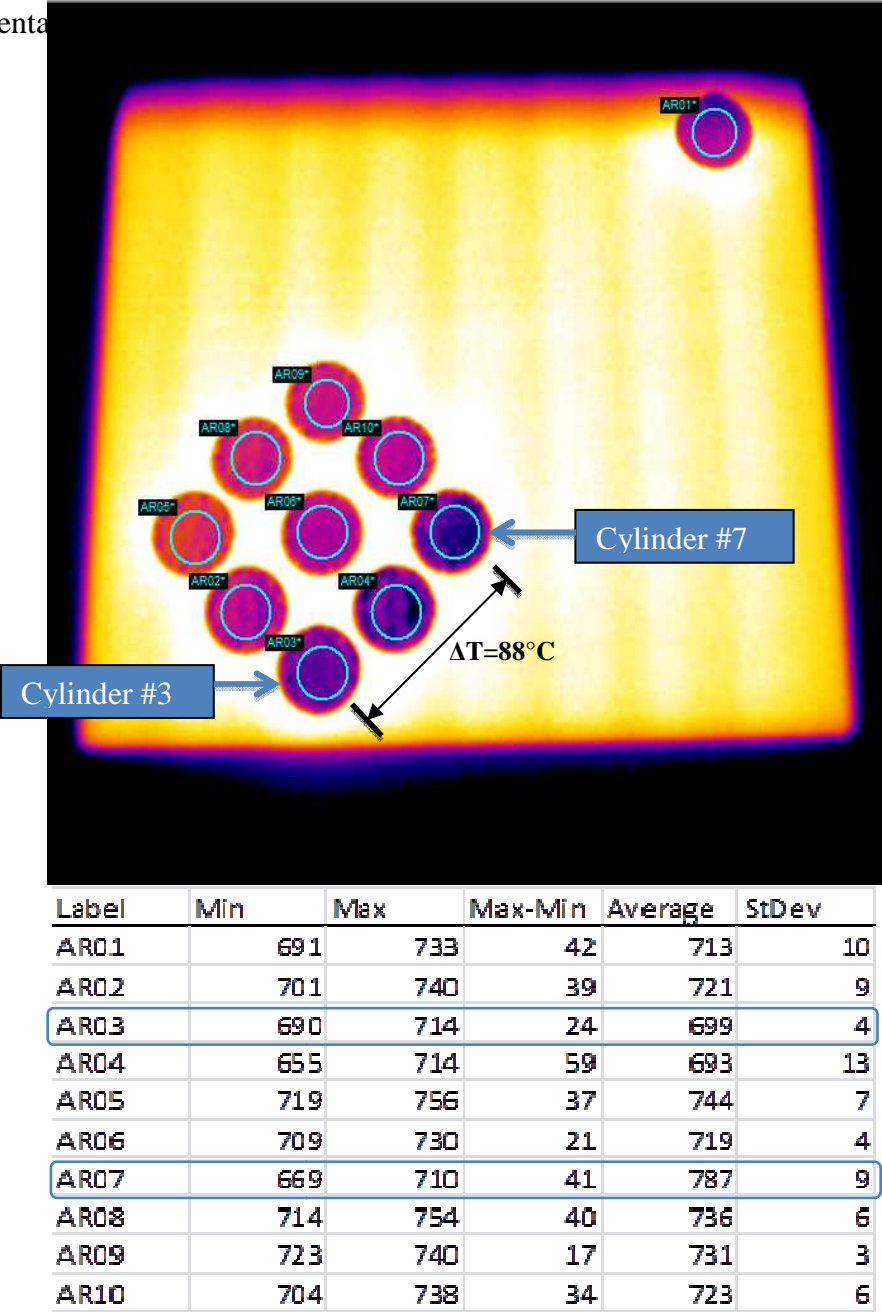
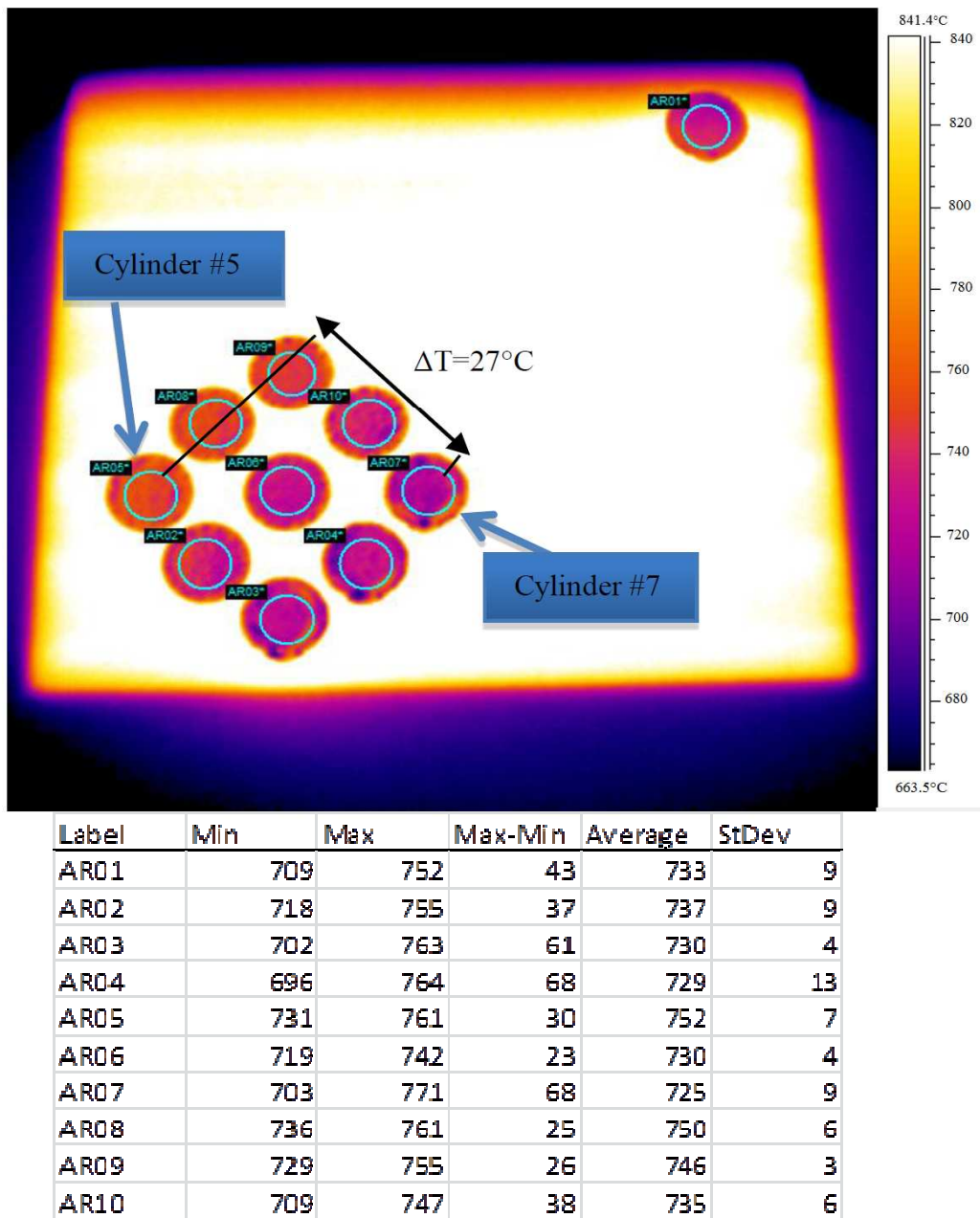


FIGURE 5-9 IR IMAGE OF BUILD SURFACE AT Z=36.24 MM – NO PARAMETER MODIFICATION



**FIGURE 5-10 IR IMAGE OF BUILD SURFACE AT Z=86.40 MM – WITH PARAMETER MODIFICATION.**

#### **5.4.2 PARAMETER MODIFICATION- PER BUILD**

Parameters for four different build were modified to measure the effects of parameter modification the surface temperature measured with IR. Each build consisted of a row of five cylinders (Figure 511) and each build has its own archive of IR images with a different reflected temperature since each build's parameters maintained the build chamber at a different temperature. The four builds were

labeled: standard build, cold build, elevated build, and hot build. Table 5-7 summarizes the parameters used.

Surface temperatures of all five cylinders were recorded and averaged for the entirety of the build (see Appendix A for the corresponding temperature plots). The standard build had a surface temperature range of 720 °C - 830 °C, the cold build ranged from 650 °C - 780 °C, the elevated build ranged from 600 °C – 840 °C, and the hot build ranged from 940 °C – 1050 °C. From these temperature ranges, it should be noted that parameter that had the most significant influence on temperature manipulation was the incorporation of an additional preheat cycle to the build process. The function of the preheat cycle is to heat the fresh layer of powder atop the recently melted parts and build surface to at least half the melting temperature of the material, as discussed in Chapter 1. By adding a second preheat cycle, this caused the powder bed to be maintained at a significantly higher temperature when compared to the other builds that used the standard single preheat cycle.

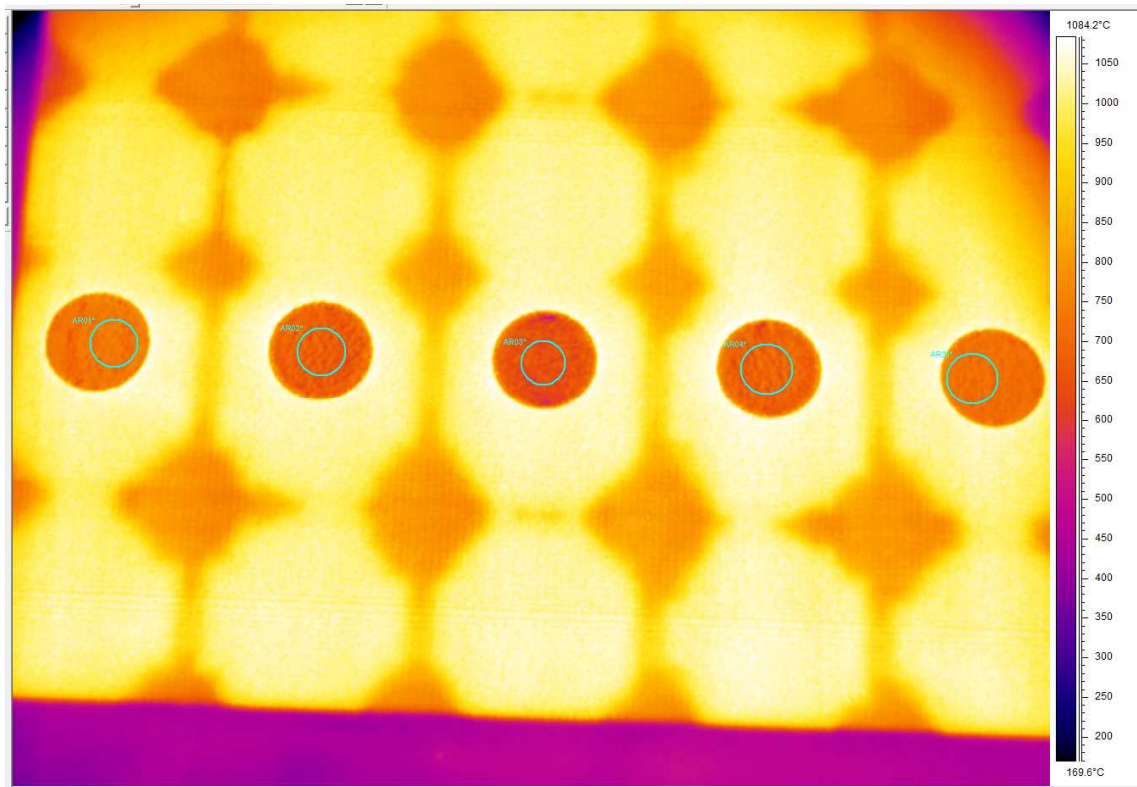


**FIGURE 5-11 IR IMAGE OF FIVE CYLINDERS DURING EBM FABRICATION (STANDARD BUILD)**



**TABLE 5-7 SUMMARY OF ASSIGNED PARAMETERS FOR FOUR BUILDS**

Standard Build- Assigned Parameters		IR Camera Parameters	
Start Temperature:	760 °C	Distance, m	0.3
*Surface Temperature:	850 °C	Refl. Temp, °C	342
Speed Function:	36	Ext. Opt. Trans.	0.94
**Max Beam Current:	17 mA	Emissivity	0.25
*This is an auto calculation parameter that the machine uses to calculate melt paramters (i.e. beam current).			
**This is the maximum allowed current during hatch melting.			
Cold Build- Assigned Parameters		IR Camera Parameters	
Start Temperature:	720 °C	Distance, m	0.3
*Surface Temperature:	750 °C	Refl. Temp, °C	300
Speed Function:	46	Ext. Opt. Trans.	0.94
**Max Beam Current:	17 mA	Emissivity	0.25
*This is an auto calculation parameter that the machine uses to calculate melt paramters (i.e. beam current).			
**This is the maximum allowed current during hatch melting.			
Elevated Build- Assigned Parameters		IR Camera Parameters	
Start Temperature:	790 °C	Distance, m	0.3
*Surface Temperature:	950 °C	Refl. Temp, °C	355
Speed Function:	30	Ext. Opt. Trans.	0.94
**Max Beam Current:	17 mA	Emissivity	0.25
*This is an auto calculation parameter that the machine uses to calculate melt paramters (i.e. beam current).			
**This is the maximum allowed current during hatch melting.			
Hot Build- Assigned Parameters		IR Camera Parameters	
Start Temperature:	850 °C	Distance, m	0.3
*Surface Temperature:	1000 °C	Refl. Temp, °C	419
Speed Function:	25	Ext. Opt. Trans.	0.94
**Max Beam Current:	17 mA	Emissivity	0.25
Pre-Heat Cycles	2		
*This is an auto calculation parameter that the machine uses to calculate melt paramters (i.e. beam current).			
**This is the maximum allowed current during hatch melting.			



## 5.5 MEASUREMENT UNCERTAINTY ANALYSIS

### 5.5.1 ERROR DUE TO UNCERTAINTY IN EMISSIVITY MEASUREMENTS

To account for the error caused by the uncertainty and deviation in measured emissivity values, all values gathered during the validation experiment (see Figure 5-6) were input into the camera's input parameters and the output temperature value was recorded. Table 5-8 shows the emissivity values from Figure 5-6, the output temperature value from the IR camera, and the percent error – using an emissivity value of 0.25 as the real value. The average error calculated may now be used in the measurement uncertainty analysis in following section. The total average error due to these fluctuations in emissivity was found to be  $\pm 3.75\%$ .

**Table 5-8 Percent error due to emissivity measurements**

Emissivity	Temp, °C	Percent Error, %
0.25	767	0.00
0.256	758	1.17
0.25	767	0.00
0.25	767	0.00
0.255	760	0.91
0.254	761	0.78
0.25	767	0.00
0.25	767	0.00
0.23	798	4.04
0.22	816	6.39
0.2	856	11.60
0.21	835	8.87
0.215	825	7.56
0.22	816	6.39
0.23	798	4.04
0.25	767	0.00
0.26	753	1.83
0.29	716	6.65
0.29	716	6.65
0.3	705	8.08
Avg. Error		3.75

### 5.5.2 TOTAL UNCERTAINTY CALCULATION

To determine the total degree of measurement uncertainty associated with the IR camera measurement, the uncertainty of the measurement devices used in the experimental set-up are included. The type K thermocouple used on the surface of blackbody specimen has a reported uncertainty of  $\pm 0.75\%$  of  $^{\circ}\text{C}$  reading (a total of three thermocouples were used) [Nakos, 2004], the thermocouple input module (NI 9213, National Instruments, Austin, TX) has an error of  $\pm 1.10^{\circ}\text{C}$  ( $\pm 0.03\%$ ) for the range of  $600^{\circ}\text{C}$  to  $800^{\circ}\text{C}$  [N.I., 2009], the deviation of the IR camera's measurement of the aperture (emissivity set equal to 0.99) to that of the thermocouple cemented on the cavity was also included in the uncertainty calculation, and the error in temperature measurement due deviation in emissivity measurement (the major contributor in the percent error). Using the fractional uncertainty equation (or root sum squares method) [Holman, 2001], the uncertainty of the IR camera was determined.

$$\frac{w_T}{T} = \left[ \sum \left( \frac{a_i w_{x_i}}{x_i} \right)^2 \right]^{1/2} \quad 5-3$$

Where -  $w_{x_i}$  is the uncertainty of the instrument, and  $a_i$  is the coefficient of the variable used in the respective measurement equation.

**TABLE 5-9 UNCERTAINTY CALCULATION**

Measurement Uncertainty Analysis			
Instrument	Uncertainty, $w_{x_i}$	$\left( \frac{a_i w_{x_i}}{x_i} \right)$	$\left( \frac{a_i w_{x_i}}{x_i} \right)^2$
Omega Type K TC	$\pm 0.75\%$	0.0075	5.625E-05
Omega Type K TC	$\pm 0.75\%$	0.0075	5.625E-05
Omega Type K TC	$\pm 0.75\%$	0.0075	5.625E-05
NI TC Input Module (NI 9213)	$\pm 1.10^{\circ}\text{C}$	$(1.10^{\circ}\text{C}/760^{\circ}\text{C})$	2.095E-06
FLIR SC645 IR Camera	$\pm 2.0\%$	0.02	0.0004
Blackbody validation experiment	$\pm 3.14\%$	0.0314	0.000986
Emissivity error	$\pm 3.75\%$	0.0375	0.0014063
	$\frac{w_T}{T} = \left[ \sum \left( \frac{a_i w_{x_i}}{x_i} \right)^2 \right]^{1/2}$		0.0544339
		$\frac{w_T}{T} =$	$\pm 5.44\%$

At the given camera angle, location, and viewing window, the IR camera uncertainty is approximated to be  $\pm 5.5\%$  in the temperature range of 465 °C to 760 °C or  $\pm 42$  °C at 760 °C - the temperature maintained for Ti-6Al-4V during the build process. It is important to note that there are other possible sources of error that were not included in the calculation, and further work will include identifying these sources, and improving on the experimental set-up to minimize this error calculation.

## CHAPTER 6 INFRARED IMAGING AS A PROCESS DEVELOPMENT TOOL

A key advantage given by additive manufacturing and EBM is the ability to develop complex geometries with internal features in fully-dense metallic components. A function of interest for these internal features is to serve as internal cooling channels – a capability that has been under development by organizations such as Radiabeam Technologies in the design and production of very high average power particle accelerators [RadiaBeam Technologies, LLC and Frigola, *et. al.*, 2010]. Commonly referred to as electron “guns”, these electron sources are critical to the generation of high brightness electron beams used in research, defense, and industrial applications. A key issue in these components is effective cooling of these electron guns, since it limits the time the device may be in active state, the duty-cycle, of high-average power electron guns where nearly all the radio-frequency power is dissipated on the walls due to ohmic heating [Frigola, *et. al.*, 2010]. Making use of Arcam’s EBM AM technology by RadiaBeam Technologies has centered mostly on the production of copper, normal conducting radio frequency (NCRF) electron sources [Frigola, *et. al.*, 2010]. When comparing to other AM technologies, the use of an electron beam to melt the powder, as opposed to a laser used in other systems, makes it much more efficient when processing highly-reflective metals [Frigola, *et. al.*, 2010]. Also, the lightly sintered powder serves as support for sub-sequent layers, critical for the fabrication of unsupported shapes with downward facing features, and thus necessary for the construction of internal cooling channels [Frigola, *et. al.*, 2010]. This chapter focuses on the approach taken to fabricate copper components via EBM, with an emphasis on generating tailored cooling channels within these parts.

### 6.1 ELECTRON BEAM MELTING OF COPPER

A major obstacle when fabricating copper components via EBM was the localized swelling on parts’ surfaces due to excessive heat, that is, temperature beyond the material’s melting point, 1083.2 °C -1083.6 °C [Matweb, 2013]. Figure 6-1 shows the swelling of copper cylinders, from the images it can

be seen that the top surface has experienced a curling like phenomenon due excess heat. These effects are similar to those of laser systems where high laser energy levels may cause balling of the melt and distortion of the part due to large shrinkage [Kruth, *et.al.*, 1998]. To measure this phenomenon, the IR thermal imaging system methodology was used here as in the preceding chapters. After completing the melt cycle of a given layer, an IR image was captured and the surface temperatures were measured. The IR camera input parameters are as follows: emissivity  $\epsilon=0.15$  [Matweb, 2013], reflected temperature or mean radiant temperature  $T_{mr} = 150\text{ }^{\circ}\text{C}$ , external optics transmission is 94%, and the camera distance is 0.3 m. Note that the mean radiant temperature is an estimated value, as the shield wall temperatures were not measured during the fabrication of copper, the estimated value was based on the assumption that the mean radiant temperature during Ti-6Al-4V builds was about  $400\text{ }^{\circ}\text{C}$  less than the operating temperature ( $760\text{ }^{\circ}\text{C}$  for Ti-6Al-4V). Therefore, the uncertainty in these measurements may be significantly higher than those of Ti-6Al-4V, until the appropriate shield wall temperatures are measured during copper builds.



**FIGURE 6-1 EFFECTS OF COPPER SWELLING OF CYLINDERS DURING EBM FABRICATION**

Copper builds use a copper start plate as the starting platform, as opposed to Ti-6Al-4V builds using a stainless steel start plate, so that the parts being fabricated can “stick” to the plate. Early trials

showed that copper parts would delaminate from the stainless steel plates leading to rake failures. When introducing a new material to EBM, the appropriate set of operating parameters must first be determined before beginning the construction of the actual part to be fabricated. This is done so that test specimens may be inspected for porosity, surface finish, and overall compatibility of the EBM process and the material. Initial tests in the parameter development phase, was a set of three cylinders as seen in Figure 6-2. The surface temperature of each cylinder was measured with the IR camera, by placing a circular area (ROI) on each cylinder, Figure 6-3 shows an IR image of this particular build. Temperature results were recorded and plotted, with temperature on the y-axis and layer number on the x-axis. This temperature plot is compared to the thermocouple feedback from the Arcam system in Figure 6-4. As can be seen in the figure, the temperature measured with the thermocouple may be misleading to what is actually occurring on the parts' surface.

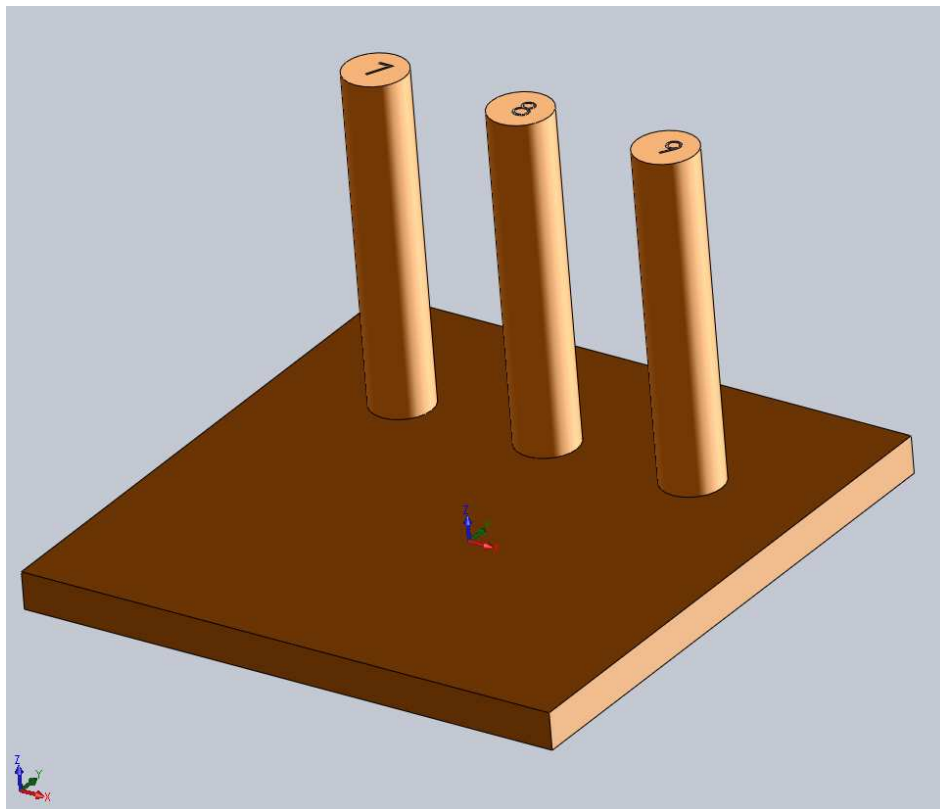


**FIGURE 6-2 CAD RENDERING OF CU CYLINDERS ON CU START PLATE**



**FIGURE 6-3 IR IMAGE OF CU CYLINDERS**

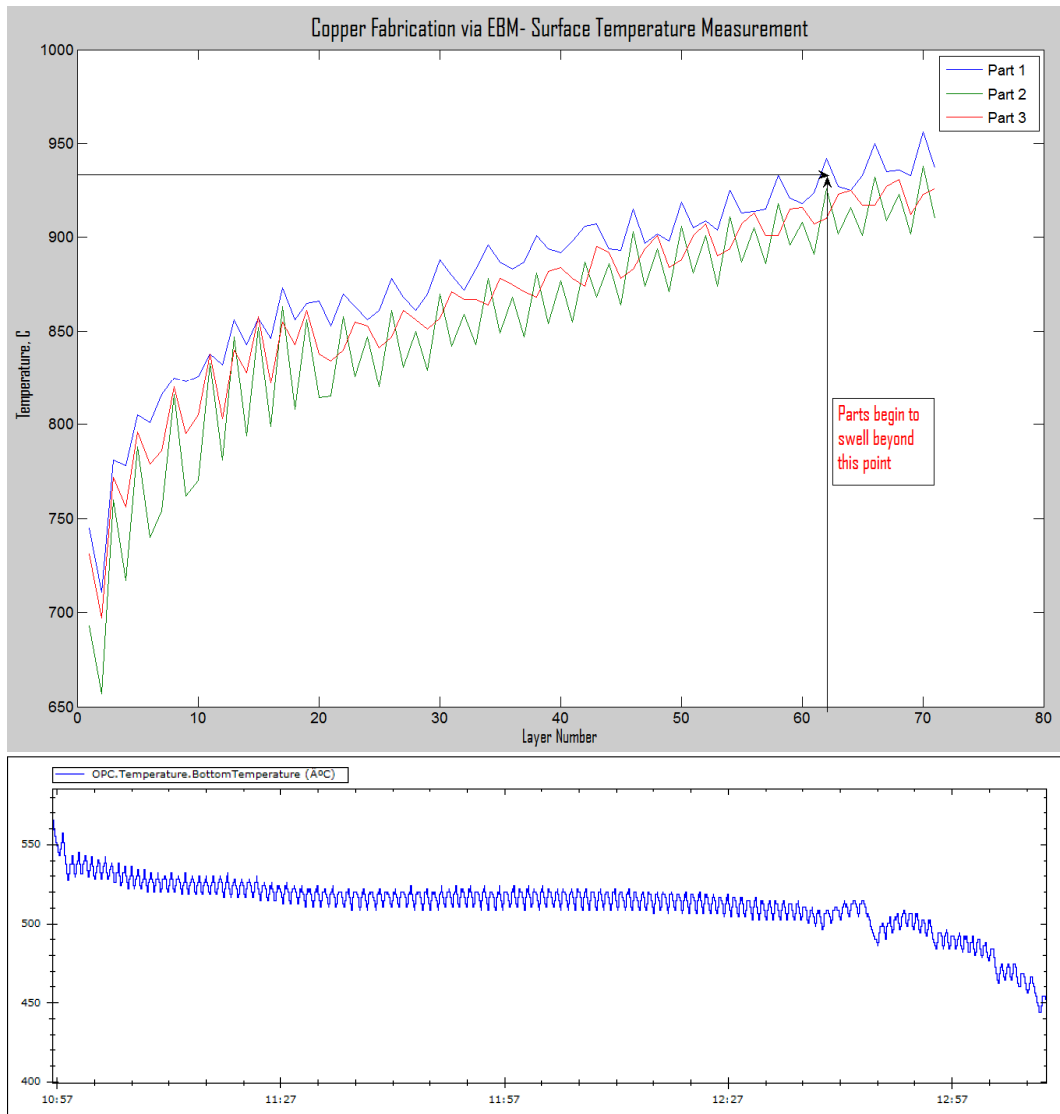


**FIGURE 6-4 SURFACE TEMPERATURE PLOT OF CU CYLINDERS VIA IR (TOP) COMPARED WITH TEMPERATURE RECORDED VIA THERMOCOUPLE UNDER START PLATE (BOTTOM)**

IR surface temperature measurements show an increase with respect to layer number, while thermocouple readings show a more constant trend. As depicted in Figure 6-4, parts began to swell or distort at about 900 °C, this distortion was noted from visual inspection of the part via the front observer window and the effects be seen in Figure 6-1. Once the part swells, it causes the rake blades, or teeth, in the raking mechanism to break once it recoats for the subsequent layers. The fabrication process must then be aborted.



## 6.2 EBM FABRICATION METHOD FOR COPPER

### 6.2.1 TIME DELAY

Initial attempts to solve the thermal management problem consisted of a time delay between layers. A time delay was incorporated into the build sequence that would halt the beam from coming on once a given layer had finished. The idea was that this time delay would permit the part to cool to an ideal temperature that would prevent part swelling for the subsequent layers. Different time delays were experimented with to measure the effects on the surface temperature. Figure 6-5 shows the surface temperature plot with the time delay being modified during the course of the build, 5 s, 7 s, and then 10 s. As seen in the plot, this did little to help maintain a low surface temperature, as it still increased as the part grew in height (layer), additionally it increased the manufacturing time significantly.

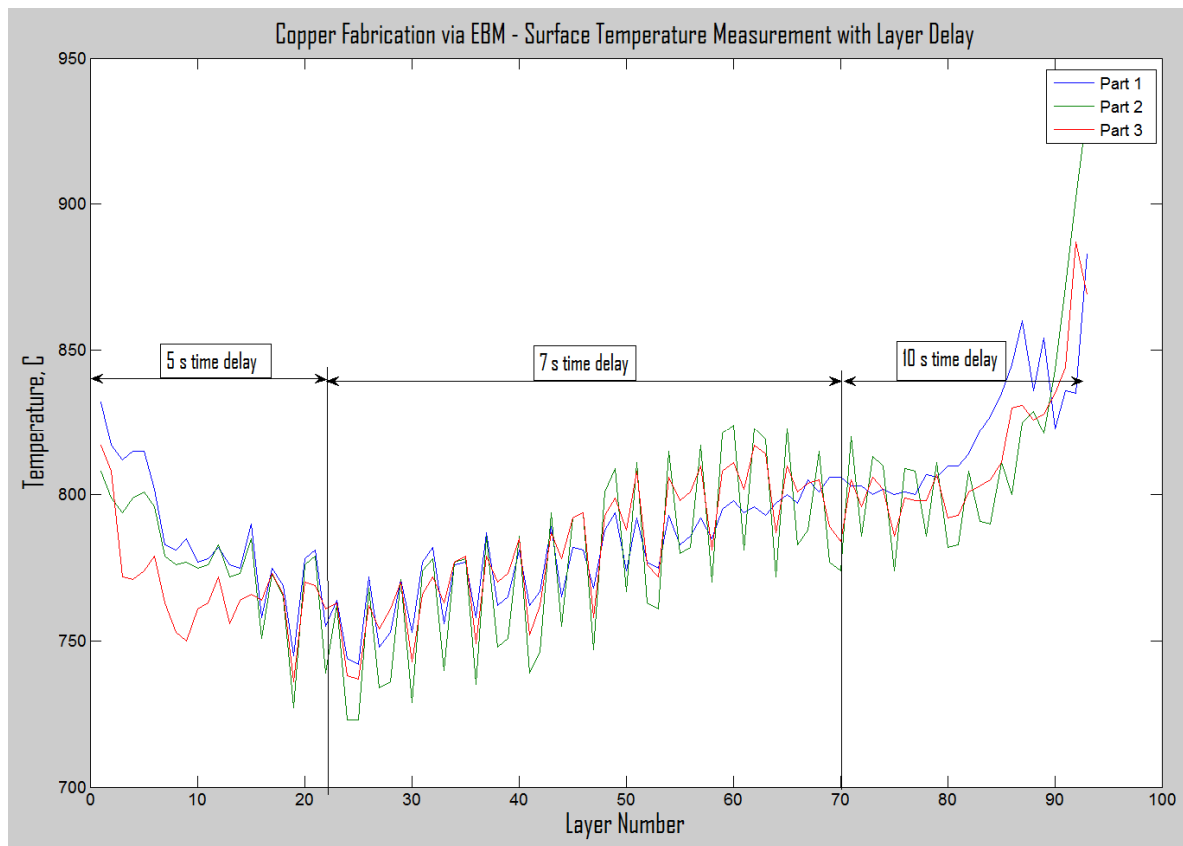


**FIGURE 6-5 SURFACE TEMPERATURE OF CU PARTS WITH INCORPORATED TIME DELAY**

## 6.2.2 HEAT SINK

A proposed solution to better manage the thermal problems in the fabrication of copper parts via EBM, was to incorporate a heat sink that can help transfer heat away from the build surface. The idea originates from the problem of the radiating fin. In the build chamber there is no heat transfer by convection since it is in a vacuum environment; convection needs the presence of a medium, such as air, for transport. The analysis then results to a combined conduction and radiative problem. The differential equation governing the temperature distribution  $T(x)$  for a steady-state condition in a fin of uniform thickness with the incident flux neglected may be written as [Love, 1968],

$$kt \frac{d^2T}{dx^2} - 2\varepsilon\sigma T^4 = 0 \quad 6-1$$

The boundary conditions are,

$$T = T_b \text{ at } x = 0 \quad 6-2$$

$$T_L = T_\infty \text{ at } x = L \quad 6-3$$

$T_b$  is the temperature at the base of the fin, or the bottom of the start plate,  $T_L$  is the temperature at the fin tip. To have successful EBM part fabrication,  $T_b$  is usually fixed to be at half the melting temperature of the material, about 555 °C for Cu. By incorporating these fins into a copper build, they helped enhance heat transfer from a surface by exposing a larger surface area to radiation [Cengel, 2007].

This was the approach taken for the fabrication of copper components via EBM. Five copper plates with dimensions: 102 mm W x 93.50 mm H x 16.30 mm thick, were positioned under the copper start plate with even spacing (about 11 mm apart), see Figure 6-6. The gaps were then filled with copper powder. Note that there was some powder left under the fins, this would permit leveling of the start plate at the top. The start plate was then placed on top of the fins, free of any powder to allow for the best contact, and therefore the maximum heat transfer. The plate was leveled as it is done with standard builds, and the machine was put in vacuum. Figure 6-7 shows the surface temperatures measured.

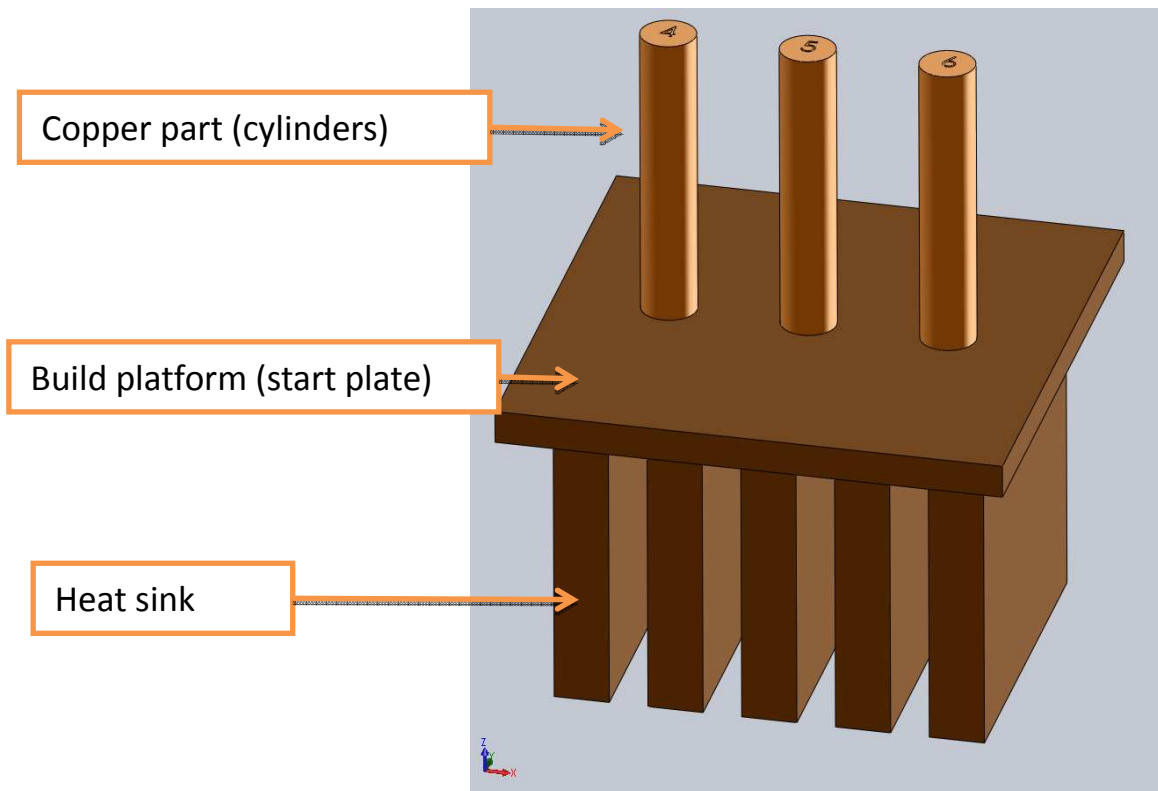


**FIGURE 6-6 CAD RENDERING OF CU PART WITH INCORPORATED HEAT SINK**

Although the implemented heat sink proved to be beneficial for an increase in part z-height (layer), from Figure 6-7 it was still apparent that there was an increase surface temperature. Parameters were then modified in an attempt to reach the goal of maintaining a constant temperature reading, mostly the post-melt heating time. This heating occurs after the process step, it is a parameter used by Arcam to heat the surface bed of the recently melted layer that reduces the thermal gradient between the powder bed and the new layer of powder that will be deposited. The post-melt heating time was gradually reduced from 15 s to 6 s, along with adjusting the time delay between layers. Note that this time delay also serves as the process step within the build cycle that permits for IR images to be captured. To further increase the heat transfer, an additional copper plate was placed under the five fins, as seen in Figure 6-8.

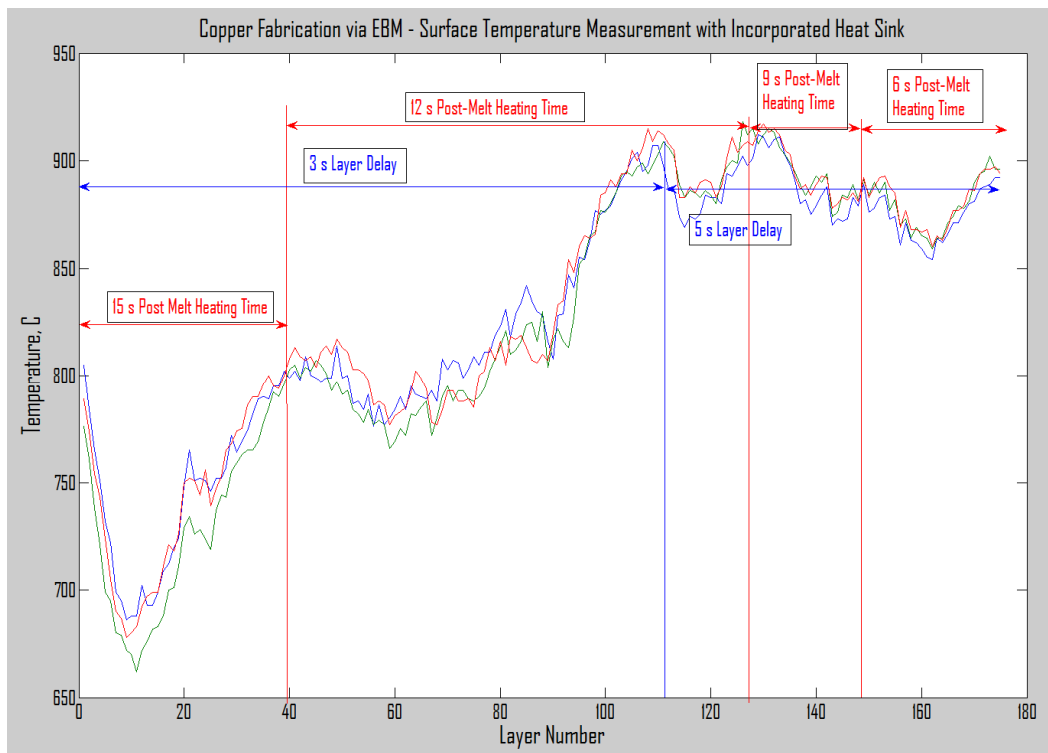


**FIGURE 6-7 SURFACE TEMPERATURE PLOT OF CU PART WITH INCORPORATED HEAT**

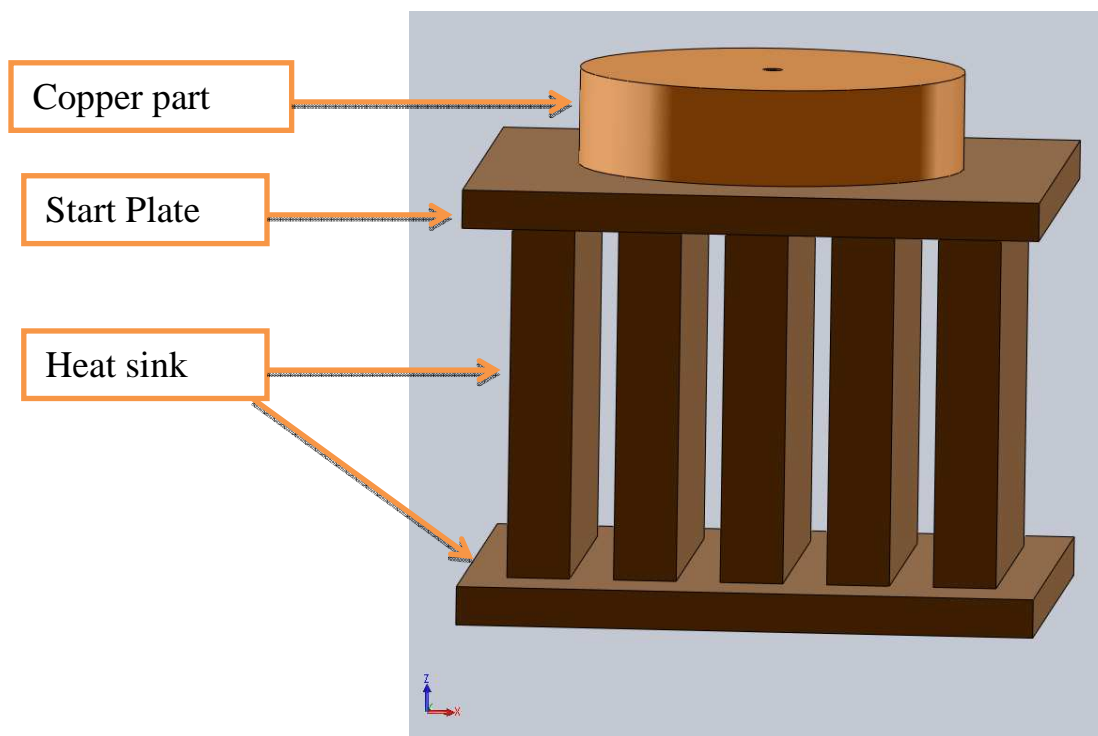


**FIGURE 6-8 CAD RENDERING OF CU PART WITH MODIFIED HEAT SINK**

Figure 6-9 shows the temperature measured with the implemented heat sink from Figure 6-8. Note that the time delay between layers was experimented with, achieving a successful constant temperature with 5-6 second time delay.

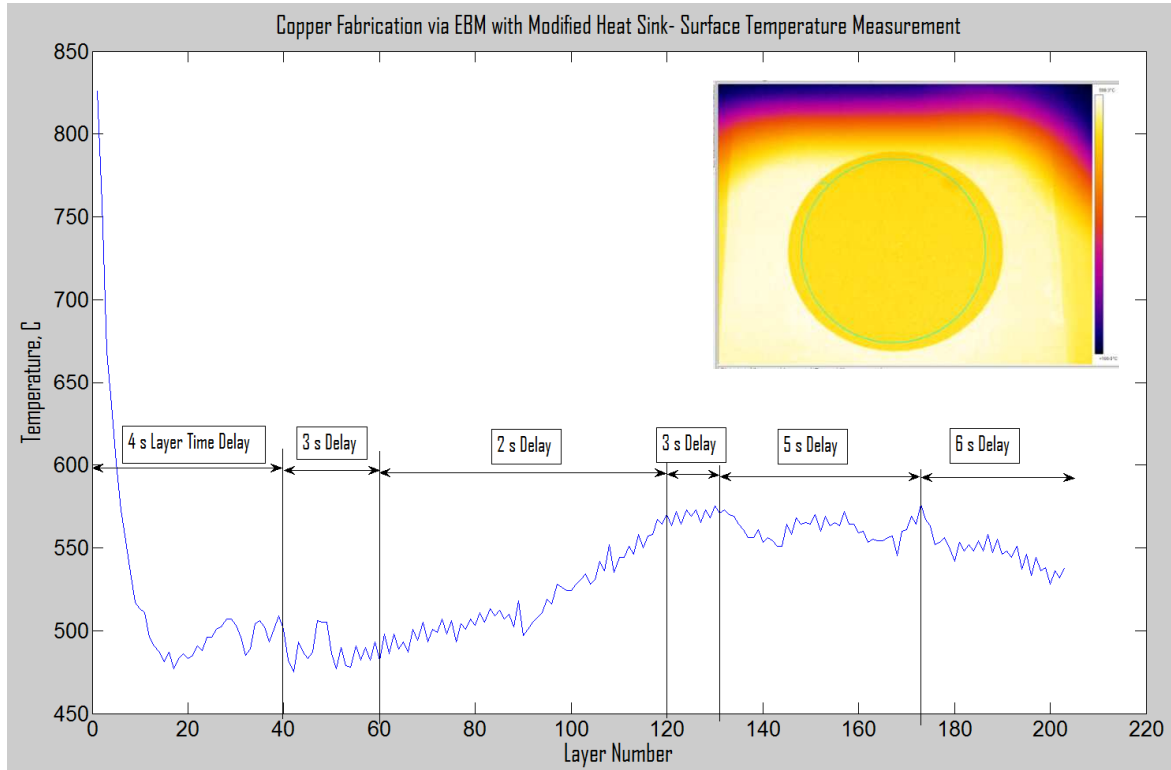


**FIGURE 6-9 SURFACE TEMPERATURE PLOT OF CU PART WITH MODIFIED HEAT SINK**

### 6.2.3 SUMMARY OF PARAMETERS FOR CU FABRICATION VIA EBM

With the modified heat sink, copper parts with internal features were successfully fabricated. A topic of concern was the ability to remove the sintered powder from these internal channels. As any sintered powder left in the channels would make the cooling of the electron gun inefficient, as it would increase the resistance for the flowing fluid. A byproduct of incorporating the heat sink into copper EBM builds was that the temperature was maintained relatively low that the powder would not sinter to the point where it became excessively unbreakable. Powder was successfully removed from the internal channels by using an ultrasonic processor (Model CPX500, Cole Parmer Instruments, Vernon Hills, IL) with a power of 500 W, frequency equal to 20 kHz, and an amplitude setting of 85 %. Water was then

run through the by using wash bottle (or squeeze bottle) filled with water and dispensing water into the inlet to make certain it was making its way through the channels and exiting the outlet.

**TABLE 6-1 CU PARAMETERS**

<b>Summary of Copper Parameters used with EBM</b>				
Preheat Cycle:	Avg. Current	# of Repititions	Max # of Repititions	Heating
	16 mA	20	25	5 s
Melt Cycle:	Beam speed	Current	Focus Offset	Heating
	500 mm/s	7 mA	20 mA	5 s

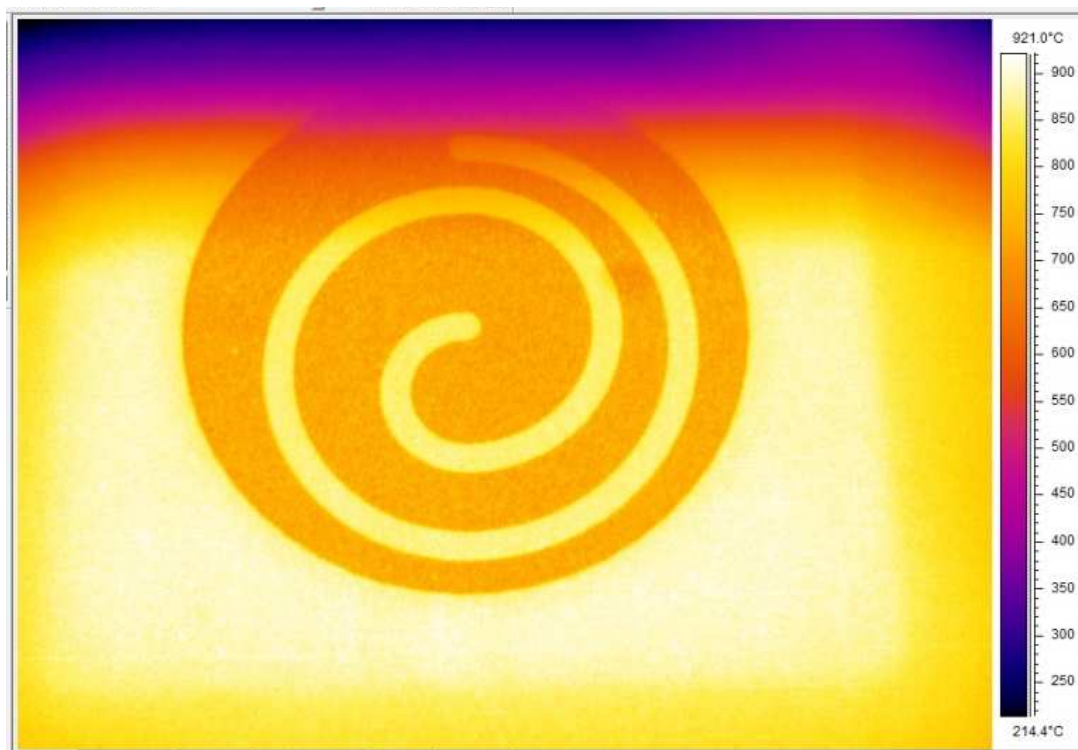


**FIGURE 6-10 IR IMAGE OF CU PART WITH INTERNAL CHANNELS**



**FIGURE 6-11 CROSS SECTION OF COPPER PART SHOWING INTERNAL CHANNELS**

Although copper part fabrication was successful in that complete parts were manufactured and proven that EBM is capable of building with highly conductive materials, there are still challenges to be solved. Porosity within these parts is still a problem that needs to be solved. After cutting these copper parts for inspection, it was observed that parts were not 100% dense; the magnitude of this porosity will be discussed in the next section. Figure 6-12 shows an IR image of the copper part, and it can be noticed that there remains un-melted particles still on part surface. This porosity may be attributed to many things, but probably the factors most liable for this are the operating temperature of copper via EBM and the focus offset. The focus offset is used to offset the focus calibrated value, this parameter can be seen as a control of the “sharpness” of the beam. The higher the offset, the less sharp the beam is. A wrong focus offset can cause poor melting, because the beam’s energy density may be too low to melt metal powder in its path. Also, the number of fins used is not the same for all copper parts, but a direct relationship to the size of the part. Since the part becomes the heat source in the heat transfer problem, an optimal fin count, size, and orientation must be determined.



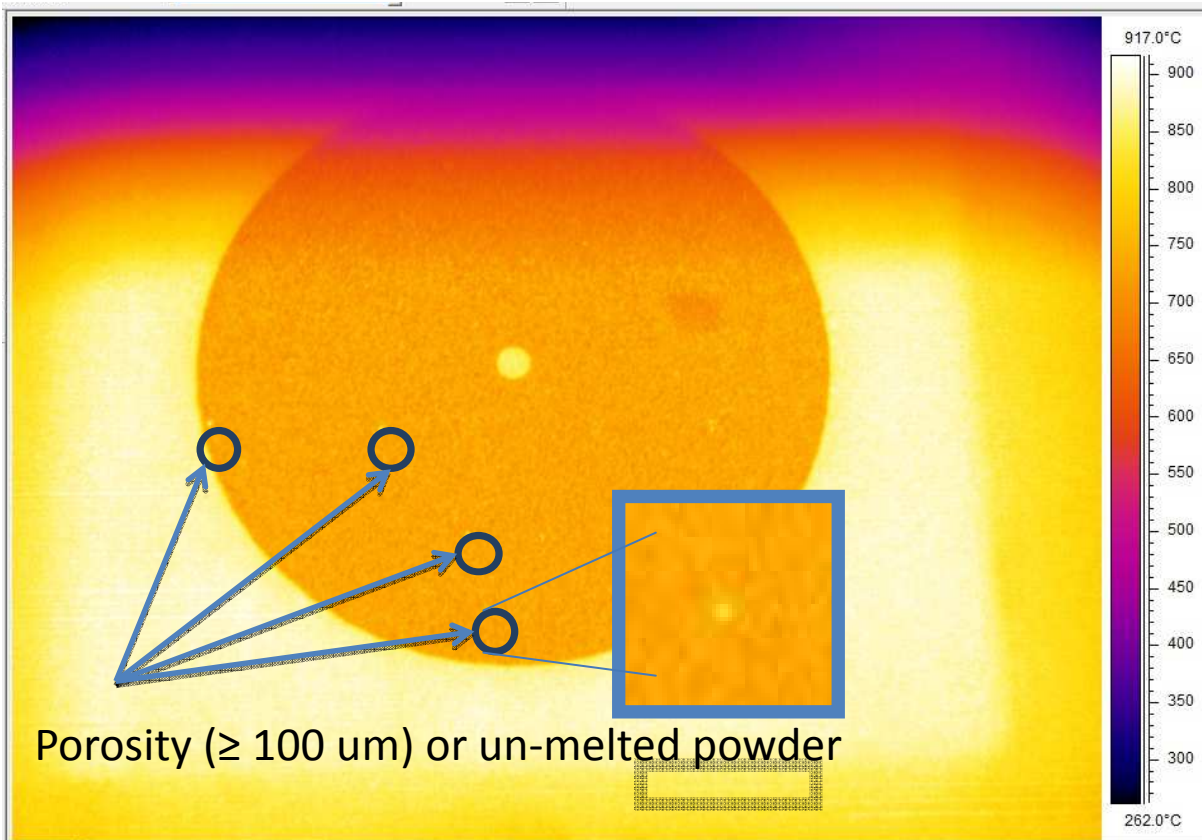


**FIGURE 6-12 IR IMAGE OF CU PART WITH OBSERVED POROSITY OR UN-MELTED PARTICLES**

## **6.2 MECHANICAL PROPERTIES OF EBM FABRICATED COPPER**

Cylinders were fabricated in the X-Y direction using the parameters listed in the previous section. Cylinders in the Z-direction failed to finish to their designed height (90 mm) due to rake failures (rake teeth would brake) and time constraints of this phase of the project, therefore only specimens built in the X-Y were tested. A total of ten cylinders were fabricated, five in one build and five in a second build, each cylinder had dimensions: 17.5 mm diameter and 90 mm length. Five of the ten samples were heat treated in the form of hot isostatic pressing (HIP). The cylinders were then machined to appropriate dimensions for static mechanical testing in accordance with ASTM E8M (round specimens, specimen 3), which has a gage length  $30 \pm 0.1$  mm and diameter  $6 \pm 0.1$  mm [ASTM International, 2012]. During the machining of the samples, four of the five raw cylinders and two of the HIP samples broke, resulting in only one as-fabricated and three HIP samples left for testing. The



specimens were tested using an MTS Landmark-(uniaxial) servohydraulic test system and MTS extensometer model: 634.31F-25 (MTS, Eden Prairie, MN) at a strain rate of 0.015/min at room temperature in accordance with the ASTM standard E8M. Figure 6-13 shows the engineering stress-strain diagram for the tested specimens and Figure 6-14 shows a fractured sample.

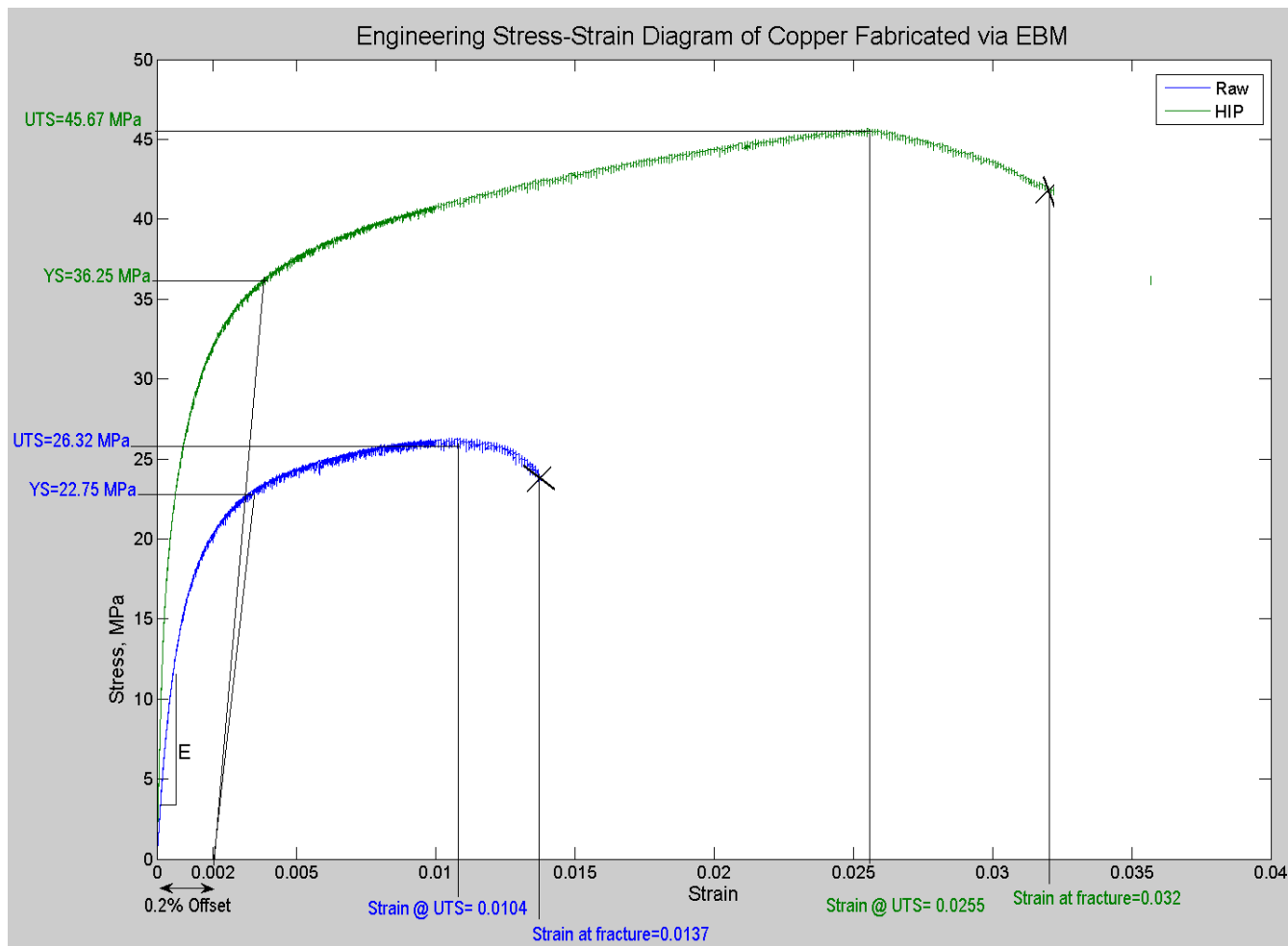


**FIGURE 6-13 ENGINEERING STRESS-STRAIN DIAGRAM OF CU FABRICATED VIA EBM**

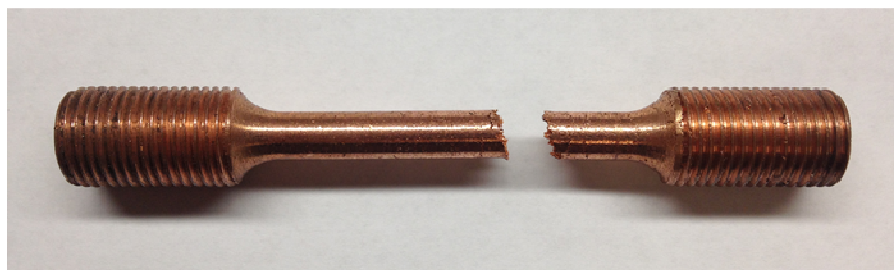


**FIGURE 6-14 CU EBM FRACTURE SAMPLE**

With the recorded data, the engineering stress  $\sigma$  was calculated by dividing the applied load by the specimen's original cross-sectional area  $A_0$ , assuming a constant stress over the cross section and throughout the region between the gauge points. The engineering strain was found by dividing the change in the specimen's gauge length  $\delta$  reading by the original gauge length  $L_0$  [Hibbeler, 2004]. The ultimate stress or ultimate tensile strength (UTS) was determined by finding the maximum on the stress-strain curve; the UTS corresponds to the maximum stress that can be sustained by the copper in tension [Callister, 2007]. The yield strength (YS) was found by employing the 0.2 % offset method, that is, a parallel line is drawn parallel the elastic to the elastic portion of the stress-strain curve at an offset of 0.002 [Callister, 2007]. YS is a measure of the metal's resistance to plastic deformation. The percent elongation was determined from the finding the strain at fracture, before the load decreases drastically, and multiplying by 100 %. The modulus of elasticity or Young's modulus  $E$  was calculated by finding the slope of the line in the linear region of the stress-strain curve.

**TABLE 6-2 MECHANICAL PROPERTIES OF CU**

Mechanical Properties of EBM and Annealed Copper				
Material	YS (avg.), MPa	UTS (avg.), MPa	Modulus, E, GPa	% Elongation
EBM- Cu Raw	22.75	26.32	20.36	1.37
EBM- Cu HIP	36.25	45.67	37.5	3.2
Cu Annealed	33.3	210	110	60
Yield Stress (YS 0.2% engineering offset), Ultimate Tensile Strength (UTS),				
E is slope of engineering stress-strain curve, % Elongation is fracture strain as a percent				
Annealed Cu data was retrieved from Matweb [Matweb, 2013]				
$A_0=29.13\text{mm}^2, L_0 = 30\text{mm}$ (gauge length)				

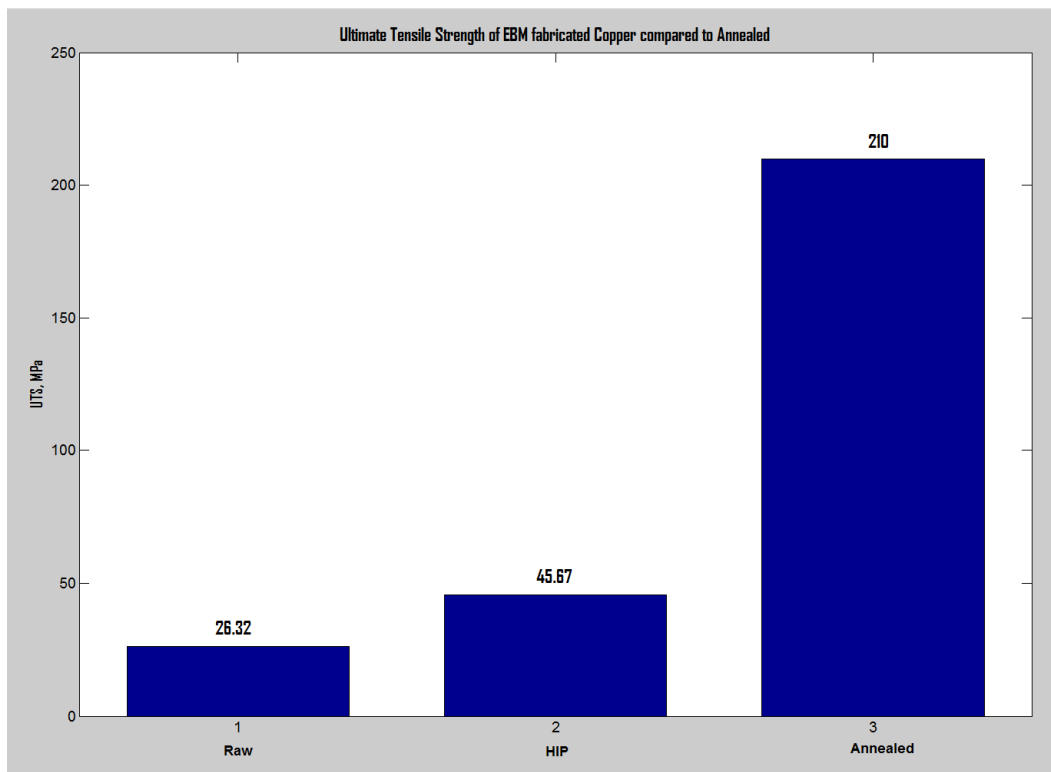


**FIGURE 6-15 ULTIMATE TENSILE STRENGTH OF EBM FABRICATED CU VERSUS ANNEALED**

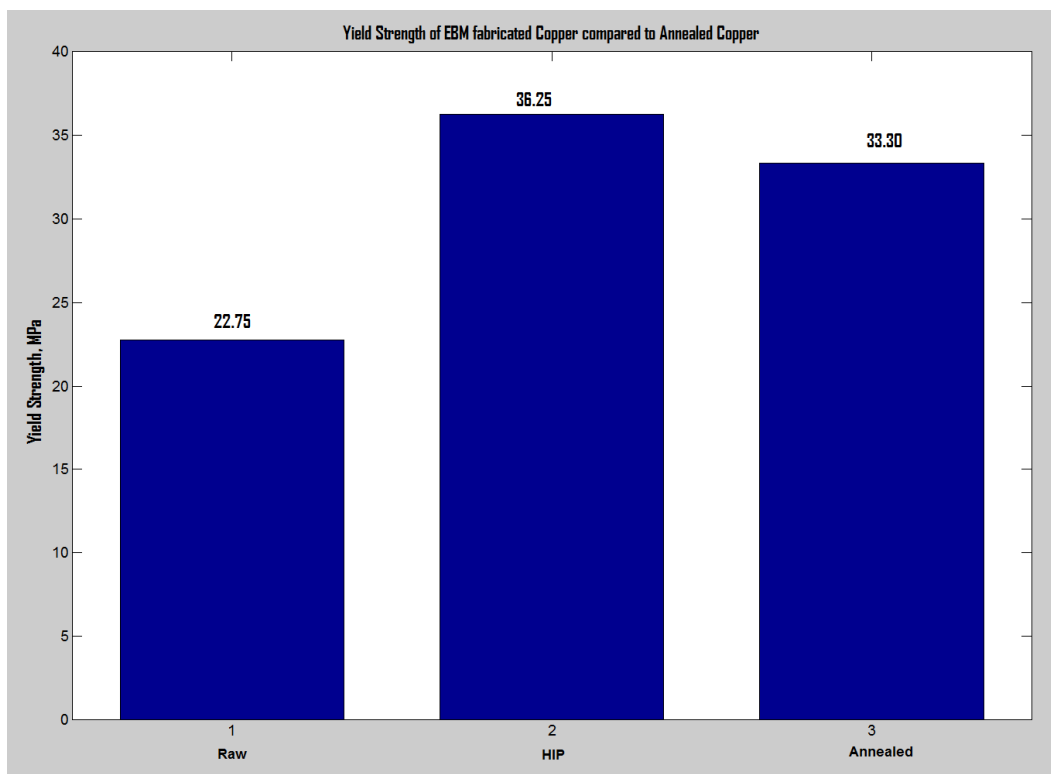


Figure 6-16 Yield Strength of EBM fabricated Cu versus Annealed

Table 6-3 lists the densities determined for the EBM ‘raw’ sample, HIPed sample, and compared to the density of the annealed. The EBM raw sample fails to meet full density by almost 5 %, and the HIPed sample by about 3 %. This indicates that even a small percent difference in density change may have a significant impact on its mechanical properties. The failure to meet or exceed the tensile strength of annealed copper may be attributed to the significant presence of porosity in the EBM built samples, as can be seen in the IR image in Figure 6-12. This can be realized from the 73 % increase in UTS from the HIPed sample to the raw sample, usually a small increase, about 3-4 %, indicates a defect free sample [Svensson, 2009]. Additionally, the density of EBM fabricated copper was determined by cutting a cylindrical section from the tensile specimen, measured and weighed, and found the density by doing a simple mass divided by volume calculation. This indicates that much improvement is required in the processing parameters, but even more in the thermal management aspect of EBM manufacturing of copper.

Another contributing factor in the acquisition of mechanical properties is the material’s strain rate sensitivity; this has proven to have great influence on the final results [ASTM International, 2012]. The strain rate of the annealed copper presented is unknown. The yield stress is almost identical in both the HIP and annealed samples, showing that both the EBM and annealed copper have almost identical elasticity, differentiating in stiffness by about 110 % (from the modulus of elasticity). Due to the annealing process, the annealed copper has a much higher UTS resulting from its high ductility when compared to the EBM HIP sample as can be seen by the significant difference in percent elongation. From these results it is evident that the fabrication method presented here should be used only as foundation to finding improved processing solutions of copper via EBM. Figure 6-17 shows one of the final copper prototypes fabricated via EBM.

**TABLE 6-3 DENSITY OF EBM FABRICATED CU VERSUS ANNEALED**

<b>Density of EBM fabricated Copper</b>		
Sample	Density, g/cc	% Difference
Annealed	7.764	N/A
EBM RAW	7.395	4.76
EBM HIP	7.524	3.09



**FIGURE 6-17 CU PARTICLE ACCELERATOR, OR ELECTRON “GUN”, PROTOTYPE FABRICATED VIA EBM**

## CHAPTER 7 CONCLUSIONS AND RECOMMENDATIONS

### 7.1 CONCLUSIONS

In the present investigation, an infrared thermal imaging system was integrated into the Arcam A2 machine commercialized by Arcam AB (Sweden). Layer-by-layer build surface temperature profiles were imaged and analyzed, providing information that was used to modify build parameters (i.e. beam current, beam speed, focus offset, heating times, etc.) for proceeding build layers. The first task completed was to make the necessary machine modifications for a successful transformation into a fully automated feedback system. In collaboration with Arcam, a pneumatic system was installed for the purpose of opening and closing a shutter mechanism to protect the infrared camera's viewing window from metallization during a build. Proceeding successful hardware installation was the development of a custom *EBM Control* (Arcam, Sweden) software version that provides "triggers" when called to allow image capture, yielding an automated image acquisition process.

Temperature data with a  $\pm 5.5$  % level of certainty was acquired, with the necessary calibration procedure. The operator must provide the camera with the target's emissivity, reflected temperature, and optics transmission as they are key input parameters necessary to support the camera's internal measurement functions to obtain absolute temperature measurements. A step-by-step procedure was developed to obtain a solid metal's emissivity. Also, a mathematical model was established to determine the view factors associated with Arcam A2's heat shield. The view factors were found to be necessary when computing the reflected temperature. Along with shield wall measurements and the view factor, it then becomes possible to determine the mean radiant temperature. The mean radiant temperature is representative of an isothermal enclosure in which radiation heat exchange with the sample equals the radiation heat exchange with the actual enclosure [Cengel, 2007].

An automated solution to capture IR images at a designated process step during the build cycle was achieved by using LabVIEW measurement and programming software. The duration of EBM builds varies significantly, ranging from 4 hours to 80 hours. For this reason, a major focus of this work was to produce an automated solution to acquire images throughout the entirety of any build. The images were captured at the designated process step during the build (layer) cycle and then archived making it possible to correlate the image number in the sequence to the layer number. By knowing this correlation, it is then possible to pinpoint any discrepancy or defect observed in a particular image to the location (Z-height) of the part. The IR images captured were analyzed and processed to search for “cold” spots or abnormal regions on the parts surface. Parameters were modified as necessary; parameters included the beam power (current), focusing current, scan speed, preheating time, and post-heating time. The automated image capture solution will be the gateway to achieving a fully-automated feedback control system that will make real-time parameter modification.

Measuring a metal’s emissivity has proven to be a challenge and a reduction in deviation may be improbable; previous work by different authors performed on the same metal lead to large scatter data, producing differences as high as 50 % with a standard deviation of 20 % or higher [Teodorescu, 2007]. This is typically due to challenges associated with the experimental set-up, measurement conditions, and most notably due to the high reactivity of metals at high temperatures [Teodorescu, 2007]. In order to accurately capture emissivity behavior, specific experimental procedures have been developed, yet this has proven to give deviation in measurement due to the nature of high sensitivity of emissivity.

A primary objective of this research was to develop a method for obtaining accurate solid metal surface temperatures in the particle bed. To accomplish this, a blackbody radiator was fabricated. This cavity-type blackbody will have radiation coming in through the opening and undergoes multiple reflections once inside allowing for the radiation to be reflected by the interior surfaces of the cavity

before the radiation can escape [Cengel, 2007]. Once fabricated, the part was taken out of the machine for cleaning of the internal cavity. Fabricating the radiator via EBM allows for the emissivity of interest to be in the material's 'EBM' form, that is, since emissivity is a function of surface morphology, and therefore the uniqueness of this surface will be the same as future builds in EBM. Experiments were then carried out to find the specific material's emissivity as a function of temperature. Emissivity of Ti-6Al-4V was averaged from the various measurements and found to be 0.25, and literature describes that the value remains nearly constant up to about 760 °C before the material begins to oxidize and the emissivity increases rapidly.

Having the ability to measure surface temperatures during a build enabled this project to modify individual part-parameters for a more uniform build, but this system now gives the capability to achieve thermal gradients within parts if desired. An experimental setup was designed to analyze how neighboring parts would affect heat transfer to each other in comparison to the heat transfer of a single part (no neighboring parts). An IR image of the build's surface was captured after every melt cycle for the entire course of the build. The results obtained from the images demonstrate that non-uniform temperatures do exist on the build's surface area. After analyzing an IR image of a standard build at a build height equal to 36.24 mm, a temperature difference of up to 88 °C was measured between part surfaces. The build parameters of individual parts were modified in an attempt to achieve more uniform surface temperatures. The temperature difference among the same cylinders was successfully reduced to 5 °C. The two parameters modified during the build were the speed function, which controls the scanning speed of the beam during melting, and the beam's current.

Infrared imaging was used as a process development tool in the EBM fabrication of copper. A major obstacle when fabricating copper components via EBM was the localized swelling on parts' surfaces due to excessive heat, that is, temperature beyond the material's melting point. IR thermography allowed for the quantification of this phenomenon by measuring the parts' surface. A



heat sink was implemented into copper builds that helped maintain a constant temperature across the duration of the build. With the modified heat sink, copper parts with internal features were successfully fabricated.

## **7.2 RECOMMENDATIONS**

The development of a thermal-imaging feedback-control system integrated into the Arcam A2 system has provided the ability to measure temperatures of the surface bed – a state of the art capability that can prove to produce valuable results. Based on the results of this work, the recommendations provided here can improve on the capabilities of newly implemented feedback system.

- Develop a closed-loop feedback control algorithm using the acquired IR images to search for any anomalies among the part's surface. Preliminary research has proven to be promising in simulating mouse clicks on the Arcam's central computer – which runs the EBM control software where parameters are modified. Once the analysis of the IR image has been performed, a decision may be made whether build parameters should be modified.
- A correlation is needed between parameters, IR surface temperature measurements and mechanical and microstructural properties of EBM built parts. This work has been started by building a row of cylinders and assigning a set of build parameters. This build is repeated with a different set of parameters for each build, followed by mechanical testing of all specimens and microstructure examination.
- An investigation of the transient heat transfer dynamics should be conducted. This can help determine any temperature losses between the transient time of melt cycle of the part and the time the image is captured.

- A correlation between material thermal properties and its effect on reflections, or mean radiant temperature should be studied to make the assignment of the IR camera input parameters (i.e. reflected temperature) a quantifiable approximation.
- An experimental procedure should be established to determine the emissivity of the metal powder. Measuring the temperature of the powder is also important as it will help quantify temperature distributions across the entire surface bed.

## REFERENCES

- [1] Additive Manufacturing [AM]. AM Basics. Web. 14 Feb. 2013.
- [2] Arpaci, V.S. “Conduction heat transfer.” Abridged Ed. Boston, MA: Pearson Custom Publishing, 1991.
- [3] Arcam AB. “Arcam EBM user’s manual.” Sweden: 2011.
- [4] ASTM International. “Standard test methods for tension testing of metallic materials.” Designation: E8/E8M -11. 2012.
- [5] Brandl, E., *et. al.* “Mechanical properties of additive manufactured titanium (Ti-6Al-4V) blocks deposited by a solid-laser and wire.” *Materials and Design* 32.10 (2011): 4665-4675. Elsevier.
- [6] Callister, W.D. “Materials science and engineering: an introduction.” New York, NY: John Wiley & Sons, Inc., 2007.
- [7] Castrejon-Garcia, R., Castrejon-Pita, J.R., and Castrejon-Pita, A.A. “Design, development, and evaluation of a simple blackbody radiative source.” *AIP Review of Scientific Instruments* (2010).
- [8] Cengel, Y.A. “Heat and mass transfer: a practical approach.” Third ed. Boston: McGraw Hill, 2007.
- [9] Coppa, P. and Consorti, A. “Normal emissivity of samples surrounded by surfaces at diverse temperatures.” *Measurement* 38 (2005): 124-131.
- [10] Cormier, D., Harryson, O., West, H. “Characterization of H13 steel produced via electron beam melting.” *Rapid Prototyping Journal* 10.1 (2004): 35-41.
- [11] De Lara, H.I.L. “Development of a non-intrusive temperature measurement technique using infrared thermography.” Thesis. University of Texas at El Paso, 2001.
- [12] Dong, H. and Bell, T. “Enhanced wear resistance of titanium surfaces by a new thermal oxidation treatment.” *Wear*, 238: 2 (2000), pp. 131-137.
- [13] Felice, R.A. “The spectropyrometer – a practical multi-wavelength pyrometer.” FAR Associates: The 8<sup>th</sup> Symposium on Temperature: Its Measurement and Control in Science and Industry, Oct. 21-24, 2002.
- [14] Felice, R.A. and Nash, D.A. “Pyrometry of materials with changing, spectrally- dependent emissivity- solid & liquid metals.” FAR Associates, 2012.
- [15] FLIR. “FLIR’s user manual- Thermacam research professional 2.10.” Boston, MA: 2010.
- [16] FLIR. “Uncooled detectors for thermal imaging cameras.” Breda, Netherlands: 2008.
- [17] Frigola, P., *et. al.*, Proceeding of IPAC’10, Kyoto, Japan (2010).
- [18] Gibson, I., Rosen, D.W., and Stucker, B. “Additive Manufacturing Technologies.” New York: Springer, 2010.
- [19] Griffith, M.L., *et.al.* “Understanding thermal behavior in the LENS process.” *Materials and Design*, 20.2-3 (1999): 107-113.
- [20] Hamilton, D.C. and Morgan, W.R. “Radiant-interchange configuration factors.” Technical Note. Purdue University. Washington: NACA, 1952.

- [21] Hibbeler, R.C. “Statics and mechanics of materials.” Upper Saddle River, NJ: Pearson Prentice Hall, 2004.
- [22] Holman, J.P. “Experimental methods for engineers.” Boston, MA: McGraw-Hill, 2001.
- [23] Howell, J.R. “A catalog of radiation heat transfer configuration factors.” 3<sup>rd</sup> ed. The University of Texas at Austin. Austin: 2010.
- [24] Hu, D. and Kobacevic, R. “Sensing, modeling and control for laser-based additive manufacturing.” *International Journal of Machine Tools and Manufacture*, 43.1 (2003): pp. 51-60.
- [25] IRISS. “10 Things you need to know about infrared windows.” IRISS, Inc., 2009.
- [26] Klinger, T. “Image processing with LabVIEW and IMAQ Vision.” Upper Saddle River: Prentice Hall, 2003.
- [27] Kruth, J.P., Leu, M.C. and Nakagawa, T. “Progress in additive manufacturing and rapid prototyping.” *Annals of the CIRP*, 47: 2 (1998), pp.: 525-540.
- [28] Love, T.J. “Radiative heat transfer.” Columbus, OH: Charles E. Merrill Publishing Company, 1968.
- [29] Maldague, X.P.V. “Theory and practice of infrared technology for nondestructive testing.” New York: John Wiley & Sons, Inc., 2001.
- [30] Mathworks. Matlab. Web. 18 Feb, 2013.
- [31] Matweb. Material property data. Web. 16 Jan. 2013.
- [32] Mireles, J. and Rodriguez, E. “Defect inspection and temperature optimization.” A technical report submitted to Lockheed Martin Aero, 2013.
- [33] Murr, L.E., *et. al.* “Microstructures and mechanical properties of electron beam-rapid manufactured Ti-6Al-4V biomedical prototypes compared to wrought Ti-6Al-4V.” *Materials Characterization* 60 (2009): 96-105. Elsevier.
- [34] My NASA data. “Electromagnetic spectrum diagram.” Web. 14 Nov. 2012. Available: <http://mynasadata.larc.nasa.gov/science-processes/electromagnetic-diagram/>
- [35] Narayana, K.B. “View factors for parallel rectangular plates.” *Heat Transfer Engineering*, 19:1 (1998), pp. 59-63.
- [36] Office of research and sponsored projects. “Organized research center profile- W.M. Keck Center for 3D Innovation.” Web. 9 Nov. 2012. Available: <http://orspprofile.utep.edu/profilesystem/editprofile.php?pid=1307&onlyview=1>
- [37] Olszewska, K. and Friedel, K. “Control of the electron beam active zone position in electron beam welding processes.” *Vacuum* 74 (2004): 29-43.
- [38] RadiaBeam Technologies, LLC: Patent US 7,411,361.
- [39] Relf, C.G. “Image acquisition and processing with LabVIEW.” Boca Raton: CRC Press, 2004.
- [40] Sparrow, E.M. and Cess, R.D. “Radiation heat transfer.” Augmented Ed. New York, NY: Hemisphere Publishing Corporation, 1978.
- [41] Svensson, M. “Material properties of EBM-manufactured Ti-6Al-4V & Ti-6Al-4V ELI under Raw and HIP Conditions.” Arcam AB, 2009.

- [42] Teodorescu, G. "Radiative emissivity of metals and oxides metals at high temperature." Dissertation. Auburn University, 2007.
- [43] Texas Instruments (Ti). Ti89. Web. 18 Feb., 2013.
- [44] Wicker, R. "Additive Manufacturing: A Nexus for Transformation." Solid Freeform Fabrication Symposium. August, 2012. Austin, TX.
- [45] Wiebelt, J.A. "Engineering radiation heat transfer." New York: Holt, Rinehart and Winston, Inc., 1966.
- [46] Xiong, Y. *et.al.* "In situ thermal imaging and three-dimensional finite element modeling of tungsten carbide-cobalt during laser deposition." *Acta Materialia*, 57 (2009): 5419-5429.

## APPENDIX A IR IMAGES OF CYLINDRICAL BUILDS WITH SURFACE TEMPERATURE PLOTS

This appendix shows various IR images captured at different times, and z-height, of a row of five cylinders. A total of four different builds were built each with different parameters; surface measurements were acquired to measure the effects of parameter control to surface temperature. In the analysis tables, cylinders are labels (from left to right), AR01, AR02, AR03, AR04, and AR05, respectively.

**TABLE A-1 STANDARD BUILD- ASSIGNED PARAMETERS FOR BUILD AND IR CAMERA**

Standard Build- Assigned Parameters			
Start Temperature:	760 °C		
*Surface Temperature:	850 °C		
Speed Function:	36		
**Max Beam Current:	17 mA		
*This is an auto calculation parameter that the machine uses to calculate melt paramters (i.e. beam current).			
**This is the maximum allowed current during hatch melting.			
IR Camera- Assigned Object Parameters			
Distance, m	Refl. Temp. °C	Ext. Opt. Temp., °C	Ext. Opt. Trans.
0.3	342	31.9	0.94
Label	Emissivity		
Image			
AR01*	0.25		
AR02*	0.25		
AR03*	0.25		
AR04*	0.25		
AR05*	0.25		

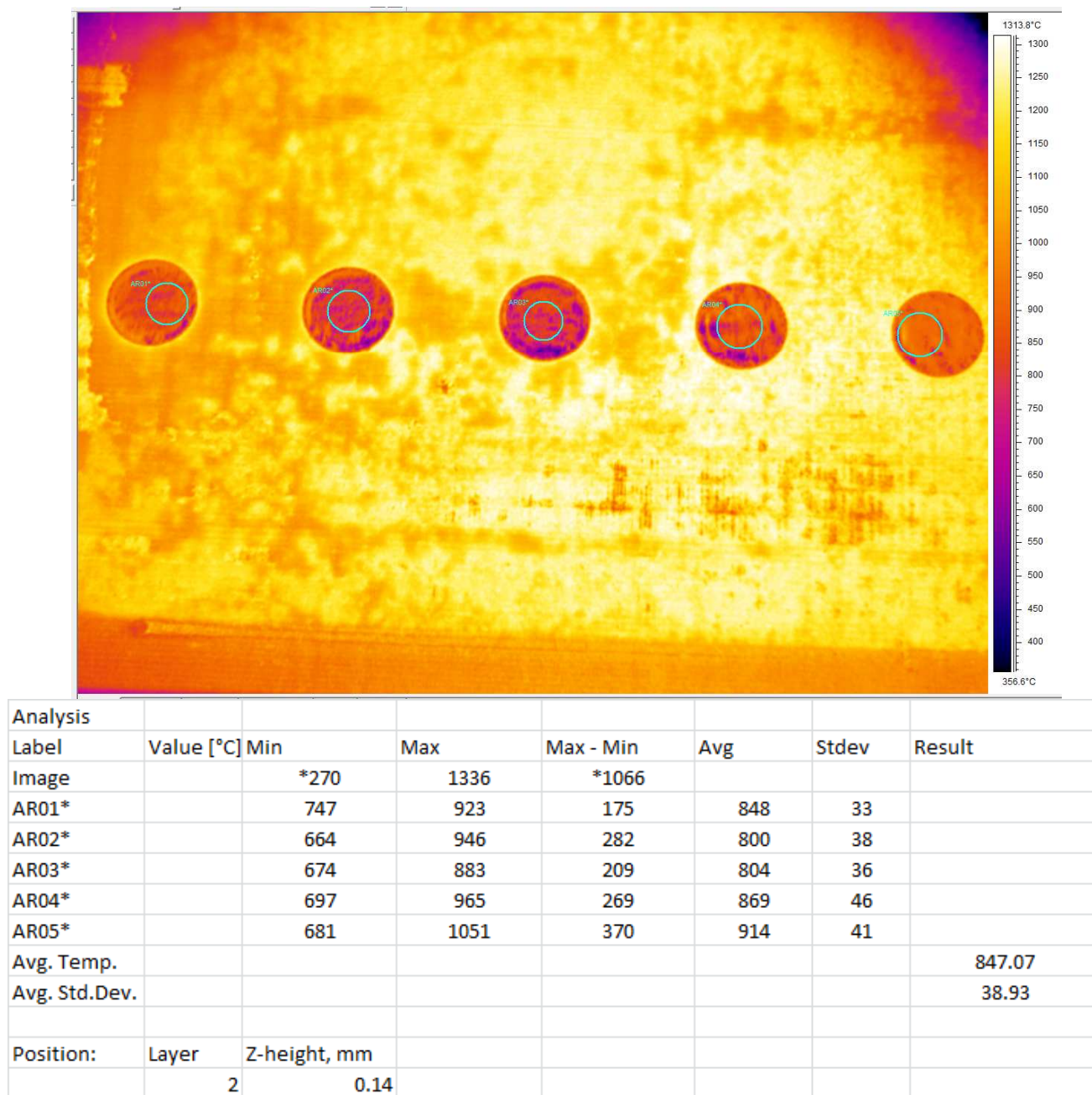
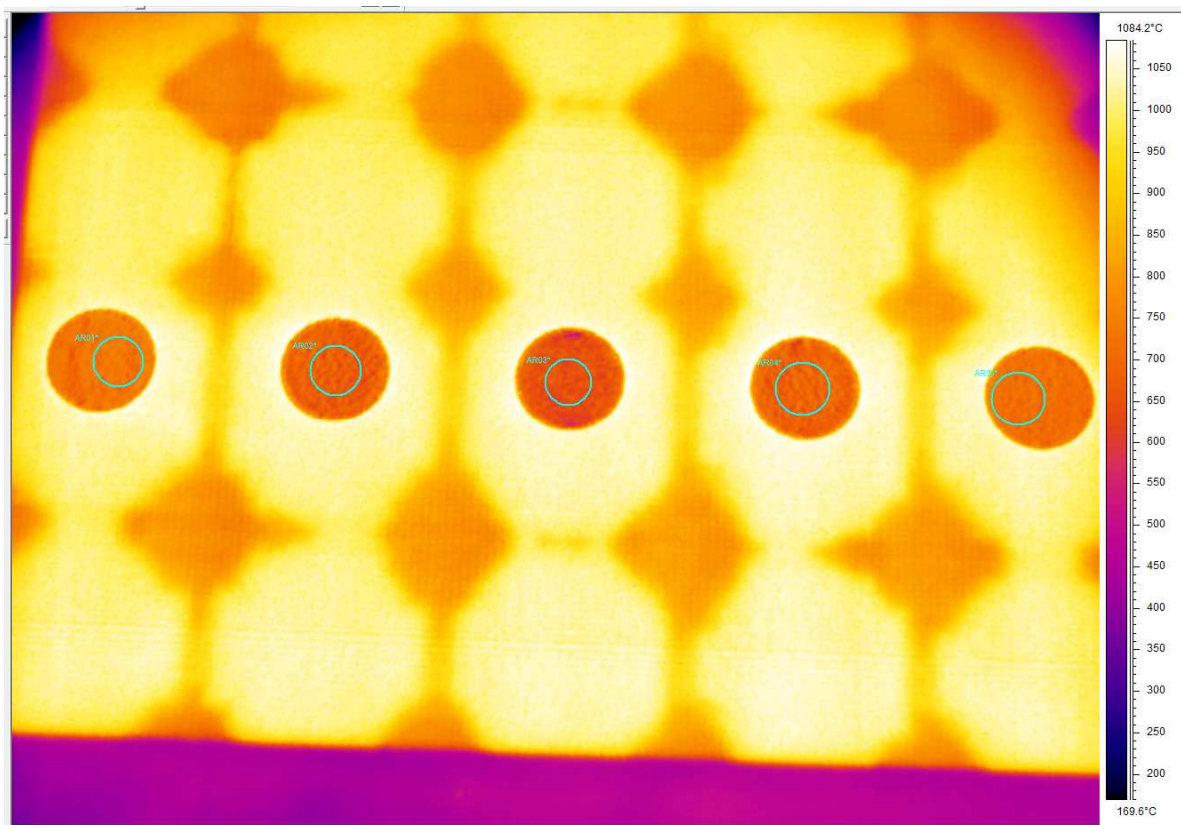


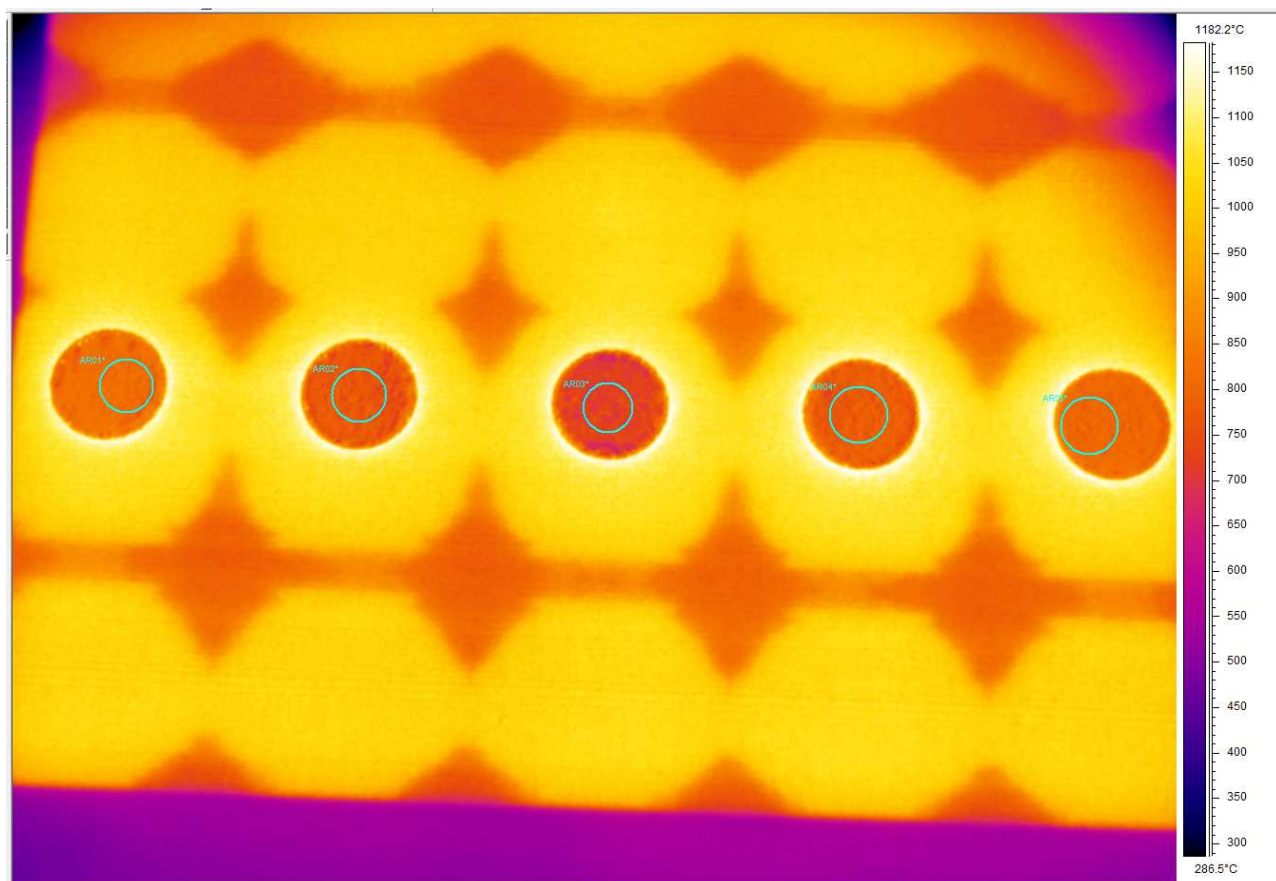
**FIGURE A-7-1 IR IMAGE OF STANDARD BUILD CYLINDERS AT Z= 0.14 MM**



Analysis							
Label	Value [°C]	Min	Max	Max - Min	Avg	Stdev	Result
Image		<100	1099	*999			
AR01*		684	765	80	732	17	
AR02*		618	743	124	678	22	
AR03*		603	713	110	647	18	
AR04*		624	754	130	691	23	
AR05*		657	755	98	718	16	
Avg. Temp.							693.28
Avg. Std. Dev.							19.03
Position:	Layer	Z-height, mm					
	50	3.5					

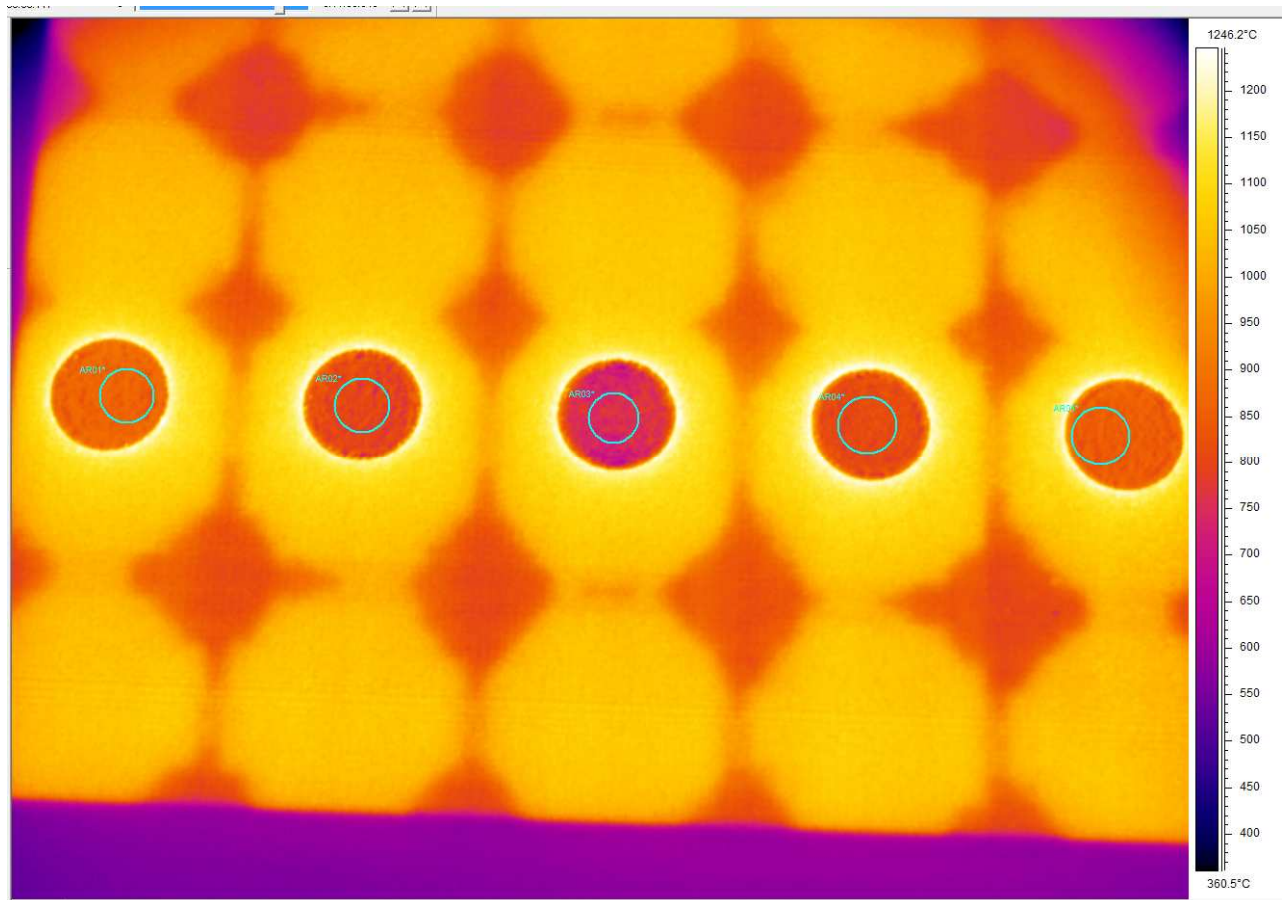
**FIGURE A-2 IR IMAGE OF STANDARD BUILD CYLINDERS AT Z= 3.5 MM**





Analysis							
Label	Value [°C]	Min	Max	Max - Min	Avg	Stdev	Result
Image		*241	1200	*959			
AR01*		739	843	104	817	15	
AR02*		703	809	106	768	17	
AR03*		680	772	92	726	15	
AR04*		737	822	85	782	15	
AR05*		760	843	82	806	12	
fo01							779.58
fo02							14.76
Position:	Layer	Z-height, mm					
	250	17.5					

**FIGURE A-3 IR IMAGE OF STANDARD BUILD CYLINDERS AT Z= 17.5 MM**



Analysis							
Label	Value [°C]	Min	Max	Max - Min	Avg	Stdev	Result
Image		326	1281	955			
AR01*		816	900	84	865	15	
AR02*		738	852	114	804	17	
AR03*		703	803	100	755	15	
AR04*		764	844	81	814	11	
AR05*		808	888	80	850	14	
Avg. Temp.							817.51
Avg. Std. Dev.							14.56
Position:	Layer	Z-height, mm					
	500	35.00					

**FIGURE A-4 IR IMAGE OF STANDARD BUILD CYLINDERS AT Z= 35.00 MM**

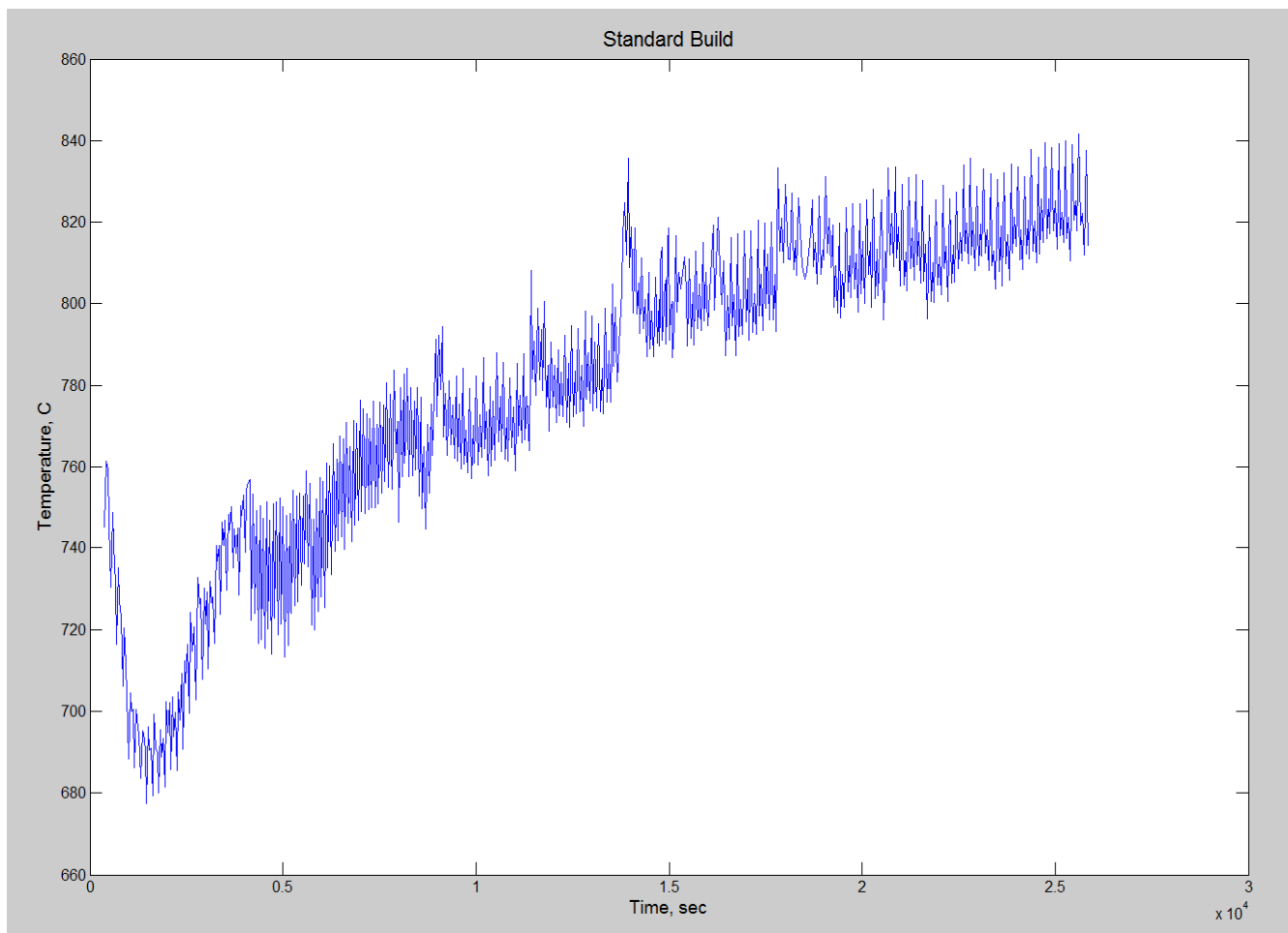


**FIGURE A-5 AVERAGE SURFACE TEMPERATURE MEASUREMENTS OF ALL FIVE CYLINDERS IN THE STANDARD BUILD THROUGHOUT THE COURSE OF THE BUILD.**

**TABLE A-2 “COLD” BUILD- ASSIGNED PARAMETERS FOR BUILD AND IR CAMERA**

"Cold" Build- Assigned Parameters			
Start Temperature:	720 °C		
*Surface Temperature:	750 °C		
Speed Function:	46		
**Max Beam Current:	17 mA		
*This is an auto calculation parameter that the machine uses to calculate melt paramters (i.e. beam current).			
**This is the maximum allowed current during hatch melting.			
IR Camera- Assigned Object Parameters			
Distance, m	Refl. Temp. °C	Ext. Opt. Temp., °C	Ext. Opt. Trans.
0.3	300	31.9	0.94
Label	Emissivity		
Image			
AR01*	0.25		
AR02*	0.25		
AR03*	0.25		
AR04*	0.25		
AR05*	0.25		

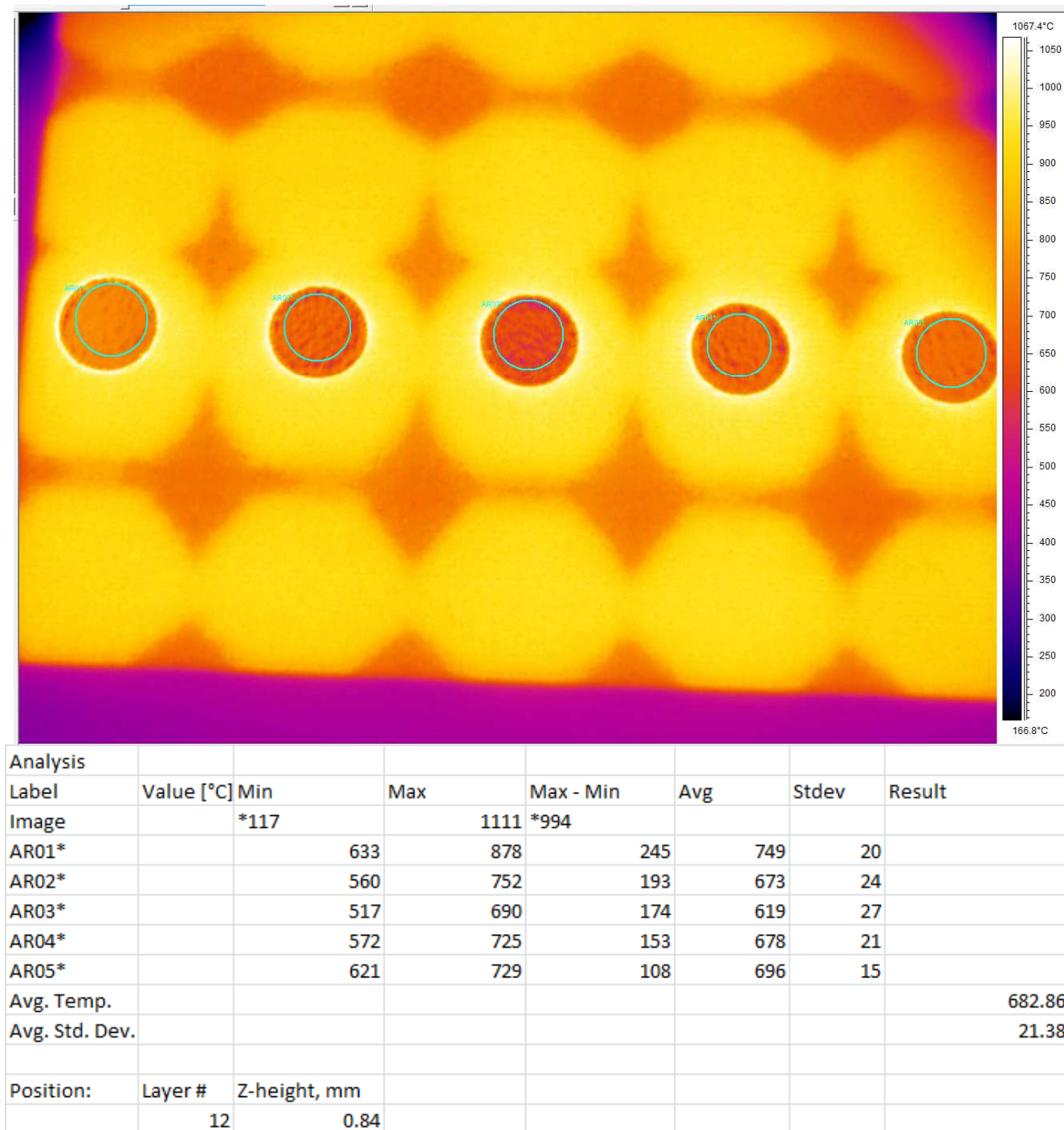


**FIGURE A-6 IR IMAGE OF COLD BUILD CYLINDERS AT Z= 0.84 MM**



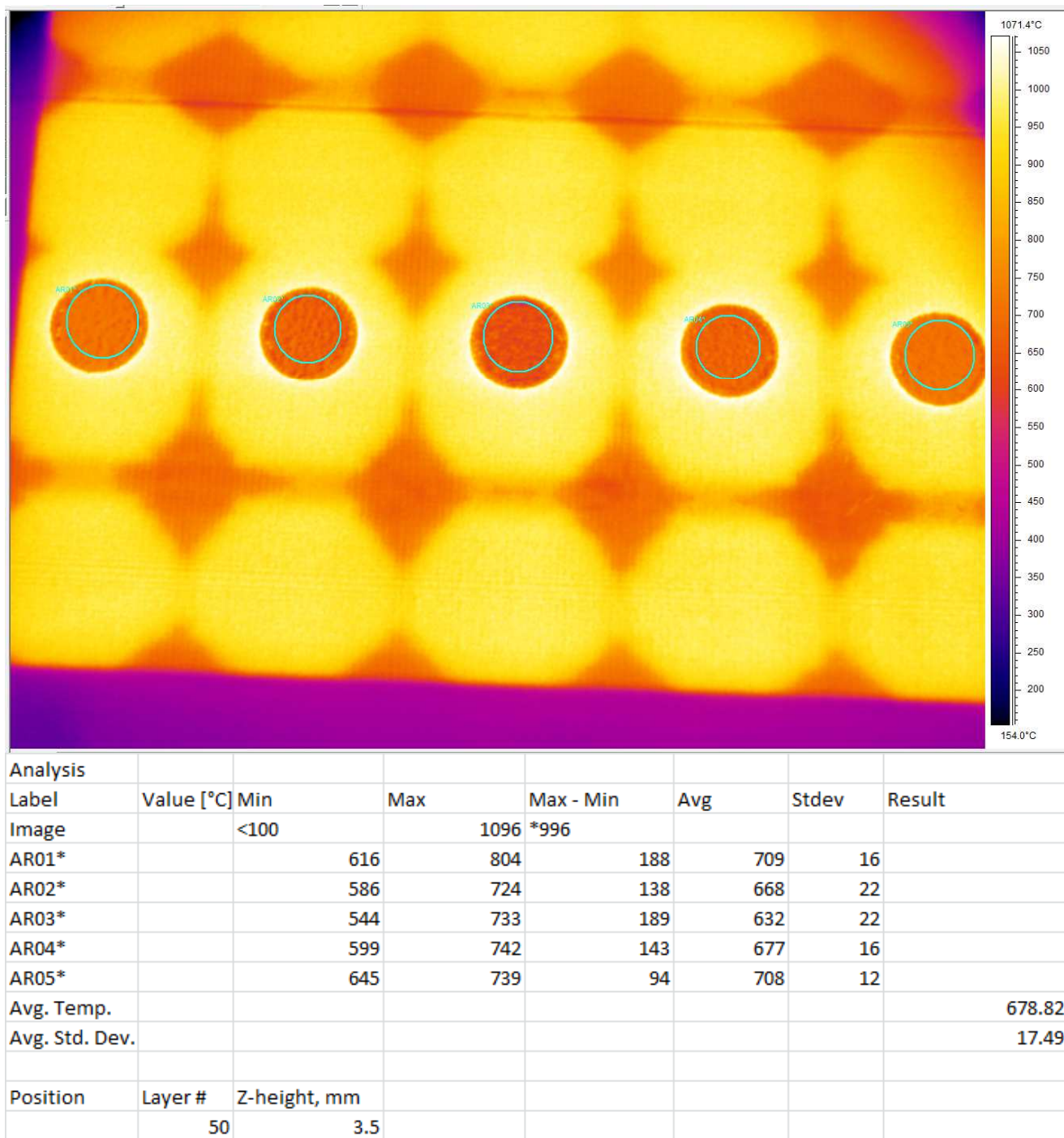


**FIGURE A-7 IR IMAGE OF COLD BUILD CYLINDERS AT Z= 3.5 MM**

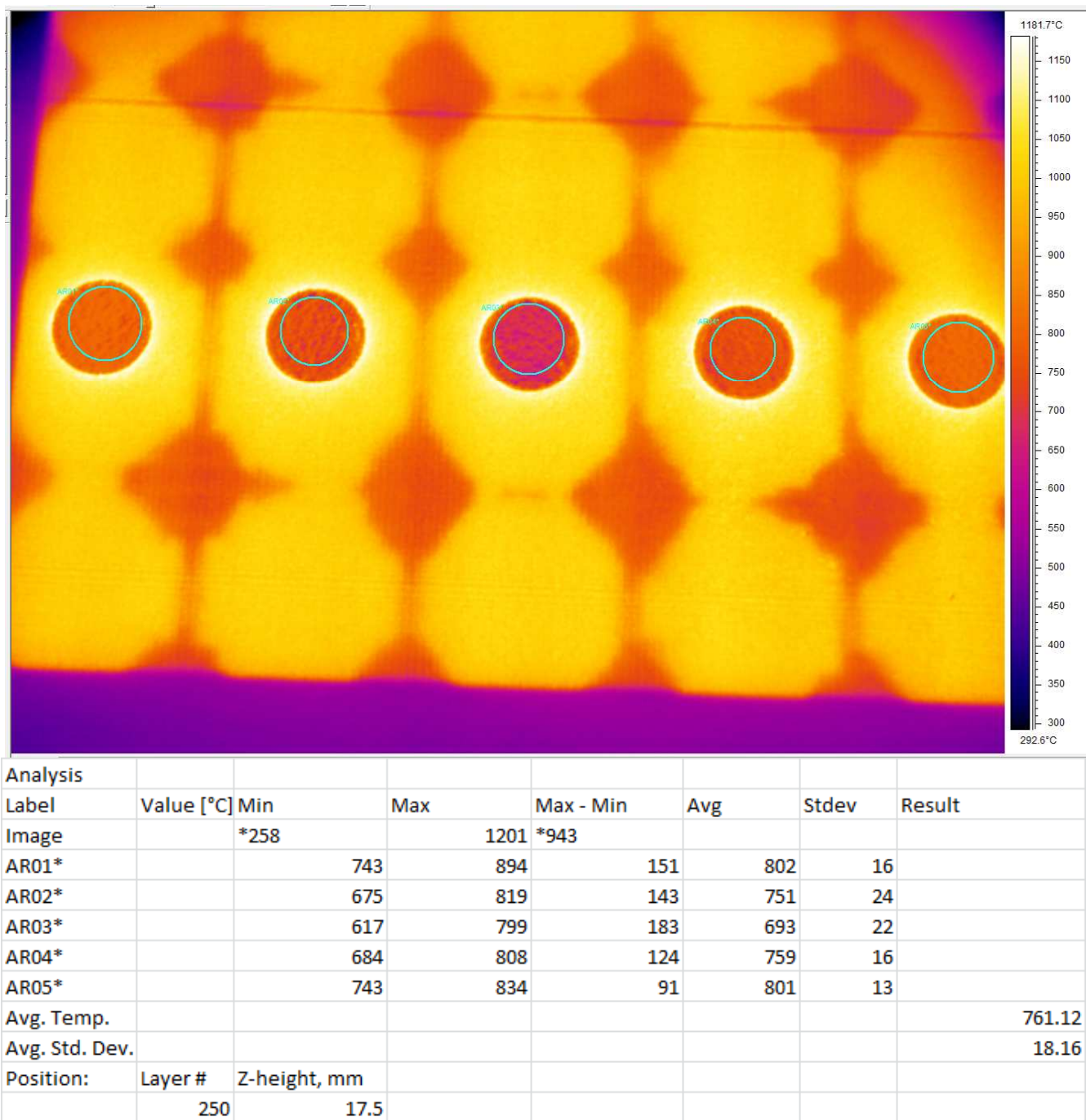
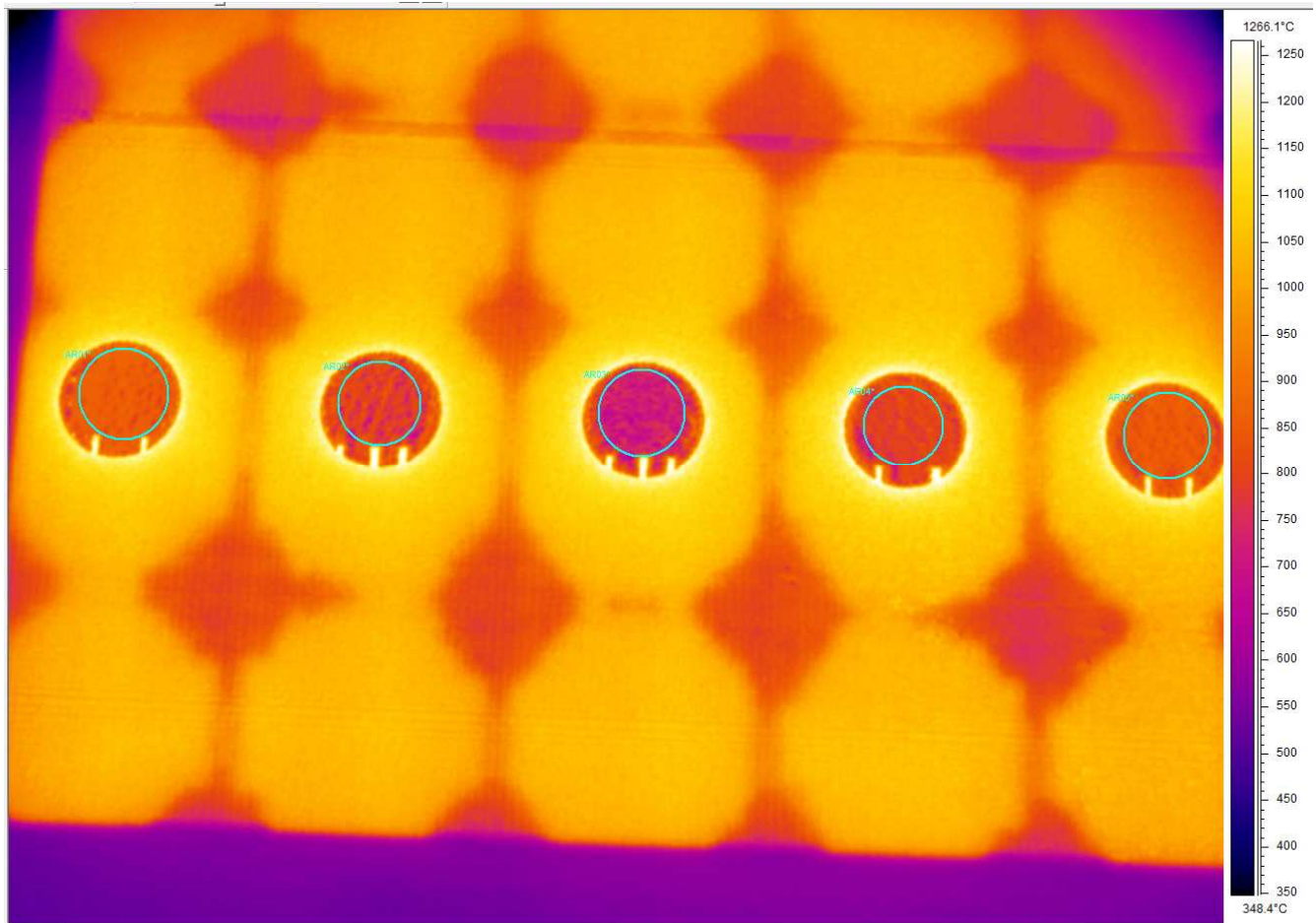


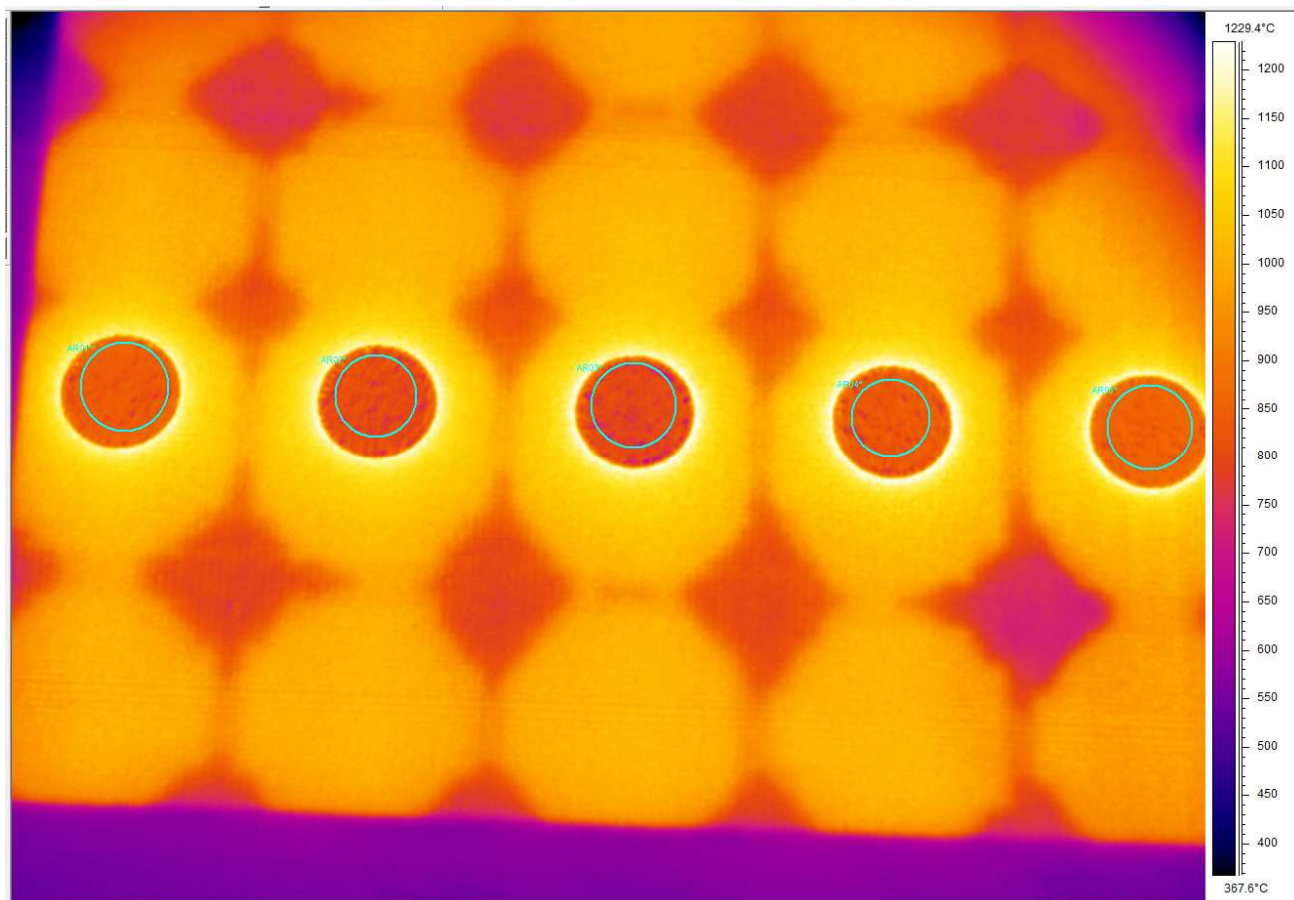
**FIGURE A-8 IR IMAGE OF COLD BUILD CYLINDERS AT Z= 17.5 MM**



Analysis							
Label	Value [°C]	Min	Max	Max - Min	Avg	Stdev	Result
Image		314	1292	979			
AR01*		773	972	199	855	18	
AR02*		682	1034	351	794	31	
AR03*		645	1167	521	730	34	
AR04*		686	852	166	800	20	
AR05*		787	986	199	849	15	
Avg. Temp.							805.54
Avg. Std. Dev.							23.8
Position:	Layer #	Z-height, mm					
	500	35.00					

**FIGURE A-9 IR IMAGE OF COLD BUILD CYLINDERS AT Z= 35.00 MM**





Analysis							
Label	Value [°C]	Min	Max	Max - Min	Avg	Stdev	Result
Image		336	1251	915			
AR01*		745	876	131	841	14	
AR02*		728	857	128	808	17	
AR03*		714	834	120	797	18	
AR04*		730	867	137	833	18	
AR05*		809	882	72	857	11	
Avg. Temp.							827.11
Avg. Std. Dev.							15.58
Position:	Layer #	Z-height, mm					
	750	52.5					

**FIGURE A-10 IR IMAGE OF COLD BUILD CYLINDERS AT Z= 52.50 MM**

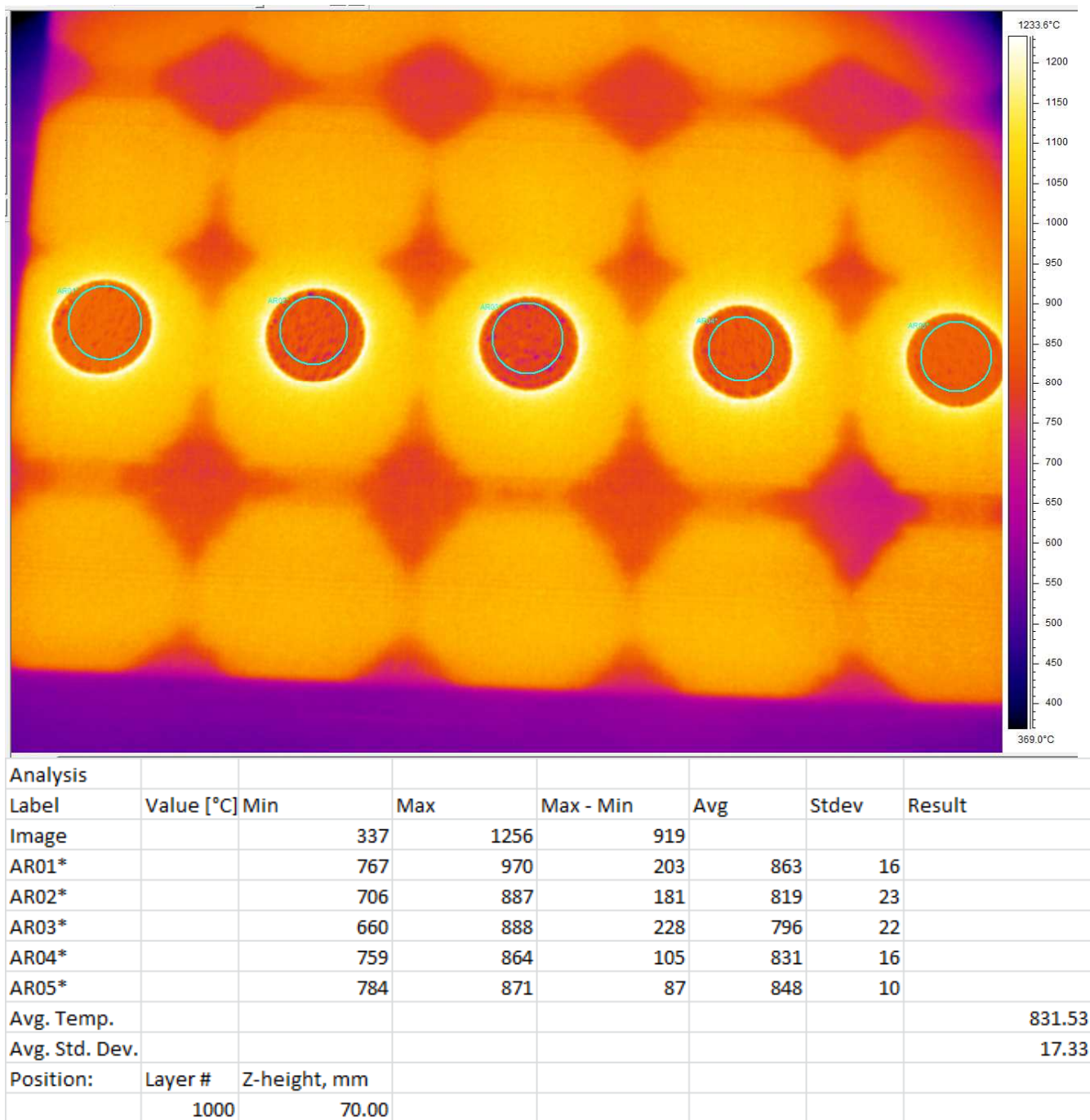


**FIGURE A-11 IR IMAGE OF COLD BUILD CYLINDERS AT Z= 70.00 MM**

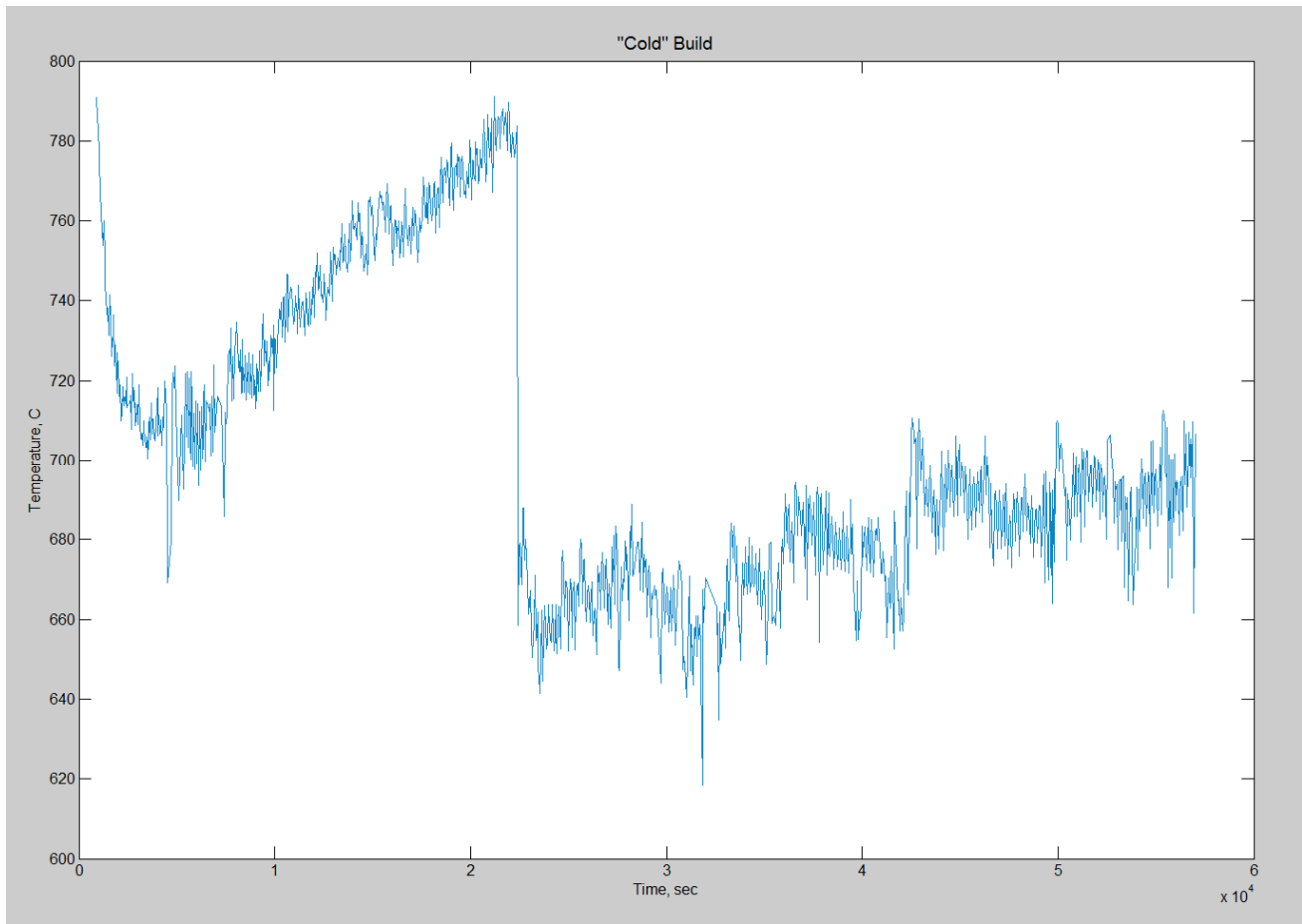


**FIGURE A-12 AVERAGE SURFACE TEMPERATURE MEASUREMENTS OF ALL FIVE CYLINDERS IN THE “COLD” BUILD THROUGHOUT THE COURSE OF THE BUILD. THE DROP IN TEMPERATURE AT ABOUT 2000 SEC WAS DUE TO A SYSTEM HALT, DUE TO OPENING THE EXTERNAL SYSTEM’S HELIUM VALVE THAT LED TO A BUILD ABORT, THE SYSTEM WAS THEN RESTARTED.**

**TABLE A-3 ELEVATED BUILD- ASSIGNED PARAMETERS FOR BUILD AND IR CAMERA**

Elevated Build- Assigned Parameters			
Start Temperature:	790 °C		
*Surface Temperature:	950 °C		
Speed Function:	30		
**Max Beam Current:	17 mA		
Preheat Cycles	1		
*This is an auto calculation parameter that the machine uses to calculate melt paramters (i.e. beam current).			
**This is the maximum allowed current during hatch melting.			
IR Camera- Assigned Object Parameters			
Distance, m	Refl. Temp. °C	Ext. Opt. Temp., °C	Ext. Opt. Trans.
0.3	355	31.9	0.94
Label	Emissivity		
Image			
AR01*	0.25		
AR02*	0.25		
AR03*	0.25		
AR04*	0.25		
AR05*	0.25		

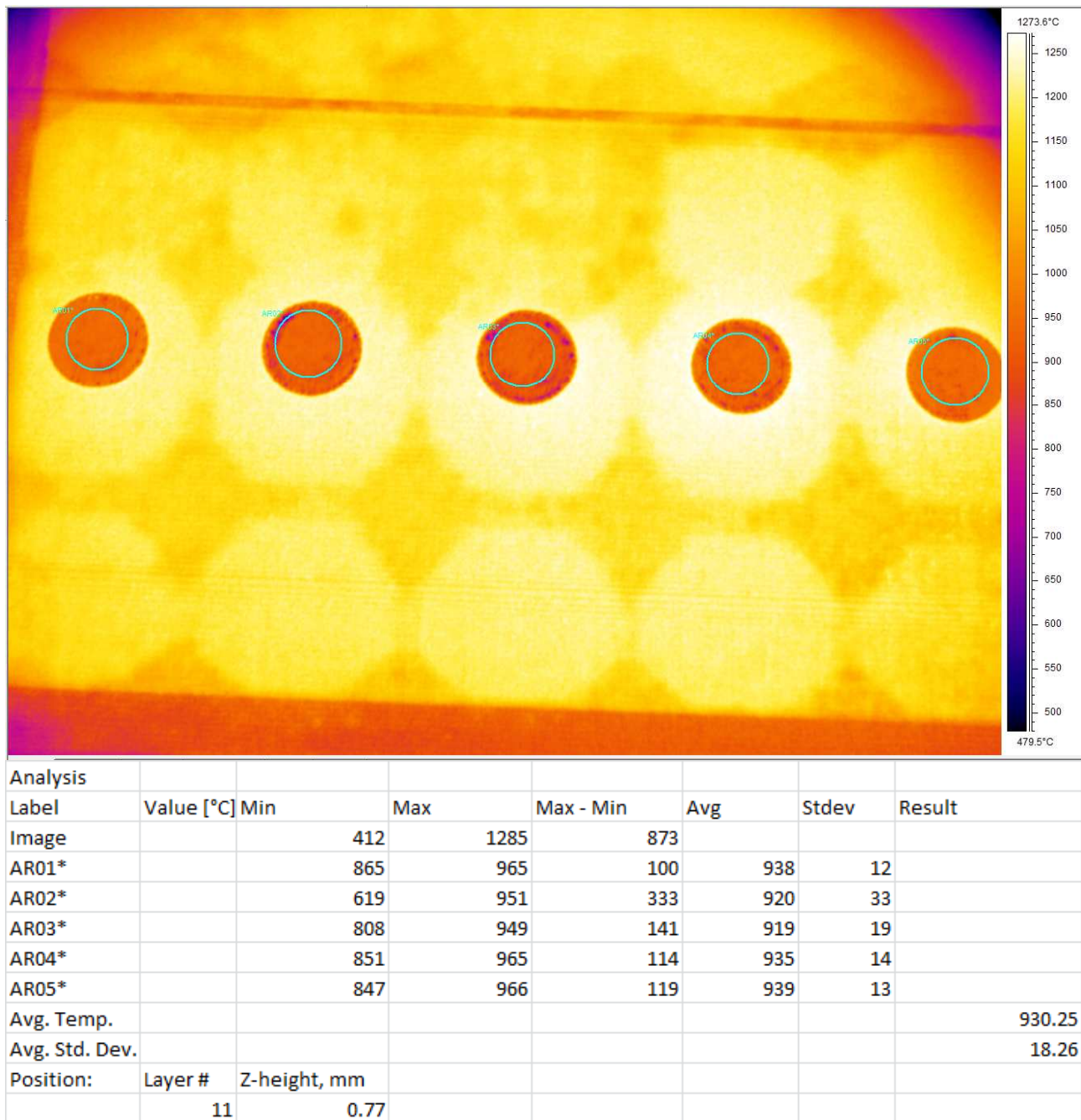


**FIGURE A-13 IR IMAGE OF ELEVATED BUILD CYLINDERS AT Z= 0.77 MM**



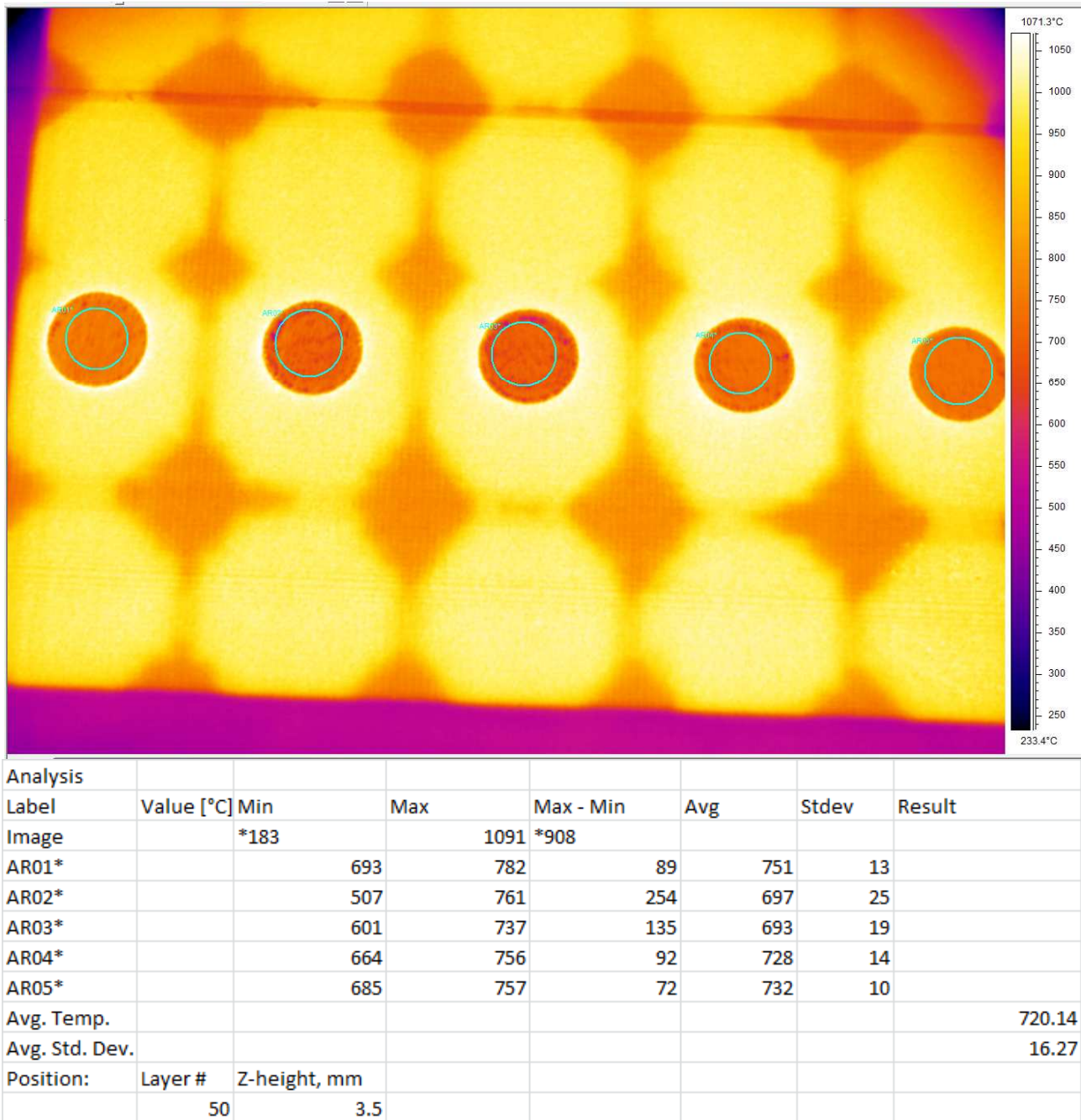


**FIGURE A-14 IR IMAGE OF ELEVATED BUILD CYLINDERS AT Z= 3.50 MM**

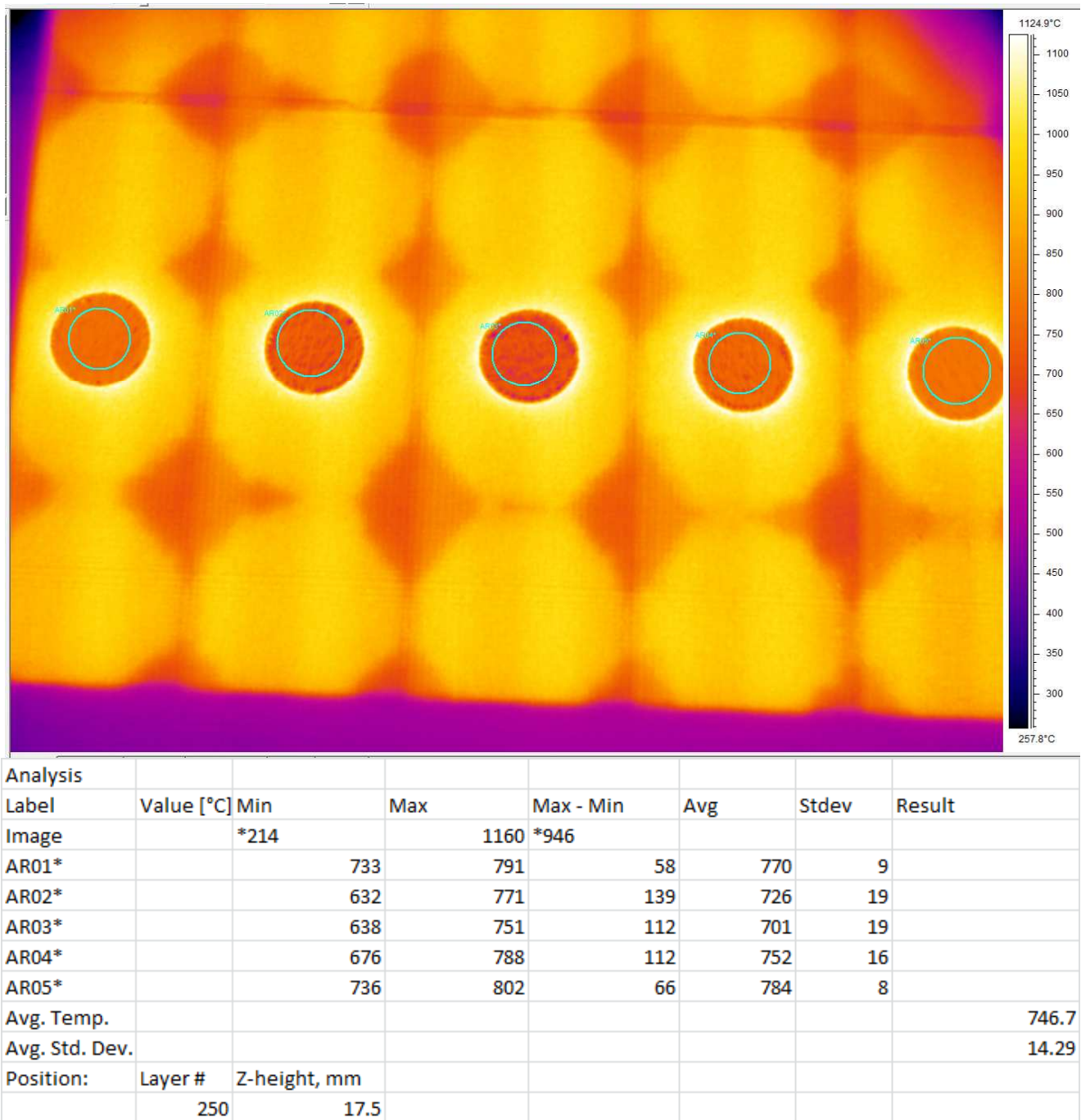


**FIGURE A-15 IR IMAGE OF ELEVATED BUILD CYLINDERS AT Z= 17.50 MM**

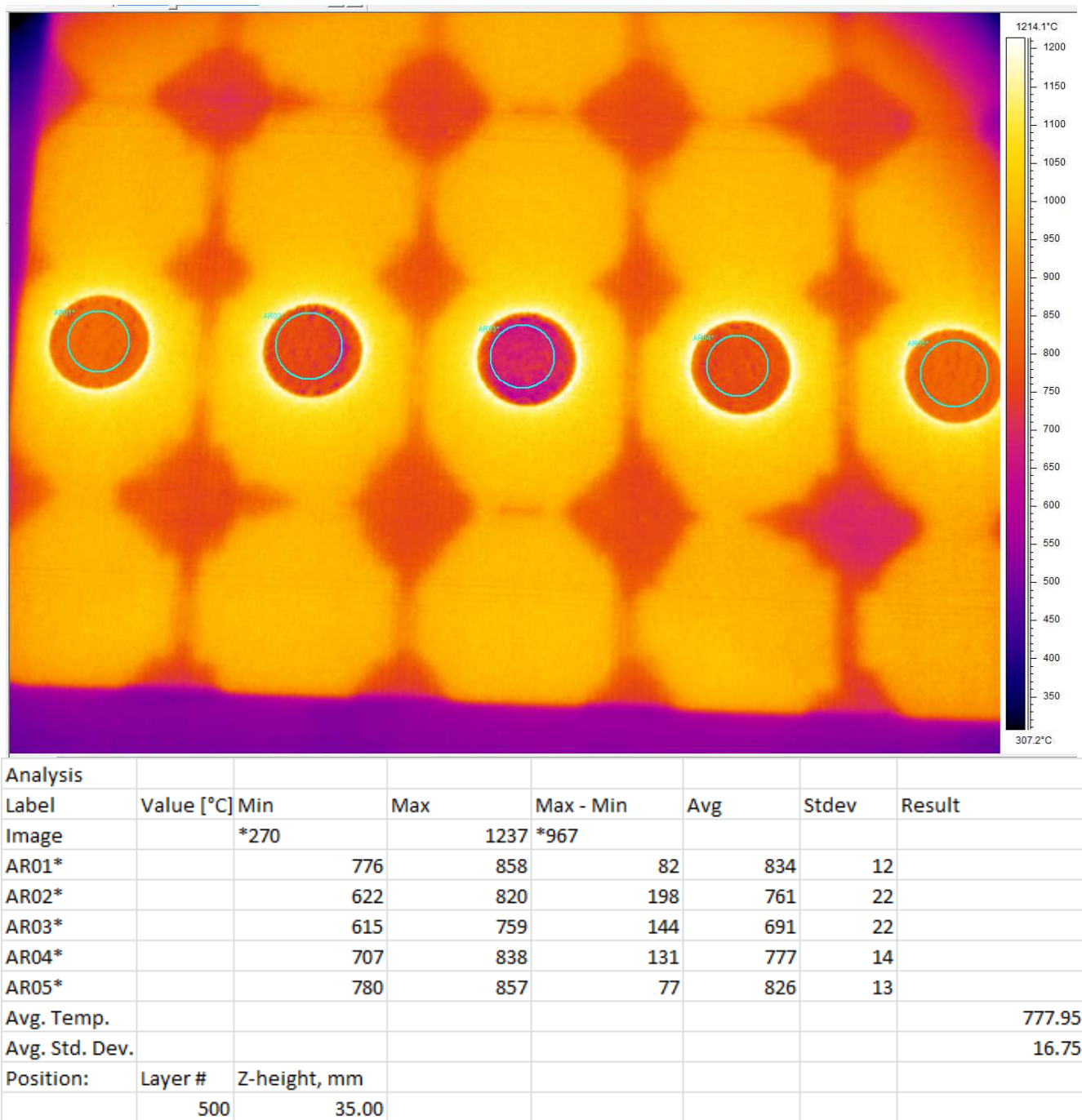
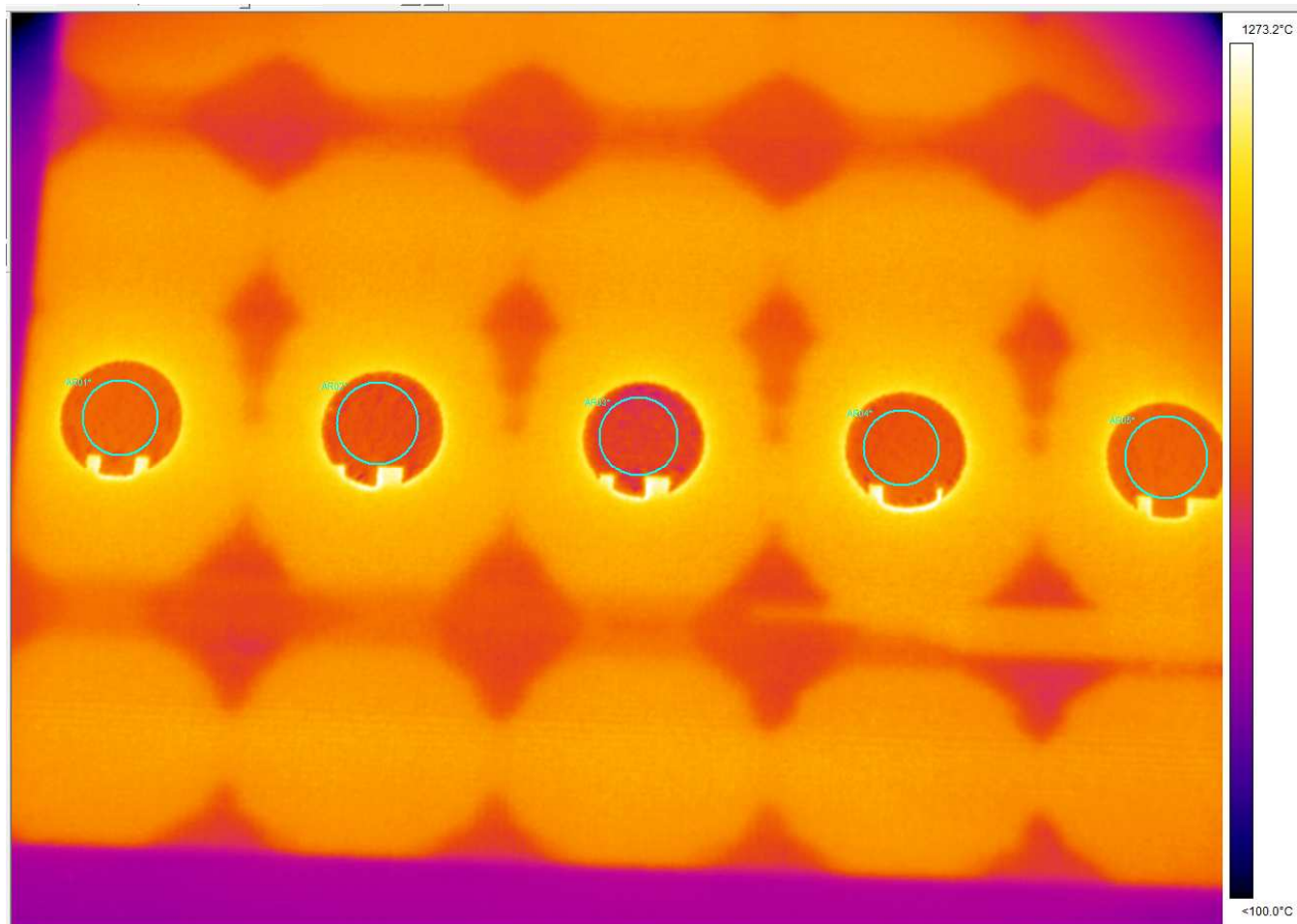


**FIGURE A-16 IR IMAGE OF ELEVATED BUILD CYLINDERS AT Z= 35.00 MM**





Analysis							
Label	Value [°C]	Min	Max	Max - Min	Avg	Stddev	Result
Image		<100	1334	*1234			
AR01*		648	777	129	711	17	
AR02*		563	964	401	643	28	
AR03*		508	1027	520	595	28	
AR04*		602	733	131	667	19	
AR05*		640	935	295	702	19	
Avg. Temp.							663.6
Avg. Std. Dev.							22.21
Position:	Layer #	Z-height, mm					
	750	52.5					

**FIGURE A-17 IR IMAGE OF ELEVATED BUILD CYLINDERS AT Z= 52.50 MM**

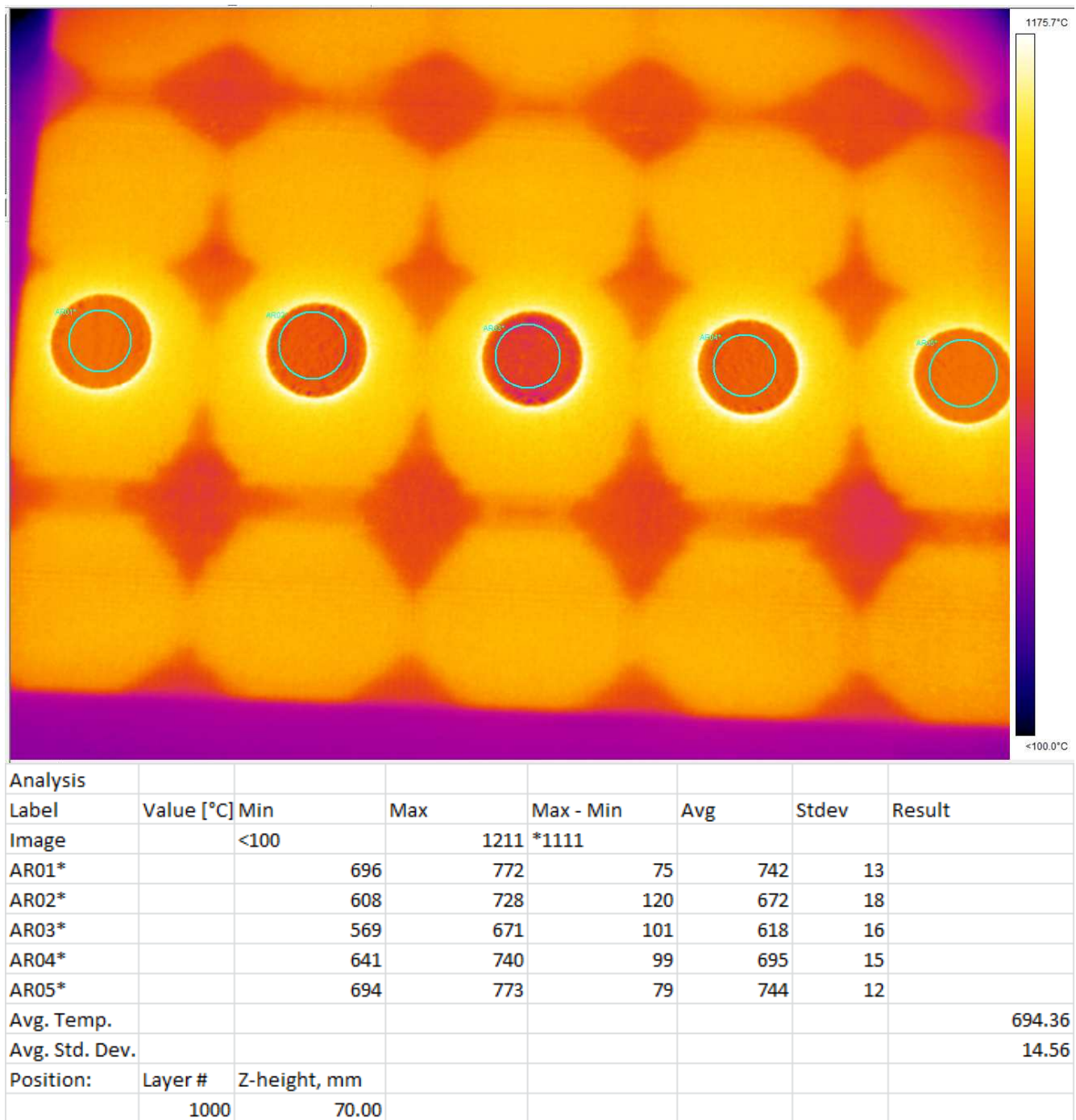


**FIGURE A-18 IR IMAGE OF ELEVATED BUILD CYLINDERS AT Z= 70.00 MM**

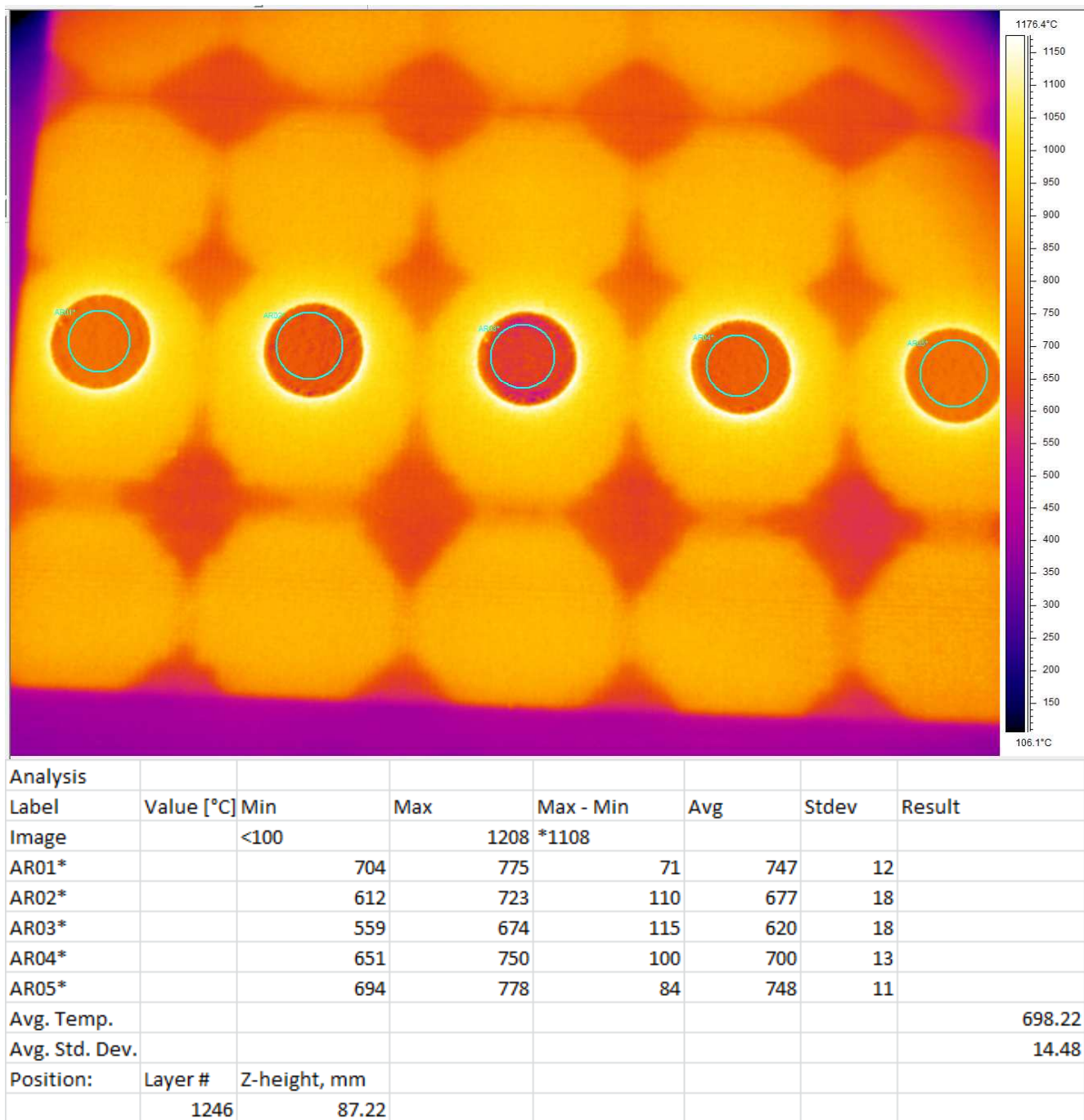


**FIGURE A-19 IR IMAGE OF ELEVATED BUILD CYLINDERS AT Z= 87.22 MM**

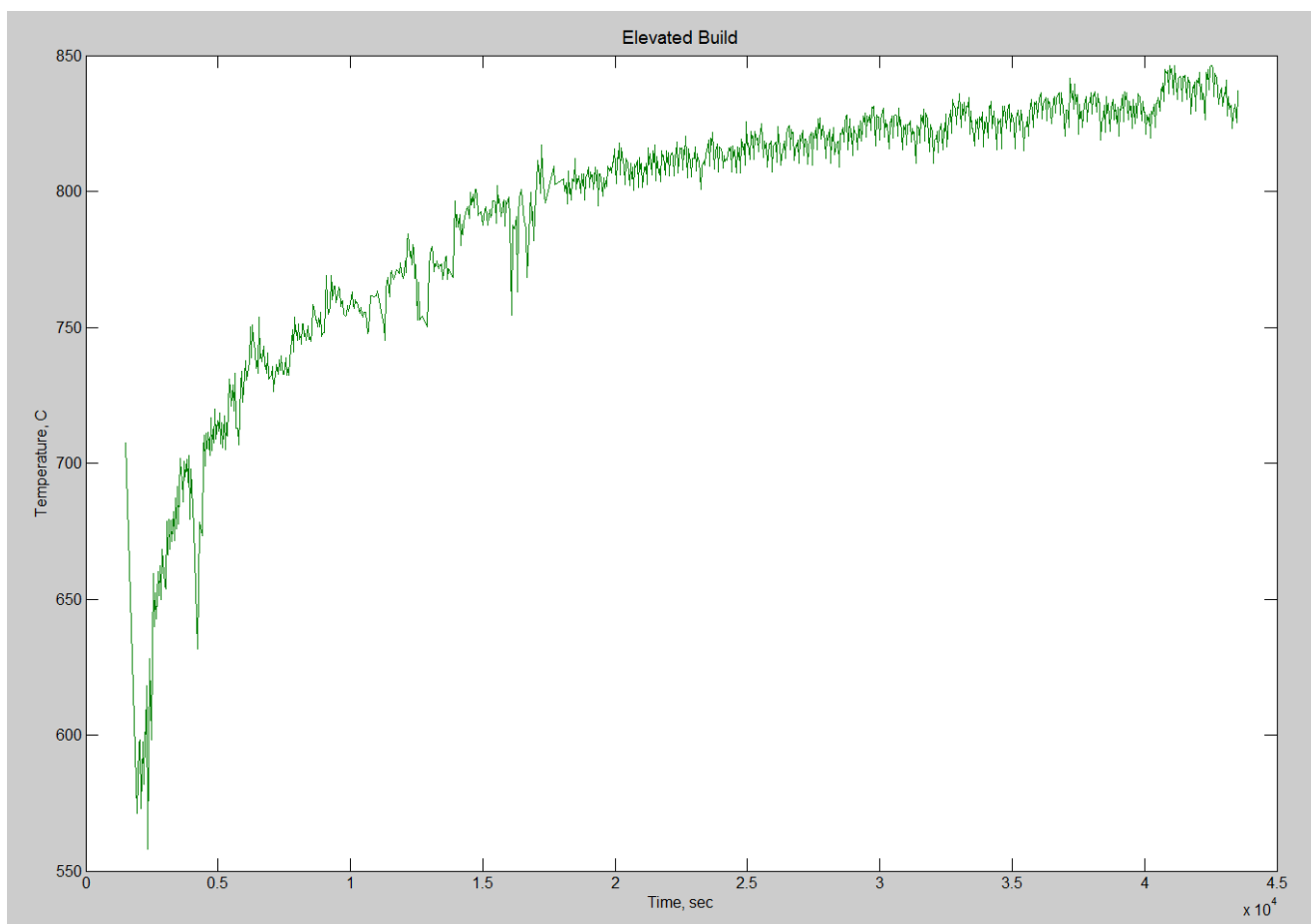
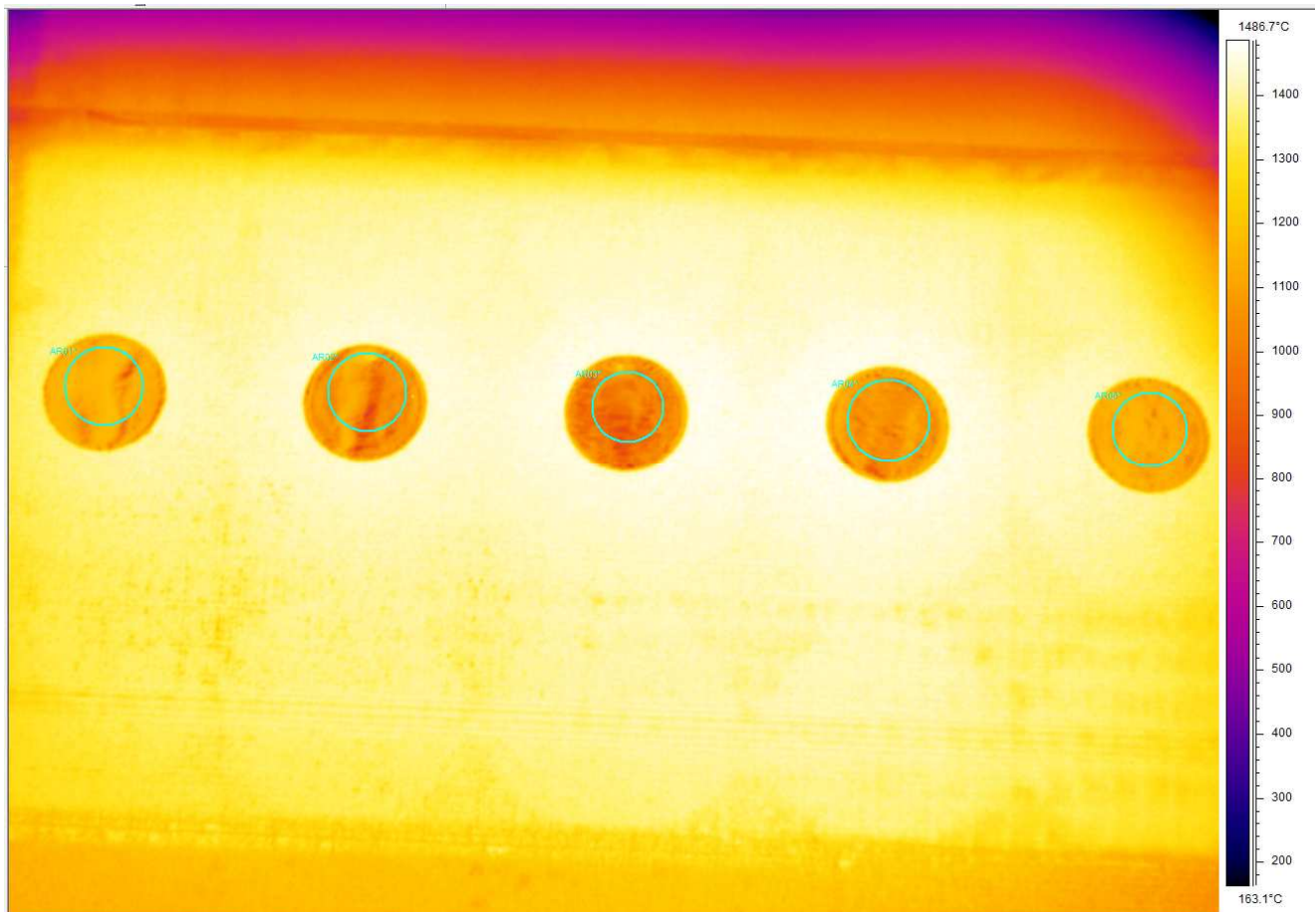


**FIGURE A-20 AVERAGE SURFACE TEMPERATURE MEASUREMENTS OF ALL FIVE CYLINDERS IN THE ELEVATED BUILD THROUGHOUT THE COURSE OF THE BUILD.**

**TABLE A-4 “HOT” BUILD- ASSIGNED PARAMETERS FOR BUILD AND IR CAMERA**

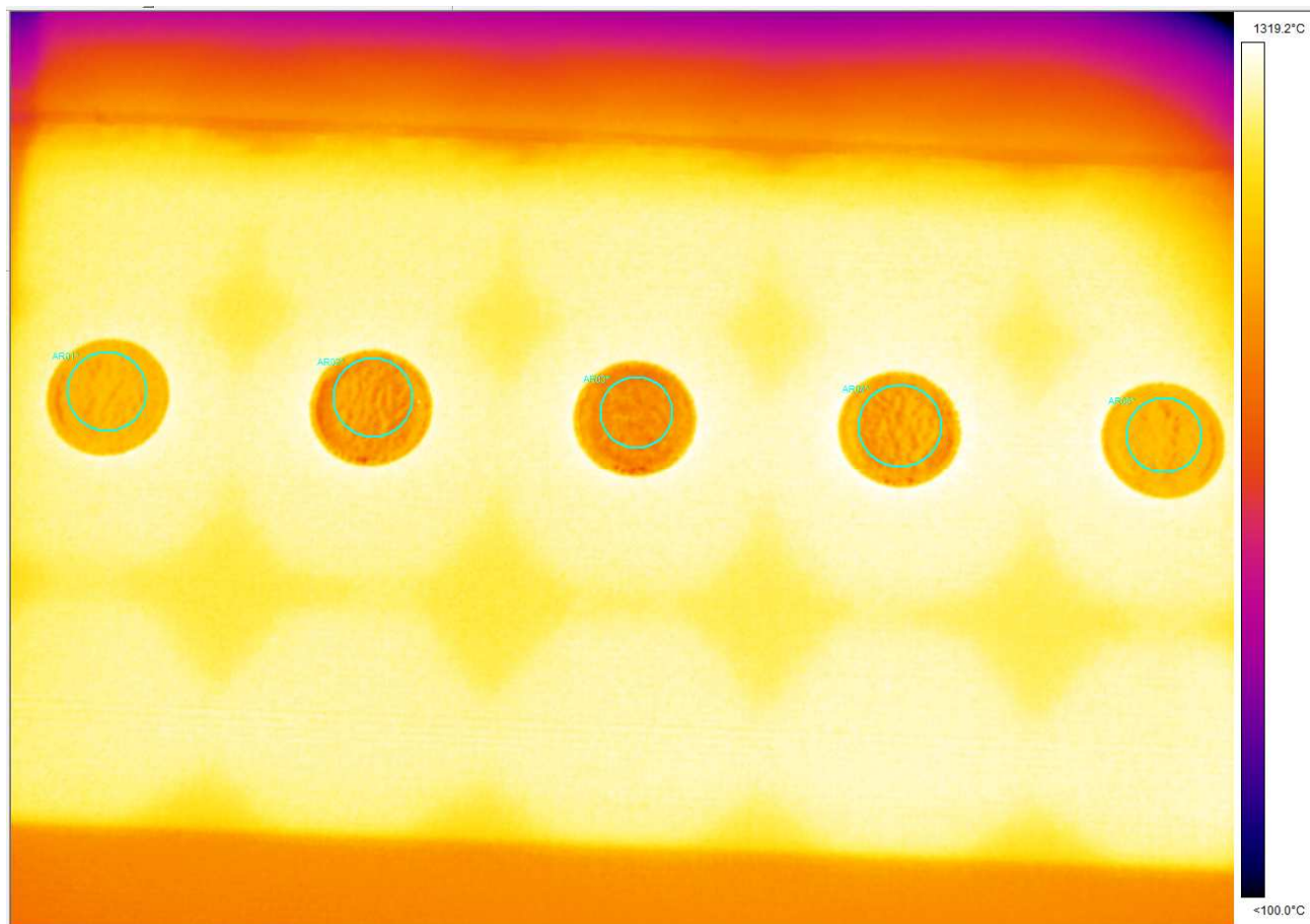
"Hot" Build- Assigned Parameters			
Start Temperature:	850 °C		
*Surface Temperature:	1000 °C		
Speed Function:	25		
**Max Beam Current:	17 mA		
Pre-Heat Cycles	2		
*This is an auto calculation parameter that the machine uses to calculate melt paramters (i.e. beam current).			
**This is the maximum allowed current during hatch melting.			
IR Camera- Assigned Object Parameters			
Distance, m	Refl. Temp. °C	Ext. Opt. Temp., °C	Ext. Opt. Trans.
0.3	419	31.9	0.94
Label	Emissivity		
Image			
AR01*	0.25		
AR02*	0.25		
AR03*	0.25		
AR04*	0.25		
AR05*	0.25		



Analysis							
Label	Value [°C]	Min	Max	Max - Min	Avg	Stdev	Result
Image		<100	1499	*1399			
AR01*		859	1192	333	1138	41	
AR02*		771	1281	510	1059	76	
AR03*		829	1156	327	983	57	
AR04*		926	1148	222	1070	30	
AR05*		1018	1175	156	1128	23	
Avg. Temp.							1075.72
Avg. Std. Dev.							45.5
Position:	Layer #	Z-height, mm					
	16	1.12					

**FIGURE A-20 IR IMAGE OF HOT BUILD CYLINDERS AT Z= 1.12 MM**





Analysis							
Label	Value [°C]	Min	Max	Max - Min	Avg	Stdev	Result
Image		<100	1345	*1245			
AR01*		932	1043	111	1005	21	
AR02*		826	1020	194	934	37	
AR03*		817	981	164	898	29	
AR04*		850	1045	195	958	37	
AR05*		858	1048	190	1007	25	
Avg. Temp.							960.49
Avg. Std. Dev.							29.9
Position:	Layer #	Z-height, mm					
	50	3.5					

**FIGURE A-21 IR IMAGE OF HOT BUILD CYLINDERS AT Z= 3.50 MM**

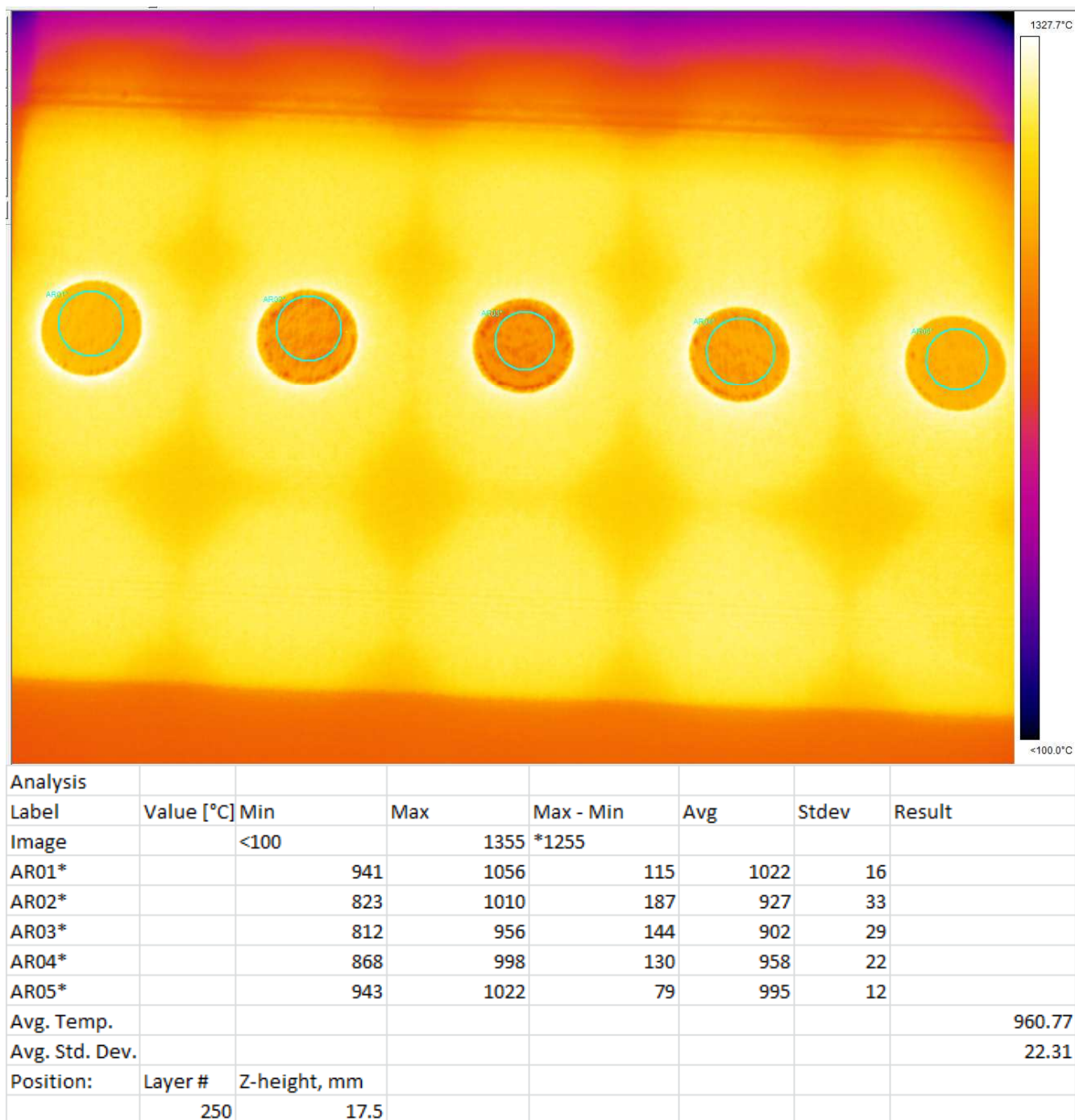


**FIGURE A-22 IR IMAGE OF HOT BUILD CYLINDERS AT Z= 17.50 MM**



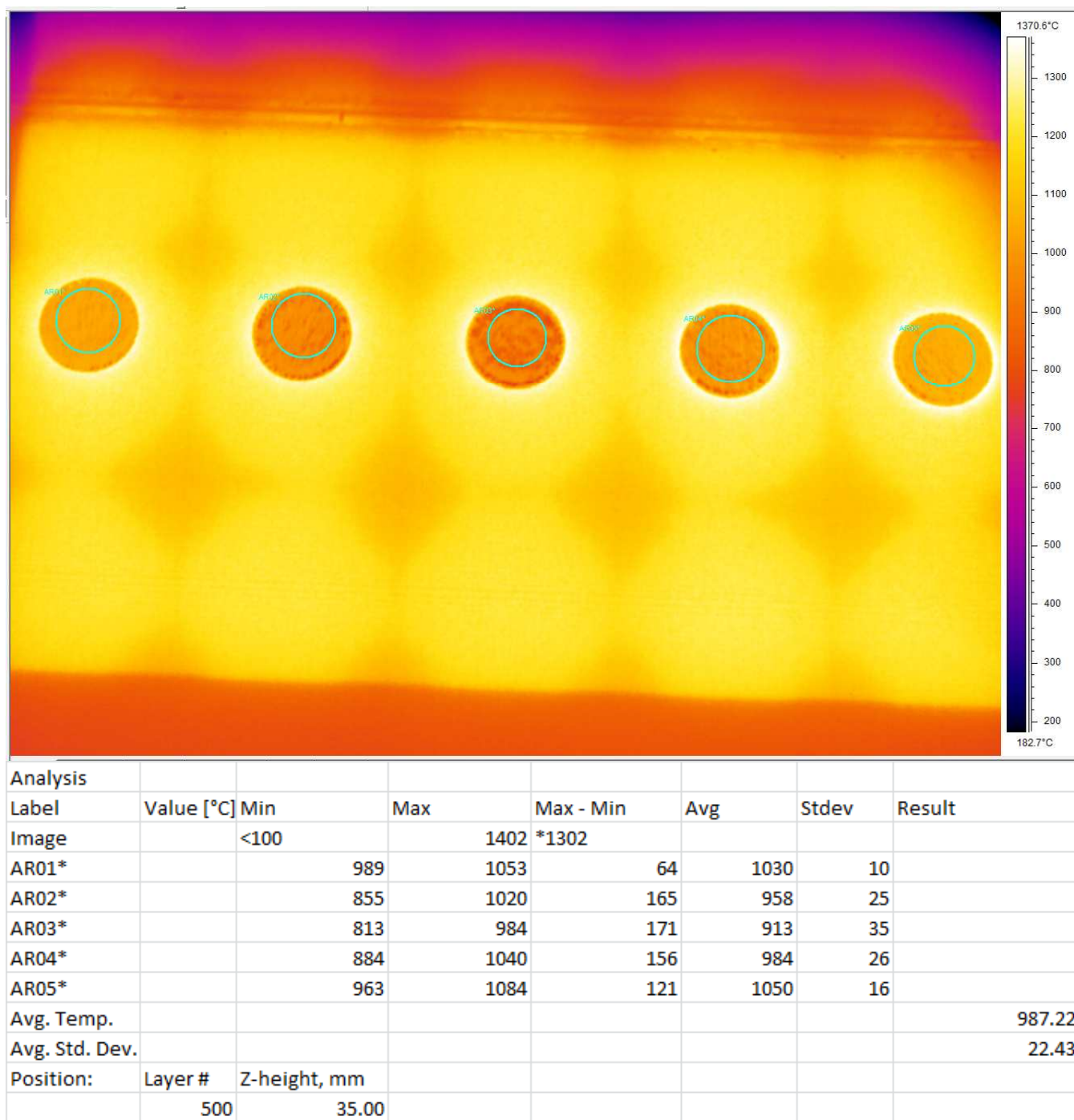


**FIGURE A-23 IR IMAGE OF HOT BUILD CYLINDERS AT Z= 35.00 MM**

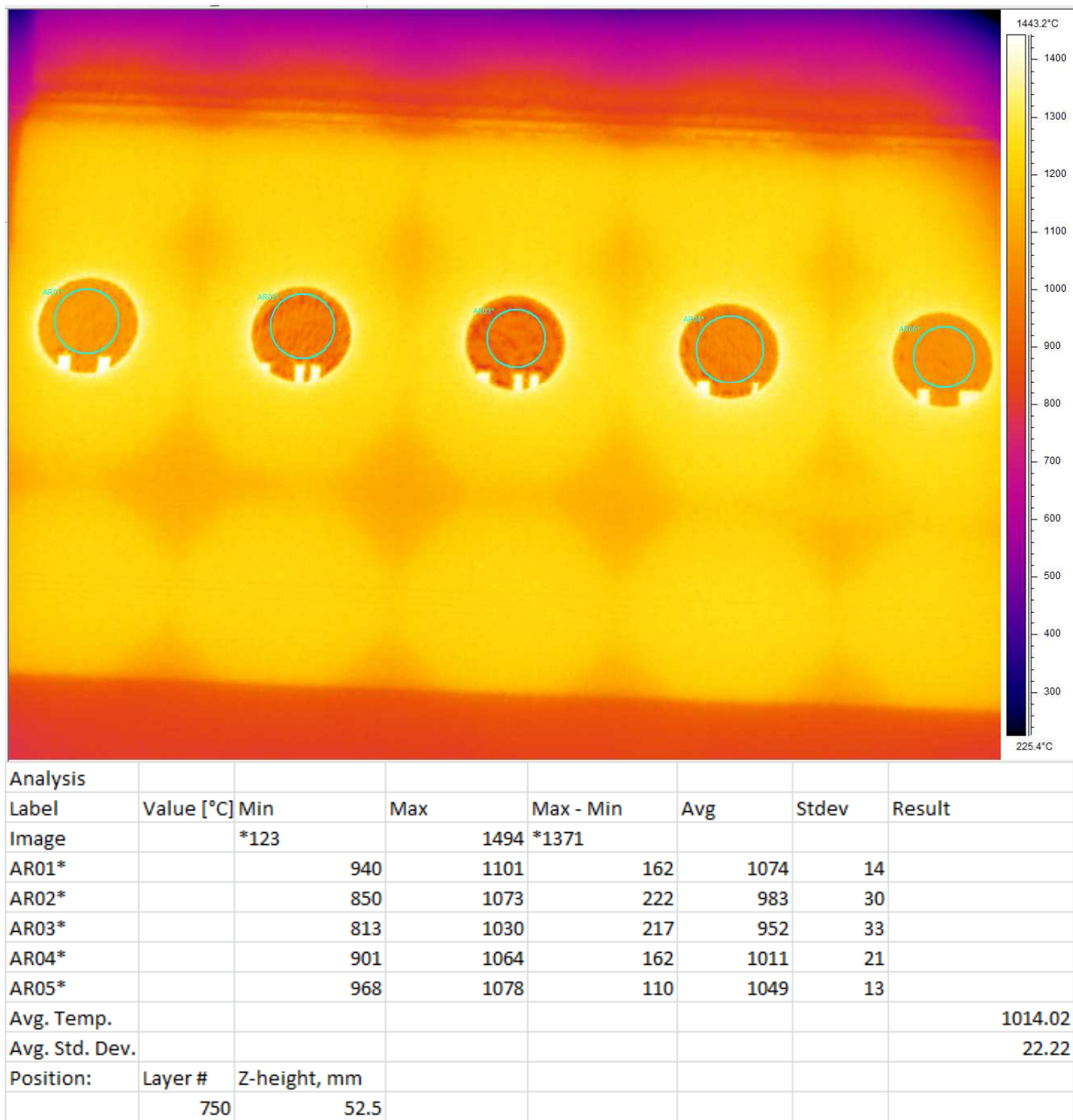


**FIGURE A-24 IR IMAGE OF HOT BUILD CYLINDERS AT Z= 52.50 MM**

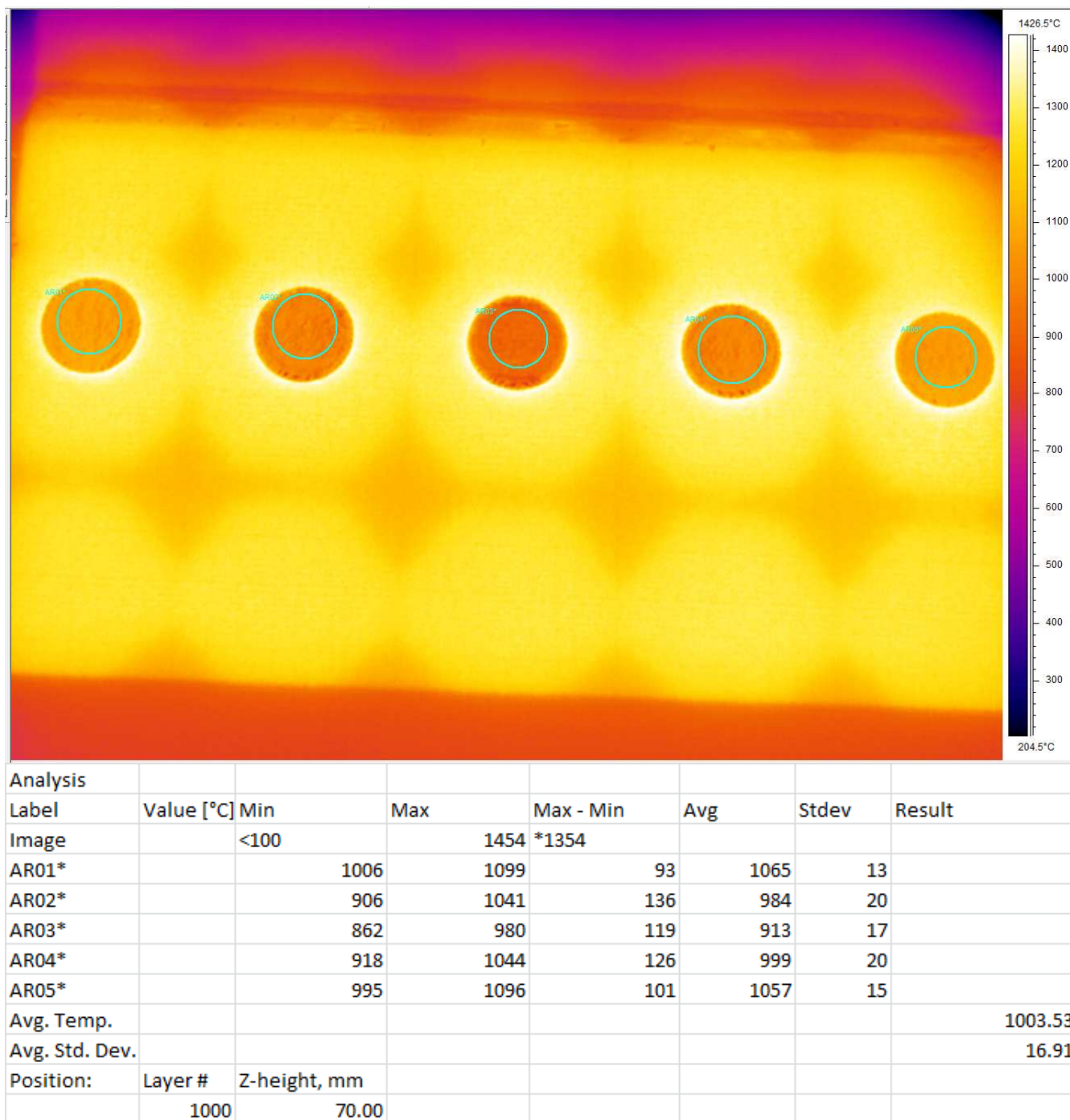
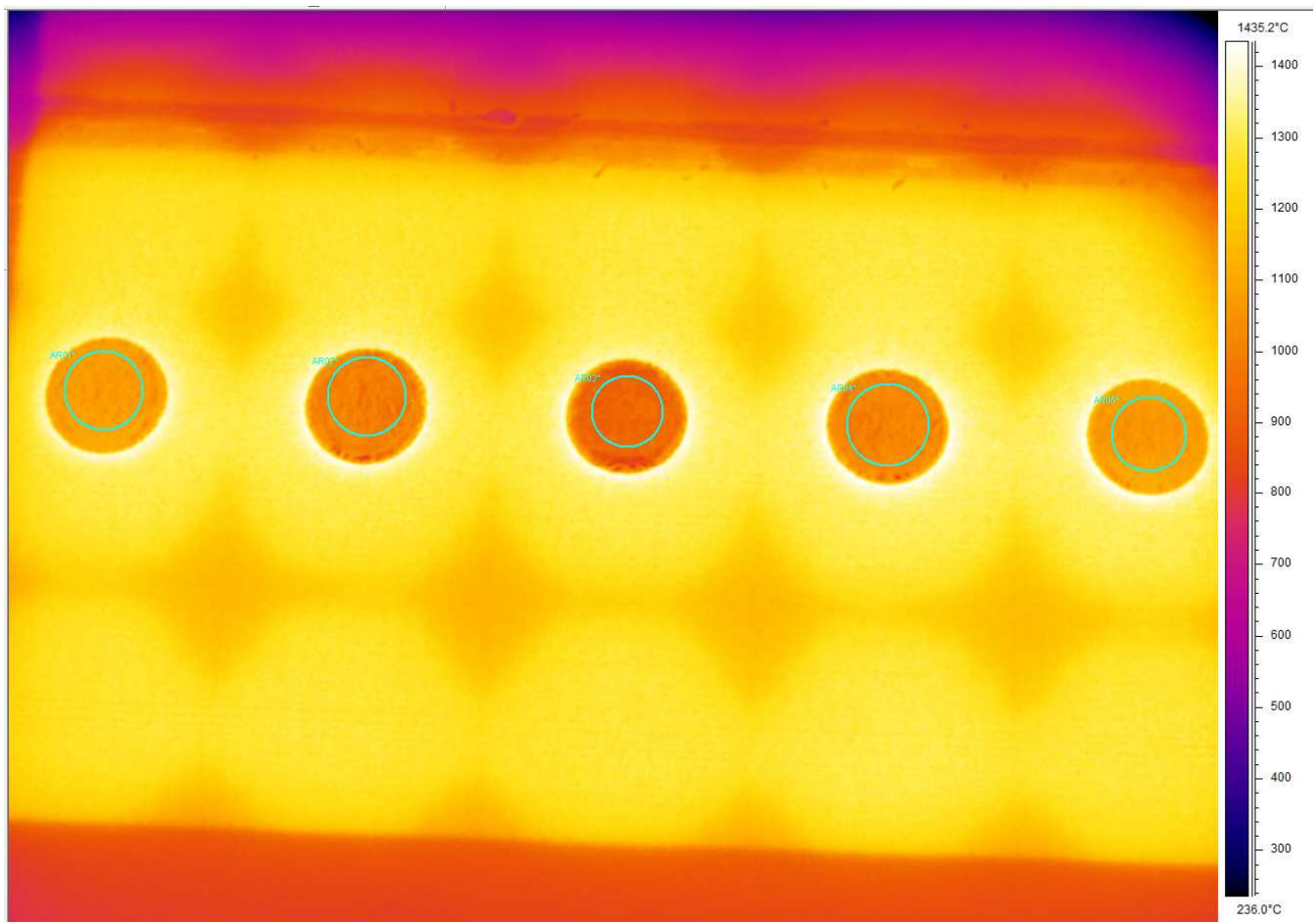


**FIGURE A-25 IR IMAGE OF HOT BUILD CYLINDERS AT Z= 70.00 MM**



Analysis							
Label	Value [°C]	Min	Max	Max - Min	Avg	Stdev	Result
Image		*130	1462	*1332			
AR01*		1031	1109	78	1078	11	
AR02*		927	1060	133	996	20	
AR03*		868	981	113	926	17	
AR04*		937	1063	125	1016	19	
AR05*		1021	1105	84	1072	14	
Avg. Temp.							1017.77
Avg. Std. Dev.							16.08
Position:	Layer #	Z-height, mm					
	1088	76.16					

**FIGURE A-26 IR IMAGE OF HOT BUILD CYLINDERS AT Z= 76.16 MM**

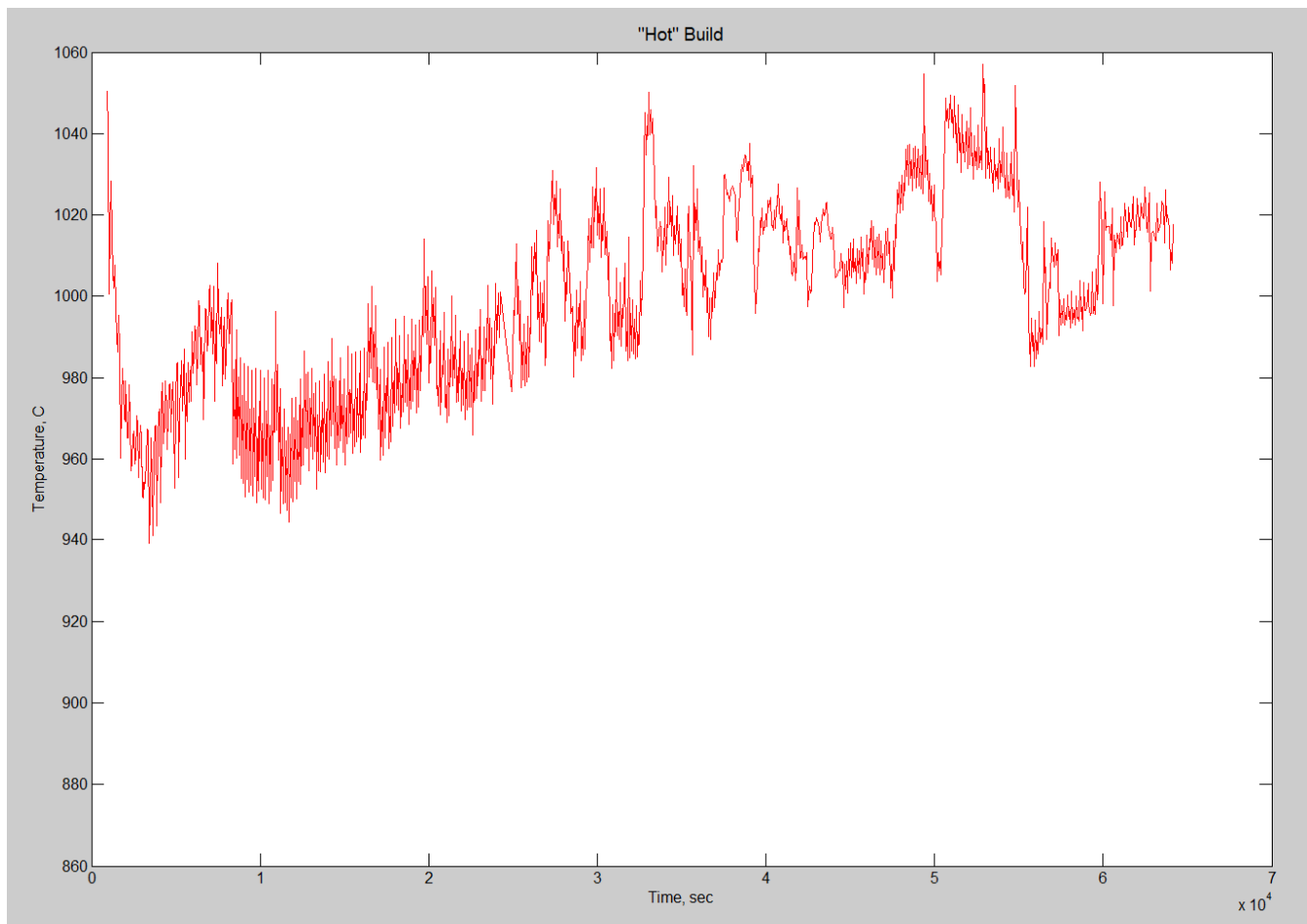


**FIGURE A-27 AVERAGE SURFACE TEMPERATURE MEASUREMENTS OF ALL FIVE CYLINDERS IN THE “HOT” BUILD THROUGHOUT THE COURSE OF THE BUILD.**

## APPENDIX B VIEW FACTOR DIAGRAMS

This appendix shows the view factor diagrams, with the associated dimensions, used in determining the view factors associated with the Arcam A2 wide heat shield. The six surface enclosure is represented by six independent surfaces that have been divided into sections that makes the use of flux algebra possible. The following figures are labeled top surface, left, right, rear, front, and bottom which represent the top shield, left, right, rear, and front heat shields, respectively. Each figure shows the corresponding sections on the bottom surface (build surface that the IR camera sees) to that of the reflective surface. All units are in millimeters.

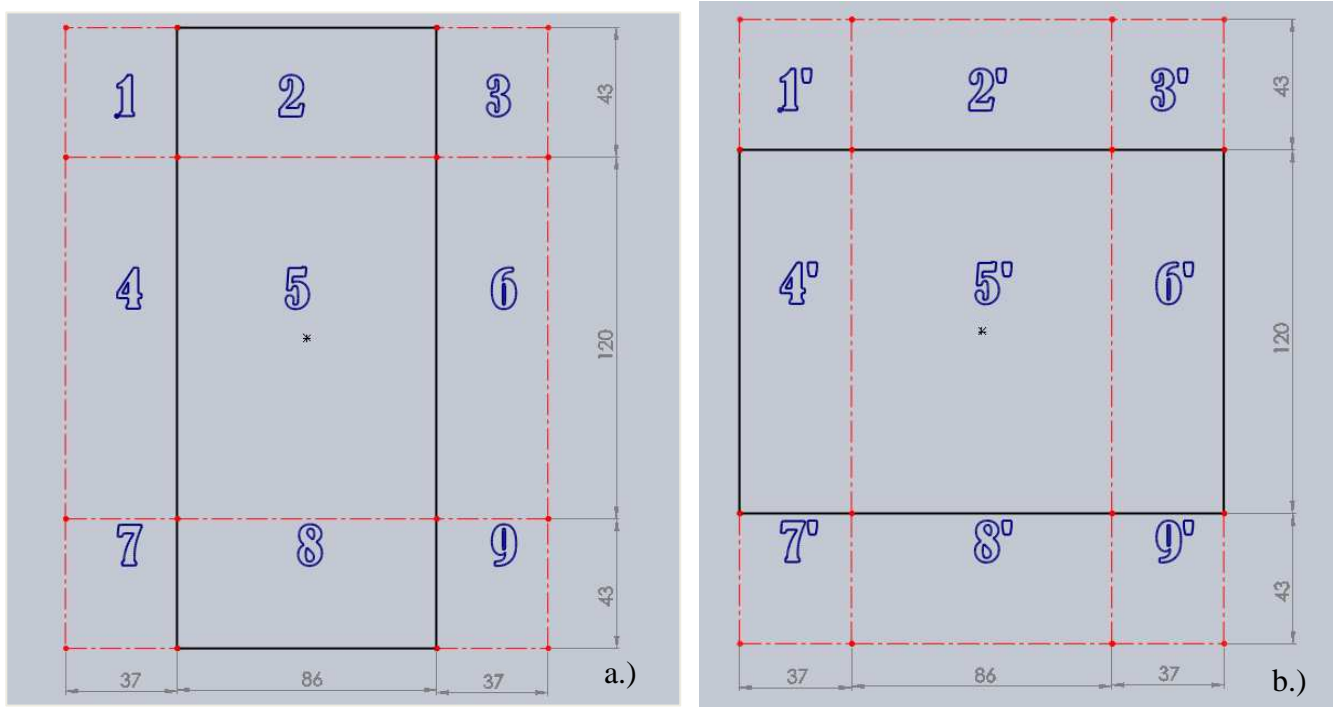


**FIGURE B-7-2 A.) TOP SURFACE, B.) BOTTOM SURFACE. THE DISTANCE BETWEEN BOTH SURFACES IS 305 MM.**



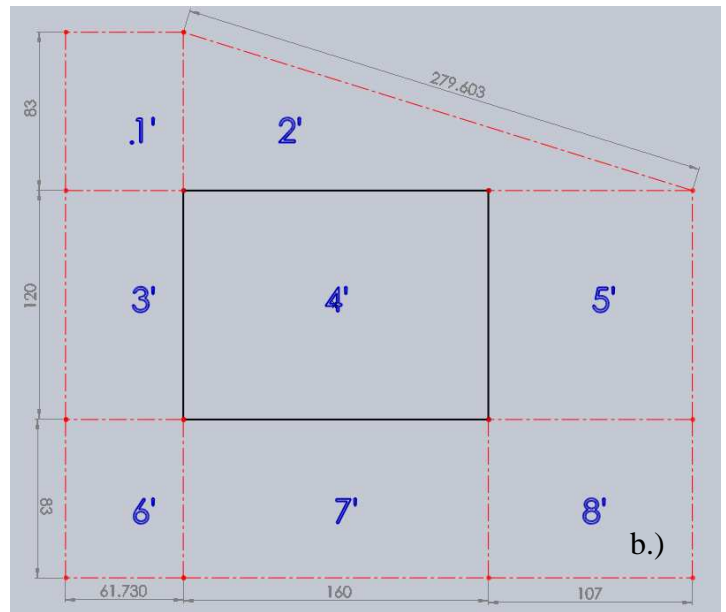
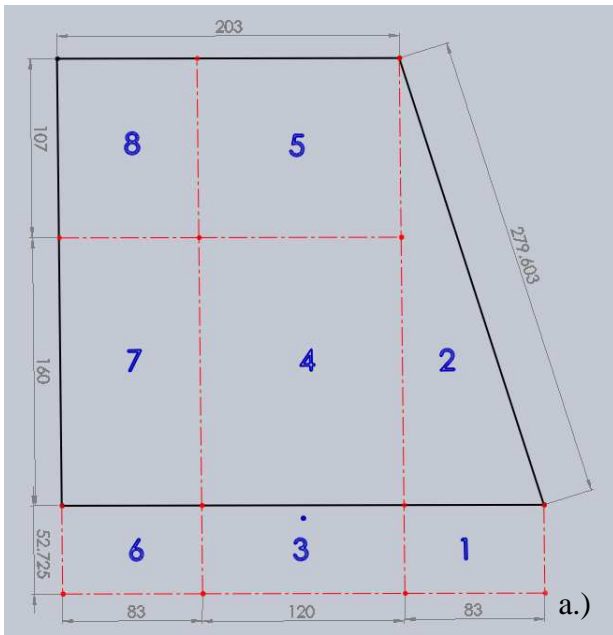


**FIGURE B-7-3 A.) LEFT/RIGHT SURFACE, B.) BOTTOM SURFACE. THE ANGLE BETWEEN BOTH SURFACES IS  $71.5^\circ$ .**

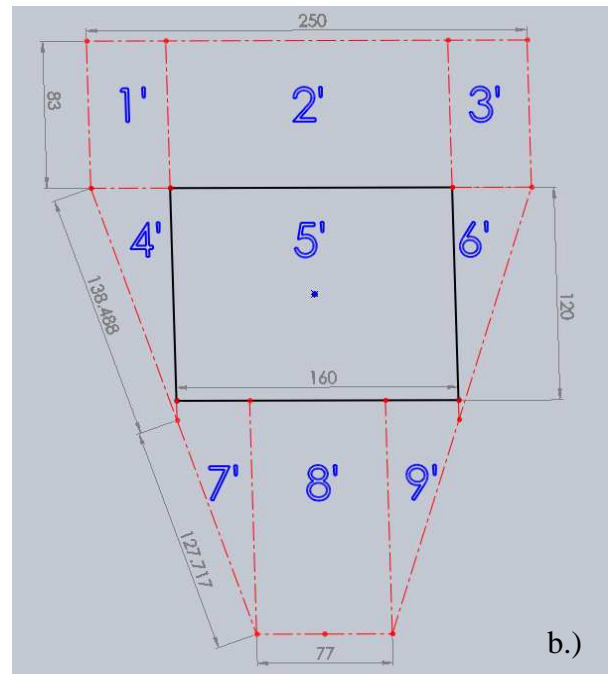
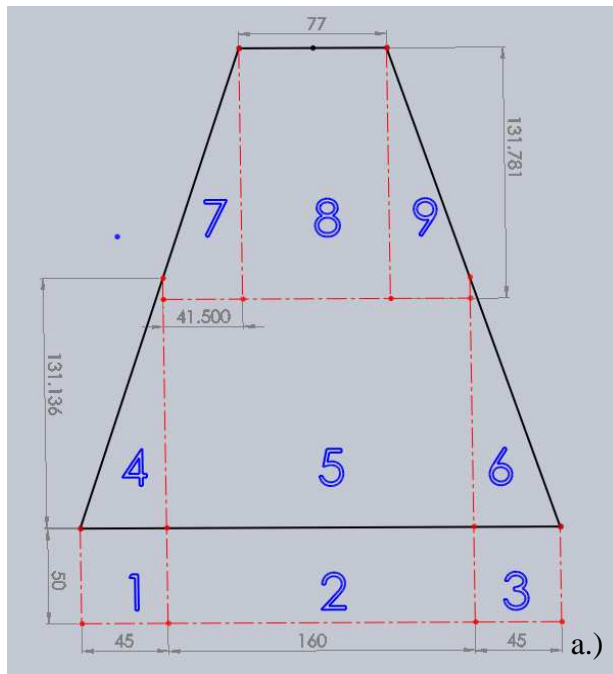


**FIGURE B-7-4 A.) FRONT SURFACE, B.) BOTTOM SURFACE. THE ANGLE BETWEEN BOTH SURFACES IS  $90^\circ$ .**

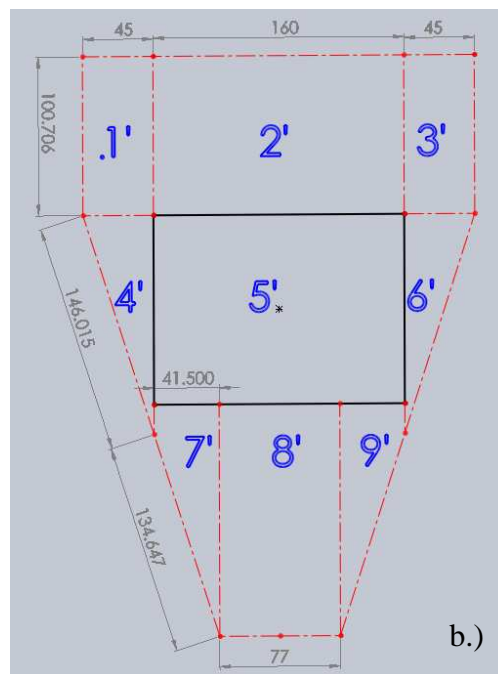
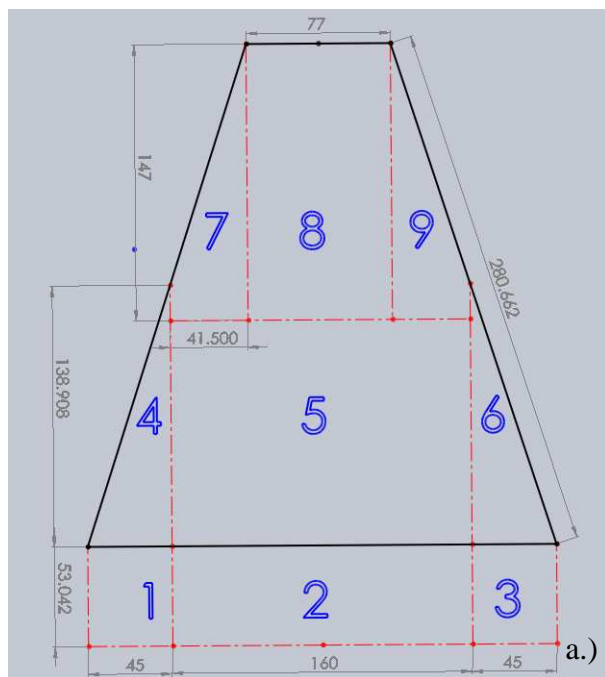


**FIGURE B-7-5 A.) REAR SURFACE, B.) BOTTOM SURFACE. THE ANGLE BETWEEN BOTH SURFACES IS 70.5°.**



## VITA

Emmanuel Rodriguez was born on January 7, 1986, in El Paso, Texas to Manuel Rodriguez and Patricia Rosales. He attended high school in Fort Hancock High School where he graduated in 2004. In July 2005, he enrolled at the local community college to begin his higher education. In his early college career he chose to pursue a career in business, but as he studied more of the profession he was about to embark on he became discouraged from the limited opportunities available and from a traditional desk job. He began to explore for something more challenging, as he researched the best careers for college students he stumbled upon engineering. He immediately became intrigued with combination of math and science to solve real world problems, and immediately switched to a career in mechanical engineering. After taking introductory courses in engineering at the community college, he became even more absorbed with an engineering career. In spring of 2008, he was awarded with Wolslager Foundation Transfer Scholarship that would fund his education at the University of Texas at El Paso (UTEP) until completion of his undergraduate studies. While an undergraduate, he worked as a research assistant at the W.M. Keck Center for 3D Innovation (Keck Center) with work related to microstreolithography. He was awarded his Bachelor of Science degree in Mechanical Engineering in December of 2010. In January 2011, he began his graduate studies at UTEP to pursue a Master of Science in Mechanical Engineering, and began research work at the Keck Center in the additive manufacturing of metals with electron beam melting technology.

Permanent address: P.O. Box 183  
Fort Hancock, TX 79839

This thesis was typed by Emmanuel Rodriguez.